Block Copolymers in Ionic Liquids

A DISSERTATION
SUBMITTED TO THE FACULTY OF THE GRADUATE SCHOOL
OF THE UNIVERSITY OF MINNESOTA
BY

Peter Mark Simone

IN PARTIAL FULFILLMENT OF THE REQUIREMENTS
FOR THE DEGREE OF
DOCTOR OF PHILOSOPHY

Timothy P. Lodge, Adviser

August 2009

Acknowledgements

Like most large accomplishments in life, completion of this thesis would not have been possible without the help and support of many people. First, I acknowledge and thank my adviser Tim Lodge for his guidance and support during my graduate career. Tim has been an outstanding teacher and mentor, from whom I have learned a great deal about polymer science and about scientific research in general. Additionally, there are many current and former members of the Lodge research group, and other research groups, that have helped me with various aspects of this project. I am particularly indebted to Yiyong He, who joined the Lodge research group as a post-doc shortly after I had begun my research. I received a great deal of general guidance from Yiyong on how to plan and carryout research and experiments, which was extremely valuable at those early stages of my project. I thank Zhibo Li and Kevin Davis for their guidance with the technique of cryo-TEM, and I also thank Kevin for his tutelage in anionic polymerization. Furthermore, I thank Mike Bluemle and Sayeed Abbas for helpful discussions pertaining to SAXS, and other topics. Finally, I thank Bryan Boudouris and Luciana Meli for assistance with various aspects of preparing and investigating block copolymer/ionic liquid solution thin films, and Paul Boswell for his assistance with the technique of impedance spectroscopy.

I must also thank my family and friends who have supported me over the past five years and beyond. First, I thank my wife Amanda. Her love and support have been unfailing throughout the ups and downs involved with both marriage and graduate school. I must also express my eternal gratitude to my parents. Without their continual love and encouragement over the course of my life I most certainly would not have made it to where I am today.

Peter Mark Simone
307 words

Abstract

In this thesis the self-assembly behavior of block copolymers diluted with ionic liquids has been investigated. Initial experiments involved characterizing the self-assembly of poly(styrene-*b*-methyl methacrylate) (PS–PMMA) and poly(butadiene-*b*-ethylene oxide) (PB–PEO) copolymers at dilute concentrations (~1 wt%) in the ionic liquids 1-butyl-3-methylimidazolium hexafluorophosphate ([BMI][PF_6]) and 1-ethyl-3-methylimidazolium bis(trifluoromethylsulfonyl)imide ([EMI][TFSI]). Dynamic light scattering and cryogenic transmission electron microscopy results showed that the ionic liquids behave as selective solvents for the PMMA and PEO blocks of the copolymers, and that the micelle morphology and self-assembly behavior of the block copolymers in the ionic liquids was analogous to that observed in conventional solvents.

At increased solution concentrations (≥ 20 wt%) the lyotropic mesophase behavior for PB–PEO diluted with [BMI][PF_6] and [EMI][TFSI], and poly(styrene-*b*-ethylene oxide) (PS–PEO) diluted with [EMI][TFSI] was investigated via small angle X-ray scattering. These experiments showed a microstructure phase progression with addition of ionic liquid that was analogous to that expected for an increase in the PEO volume fraction of the bulk copolymers. Additionally, an increase in the lamellar microstructure domain spacing with ionic liquid content indicated that both ionic liquids behave as strongly selective solvents for the PEO blocks of the copolymers.

The ionic conductivity of the concentrated PS–PEO/[EMI][TFSI] solutions was measured via impedance spectroscopy, and found to be in the range of 10^{-3} S/cm at

elevated temperatures (~100 °C). Additionally, the ionic conductivity of the solutions was observed to increase with both ionic liquid content and molecular weight of the PEO blocks of the copolymer.

Finally, preliminary investigations of the microstructure orientation in thin films of a concentrated PS–PEO/[EMI][TFSI] solution were conducted. The copolymer microstructure was observed to align perpendicular to the film surface with short term (≤ 2 hours) thermal annealing. Longer term thermal annealing resulted in a transition to parallel alignment of the copolymer microstructure relative to the film surface.

Table of Contents

List of Tables

Chapter 2

Chapter 3

List of Figures

Chapter 1

Chapter 2

Chapter 3

Chapter 4

Chapter 5

Chapter 1

Background

1.1 Introduction

A simple definition of a polymer can be given: a long chain of repeating units (monomers) covalently bound to form a single molecule. For a typical polymer, the number of monomers can range from several tens to several tens of thousands. Homopolymers are classified as consisting of only a single type of monomer. If two (or more) chemically distinct monomers make up the polymer molecule, it is referred to as a copolymer. The order of the different monomers in the copolymer chain can be completely random, possess a statistical order, or the different monomers can be ordered into blocks (*i.e.* lengths of the polymer chain consisting of a single monomer type). Copolymers belonging to the latter class are known as block copolymers.

Ionic liquids represent a class of ionic compounds characterized by melting points below 100 °C, and often below room temperature. The low melting points displayed by ionic liquids, relative to more common ionic compounds, are a result of their large, asymmetric, molecular constituent ions.

Block copolymers and ionic liquids represent two very active areas of research that span several scientific disciplines. They both represent classes of "designer compounds", which are known for the controllability of their physical and chemical properties through careful selection of their components. For block copolymers, much interest lies in controlling the spontaneous nano-scale ordering of their individual molecules, while for ionic liquids, the control and understanding of their solvation and other unique properties has received much attention. In light of the current interest in both block copolymers and ionic liquids, the premise of this thesis project is to study the behavior of block copolymers in ionic liquid solvents.

1.2 Block Copolymers

As mentioned above, one of the arrangements of the different monomer types in a copolymer is into blocks consisting of a single monomer type. These types of copolymers are known as block copolymers, and have been the topic of a vast amount of research, owing to their many unique properties.[1] The simplest block copolymer consists of two blocks of different monomers (A and B) covalently bound into a single linear chain. Obviously, moving beyond this simple AB diblock copolymer case, by varying the number of blocks, the block identities, and the connectivity of the blocks (*i.e.,* star copolymers, graft copolymers, etc.) results in a virtually limitless range of different block copolymers that could potentially be made.

1.2.1 Block Copolymer Self-Assembly in the Bulk

Arguably, the most interesting and useful property of block copolymers is their spontaneous ordering on the nano-scale into well defined microstructures.[2,3] This

behavior is the result of chemical incompatibility between the dissimilar monomers that make up the blocks of the copolymer. As a result of their typically high molecular weight, the entropy benefit for mixing the blocks of the copolymer is low, thus, even small incompatibility will result in a drive for the blocks to segregate. The common microstructures formed by a simple AB diblock copolymer include cubic lattices of spheres (S), hexagonally packed cylinders (C), the bicontinuous gyroid (G), and lamellae (L) (Figure 1.1). The segregated domains of the copolymer microstructures essentially consist of a single block type, and are typically in the size range of 10–100 nm. The unfavorable enthalpic interactions between the blocks of the copolymer result in a drive for the blocks to adopt a fully stretched conformation in order to reduce the interfacial contact area between the microstructure domains. However, there is a large entropic penalty associated with a fully stretched chain. Thus, from an entropic standpoint, there exists a drive for the copolymer blocks to adopt a random coil conformation. The self–assembly behavior for a particular copolymer is thus governed by the free energy balance between reducing the interfacial contacts between dissimilar blocks, and reducing the degree of chain stretching.

In relation to its microstructure phase behavior, a block copolymer is typically described by three parameters. First is the total degree of polymerization (N) for the copolymer. Second is the block volume fraction (f) (copolymer composition), where for a simple AB diblock $f_A = N_A/N$. Finally, the thermodynamic interaction between the different monomer types is given by the Flory–Huggins interaction parameter (χ). The interaction parameter represents the energy cost for interchanging two dissimilar

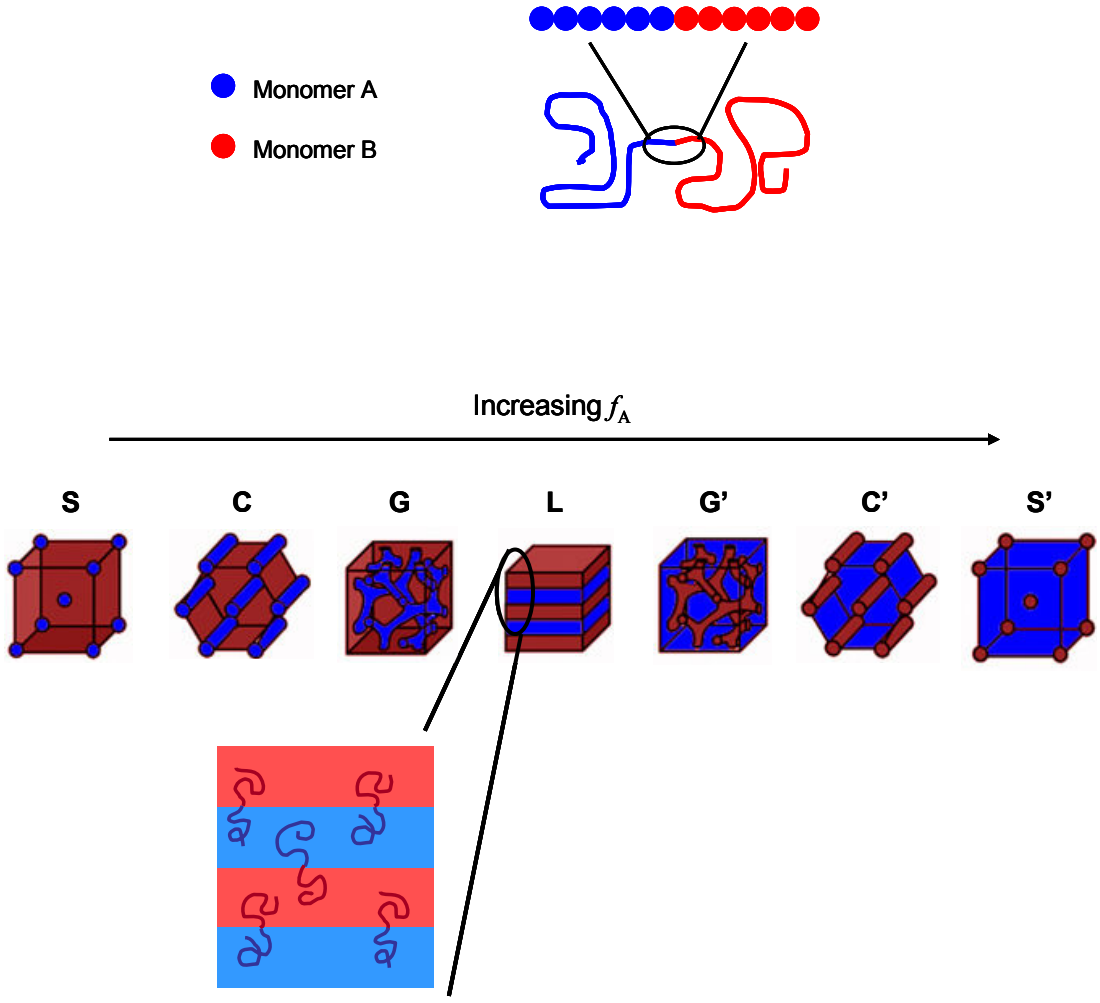

Figure 1.1: Schematic representation of an AB diblock copolymer and common self-assembled AB diblock copolymer microstructures: Cubic lattice of spheres (bcc symmetry) (S); Hexagonally packed cylinders (C); Bicontinuous gyroid (G); Lamellae (L).

monomers, relative to the pure states. Thus positive χ values indicate unfavorable interactions between the different monomer types, and negative values represent favorable interactions that promote mixing of the blocks. Typically, χ displays an inverse dependence on temperature, and thus thermotropic transitions are often observed in the phase behavior of block copolymers. The first two parameters, N, and f, can be controlled via the stoichiometry of the polymerization, and χ is controlled by the choice of monomers and temperature.

The product χN, referred to as the degree of segregation, can be taken as a measure of the free energy balance between the monomer interactions and the block stretching. Thus, the magnitude of χN, along with the copolymer composition, determines the thermodynamically stable microstructure for a particular copolymer. Matsen and coworkers have extended earlier theories involving the melt phase behavior of block copolymers,[4–7] and have mapped the theoretical χN vs. f phase diagram for AB diblock copolymers.[8–10] Experimental diblock behavior has been shown to agree well with the theoretically obtained phase diagram.[11] Additionally, Cochran, *et al.* have theoretically established the stability of the gyroid microstructure at high degrees of segregation.[12] For AB diblocks, the χN vs. f phase diagram shows a general progression from lamellar microstructure, to the gyroid, to hexagonal packed cylinders, to body centered cubic packed spheres, as the asymmetry of the copolymer molecule is increased from the symmetric diblock case ($f_A = 0.5$). This behavior comes from a drive to reduce free energy by adopting a microstructure domain interface that is curved toward the minority block domain (*i.e.*, cylinders in C, and spheres in S). The interfacial

curvature allows the blocks of the majority domain to relax, thus increasing conformational freedom.

Many current applications of block copolymers do not take specific advantage of their self-assembled microstructures. However, there are some examples of block copolymer applications that do rely on their ability to spontaneously assemble into well ordered structures on the nano-scale. Perhaps one of the most reported applications is the use of self-assembled block copolymers as nano-porous materials, or as templates for the preparation of nano-scale materials.[13–16] However, one drawback to utilization of self-assembled block copolymers is that on a larger scale, the microstructures exist in isotropically oriented domains or grains, which are typically several microns per side. Thus, it is often necessary to employ some type of alignment procedure in order to obtain anisotropic microstructure orientations. One potential way to avoid the need to align the copolymer microstructure would be to utilize block copolymers that display the bicontinuous gyroid microstructure.[17]

1.2.2 Block Copolymer Self-Assembly in Solution

The self-assembly behavior of block copolymers in solution has also garnered much research interest.[1,18] In dilute solutions, amphiphilic block copolymers have been shown to display self-assembly behavior analogous to that of low molecular weight amphiphiles, such as surfactants and lipids.[19,20] The general self-assembly process consists of association of the insoluble (lyophobic) copolymer blocks to form the densely packed cores of micellar structures, which possess a solvated shell, or corona, formed by the soluble (lyophilic) copolymer blocks. This self-assembly process is

spontaneous at copolymer concentrations above the critical micelle concentration (CMC). At the CMC, the formation of micelles is marked by a discontinuity in the change of solution properties, such as surface tension, and turbidity, with amphiphile concentration. The CMC tends to decrease rapidly as amphiphile molecular weight increases, thus amphiphilic block copolymers tend to display vanishingly low CMCs. As a result, amphiphilic block copolymers tend to form micelles characterized by fairly high aggregation numbers ($N_{agg} \geq 100$ chains), as well as kinetically frozen micelles that are characterized by undetectably slow exchange of single copolymer chains (unimers).[21,22] In addition to extremely low CMCs, the self-assembly behavior of amphiphilic block copolymers offers other advantageous characteristics. For example, block copolymers tend to form larger, more physically robust micelle structures than conventional low molecular weight surfactants,[23,24] and they offer the potential to readily tune the size and morphology of the micelle structures simply by changing the molecular weight or architecture of the copolymer blocks.[25] Thus, block copolymer micelles have been investigated for use in a wide array of applications, such as nanoparticle synthesis, chemical separations, and various biomedical applications.[18]

The most common micelle morphologies observed for simple AB diblock copolymers include spheres, cylinders (worms), and bilayer vesicles (Figure 1.2). The thermodynamically stable micelle morphology for a particular block copolymer is determined by a balance between the free energies of the micelle core (F_{core}), the micelle corona (F_{corona}) and the core-corona interface (F_{int}). The three free energy terms F_{core}, F_{corona}, and F_{int} are mainly dependent upon the stretching of the core chains, the

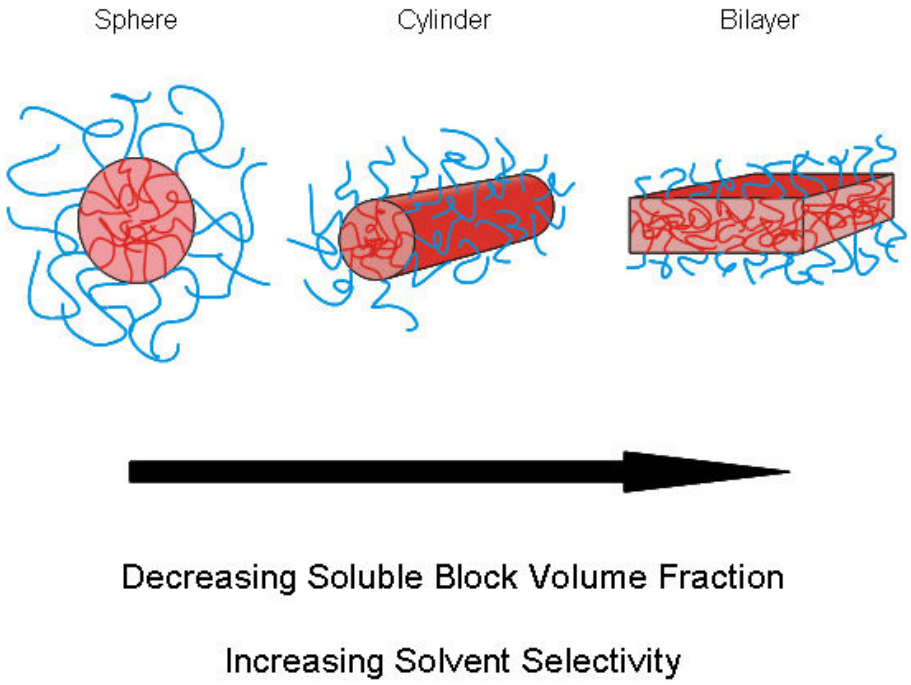

Figure 1.2: Common micelle morphologies observed for AB diblock copolymers. The arrow represents the progression of morphology with decreasing volume fraction of the soluble block or increasing solvent selectivity.

stretching of the corona chains, and the interfacial tension at the core-corona interface, respectively. Thus, the morphology of block copolymer micelles can be controlled by changing the lengths of the copolymer blocks (*i.e.*, changing *f*), or by changing the selectivity of the solvent, or both. For example, in the case of a block copolymer with a soluble block that is longer than the insoluble block, a spherical micelle shape is preferred. This is because the spherical shape allows the most space for the corona chains, and thus they are able to adopt less stretched conformations resulting in lower values of F_{corona}. As the length of the soluble block is decreased the shorter corona chains experience less crowding, and thus an increase in N_{agg} is observed. This results in an increase in the micelle core radius (R_c) and thus an increase in F_{core} due to a higher degree of stretching for the core chains in order to maintain a uniform core density. Additionally, F_{int} also increases as the corona block length decreases due to decreased shielding of the unfavorable interactions between the solvent and the core blocks. These factors lead to a drive for the micelle to adopt a morphology with a lower degree of interfacial curvature, in order to lower the core-corona interfacial tension, and the degree of stretching of the core blocks. Thus a transition from spherical micelles to cylindrical micelles, and ultimately to bilayer vesicles is observed upon reduction of the soluble copolymer volume fraction, at constant solvent selectivity.

Similarly, the stable micelle morphology can also be controlled by changing the selectivity of the solvent. At low solvent selectivity, N_{agg} and the core-corona interfacial tension are typically low, and thus the total free energy of the micelle is dominated by F_{corona}. Thus, spherical micelles are preferred in order to minimize the extent of corona

chain stretching. As solvent selectivity is increased, N_{agg} of the spherical micelles also increases, due to a drive to reduce the unfavorable interactions between the core blocks and the solvent by reducing the net interfacial surface area per chain. As the solvent selectivity is further increased, the entropic stretching penalty for the core chains with increasing N_{agg} becomes too great, and a transition from spheres to cylinders is observed. The sphere to cylinder transition also results in a decrease in the core-corona interfacial tension due to a decrease in the interfacial curvature. Finally, at sufficient solvent selectivity a transition from cylinders to bilayer vesicles occurs, resulting in a further decrease in the core-corona interfacial curvature. In practice, solvent selectivity can be controlled by changing or blending solvents,[26] or by changing temperature.[27]

Multiple theoretical studies relating to the self-assembly of block copolymers in dilute solution have been performed. Methods based on scaling theories,[28,29] and mean field calculations have been employed.[30,31] Recently, Zhulina, *et al.* have compared theoretical and experimental results of the thermodynamic stability ranges for spherical, cylindrical, and bilayer vesicle morphologies.[32] Among other things, their results predict the stability of crew-cut (corona thickness less than core radius) spherical micelles, and show that F_{core} is small compared to F_{corona} and F_{int} for all morphologies. However, F_{core} was shown to be important in determining the transitions between different micelle morphologies.

As the concentration of block copolymer in solution is increased, the formation of ordered microstructures, akin to those of the bulk copolymer, is observed. For an AB diblock, the presence of the solvent results in two additional interaction parameters for

the system. In addition to the interaction parameter between the blocks of the copolymer (χ_{AB}), the system is also characterized by the interactions between the solvent (S) and two copolymer blocks (χ_{AS}, χ_{BS}). In general, the quality of a solvent can be defined as poor ($\chi > 0.5$), marginal (theta-solvent) ($\chi = 0.5$), or good ($\chi < 0.5$).

For the case of a neutrally good solvent ($\chi_{AS} = \chi_{BS} < 0.5$), the solvent effectively screens the unfavorable interactions between the copolymer blocks. Thus, the block interactions for a copolymer diluted with a neutral solvent are typically described by an effective interaction parameter (χ_{eff}). Generally, the effective interaction parameter can be estimated from the melt phase interaction parameter using the dilution approximation ($\chi_{eff} = \phi\chi_{AB}$), where ϕ is the copolymer concentration. Thus, the general decrease in the unfavorable interactions between the blocks of the copolymer shows that dilution with a neutral solvent will have a qualitatively similar effect on the melt phase behavior as an increase in temperature. The overall reduction in the strength of the block interactions results in an increase in the interfacial area per chain, which is due to relaxation in the degree of chain stretching and subsequent expansion in the lateral dimension. This reduction in the degree of chain stretching normal to the domain interface results in a characteristic decrease in the overall domain spacing of block copolymer microstructures when they are diluted with a neutral solvent.

A selective solvent displays a differential affinity for the copolymer blocks ($\chi_{AS} \neq \chi_{BS}$). Here, the case where the solvent is a good solvent for one of the copolymer blocks and poor for the other will be considered. In this case, dilution of the block copolymer results in preferential swelling of the microstructure domains composed of

the soluble copolymer blocks. This can be taken as an analogous increase in the copolymer volume fraction of the soluble blocks. Additionally, the introduction of unfavorable interactions between the solvent and the insoluble blocks results in an overall increase in the degree of segregation. Thus, the drive to reduce the unfavorable interactions leads to increased chain stretching normal to the domain interface, in order to reduce the interfacial area per chain. This results in the characteristic increase in microstructure domain spacing observed with dilution of a block copolymer with a strongly selective solvent. Thus, dilution with a selective solvent has a qualitatively similar effect on the melt phase behavior as a simultaneous increase in soluble block volume fraction and decrease in temperature. However, additional complexity over this idealized strongly selective solvent case is expected with varying degrees of solvent selectivity (*i.e.*, a solvent that is differentially good for both blocks, good for one block and a theta solvent for the other, etc.).

Due to changes in the effective f and χ upon dilution of an ordered block copolymer with solvent, it is clear that such systems should display lyotropic phase transitions upon varying solution concentration. Many theoretical and experimental studies have been aimed at understanding the behavior of a wide range of different copolymer solutions, both aqueous and organic. For example, Huang and Lodge utilized self-consistent mean-field theory to construct the phase diagrams for ordered block copolymer solutions as a function of solvent selectivity, temperature, concentration, copolymer composition, and total molecular weight.[33] One key result from this study was increasing solvent selectivity causes the block copolymers to form ordered

structures at lower degrees of segregation. Additionally, it was shown that for a constant degree of segregation, increasing solvent selectivity for the minority (B) block results in a general phase transition sequence of: disorder → S_B → C_B → L → C_A → S_A → phase separation (note that complex ordered phases such as G were not explicitly treated).

Additionally, Hanley, *et al*. have performed extensive experimental investigations of the phase behavior of poly(styrene-*b*-isoprene) (PS–PI) diblocks in solvents of various selectivity.[34–37] Figure 1.3 shows representative temperature vs. concentration phase diagrams mapped by Hanley for a PS–PI diblock in four different solvents of varying selectivity. The wealth of experimental results obtained by Hanley both support theoretical results, and show phase behavior not predicted by theory. For example, an increase in the order-disorder transition temperature (*i.e.*, increasing stability of the ordered phase) with increasing solvent selectivity, from bis(2-ethylhexyl) phthalate (DOP), to di-*n*-butyl phthalate (DBP), to diethyl phthalate (DEP), is observed. Additionally, fairly wide regions of coexisting L and C microstructure are attributed to exacerbation of the chain packing frustration of the G phase as the effective degree of segregation is increased due to the addition of selective solvents such as DEP.

1.3 Ionic Liquids

1.3.1 Ionic Liquid Background

The contemporary definition of an ionic liquid is, a salt with a melting temperature below 100 °C. The preparation of ethylammonium nitrate in 1914 is often cited as the first reported ionic liquid synthesis.[38] However, the modern era for ionic liquids did not begin until the late 1970s and early 1980s when the synthesis and

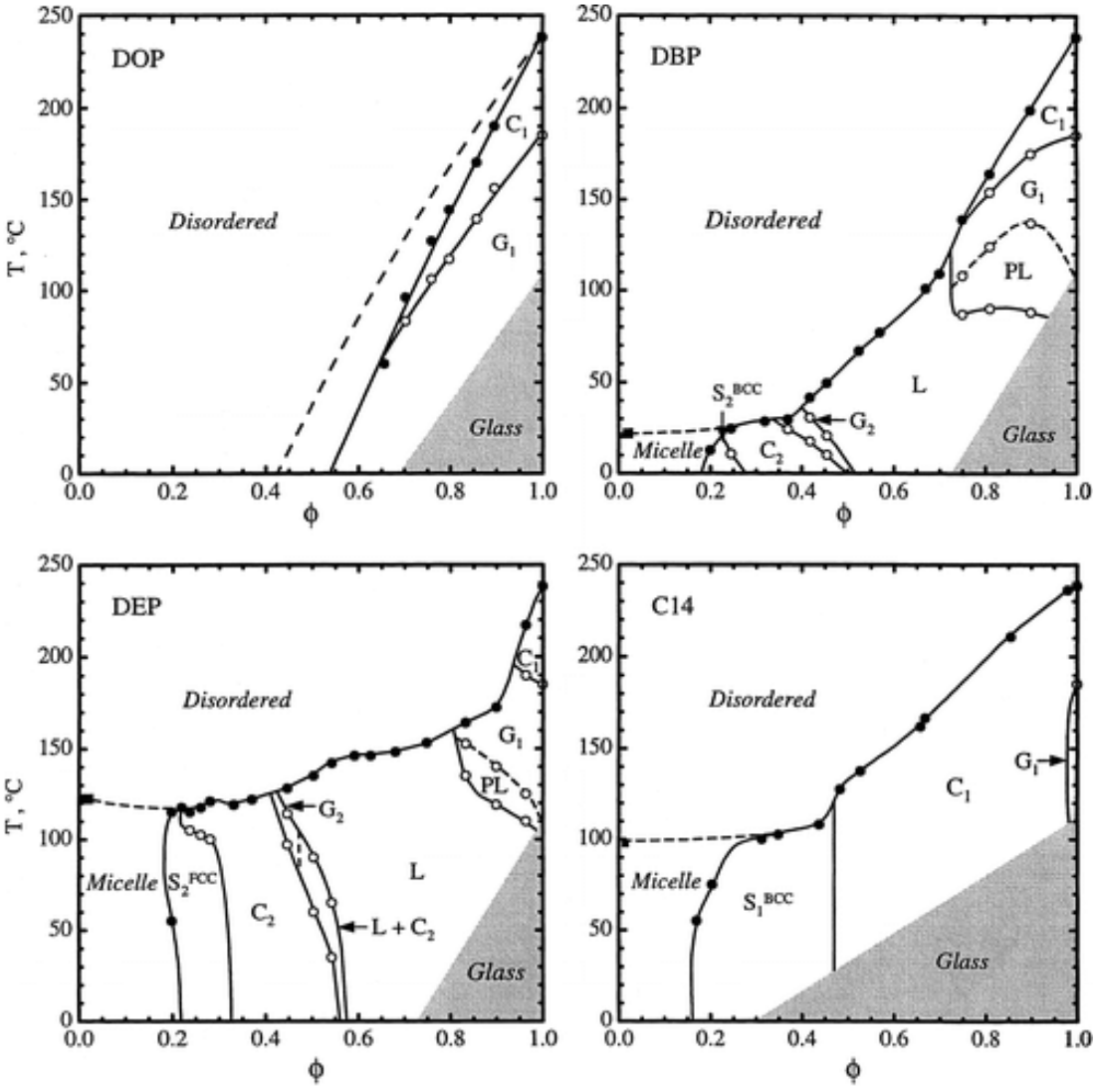

Figure 1.3: Phase diagrams for PS–PI diblock copolymer solutions in bis(2-ethylhexyl) phthalate (DOP), di-*n*-butyl phthalate (DBP), diethyl phthalate (DEP), and *n*-tetradecane (C14). Molecular weight of the styrene block is 11 kg/mol, and molecular weight of the isoprene block is 21 kg/mol Solvent selectivity for the styrene blocks of the copolymer increases as DOP < DBP < DEP. C14 is selective for the isoprene blocks of the copolymer. Subscript 1 on the microstructure labels represents PS blocks residing in the minor domains of the microstructure, and subscript 2 represents PI blocks residing in the minor domains. PL represents the metastable perforated lamellae microstructure. (Reproduced with permission from Macromolecules, Vol. 33, 5918–5931 (2000). Copyright 2000, American Chemical Society.)

properties of several pyridinium- and imidazolium- based chloroaluminate ionic liquids were reported.[39,40] These haloaluminate ionic liquids were shown to be useful as novel solvents,[41] however, their popularity did not catch on due to the reactivity of the haloaluminate anions with water. Then, in the early to mid 1990s, the first reports on alkylimidazolium–based ionic liquids with water-stable anions were published.[42–44] These types of ionic liquids with anions, such as tetrafluoroborate, hexafluorophosphate, and nitrate, have led to the groundswell of research involving ionic liquids and their potential applications in the last 10–15 years.[45–49]

Some of the more common ions currently used to prepare ionic liquids are shown in Scheme 1.1. As can be seen, the ions are typically large, asymmetric and possess delocalized charge. These ion characteristics lead to a reduction in the effective Coulombic attraction between the ions, and in a hindrance to their ability to form well ordered crystal lattices. This results in the uniquely low melting points for ionic liquids, as compared to inorganic salts (*e.g.*, NaCl m.p. ~800 °C). For example, it has been shown for several series of 1-alkyl-3-methylimidazolium based ionic liquids that an increase in the alkyl chain length of the cation results in a decrease in the observed melting temperature.[50–52] Interestingly, longer alkyl chains ($C_n \geq 10$) were shown to result in an increase in ionic liquid melting point, and also lead to the appearance of liquid crystalline phases in the ionic liquid phase diagrams.[50,53] These results are attributed to an increase in dispersive interactions between the alkyl chains as their length is increased. In another study of ionic liquid melting temperatures, Krossing, *et al.* used a Born-Haber-Fajans cycle to calculate the molar Gibbs energy of fusion

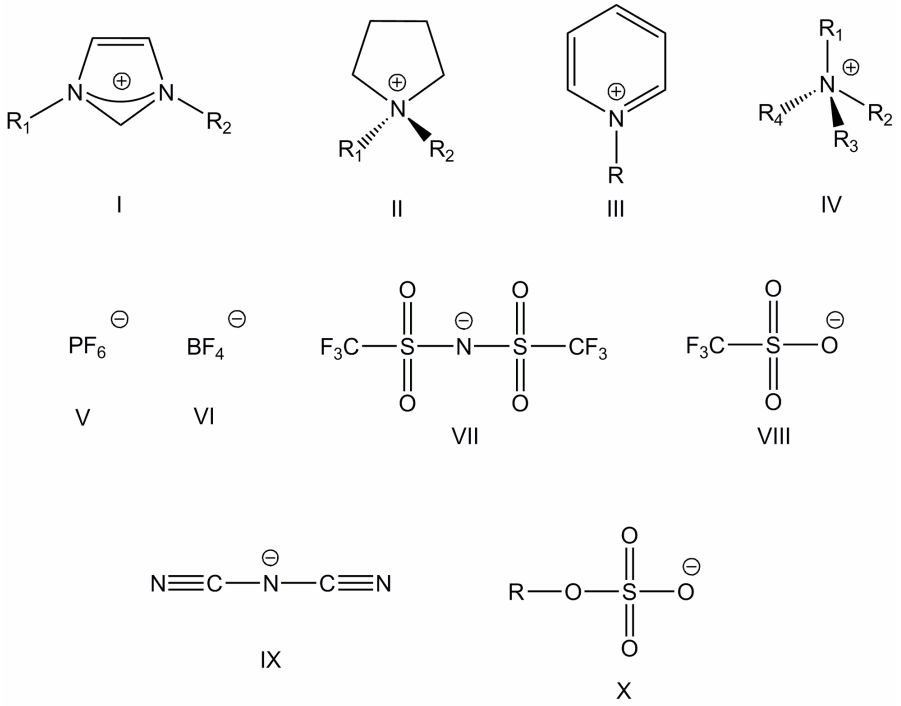

Scheme 1.1: Common ions used to prepare ionic liquids. I: 1,3-dialkylimidazolium; II: 1,1-dialkylpyrrolidinium; III: 1-alkylpyridinium; IV: Tetraalkylammonium; V: Hexafluorophosphate; VI: Tetrafluoroborate; VII: Bis(trifluoromethylsulfonyl)imide (TFSI); VIII: Trifluoromethanesulfonate (TfO); IX: Dicyanimide; X: Alkylsulfate.

($\Delta_{fus}G_m$) for several ionic liquids.[54] The cycle related $\Delta_{fus}G_m$ to the lattice Gibbs energy for sublimation of the ions ($\Delta_{latt}G_m$) and the Gibbs energy of solvation ($\Delta_{solv}G_m$) for the transfer of gas phase ions to the ionic liquid medium. The overall result of negative $\Delta_{fus}G_m$ for the ionic liquids was due to the relatively low $\Delta_{latt}G_m$ values that could easily be overcome by the solvation free energy of the ions in the bulk ionic liquid. The low lattice energies for the ionic liquids were attributed to the large size and conformational flexibility of the ions.

In addition to uniquely low melting temperatures for ionic compounds, ionic liquids also possess many other interesting and potentially useful properties. Perhaps one of the most well known and well cited ionic liquid properties is their negligible volatility. Indeed, ionic liquid vapor pressures are undetectable at room temperature, however, several reports have detected measurable vapor pressures for ionic liquids at reduced pressure and elevated temperature.[55–57] In addition to being relatively non volatile, many ionic liquids also possess fairly high thermal stability. Depending on the rate and duration of heating, and the atmosphere (*i.e.*, ambient vs. inert), ionic liquids typically begin to display mass loss due to degradation in the range of 200–400 °C.[58–60] Additionally, it has been shown that ionic liquid stability is dependent upon the ion identities, particularly the anion identity, where less nucleophilic anions result in greater ionic liquid thermal stability.[45] Thus, high thermal stability, coupled with low melting points and negligible volatility give ionic liquids a uniquely wide usable liquid phase range, up to several hundred degrees in some cases.

1.3.2 Ionic Liquids as Solvents

A wide liquid phase range is one of many characteristics that have spurred the investigation and use of ionic liquids as alternative solvents in many applications, particularly synthesis and catalysis.[61–64] Additionally, ionic liquids have generally been touted as potential "green" replacements for volatile organic solvents in many applications. This is a result of their nonvolatile nature and their potential recyclability.[45] Typically, recycling protocols for ionic liquids used in synthesis and catalysis take advantage of the low solubility of many ionic liquids in organic solvents and/or water, which allows simple extraction of organic or salt byproducts. Additionally, low ionic liquid volatility allows for direct distillation of volatile reaction products. However, there has been some tempering of the blanket classification of ionic liquids as green solvents. This has mainly been the result of limited toxicity information for many ionic liquids, which is generally due to the high rate of synthesis of new ionic liquids.[65,66]

Regardless of their eco-un/friendliness, the use of ionic liquids as alternative solvents has been established, and has resulted in a wide area of research involved with characterizing and potentially predicting the solvent properties of ionic liquids. These efforts have been driven by the potential of utilizing ionic liquids as "designer solvents". By characterizing the physical and chemical solvent properties of a wide range of ionic liquids, it is hoped that trends based on the constituent ion identities can be used to predict the solvent properties of new ion combinations. In this way ionic liquid solvents could potentially be designed, through judicious ion selection, to possess

specific properties desirable for a certain application. Multiple techniques for characterizing ionic liquid solvent properties have been employed, including solvatochromic probe interactions,[67–71] liquid-liquid[72] and liquid-gas[73] partitioning of solutes, and dielectric spectroscopy.[74,75] The results obtained from many of these techniques have been recently reviewed.[76,77] One of the most commonly used empirical polarity scales is based on the solvatochromic shift in the visible absorption spectrum of the zwitter-ionic dye betaine-30 (Reichardt's dye) upon dissolution in solvents of differing polarity.[78] The shift is often expressed in terms of a normalized shift factor $\left(E_{\mathrm{T}}^{\mathrm{N}}\right)$, which is defined as one for water and zero for tetramethylsilane. The $E_{\mathrm{T}}^{\mathrm{N}}$ values have been compiled for many ionic liquids,[79] and in general they fall within the range of 0.50–0.70 for imidazolium based ionic liquids. This suggests these ionic liquids display polarity similar to short chain alcohols (*e.g.*, ethanol, 1-propanol). Alternatively, another solvatochromic probe method developed by Kamlet, Abboud, and Taft[80,81] uses combinations of different dyes to determine the contributions of different solvent properties to the solvatochromic shifts observed. Crowhurst, *et al*. have applied the Kamlet-Abboud-Taft method to several ionic liquids, using three dyes (Reichardt's dye, *N,N*-diethyl-4-nitroaniline, and 4-nitroaniline).[71] They were able to evaluate the dipolar/polarizability factor (π^*), H-bond basicity (β) and H-bond acidity (α) for several imidazolium and pyrrolidinium based ionic liquids. In general they found fairly high π^* values, close to those of water and DMSO. They also observed a fairly wide range of α and β values, where the H-bond acidity was mainly determined by the cation identity and the H-bond basicity depended on the anion. In general there is some level of

discrepancy between ionic liquid solvent properties determined via different experimental methods, in particular, polarity values which range from moderately to highly polar. This highlights the difficulty in applying solution characterization methods, traditionally developed for neutral molecular solvents, to ionic liquids, where a single ionic liquid is capable of participating in multiple solvent-solute interactions (*e.g.*, dispersion interactions, dipole-dipole, ion-dipole).

1.3.3 Ionic Liquid Electrochemical Properties

In addition to wide liquid phase ranges and low vapor pressures, ionic liquids also possess unique properties that expand their potential applications beyond simply being used as alternative solvents. Most ionic liquids display very good electrochemical stability, as shown by the wide range of voltages over which they are electrochemically inert. The electrochemical "window" for a particular ionic liquid is typically limited by the reduction potential of the cation and oxidation potential of the anion. Typically, cyclic voltammetry or linear sweep voltammetry is used to measure the electrochemical widows of ionic liquids. The electrochemical windows for many ionic liquids have been reported and several generalities can be drawn from the tabulated results.[45,48,82] In general, many ionic liquids display fairly wide electrochemical windows, usually in the 4–6 V range. The overall trend in cation stability follows: pyridinium < imidazolium ≤ pyrrolidinium ≤ ammonium, while anion stability tends to follow: halides (Cl^-, Br^-) < PF_6^- ≤ TfO ≈ TFSI ≈ BF_4^- (see Scheme 1.1 for ion structures).[45] In addition, it has been shown that the electrochemical stability of ionic liquids is highly dependent upon their purity. In particular, residual halide impurities from ionic liquid synthesis lead to a

much lower anodic potential limit due to much easier oxidation of the halide ions than other commonly used anions. Additionally, water has been shown to be a detrimental impurity as well. For example, Schröder, *et al.* observed a decrease in the electrochemical window of 1-butyl-3-methylimidazolium [BF_4] ([BMI][BF_4]) from 4.10 V to 1.95 V upon addition of 3 wt% water.[83]

In addition to wide electrochemical windows, ionic liquids also generally display fairly good ionic conductivity (σ). This is not a very surprising result, since ionic liquids are composed completely of ionic species. However, the ionic conductivity observed for an average ionic liquid (several mS cm^{-1}) is much lower than that observed for common aqueous electrolytes, such as concentrated potassium hydroxide solutions typically used in alkaline batteries, where $\sigma \sim$ 540 mS cm^{-1}.[82] The ionic conductivities of many ionic liquids are generally closer to the range observed for common non-aqueous solvent/electrolyte systems, such as [Li][TFSI] (1 M) in ethylene carbonate:dimethoxyethane (1:1), where $\sigma \sim$ 10-20 mS cm^{-1}.[82]

The ionic conductivity of ionic liquids is generally limited by their relatively high viscosities, which are typically in the range of several tens to several hundreds in units of cP. The relatively large size of many typical ionic liquid constituent ions also acts to limit their ultimate conductivity. The ion size and viscosity of the ionic liquid can be related to the self-diffusion coefficients for the ions (D_{cation} and D_{anion}) using the Stokes–Einstein equation.

$$D = \frac{k_{\text{b}}T}{c\pi\eta R_{\text{h}}} \tag{1.1}$$

In Equation 1.1 k_b is Boltzmann's constant, T is the absolute temperature, c is a constant ($4 \leq c \leq 6$), η is the solvent (ionic liquid) viscosity, and R_h is the hydrodynamic radius of the diffusing particle. Subsequently, the self-diffusion coefficients of the ions can be related to the molar conductivity of the ionic liquid (Λ) by the Nernst–Einstein equation.

$$\Lambda = \frac{F^2\left(D_{\text{cation}} + D_{\text{anion}}\right)}{RT} \tag{1.2}$$

In Equation 1.2, F is Faraday's constant, and R is the universal gas constant. The molar conductivity of the ionic liquids is given as,

$$\Lambda = \frac{\sigma}{C} = \sigma\frac{M}{\rho} \tag{1.3}$$

where M, ρ, and C are the molar mass, density, and molar concentration of the ionic liquid, respectively. Thus, from Equations 1.1 and 1.2 it is shown that the diffusion rate of the ions and the ionic liquid conductivity are inversely proportional to the ion size (R_h) and the viscosity of the ionic liquid.

Additionally, from equation 1.3, it follows that the ionic conductivity of an ionic liquid is directly proportional to the number of ions (*i.e.*, charge carriers) present per volume. This highlights another potential limitation to the ultimate ionic conductivity of ionic liquids. The Coulombic attraction between the ions, while relatively low for ionic liquids, still results in the formation of neutral ion pairs, and a subsequent decrease in the number of free charge carriers. Watanabe, *et al.* have investigated the extent of ion pairing for a number of ionic liquids, along with the effects of changing the ion identities.[84–87] In these studies, the researchers determined the molar conductivity for

the ionic liquids via complex impedance measurements (Λ_{imp}) and via pulsed–gradient spin–echo (PGSE)–NMR (Λ_{NMR}). The ionic conductivity for the ionic liquids, determined from impedance spectroscopy, and their molar concentrations were used to calculate Λ_{imp}. Thus, Λ_{imp} is determined by the number of free charge carriers that contribute to the ionic conductivity that is measured by impedance spectroscopy. Conversely, Equation 1.2 is applied to calculate Λ_{NMR} from the ion diffusion coefficients obtained from PGSE–NMR. The diffusion coefficients from PGSE–NMR are based on the diffusion of all the ionic species, including neutral ion pairs, which do not contribute to Λ_{imp}. Thus, the ratio $\Lambda_{imp}/\Lambda_{NMR}$ provides a measure of the extent of ion pairing in the ionic liquid. In general, Watanabe, *et al*. have found $\Lambda_{imp}/\Lambda_{NMR} < 1$ for all the ionic liquids studied, signifying that not all diffusive species in the ionic liquids contribute to the ionic conductivity. The $\Lambda_{imp}/\Lambda_{NMR}$ ratios typically fell in the range of 0.50–0.70, indicating a reduced, yet still fairly high ionicity of the ionic liquids.

Despite the limitations to ionic liquid conductivity discussed above, many ionic liquids still possess ionic conductivity on par with that of common non-aqueous liquid electrolytes.[82,88] However, many non-aqueous electrolytes incorporate volatile and/or flammable organic solvents. Thus, the other unique properties possessed by ionic liquids, such as wide liquid phase range, negligible vapor pressure, and non-flammability make them excellent candidates as alternative electrolyte materials.[48,82,89] Indeed, ionic liquids have been explored as electrolytes in various devices such as lithium ion batteries,[90–96] fuel cells,[97–104] and dye-sensitized solar cells.[105]

1.4 Polymers and Ionic Liquids

In light of the intense interest in ionic liquids as unique solvents and electrolyte materials, it is not surprising there has also been growing interest in the use of ionic liquids in polymer science.[106–108] One broad application of ionic liquids in polymer science has been their use as alternative solvents in applications such as polymer synthesis and processing, and the self-assembly of amphiphilic block copolymers. A second area of interest has been the combination of ionic liquids and polymers in order to prepare solid or quasi–solid materials that retain, and take advantage of, the unique properties of ionic liquids (*e.g.*, non-volatility, ionic conductivity), while circumventing the material drawbacks of their liquid nature.

1.4.1 Ionic Liquids as Solvents

The use of ionic liquids as solvents for polymerizations has been one of the major areas of study involving polymers and ionic liquids.[45,63,109] Multiple types of polymerizations have been reported, including conventional free radical,[110–114] atom transfer radical polymerization (ATRP),[115] reversible addition-fragmentation chain transfer (RAFT),[116] group transfer polymerization,[117] and cationic ring opening polymerization.[118] Many of the studies have reported improvements in the polymerization process, and the characteristics of the final product for polymerizations conducted in ionic liquids as compared to conventional solvents. For example, in the free radical polymerization of styrene and methyl methacrylate, it has been reported that polymerization rates and molecular weights of the final polymers were higher for polymerizations run in [BMI][PF_6], as compared to those run in benzene or the

bulk.[111,114] These results were found to be due to an increase in the rate of propagation, as well as a decrease in the rate of termination. The increased propagation rate is a result of the increased polarity of the ionic liquid medium, which has a stabilizing effect on transition states involving charge transfer between the monomer and polymeric radical. The decreased rate of termination is due to decreased diffusion of free radicals as a result of high ionic liquid viscosity and, in the case of polystyrene, decreasing solubility of the growing macroradicals in the ionic liquid.

There have been relatively few systematic studies aimed specifically at investigating the general solubility of polymers in ionic liquids. One fairly comprehensive study was performed by Snedden and coworkers.[119] These researchers prepared dilute solutions of 17 different homopolymers and copolymers in three different ionic liquids and monitored the phase separation over the course of several months. In general Snedden, *et al.* reported fairly varied, unpredictable results. In addition, the authors also highlighted the observation of solid–liquid phase separation over periods of days to weeks for many of the initially homogeneous polymer/ionic liquid solutions.

Ueki, *et al.* have studied the thermoresponsive solid–liquid phase behavior of poly(*N*-isopropylacrylamide) (PNIPAm) and poly(benzyl methacrylate) (PBnMA) in 1-ethyl-3-methylimidazolium [TFSI] ([EMI][TFSI]). PNIPAm exhibited upper critical solution temperature (UCST) type phase behavior, which is the opposite of its behavior in aqueous solution.[120] Conversely, PBnMA displayed lower critical solution temperature (LCST) type phase behavior in [EMI][TFSI].[121] Additionally, the

researchers were able to tune the phase separation temperature by changing the ionic liquid, or by copolymerizing solvophilic (methyl methacrylate) or solvophobic (styrene) monomers into the PBnMA chain. These studies have led to the preparation of PBnMA-*b*-PNIPAm diblock copolymers that display doubly thermosensitive micellization in a blend (1:1 w/w) of [EMI][TFSI] and [BMI][TFSI].[122] The block copolymers form micelles below the UCST of the PNIPAm blocks and above the LCST of the PBnMA blocks. Between the two temperatures the block copolymers are dissolved as single chains in the ionic liquid solvent.

There have also been other studies reporting ionic liquids behaving as selective solvents for amphiphilic block copolymers. He, *et al.* have reported on the self-assembly of several poly(butadiene-*b*-ethylene oxide) (PB–PEO) copolymers in [BMI][PF_6].[123] Overall, the observed copolymer micellization behavior was analogous to that observed for the PB–PEO copolymers in aqueous solution.[124,125] The insoluble PB blocks aggregate to form the cores of micelles, with the PEO blocks forming a well solvated micellar corona. As discussed above in Section 1.3.2, ionic liquids can be generally classified as moderately to highly polar solvents, thus they tend to be good solvents for polar polymers such as PEO and poor solvents for non-polar, hydrocarbon based polymers such as PB. A general micelle morphological progression from spheres to cylinders to bilayer vesicles was observed by He, as the length of the soluble PEO blocks was reduced. These dilute PB–PEO/ionic liquid solution studies have also led to a unique application for block copolymer micelles in ionic liquids, known as the "micelle shuttle".[126,127] This system is characterized by thermally induced transfer of

intact PB–PEO micelles between an aqueous and an ionic liquid phase. This work has been extended even further through the use of a PNIPAm–PEO block copolymer that displays not only intact transfer between aqueous and ionic liquid phases, but also thermally induced micellization/demicellization behavior in both phases.[128]

In addition to synthetic polymers, there are multiple reports of ionic liquids being applied as solvents for biomacromolecules.[129–131] In particular, it has been shown that 1-alkyl-3-methylimidazolium based ionic liquids with strong H–bond accepting anions, particularly Cl^-, are good solvents for cellulose.[129] Processing of cellulose from the ionic liquid solutions was also explored, and it was shown that fibers, films, and other structures could be formed using different techniques. The high solubility is attributed to the H–bond interactions that form between the hydroxyl protons of the cellulose molecules and Cl^- ions of the ionic liquid.[132]

1.4.2 "Solid" Ionic Liquids

Another vast research arena involving ionic liquids and polymers is the use of polymeric materials to impart solid or quasi-solid structure to ionic liquids. As discussed above, ionic liquids possess several properties that make them good candidates as electrolyte materials. However, in many applications or devices, a solid electrolyte material would be more robust and versatile than a liquid. Thus, the overall goal behind much of the research in this area is to prepare polymer/ionic liquid composites that possess solid-like structure, yet still display ionic conductivity close to that of the neat ionic liquid.

One route to a solid structure has been to simply blend ionic liquids with

polymers to form so-called "ion gel electrolytes". Polymeric materials employed range from simple homopolymers,[133–136] typically PEO, and copolymers,[137–140] typically poly(vinylidene fluoride-*co*-hexafluoropropylene) (P(VdF-*co*-HFP)). These materials are typically prepared either by a solvent casting method, or by a hot-pressing method where the polymer and ionic liquid are combined, and then annealed and pressed at elevated temperature to form films. Room temperature ionic conductivity values for these types of electrolyte materials usually fall within the range of 10^{-5}–10^{-2} S cm^{-1}.

Additionally, chemically[141–146] and physically[147–149] cross–linked polymer networks swollen with ionic liquids have also been investigated for use as ion gels. Chemically cross–linked ion gels are typically prepared either by cross–linking functionalized polymer chains dissolved in an ionic liquid, or by performing in situ free radical polymerization, with an added cross-linking agent, in an ionic liquid solvent. A study by Susan, *et al.* reports on the characteristics of ion gels formed by free radical polymerization of methyl methacrylate (MMA) in [EMI][TFSI] with ethylene glycol dimethacrylate as the cross-linking agent for the PMMA chains.[143] The cross–linked gels were found to be fairly robust, and displayed good ionic conductivity, in the range of 10^{-2} S cm^{-1} at room temperature. Perhaps the most interesting result was that the number of free charge carriers in the ion gel at certain compositions exceeded that in the neat ionic liquid. This was attributed to interactions between the PMMA matrix and the ions of the ionic liquid, which lead to increased ion dissociation.

Physically cross–linked ion gels take advantage of the selective solvation of ionic liquids towards different polymer types. If an ABA triblock copolymer is

prepared, where the A blocks are incompatible with the ionic liquid and the B block is compatible, then the A blocks will self-assemble to form micelles. When a sufficient copolymer concentration is reached, a network is formed due to bridging of ABA chains between two different A block aggregate domains, which act as the cross–linking points in the polymer network. He, *et al.* have reported on the preparation of physically cross–linked ion gels using a poly(styrene-*b*-ethylene oxide-*b*-styrene) triblock copolymer in [BMI][PF_6].[147] With as little as 5 wt% copolymer, gels were formed, which displayed ionic conductivity close to that of the neat ionic liquid. Additionally, thermoresponsive ion gels were also prepared by incorporating PNIPAm blocks into the copolymers and taking advantage of the UCST phase behavior of PNIPAm in [EMI][TFSI].[148,149]

1.5 Research Motivation and Overview

The original motivation for this thesis project was grounded in studying the characteristics of block copolymer self–assembly in ionic liquids. The question was whether the self–assembly behavior of block copolymers in this new class of solvents was analogous to that which had previously been reported in more common solvents. Thus initial experiments were directed towards characterizing the dilute solution self–assembly behavior of amphiphilic block copolymers dissolved in ionic liquids. The experimental techniques used for these dilute solution investigations were dynamic light scattering (DLS) and cryogenic transmission electron microscopy (cryo–TEM). Overall, the results of these experiments showed that the dilute solution self–assembly behavior of the block copolymers studied was similar to the classical behavior observed for many amphiphilic block copolymers in organic solvents and water. These experiments are

presented and discussed in Chapter 3.

Subsequent experiments were aimed at characterizing the microstructure phase behavior of concentrated solutions of block copolymers in ionic liquids. Again, the overall motivation for these experiments was to investigate how the self–assembled microstructure for the block copolymers in ionic liquids compared with that reported for copolymers in more common solvents. The main experimental technique used for these investigations was small angle X-ray scattering (SAXS). The results of these experiments are presented and discussed in Chapter 4. The overall results show that the phase behavior observed for the concentrated block copolymer/ionic liquid solutions is analogous to the classical behavior observed for many concentrated block copolymer solutions prepared with more common solvents.

The experiments described in Chapter 4 that involve characterizing the microstructure of concentrated block copolymer/ionic liquid solutions were conducted with an eye towards potential application of these materials as nanostructured electrolytes. Taking the ion gel materials described in Section 1.4.2 a step further, it could be beneficial in some applications if the electrolyte possessed a well ordered structure on the nano-scale. Nanostructured ionic liquid electrolytes have been recently reported by the groups of Ohno and Kato, who utilized liquid crystalline materials that display hexagonal columnar and bicontinuous cubic structures.[150–152] The researchers incorporated ionic liquid moieties into the liquid crystalline molecules, which, upon self-assembly, formed electrolyte materials with well ordered conducting domains. Additionally, it was shown that macroscopic alignment of the conducting domains

resulted in anisotropic conductivity through the electrolyte material. The concentrated block copolymer solutions presented in Chapter 4 also possess well ordered structure on the nano-scale as a result of the spontaneous segregation of the copolymer blocks. The ionic liquids utilized in these experiments behave as selective solvents, and thus the majority segregates into the microstructure domains formed by the soluble copolymer block. In this way, the ionic liquid is confined to the same microstructure as the copolymer matrix.

Thus, the remainder of this thesis describes studies aimed at characterizing and/or optimizing concentrated block copolymer/ionic liquid solution properties pertinent to the potential application of these materials as nanostructured electrolytes. Chapter 5 presents work done to characterize the ionic conductivity of concentrated block copolymer/ionic liquid solutions. The main experimental technique utilized in these studies was impedance spectroscopy. Additionally, Chapter 6 presents the results of experiments aimed at investigating the microstructure orientation in thin films of the concentrated block copolymer/ionic liquid solutions.

1.6 References

1. Hamley, I. W. *The Physics of Block Copolymers*; Oxford University Press: New York, 1998.

2. Bates, F. S.; Fredrickson, G. H. *Phys. Today* **1999**, *52*, 32–38.

3. Lodge, T. P. *Macromol. Chem. Phys.* **2003**, *204*, 265–273.

4. Helfand, E.; Tagami, Y. *J. Phys. Chem.* **1972**, *56*, 3592–3601.

5. Helfand, E.; Wasserman, Z. R. *Macromolecules* **1976**, *9*, 879–888.

6. Semenov, A. N. *Sov. Phys. JETP* **1985**, *61*, 733–742.

7. Leibler, L. *Macromolecules* **1980**, *13*, 1602–1617.

8. Matsen, M. W.; Schick, M. *Phys. Rev. Lett.* **1994**, *72*, 2660–2663.

9. Matsen, M. W.; Schick, M. *Macromolecules* **1994**, *27*, 7157–7163.

10. Matsen, M. W.; Bates, F. S. *Macromolecules* **1996**, *29*, 1091–1098.

11. Khandpur, A. K.; Förster, S.; Bates, F. S.; Hamley, I. W.; Ryan, A. J.; Bras, W.; Almdal, K.; Mortensen, K. *Macromolecules* **1995**, *28*, 8796–8806.

12. Cochran, E. W.; Garcia-Cervera, C. J.; Fredrickson, G. H. *Macromolecules* **2006**, *39*, 2449–2451.

13. Hillmyer, M. A.; *Adv. Polym. Sci.* **2005**, *190*, 137–181.

14. Shin, K.; Leach, K. A.; Goldbach, J. T.; Kim, D. H.; Jho, J. Y.; Tuominen, M.; Hawker, C. J.; Russell, T. P. *Nano Lett.* **2002**, *2*, 933–936.

15. Lee, J. I.; Cho, S. H.; Park, S.-M.; Kim, J. K.; Kim, J. K.; Yu, J.-W.; Kim, Y. C.; Russell, T. P. *Nano Lett.* **2008**, *8*, 2315–2320.

16. Crossland, E. J. W.; Ludwigs, S.; Hillmyer, M. A.; Steiner, U. *Soft Matter* **2007**, *3*, 94–98.

17. Hashimoto, T.; Tsutsumi, K.; Funaki,Y. *Langmuir*, **1997**, *13*, 6869–6872.

18. Alexandridis, P.; Lindman, B., Eds. *Amphiphilic Block Copolymers: Self-Assembly and Applications*; Elsevier Science: Amsterdam, 2000.

19. Tanford, C. *The Hydrophobic Effect: Formation of Micelles and Bilogical Membranes*, 2nd ed.; Wiley: New York, 1980.

20. Israelachvili, J. N. *Intermolecular and Surface Forces*; Academic Press: San Diego, 1991.

21. Won, Y.-Y.; Davis, H. T.; Bates, F. S. *Macromolecules* **2003**, *36*, 953–955.

22. Rager, T.; Meyer, W. H.; Wegner, G. *Macromol. Chem. Phys.* **1999**, *200*, 1672–1680.

23. Won, Y.-Y.; Davis, H. T.; Bates, F. S. *Science* **1999**, *283*, 960–963.

24. Discher, B. M.; Won, Y.-Y.; Ege, D. S.; Lee, J. C.-M.; Bates, F. S.; Discher, D. E.; Hammer, D. A. *Science* **1999**, *284*, 1143–1146.

25. Lodge, T. P.; Bang, J.; Li, Z.; Hillmyer, M. A.; Talmon, Y. *Faraday Discuss.* **2005**, *128*, 1–12.

26. Bang, J.; Jain, S.; Li, Z.; Lodge, T. P.; Pedersen, J. S.; Kesselman, E.; Talmon, Y. *Macromolecules* **2006**, *39*, 1199–1208.

27. LaRue, I.; Adam, M.; Pitsikalis, M.; Hadjichristidis, N.; Rubinstein, M.; Sheiko, S. S. *Macromolecules* **2006**, *39*, 309–314.

28. Halperin, A. *Macromolecules* **1987**, *20*, 2943–2946.

29. Birshtein, T. M.; Zhulina, E. B. *Polymer* **1989**, *30*, 170–177.

30. Leibler, L.; Orland, H.; Wheeler, J. C. *J. Phys. Chem.* **1983**, *79*, 3550–3557.

31. Noolandi, J.; Hong, K. M. *Macromolecules* **1983**, *16*, 1443–1448.

32. Zhulina, E. B.; Adam, M.; LaRue, I.; Sheiko, S. S.; Rubinstein, M. *Macromolecules* **2005**, *38*, 5330–5351.

33. Huang, C.-I.; Lodge, T. P. *Macromolecules*, **1998**, *31*, 3556–3565.

34. Lodge, T. P.; Hanley, K. J.; Pudil, B.; Alahapperuma, V. *Macromolecules* **2003**, *36*, 816–822.

35. Lodge, T. P.; Pudil, B.; Hanley, K. J. *Macromolecules* **2002**, *35*, 4707–4717.

36. Hanley, K. J.; Lodge, T. P.; Huang, C.-I. *Macromolecules* **2000**, *33*, 5918–5931.

37. Hanley, K. J.; Lodge, T. P. *J. Polym. Sci. Part B: Polym. Phys.* **1998**, *36*, 3101–3113.

38. Walden, P. *Bull. Acad. Imper. Sci. (St. Petersburg)* **1914**, 1800.

39. Gale, R. J.; Gilbert, B.; Osteryoung, R. A. *Inorg. Chem.* **1978***, 17*, 2728–2729.

40. Wilkes, J. S.; Levisky, J. A.; Wilson, R. A.; Hussey, C. L. *Inorg. Chem.* **1982**, *21*, 1263.

41. Hussey, C. L. *Pure & Appl. Chem.* **1988**, *60*, 1763–1772.

42. Wilkes, J. S.; Zaworotko, M. J. *J. Chem. Soc., Chem. Commun.* **1992**, 965–967.

43. Fuller, J.; Carlin, R. T.; De Long, H. C.; Haworth, D. *J. Chem. Soc., Chem. Commun.* **1994**, 299.

44. Bonhôte, P.; Dias, A.-P.; Papageorgiou, N.; Kalyanasundaram, K.; Grätzel, M. *Inorg. Chem.* **1996**, *35*, 1168–1178.

45. Wasserscheid, P.; Welton, T., Eds. *Ionic Liquids in Synthesis, 2nd ed.*; Wiley-VCH: Weinheim, 2008.

46. Weingärtner, H. *Angew. Chem. Int. Ed.* **2007**, *46*, 2–19.

47. Plechkova, N.; Seddon, K. R. *Chem. Soc. Rev.* **2008**, *37*, 123–150.

48. Ohno, H., Ed. *Electrochemical Aspects of Ionic Liquids*; John Wiley & Sons, Inc.: Hoboken, 2005.

49. Rogers, R. D.; Seddon, K. R., Eds. *ACS Symposium Series, 901*; American Chemical Society: Washington, DC, 2005.

50. Holbrey, J. D.; Seddon, K. R. *J. Chem. Soc., Dalton Trans.* **1999**, 2133–2139.

51. Huddleston, J. G.; Visser, A. E.; Reichert, W. M.; Willauer, H. D.; Broker, G. A.; Rogers, R. D. *Green Chem.* **2001**, *3*, 156–164.

52. Tokuda, H.; Hayamizu, K.; Ishii, K.; Susan, M. A. B. H.; Watanabe, M. *J. Phys. Chem. B* **2005**, *109*, 6103–6110.

53. Gordon, C. M.; Holbrey, J. D.; Kennedy, A. R.; Seddon, K. R. *J. Mater. Chem.* **1998**, *8*, 2627–2636

54. Krossing, I.; Slattery, J. M.; Daguenet, C.; Dyson, P. J.; Oleinikova, A.; Weingärtner, H. *J. Am. Chem. Soc.* **2006**, *128*, 13427–13434.

55. Earle, M. J.; Esperanca, J. M. S. S.; Gilea, M. A.; Lopes, J. N. C.; Rebelo, L. P. N.; Magee, J. W.; Seddon, K. R.; Widegren, J. A. *Nature* **2006**, *439*, 831–834.

56. Zaitsau, D. H.; Kabo, G. J.; Strechan, A. A.; Paulechka, Y. U.; Tschersich, A.; Verevkin, S. P.; Heintz, A. *J. Phys. Chem. A* **2006**, *110*, 7303–7306.

57. Armstrong, J. P.; Hurst, C.; Jones, R. G.; Licence, P.; Lovelock, K. R. J.; Satterley, C. J.; Villar-Garcia, I. J. *Phys. Chem. Chem. Phys.* **2007**, *9*, 982–990.

58. Ngo, H. L.; LeCompte, K.; Hargens, L.; McEwan, A. B. *Thermochim. Acta* **2000**, *357–358*, 97–102.

59. Kosmulski, M.; Gustafsson, J.; Rosenholm, J. B. *Thermichim. Acta* **2004**, *412*, 41–53.

60. Baranyai, K. J.; Deacon, G. B.; MacFarlane, D. R.; Pringle, J. M.; Scott, J. L. *Aust. J. Chem.* **2004**, *57*, 145–147.

61. Welton, T. *Chem. Rev.* **1999**, *99*, 2071–2083.

62. Pârvulescu, V. I.; Hardacre, C. *Chem. Rev.* **2007**, *107*, 2615–2665.

63. Kubisa, P. *Prog. Polym. Sci.* **2004**, *29*, 3–12.

64. Jain, N.; Kumar, A.; Chauhan, S.; Chauhan, S. M. S. *Tetrahedron* **2005**, *61*, 1015–1060.

65. Zhao, D.; Liao, Y.; Zhang, Z. *Clean* **2007**, *35*, 42–48.

66. Jastorff, B.; Mölter, K.; Behrend, P.; Bottin-Weber, U.; Filser, J.; Heimers, A.; Ondruschka, B.; Ranke, J.; Schaefer, M.; Schröder, H.; Stark, A.; Stepnowski, P.; Stock, F.; Störmann, R.; Stolte, S.; Welz-Biermann, U.; Ziegert, S.; Thöming, J. *Green Chem.* **2005**, *7*, 362–372.

67. Carmichael, A. J.; Seddon, K. R. *J. Phys. Org. Chem.* **2000**, *13*, 591–595.

68. Muldoon, M. J.; Gordon, C. M.; Dunkin, I. R. *J. Chem. Soc., Perkin Trans. 2* **2001**, 433–435.

69. Fletcher, K. A.; Storey, I. A.; Hendricks, A. E.; Pandey, S.; Pandey, S. *Green Chem.* **2001**, *3*, 210–215.

70. Baker, S. N.; Baker, G. A.; Bright, F. V. *Green Chem.* **2002**, *4*, 165–169.

71. Crowhurst, L.; Mawdsley, P. R.; Perez-Arlandis, J. M.; Salter, P. A., Welton, T. *Phys. Chem. Chem. Phys.* **2003**, *5*, 2790–2794.

72. Abraham, M. H.; Zissimos, A. M.; Huddleston, J. G.; Willauer, H. D.; Rogers, R. D.; Acree, W. E. *Ind. Eng. Chem. Res.* **2003**, *42,* 413–418.

73. Anderson, J. L.; Ding, J.; Welton, T.; Armstrong, D. W. *J. Am. Chem. Soc.* **2002**, *124*, 14247–14254.

74. Wakai, C.; Oleinikova, A.; Ott, M.; Weingärtner, H. *J. Phys. Chem. B* **2005**, *109*, 17028–17030.

75. Weingärtner, H. *Z. Phys. Chem.* **2006**, *220*, 1395–1405.

76. Poole, C. F. *J. Chromatogr. A* **2004**, *1037*, 49–82

77. Chiappe, C.; Pieraccini, D. *J. Phys. Org. Chem.* **2005**, *18*. 275–297.

78. Reichardt, C. *Solvents and Solvent Effects in Chemistry*, Wiley-VCH: Weinheim, 2003.

79. Reichardt, C. *Green Chem.* **2005**, *7*, 339–351.

80. Kamlet, M. J.; Abboud, J. L. M.; Taft, R. W. *Prog. Phys. Org. Chem.* **1981**, *13*, 485.

81. Taft, R. W.; Abboud, J. L. M.; Kamlet, M. J.; Abraham, M. H. *J. Solution Chem.* **1985**, *14*, 153.

82. Galiński, M.; Lewandowski, A.; Stepniak, I. *Electrochim. Acta* **2006**, *51*, 5567–5580.

83. Schröder, U.; Wadhawan, J. D.; Compton, R. G.; Marken, F.; Suarez, P. A. Z.; Consorti, C. S.; de Souza, R. F.; Dupont, J. *New J. Chem.* **2000**, *24*, 1009–1015.

84. Noda, A.; Hayamizu, K.; Watanabe, M. *J. Phys. Chem. B* **2001**, *105*, 4603–4610.

85. Tokuda, H.; Hayamizu, K.; Ishii, K.; Susan, M. A. B. H.; Watanabe, M. *J. Phys. Chem. B* **2004**, *108*, 16593–16600.

86. Tokuda, H.; Hayamizu, K.; Ishii, K.; Susan, M. A. B. H.; Watanabe, M. *J. Phys. Chem. B* **2005**, *109*, 6103–6110.

87. Tokuda, H.; Ishii, K.; Susan, M. A. B. H.; Tsuzuki, S.; Hayamizu, K.; Watanabe, M. *J. Phys. Chem. B* **2006**, *110*, 2833–2839.

88. Xu, K. *Chem. Rev.* **2004**, *104*, 4303–4417.

89. Fernicola, A.; Scrosati, B.; Ohno, H. *Ionics* **2006**, *12*, 95–102.

90. Seki, S.; Ohno, Y.; Miyashiro, H.; Kobayashi, Y.; Usami, A.; Mita, Y.; Terada, N.; Hayamizu, K.; Tsuzuki, S.; Watanabe, M. *J. Electrochem. Soc.* **2008**, *155*, A421–A427.

91. Seki, S.; Ohno, Y.; Kobayashi, Y.; Miyashiro, H.; Usami, A.; Mita, Y.; Tokuda, H.; Watanabe, M.; Hayamizu, K.; Tsuzuki, S.; Hattori, M.; Terada, N. *J. Electrochem. Soc.* **2007**, *154*, A173–A177.

92. Hayashi, K.; Nemoto, Y.; Akuto, K.; Sakurai, Y. *J. Power Sources* **2005**, *146*, 689–692.

93. Garcia, B.; Lavallée, S.; Perron, G.; Michot, C.; Armand, M. *Electrochim. Acta* **2004**, *49*, 4583–4588.

94. Sakaebe, H.; Matsumoto, H.; Tatsumi, K. *J. Power Sources* **2005**, *146*, 693–697.

95. Ishikawa, M.; Sugimoto, T.; Kikuta, M.; Ishiko, E.; Kono, M. *J. Power Sources* **2006**, *162*, 658–662.

96. Matsumoto, H.; Sakaebe, H.; Tatsumi, K.; Kikuta, M.; Ishiko, E.; Kono, M. *J. Power Sources* **2006**, *160*, 1308–1313.

97. Angell, C. A.; Byrne, N.; Belieres, J.-P. *Acc. Chem. Res.* **2007**, *40*, 1228–1236.

98. Xu, W.; Angell, C. A. *Science* **2003**, *302*, 422–425.

99. Nakamoto, H.; Watanabe, M. *Chem. Commun.* **2007**, 2539–2541.

100. Nakamoto, H.; Noda, A.; Hayamizu, K.; Hayashi, S.; Hamaguchi, H.; Watanabe, M. *J. Phys. Chem. C* **2007**, *111*, 1541–1548.

101. Matsuoka, H.; Nakamoto, H.; Susan, M. A. B. H.; Watanabe, M. *Electrochim. Acta* **2005**, *50*, 4015–4021.

102. Noda, A.; Susan, M. A. B. H.; Kudo, K.; Mitsushima, S.; Hayamizu, K.; Watanabe, M. *J. Phys. Chem. B* **2003**, *107*, 4024–4033.

103. Susan, M. A. B. H.; Noda, A.; Mitsushima, S.; Watanabe, M. *Chem. Commun.* **2003**, 938–939.

104. Ogihara, W.; Kosukegawa, H.; Ohno, H. *Chem. Commun.* **2006**, 3637–3639.

105. Gorlov, M.; Kloo, L. *Dalton Trans.* **2008**, 2655–2666.

106. Winterton, N. *J. Mater. Chem.* **2006**, *16*, 4281–4293.

107. Ueki, T.; Watanabe, M. *Macromolecules* **2008**, *41*, 3739–3749.

108. Lu, J.; Yan, F.; Texter, J. *Prog. Polym. Sci.* **2009**, *34*, 431–448.

109. Brazel, C. S.; Rogers, R. D., Eds. *ACS Symposium Series, 913*; American Chemical Society: Washington, DC, 2005.

110. Harrison, S.; Mackenzie, S. R.; Haddleton, D. M. *Chem. Commun.* **2002**, 2850–2851.

111. Harrison, S.; Mackenzie, S. R.; Haddleton, D. M. *Macromolecules* **2003**, *36*, 5072–5075.

112. Zhang, H.; Hong, K.; Mays, J. W. *Macromolecules* **2002**, *35*, 5738–5741.

113. Zhang, H.; Hong, K.; Jablonsky, M.; Mays, J. W. *Chem. Commun.* **2003**, 1356–1357.

114. Hong, K.; Zhang, H.; Mays, J. W.; Visser, A. E.; Brazel, C. S.; Holbrey, J. D. Reichert, W. M.; Rogers, R. D. *Chem Commun.* **2002**, 1368–1369.

115. Biedroń, T.; Kubisa, P. *J. Polym. Sci. Part A: Polym. Chem.* **2002**, *40*, 2799–2809.

116. Perrier, S.; Davis, T. P.; Carmichael, A. J.; Haddleton, D. M. *Eur. Polym. J.* **2003**, *39*, 417–422.

117. Vijayaraghavan, R.; MacFarlane, D. R. *Chem. Commun.* **2005**, 1149–1151.

118. Biedroń, T.; Bednarek, M.; Kubisa, P. *Macromol. Rapid Commun.* **2004**, *25*, 878–881.

119. Snedden, P.; Cooper, A. I.; Scott, K.; Winterton, N. *Macromolecules* **2003**, *36*, 4549–4556.

120. Ueki, T.; Watanabe, M. *Chem. Lett.* **2006**, *35*, 964–965.

121. Ueki, T.; Watanabe, M. *Langmuir* **2007**, *23*, 988–990.

122. Ueki, T.; Watanabe, M.; Lodge, T. P. *Macromolecules* **2009**, *42*, 1315–1320.

123. He, Y.; Li, Z.; Simone, P.; Lodge, T. P. *J. Am. Chem. Soc.* **2006**, *128*, 2745–2750.

124. Won, Y.-Y.; Brannan, A. K.; Davis, H. T.; Bates, F. S. *J. Phys. Chem. B* **2002**, *106*, 3354–3364.

125. Jain, S.; Bates, F. S. *Science* **2003**, *300*, 460–464.

126. He, Y.; Lodge, T. P. *J. Am. Chem. Soc.* **2006**, *128*, 12666–12667.

127. Bai, Z.; He, Y.; Lodge, T. P. *Langmuir* **2008**, *24*, 5284–5290.

128. Bai, Z.; He, Y.; Young, N. P.; Lodge, T. P. *Macromolecules* **2008**, *41*, 6615–6617.

129. Swatloski, R. P.; Spear, S. K.; Holbrey, J. D.; Rogers, R. D. *J. Am. Chem. Soc.* **2002**, *124*, 4974–4975.

130. Xie, H.; Li, S.; Zhang, S. *Green Chem.* **2005**, *7*, 606–608.

131. Ohno, H.; Nishimura, N. *J. Electrochem. Soc.* **2001**, *148*, E168–E170.

132. Remsing, R. C.; Swatloski, R. P.; Rogers, R. D.; Moyna, G. *Chem. Commun.* **2006**, 1271–1273

133. Lewandowski, A.; Świderska, A. *Solid State Ionics* **2004**, *169*, 21–24.

134. Shin, J.-H.; Henderson, W. A.; Tizzani, C.; Passerini, S.; Jeong, S.-S.; Kim, K.-W. *J. Electrochem. Soc.* **2006**, *153*, A1649–A1654.

135. Zhu, C.; Cheng, H.; Yang, Y. *J. Electrochem. Soc.* **2008**, *155*, A569–A575.

136. Kim, Y. H.; Cheruvally, G.; Choi, J. W.; Ahn, J. H.; Kim, K. W.; Ahn, H. J.; Choi, D. S.; Song, C. E. *Macromol. Symp.* **2007**, *249–250*, 183–189.

137. Sutto, T. E.; *J. Electrochem. Soc.* **2007**, *154*, P101–P107.

138. Fuller, J.; Breda, A. C.; Carlin, R. T. *J. Electrochem. Soc.* **1997**, *144*, L67–L70.

139. Yeon, S.-H.; Kim, K.-S.; Choi, S.; Cha, J.-H.; Lee, H. *J. Phys. Chem. B* **2005**, *109*, 17928–17935.

140. Singh, B.; Sekhon, S. S. *Chem. Phys. Lett.* **2005**, *414*, 34–39.

141. Klingshirn, M. A.; Spear, S. K.; Subramanian, R.; Holbrey, J. D.; Huddleston, J. G.; Rogers, R. D. *Chem. Mater.* **2004**, *16*, 3091–3097.

142. Noda, A.; Watanabe, M. *Electrochim. Acta* **2000**, *45*, 1265–1270.

143. Susan, M. A. B. H.; Kaneko, T.; Noda, A.; Watanabe, M. *J. Am. Chem. Soc.* **2005**, *127*, 4976–4983.

144. Rupp, B.; Schmuck, M.; Balducci, A.; Winter, M.; Kern, W. *Eur. Polym. J.* **2008**, *44*, 2986–2990.

145. Tigelaar, D. M.; Meador, M. A. B.; Bennett, W. R. *Macromolecules* **2007**, *40*, 4159–4164.

146. Tiyapiboonchaiya, C.; MacFarlane, D. R.; Sun, J.; Forsyth, M. *Macromol. Chem. Phys.* **2002**, *203*, 1906–1911.

147. He, Y.; Boswell, P. G.; Bühlmann, P.; Lodge, T. P. *J. Phys. Chem. B* **2007**, *111*, 4645–4652.

148. He, Y.; Lodge, T. P. *Chem. Commun.* **2007**, 2732–2734.

149. He, Y.; Lodge, T. P. *Macromolecules*, **2008**, *41*, 167–174.

150. Yoshio, M.; Kagata, T.; Hoshino, K.; Mukai, T.; Ohno, H.; Kata, T. *J. Am. Chem. Soc.* **2006**, *128*, 5570–5577.

151. Ichikawa, T.; Yoshio, M.; Hamasaki, A.; Mukai, T.; Ohno, H.; Kato, T. *J. Am. Chem. Soc.* **2007**, *129*, 10662–10663.

152. Shimura, H.; Yoshio, M.; Hoshino, K.; Mukai, T.; Ohno, H.; Kato, T. *J. Am. Chem. Soc.* **2008**, *130*, 1759–1765.

Chapter 2

Materials and Experimental Techniques

2.1 Introduction

This chapter outlines the main synthetic and experimental techniques employed in this thesis project. The main focus will be on describing general background and procedures for materials synthesis and experiments. More specific experimental details will be briefly described in the following chapters where the results of the specific experiments are presented.

2.2 Polymer Synthesis and Characterization

2.2.1 Living Anionic Polymerization

The polymers used in this thesis project were synthesized exclusively via living anionic polymerization (LAP). Living anionic polymerization has been proven to be a useful tool for synthesizing well defined polymers and copolymers, and detailed treatments of the general technique are available.[1,2] In LAP, the rate of initiation is high compared with the propagation rate, which results in simultaneous initiation of growing chain ends. Additionally, chain transfer and chain termination reactions can be virtually

eliminated from LAP if the polymerization is performed under appropriate conditions. In particular, the presence of impurities such as water, alcohols, and oxygen must be guarded against, as these compounds can readily react with the living anionic chain ends. The combination of simultaneous chain initiation and low occurrence of chain transfer or termination reactions allows for the synthesis of polymers with low polydispersity using LAP. Additionally, the number average degree of polymerization for the final product can be predicted based on the ratio of monomer to initiator. Moreover, due to the absence of chain termination, the "living" anionic chain ends remain active even after all the initial monomer has been consumed. This allows for sequential addition, and polymerization of different monomers. Thus, LAP can be utilized to prepare model block copolymers with low polydispersity and well defined block lengths that can be readily controlled by the stoichiometry between the initiator and the monomers.

This section describes the synthetic procedure used for the preparation of poly(styrene-*b*-ethylene oxide) diblock copolymers. The overall procedure consisted of two main steps. First, a hydroxyl–terminated polystyrene homopolymer (PS–OH) was synthesized and purified. Second, the PS–OH was reinitiated, and used as the "macroinitiator" for the living anionic synthesis of ethylene oxide. The general procedure is modeled after that developed by Hillmyer and Bates for the synthesis of polyalkane–poly(ethylene oxide) copolymers.[3]

In order to ensure water and oxygen–free conditions for living anionic polymerization, all glassware was kilned at 500–570 °C to remove organic impurities

and flame dried under reduce pressure to remove adsorbed moisture. All purification and polymerization procedures were carried out on a laboratory scale synthesis line under vacuum (≤ 50 mtorr), or high purity argon.[4] Finally, all monomers and solvents were rigorously degassed and purified prior to use. Cyclohexane and tetrahydrofuran were purified on a home-built solvent purification line.[5] Cyclohexane was passed through an activated alumina column to remove protic impurities and through a column containing a supported copper catalyst to remove oxygen. Tetrahydrofuran was sparged with argon to remove oxygen and passed twice through an activated alumina column. Styrene was purified by first stirring over calcium hydride for ~ 12 hours. After 3 freeze-pump-thaw cycles to degas the styrene, it was transferred via distillation under reduced pressure to a flask containing di-*n*-butylmagnesium. Styrene was stirred over di-*n*-butylmagnesium for approximately six hours and then vacuum distilled to an air-free burette. Ethylene oxide was purified by stirring over butylmagnesium chloride for 30 minutes at 0 °C, twice. Ethylene oxide was then transferred to an air-free burette which was kept submersed in a dry ice/isopropanol bath (~ −80 °C).

The polymerization of the PS–OH homopolymer was performed as follows. A solvent flask containing cyclohexane and burettes containing styrene and ethylene oxide were connected to the polymerization reactor via threaded glass ports with Teflon o-rings and nylon bushings to form an airtight seal. The reactor was connected to the vacuum synthesis line and evacuated and purged with high purity argon five times to ensure an inert atmosphere for the living anionic polymerization. Cyclohexane was then added to the reactor and the *sec*-butyllithium initiator solution (~ 1.4 M in cyclohexane)

was added through a port equipped with a rubber septum, using a gas-tight syringe. Next, styrene monomer was added and the polymerization was run at 40 °C for ~4 hours with stirring. After 4 hours the polymerization mixture was cooled to room temperature and ethylene oxide was added. A ten times molar excess of ethylene oxide to living chain ends was added to ensure complete end-capping of all the living polystyrene chains. Despite the large excess, only a single ethylene oxide unit is added to each living chain end due to strong association between the oxyanion and the lithium counter ion, which prevents propagation of the ethylene oxide. After addition of ethylene oxide, the polymerization mixture was stirred for ~12 hours at room temperature. The living chains were then terminated by injecting degassed methanol, in excess. The final polymer was precipitated in a mixture of methanol and isopropanol (3:1 by volume). The polymer was dried under vacuum at 50–60 °C for two days, and then at ~110 °C for 12 hours.

The general procedure for reinitiation of the PS–OH homopolymer, and polymerization of ethylene oxide is as follows. The polymerization reactor setup was similar to that described for the PS–OH polymerization above. However, tetrahydrofuran was used as the solvent for the ethylene oxide polymerization, and the only monomer burette attached to the reactor was for the ethylene oxide. Prior to sealing and purging the reactor, the desired amount of PS–OH homopolymer was added. After evacuating and purging the reactor with argon five times, the THF solvent was added to the reactor and stirred until the PS–OH homopolymer was completely dissolved. Once completely dissolved, the PS–OH homopolymer was reinitiated by

titration with a THF/potassium naphthalenide solution. The titration solution was prepared by dissolving freshly cut potassium in THF, followed by addition of ~ 10% molar excess of naphthalene under argon purge (final solution concentration ~ 0.1 M). The dark green potassium naphthalenide solution was added to the polymerization reactor via cannulation through a port equipped with a rubber septum. The endpoint of the titration was signaled by the persistence of a faint green tint in the polymerization solution for at least 30 minutes, indicating the conversion of the hydroxyl end-groups to potassium alkoxides. Next, the temperature of the polymerization solution was reduced to ~ 10 °C and the ethylene oxide monomer was slowly added in order to avoid an extreme increase in reactor pressure. After addition of ethylene oxide, the reactor temperature was slowly increased to 45 °C, and the polymerization was allowed to proceed for approximately 24 hours. The reactor was then cooled to room temperature and the polymerization was terminated by the addition of excess acidic methanol. The THF solvent was removed via rotary evaporation, and the polymer product was redissolved in dichloromethane. The polymer solution was washed three times with an aqueous sodium bicarbonate solution (~ 5 wt%), followed by washing three times with distilled water. The polymer was then precipitated in hexane, and finally redissolved in benzene and freeze dried to produce a fine white powder as the final product. Scheme 2.1 represents the total PS–PEO synthesis procedure. The molecular characteristics of the PS–OH homopolymer and the PS–PEO copolymers are listed in Table 2.1. The polymers were characterized using a combination of size exclusion chromatography and ^{1}H-NMR, as described in the following sections.

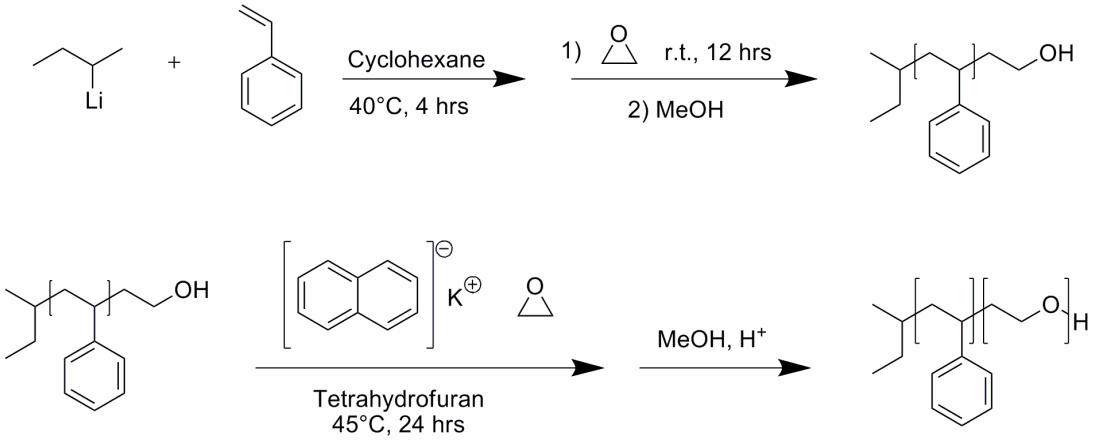

Scheme 2.1: Synthesis scheme for living anionic polymerization of PS–PEO.

Table 2.1: Molecular characteristics of PS–OH and PS–PEO Block Copolymers

Polymer	M_{PS} (kg/mol)[a]	M_{PEO} (kg/mol)[b]	PDI[c]	f_{PEO}[d]
PS–OH	19.7	–	1.02	–
SO(20–5)	19.7	4.8	1.04	0.18
SO(20–6)	19.7	6.3	1.03	0.23
SO(20–8)	19.7	8.3	1.08	0.28
SO(20–13)	19.7	13.4	1.06	0.39

[a] Molecular weight of PS–OH homopolymer determined via SEC with multiangle light scattering detection.
[b] Molecular weight of PEO blocks determined via ^{1}H–NMR.
[c] PDI values determined as M_w/M_n from SEC calibrated with PS standards
[d] Copolymer PEO volume fraction calculated using bulk densities for PS (1.05 g/cm^3) and PEO (1.13 g/cm^3).

2.2.2 Size Exclusion Chromatography

Molecular weights and molecular weight distributions of the block copolymers used in this thesis were measured via size exclusion chromatography (SEC). Two different SEC set-ups were employed. SEC setup one was a home-built apparatus consisting of an Alltech 426 HPLC pump, three Phenomenex Phenogel columns with pore sizes of 10^3, 10^4, and 10^5 Å. The detectors for this set-up consisted of an interferometric refractometer (OPTILAB, Wyatt Technology Corp.) and a multiangle light-scattering detector (DAWN, Wyatt Technology Corp.). The mobile phase was tetrahydrofuran at room temperature and a flow rate of 1 mL/min. Calibration was performed with polystyrene standards (Polymer Laboratories). SEC setup two consisted of an Agilent 1100 series liquid chromatograph equipped with three PLgel Mixed C columns, and a Hewlett-Packard 1047A refractive index detector. The mobile phase was chloroform at 35 °C and a flow rate of 1 mL/min. Calibration was performed with polystyrene standards (Polymer Laboratories).

The absolute molecular weight of the PS-OH homopolymer was determined via SEC utilizing setup one. The multiple angle light scattering detector allowed for the calculation of the absolute molecular weight of the PS–OH homopolymer. The molecular weight and PDI were 19.7 kg/mol and 1.02, respectively. Additionally, sequential growth of the PEO blocks of the PS–PEO copolymers was confirmed using SEC setup two. A plot of the SEC traces for the PS–OH homopolymer and the four PS–PEO copolymers are shown in Figure 2.1. PDI values for the PS–PEO copolymers were calculated from the SEC traces in Figure 2.1, and are listed in Table 2.1.

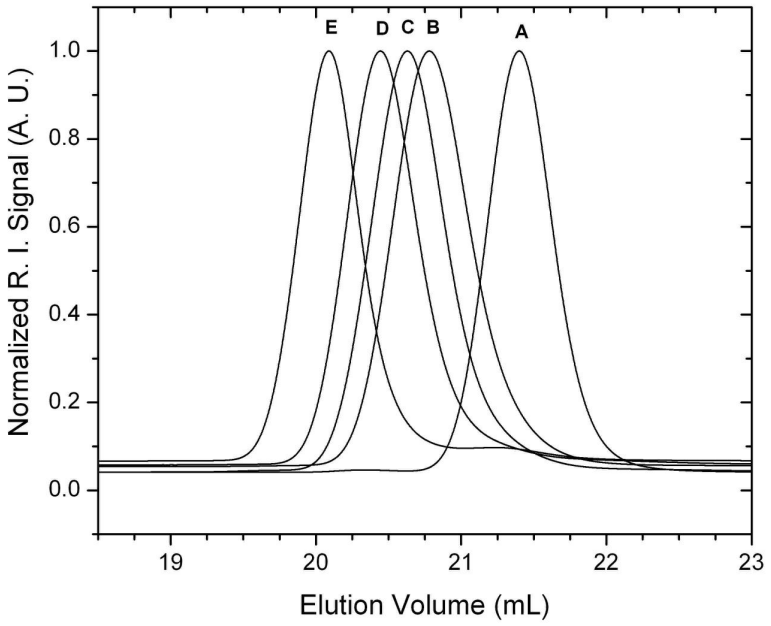

Figure 2.1: SEC traces for A) PS–OH; B) SO(20–5); C) SO(20–6); D) SO(20–8); E) SO(20–13). Mobile phase is chloroform at 35 °C and a flow rate of 1 ml/min.

2.2.3 ^{1}H Nuclear Magnetic Resonance Spectroscopy

The molecular weight of the PEO blocks of the PS–PEO copolymers, and thus total copolymer molecular weight and composition, were characterized via ^{1}H-Nuclear Magnetic Resonance (NMR) Spectroscopy. ^{1}H-NMR spectra were obtained using a Varian VAC 300 MHz spectrometer. Samples were prepared in deuterated chloroform, and resonance peak shifts are referenced to TMS. A representative ^{1}H-NMR spectrum for the SO(20–8) copolymer is shown in Figure 2.2. The resonance peak at ~ 3.6–3.7 ppm corresponds to the CH_2 protons of the PEO chain (–C**H$_2$**–C**H$_2$**–O–). The broad peaks from ~ 6.3–7.3 ppm correspond to the five protons of the aromatic ring of the

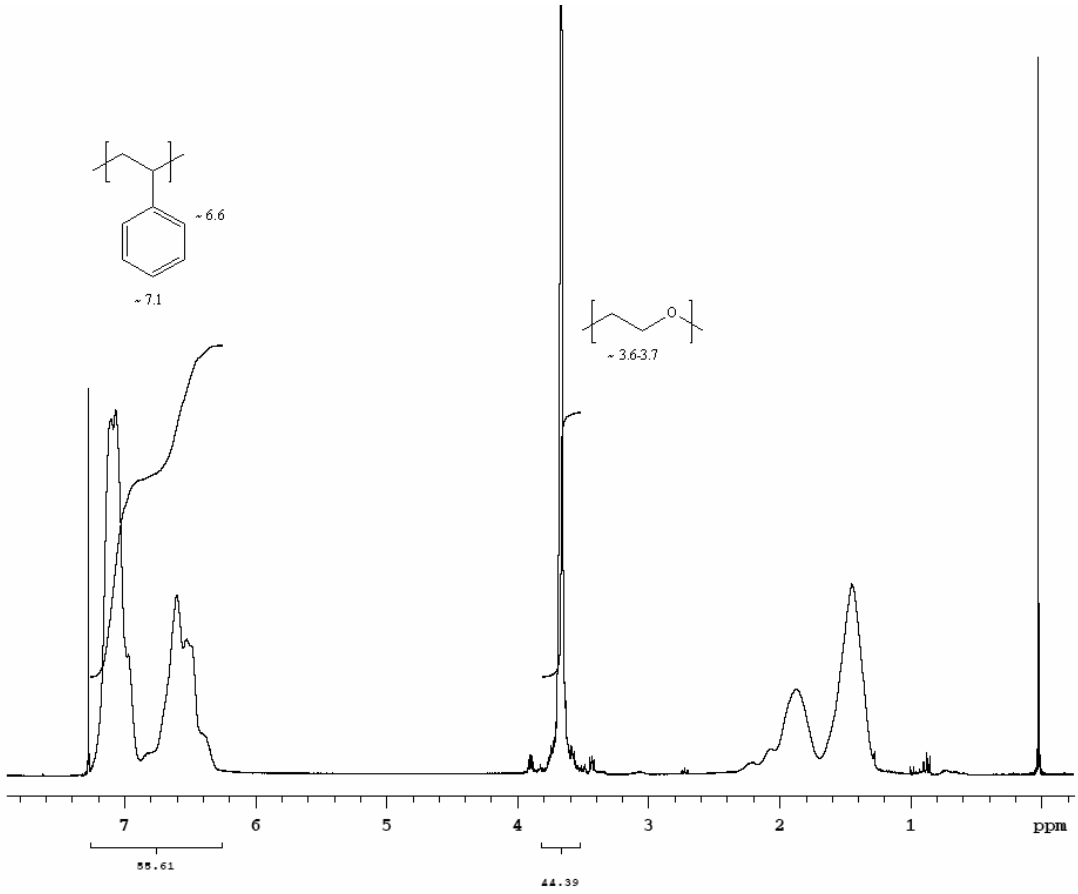

Figure 2.2: ^{1}H-NMR (300 MHz) spectrum of SO(20–8). Sample prepared with deuterated chloroform, and referenced to TMS.

styrene monomers. The broad peaks located at ~ 1.3–2.3 ppm correspond to the protons on the backbone chain of the PS blocks. By integrating the area under the resonance peaks corresponding to protons of the PEO blocks (~ 3.6–3.7 ppm) and the aromatic protons of the PS blocks (~ 6.3–7.3 ppm), the mole percent of PEO in the copolymer can be calculated as,

$$\text{mol \% PEO} = \frac{\frac{A(3.6 \sim 3.7\,ppm)}{4}}{\frac{A(3.6 \sim 3.7\,ppm)}{4} + \frac{A(6.3 \sim 7.3)}{5}} = \frac{\frac{44.39}{4}}{\frac{44.39}{4} + \frac{55.61}{5}} = 49.9 \text{ mol\% PEO}$$

where 49.9 mol% PEO is calculated from the SO(20–8) ^{1}H-NMR spectrum shown in Figure 2.2. The corresponding weight percent of PEO for the copolymer is simply calculated from the mole percent PEO and the molecular weights of the styrene (104.15 g/mol) and ethylene oxide (44.05 g/mol) monomers. For the SO(20–8) copolymer, a value of 29.6 wt% PEO is obtained. Finally, utilizing the molecular weight of the parent PS–OH block (19.7 kg/mol), obtained from SEC with light scattering detection, the molecular weight of the PEO block can be calculated from the PEO wt%. Table 2.1 lists the molecular characteristics of the PS–PEO copolymers. Volume fraction of PEO for the PS–PEO copolymers (f_{PEO}) was calculated from the PEO weight fraction, assuming block densities equal to bulk PS (1.05 g/cm^3) and PEO (1.13 g/cm^3).

2.3 Ionic Liquid Synthesis and Characterization

The synthesis of ionic liquids generally consists of two main steps. First is the preparation of the desired cation. This is typically accomplished via protonation or quaternization of an amine, phosphine, or sulfide (see Scheme 1.1 for common ionic

liquid ions) using either a free acid or haloalkane. The second general synthesis step consists of anion exchange. This is typically accomplished simply by combining the product salt from the cation synthesis with a salt (typically Li^+ or Ag^+ based) containing the desired anion. The anion exchange portion of the synthesis is not always necessary, for example, dialkylimidazolium halide ionic liquids can be obtained simply by reaction of the appropriate alkylimidazole with a haloalkane. In the past 10–15 years a wide variety of ionic liquid synthetic procedures have been reported, owing to the large number of ions that can be employed for preparing ionic liquids.[6]

Ionic liquids for this thesis project were obtained from commercial suppliers and through in–house synthesis. The initial ionic liquid used for experiments in this thesis was 1–butyl–3–methylimidazolium hexafluorophosphate [BMI][PF_6]. Dialkylimidazolium cations combined with the [PF_6] anion were among the first air and water stable ionic liquids reported,[7] and thus represent some of the first ionic liquids readily available from commercial sources. The [BMI][PF_6] ionic liquid used in this thesis was purchased from Solvent Innovation GmbH, and was a clear, colorless liquid at room temperature. Prior to use the [BMI][PF_6] was dried under vacuum (ca. 10 mTorr) at 60–70 °C for 2–3 days to remove absorbed moisture, and then stored either in a glove box under argon or in a vacuum-sealed desiccator.

[EMI][TFSI] was prepared via anion exchange between 1-ethyl-3-methylimidazolium bromide [EMI][Br] (Solvent Innovation GmbH) and lithium bis(trifluoromethylsulfonyl)imide ([Li][TFSI]) (IoLiTec) in water at 70 °C for 12 hours. Both [EMI][Br] and [Li][TFSI] are water soluble, while [EMI][TFSI] is not. Thus over

the course of the anion exchange the reaction mixture phase separates into aqueous and [EMI][TFSI] layers. After the reaction the aqueous layer was removed and the ionic liquid was repeatedly washed with distilled water. To further purify the ionic liquid, it was stirred over activated carbon (Sigma-Aldrich) for several hours. The final [EMI][TFSI] product was a clear, very faint yellow liquid. ^{1}H–NMR spectra for [BMI][PF_6] and [EMI][TFSI] are shown in Figures 2.3 and 2.4, respectively. The spectra for [BMI][PF_6] and [EMI][TFSI] were obtained in deuterated methanol and deuterated DMSO, respectively. The resonance peak chemical shift values for the two ionic liquids compare well with those reported in literature.[8,9]

Figure 2.5 shows differential scanning calorimetry (DSC) traces for [BMI][PF_6] and [EMI][TFSI]. The samples were equilibrated at 40 °C, then cooled, and then heated back to 40 °C. The cooling and heating rates were both 10 °C per minute. For [BMI][PF_6] no crystallization was observed upon cooling the sample, which is consistent with many ionic liquids, where the large size and asymmetry of their constituent ions prevents efficient crystallization.[6] The glass transition temperature (T_g) for [BMI][PF_6] was measured to be ~ −78 °C (taken as the transition midpoint), which is consistent with other reported values.[8] Two melting points (T_{mp}) were observed for [BMI][PF_6], −6.4 °C and 9.9 °C. The T_{mp} at 9.9 °C corresponds well with reported values.[8] The appearance of two melting points is most likely the result of crystal polymorphism, which has been reported for ionic liquids.[10,11] For [EMI][TFSI], a T_g was observed at ~ −92 °C. A literature value for the T_g of [EMI][TFSI] obtained using

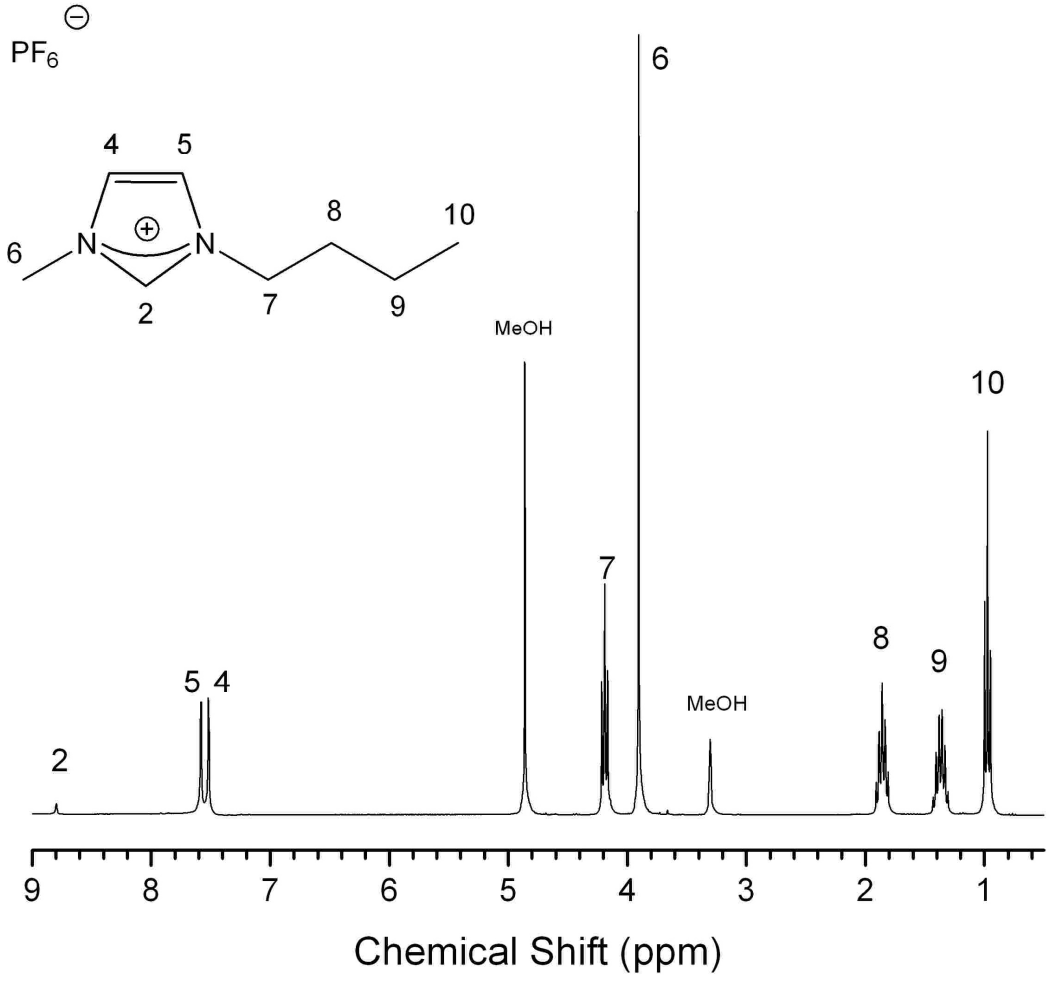

Figure 2.3: ^{1}H–NMR spectrum (300 MHz, deuterated methanol) for [BMI][PF_6].

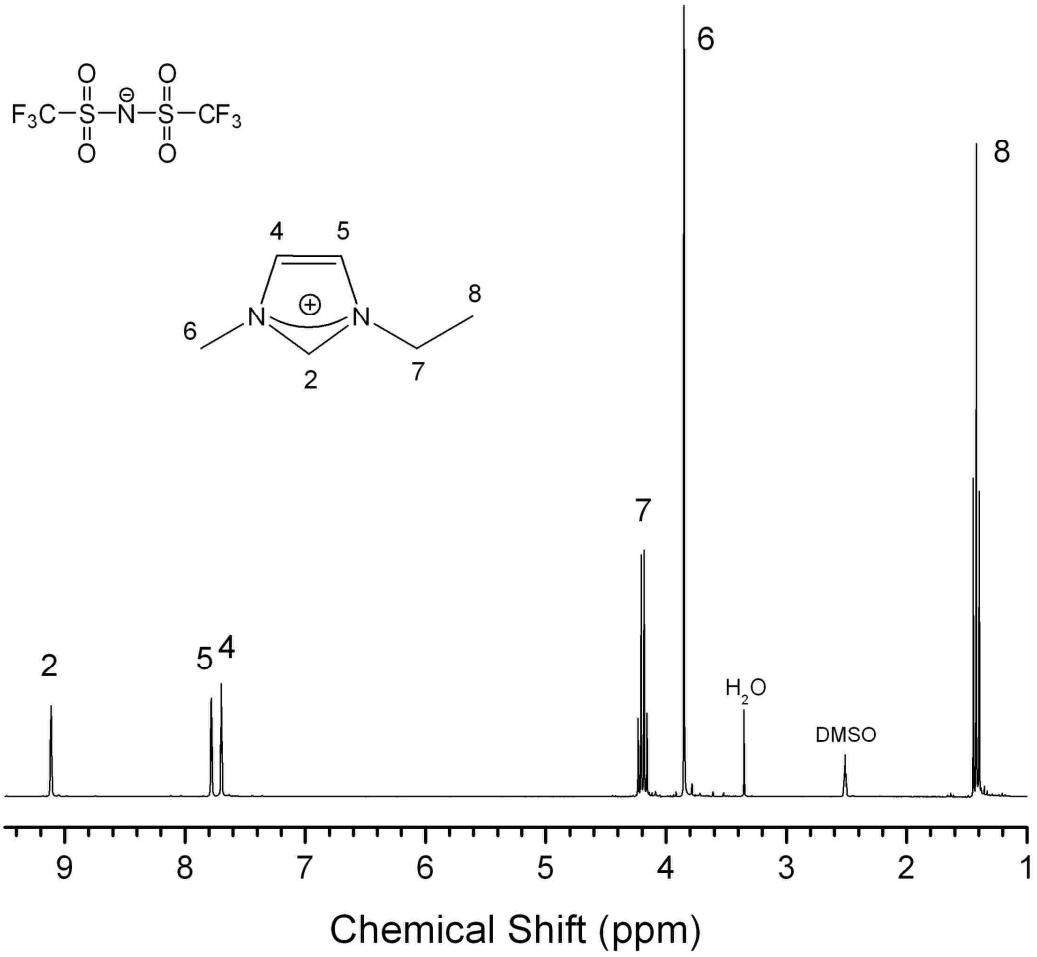

Figure 2.4: ^{1}H–NMR spectrum (300 MHz, deuterated DMSO) for [EMI][TFSI].

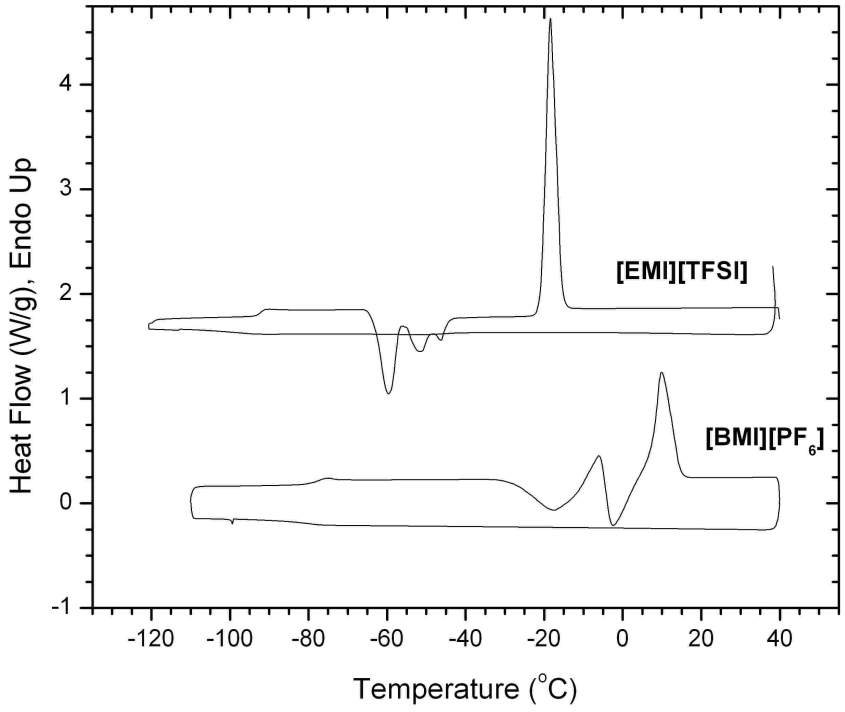

Figure 2.5: DSC traces for [BMI][PF_6] and [EMI][TFSI]. Samples were cooled from 40 °C, and then heated back to 40 °C. Cooling and heating rates were both 10 °C/min.

"fast cooling" is −87 °C.[12] Multiple crystallization peaks are observed for [EMI][TFSI] upon heating the sample from −120 °C; however, a single T_{mp} is observed at −18 °C, which agrees fairly well with previously reported values.[13]

Figure 2.6 shows the viscosity of [BMI][PF_6] and [EMI][TFSI] vs. temperature. The viscosities were measured on a Rheometrics Fluids Spectrometer RFS II with concentric cylinders, and were found to agree well with other reported values (± 10% at all temperatures).[12,14] As can be seen, the viscosities of both ionic liquids are strongly dependent upon temperature. The viscosity data was fitted to the Vogel–Tamman–Fulcher (VTF) equation,

$$\eta = \eta_o \exp\left[B/\left(T - T_o\right)\right] \tag{2.1}$$

and values of the fitting parameters (η_o, B, and T_o) are given in Table 2.2.

Table 2.2: VTF Equation Parameters for Viscosity Data

	η_o (cP)	B (K)	T_o (K)
[BMI][PF_6]	0.065 ± 0.014	1135 ± 67	161 ± 4
[EMI][TFSI]	0.14 ± 0.02	845 ± 51	145 ± 5

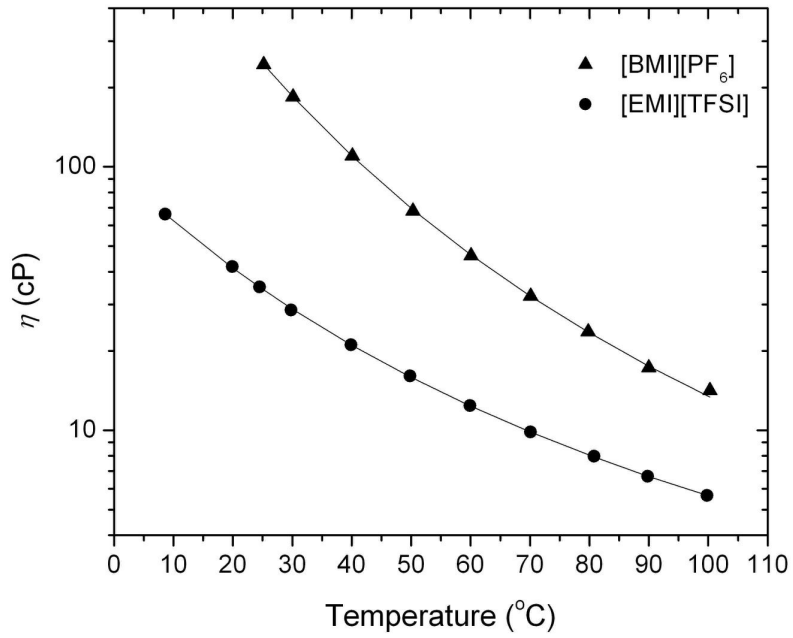

Figure 2.6: Viscosity vs. temperature for the ionic liquids [BMI][PF_6] and [EMI][TFSI]. Solid lines show VTF equation fits.

2.4 Solution Preparation

The general procedure used for preparing the copolymer/ionic liquid solutions is as follows. The appropriate amounts of polymer and ionic liquid were combined by weight, followed by addition of dichloromethane to a 1:1 v/v cosolvent to ionic liquid ratio for dilute solution experimental samples (DLS, cryo-TEM), and approximately 5 wt% for concentrated solution experimental samples (SAXS, impedance spectroscopy). The cosolvent is used to expedite the dissolution of the polymers, which is a slow process in the ionic liquid due to its selective solvation of the copolymer blocks and relatively high viscosity compared to more common organic solvents. For example, room temperature viscosities for [BMI][PF_6] and [EMI][TFSI] are ~240 cP and ~35 cP, respectively. The solutions were stirred in capped vials for several hours to ensure complete dissolution of the polymers. The dichloromethane was then evaporated by first stirring the solutions under dry N_2 purge for ~ 24 hours. Subsequently, the solutions were dried under vacuum (ca. 10 mTorr) at 60 ± 5 °C until constant weight was reached. This solution preparation procedure takes advantage of the negligible volatility of the ionic liquids, and serves to remove not only the dichloromethane cosolvent, but also to remove any water that has been absorbed by the ionic liquids during solution preparation due to their hygroscopic nature. After preparation, all copolymer/ionic liquid solutions were stored in a vacuum-sealed desiccator to guard against absorption of atmospheric moisture.

2.5 Dynamic Light Scattering

Dynamic light scattering (DLS) is a widely used technique for measuring

structural characteristics, such as size and size distribution, of particles in solution. The basic premise of dynamic light scattering is to measure the temporal fluctuations in the intensity of scattered light from a solution of particles, and correlate them to the particle motion. The fluctuations in scattered light intensity are a result of local changes in the refractive index (n) of the solution due to concentration fluctuations resulting from random Brownian motion of the particles. Thus, the fluctuations in scattering intensity contain information about the diffusion of the particles in solution.

The measured function in a typical DLS experiment is the intensity autocorrelation function, given in Equation 2.2.

$$G_2(t) = \lim_{T\to\infty} \frac{1}{T} \int_0^T I_S(t') I_S(t'+t) dt' \tag{2.2}$$

The intensity autocorrelation function is obtained by multiplying the scattered light intensity (I_S) at time t' by the intensity measured after a delay time (t), and then summing the results over a much longer time interval T. This process is then repeated for many different delay times, which typically range from 10^{-6}–10^{2} s. The Siegert relation (Equation 2.3) connects the measured $G_2(t)$ with the scattered electric field, from which information on the diffusion of particles in the solution can be extracted.[15]

$$G_2(t) = B\left(1 + \beta |g_1(t)|^2\right) \tag{2.3}$$

In Equation 2.3, B is the baseline in the measured $G_2(t)$ vs. t plot, β is the spatial coherence factor related to the laser and detector optics, and $g_1(t)$ is the normalized electric field autocorrelation function.

For the simple case of rigid, monodisperse, spherical particles, $g_1(t)$ is given by a

single exponential expression.

$$g_1(t) = \exp(-\Gamma t) \tag{2.4}$$

In Equation (2.4) Γ is the decay rate associated with the particle diffusion, and is defined as

$$\Gamma = D_m q^2 \tag{2.5}$$

where q is the scattering vector, defined as the difference between the incident and scattered wave vectors, and is calculated as

$$q = \frac{4\pi n}{\lambda_o} \sin\frac{\theta}{2} \tag{2.6}$$

In Equation (2.6) n is the refractive index of the solvent, λ_o is the vacuum wavelength of the incident light, and θ is the scattering angle. For a solution containing particles of two distinct sizes, $g_1(t)$ can be defined by the following double exponential expression,

$$g_1(t) = A_1 \exp(-\Gamma_1 t) + A_2 \exp(-\Gamma_2 t) \tag{2.7}$$

where Γ_1 and Γ_2 correspond to the decay rates associated with the diffusion of the two distinct particle sizes.

Rather than the simple cases of one or two decay rates described above, it is often more appropriate to describe the electric field autocorrelation function with a distribution of decay rates. This is often the case for solutions of amphiphilic molecules, where the micellar aggregate structures possess a distribution of sizes. In this case,

$$g_1(t) = \int_0^\infty G(\Gamma)\exp(-\Gamma t)d\Gamma \tag{2.8}$$

where $G(\Gamma)$ is the distribution function of the decay rates. Koppel first proposed the use

of cumulant analysis for such a system, where the field correlation function is given by the logarithm of the moment generating equation.[16]

$$\ln g_1(t) = -\overline{\Gamma} t + \left(\frac{1}{2!}\right)\mu_2 t^2 - \left(\frac{1}{3!}\right)\mu_3 t^3 + \ldots \tag{2.9}$$

From this equation the first three cumulants ($\overline{\Gamma}$, μ_2, μ_3) represent the first three moments of the distribution of decay rates. The first cumulant is defined as,

$$\overline{\Gamma} = \int_0^\infty \Gamma G(\Gamma) d\Gamma \tag{2.10}$$

and is the average decay rate of the distribution. The second cumulant represents the variance of the distribution. Thus $\mu_2/\overline{\Gamma}^2$ is a good measure of the width of the decay rate distribution, and is often taken as a measure of the polydispersity in mobility (i.e. size) of the particles in solution.

In practice, Γ is obtained from the appropriate expression for the electric field auto correlation function (Equations 2.4, 2.7, 2.9) at several scattering angles and plotted versus q^2 to obtain D_m for the particles in solution (Equation 2.5). Then, assuming the solution is sufficiently dilute, D_m can be taken as the tracer diffusion coefficient (D_t) for a single particle, and the Stokes–Einstein relation can be used to extract the hydrodynamic radius (R_h) of the particles.

$$D_\mathrm{t} = \frac{kT}{6\pi\eta_\mathrm{s} R_\mathrm{h}} \tag{2.11}$$

In Equation 2.11 η_s is the solvent viscosity.

Additionally, the distribution of decay rates can be obtained via Laplace inversion of Equation 2.8. The inversion routine known as REPES[17] will be used in this thesis.

Samples for DLS were prepared using the general solution preparation procedure described in Section 2.4. Prior to DLS experiments, dust was removed from the solutions by filtering them through 0.45 μm PTFE syringe filters into sample tubes that had been fashioned from glass tubing with an inner diameter of 0.51 cm and an outer diameter of 0.71 cm. Prior to addition of the solutions, the sample tubes had been rinsed several times with both filtered THF and chloroform to clean them and remove dust. After addition of the solutions the DLS sample tubes were either flame-sealed or sealed with several layers of Parafilm. The scattering measurements were made using a homemade setup consisting of a Brookhaven BI-DS photomultiplier, a Lexel Ar^+ laser with a wavelength of 488 nm, and a Brookhaven BI-9000 correlator. The photomultiplier was mounted on an adjustable goniometer, and the intensity correlation functions [$G_2(t)$] were measured at five different scattering angles between 40° and 120°. The samples were seated in a silicon oil bath, which served as an index matching fluid and to control the sample temperature. When scattering experiments were conducted at temperatures above room temperature the samples were equilibrated in the oil bath for at least 1 hour prior to data collection.

2.6 Cryogenic Transmission Electron Microscopy

Transmission electron microscopy (TEM) is used extensively to characterize the nano-scale structure of solid materials, and soft materials such as block copolymers.[18] This is due to the ability to achieve nanometer and even sub-nanometer scale resolution with TEM. Cryogenic transmission electron microscopy (cryo-TEM) is a specialized technique that allows the use of TEM for characterizing nano-scale particles in solution.

Solution samples are not compatible with conventional TEM for two main reasons. First, high vacuum must be maintained inside the electron microscope to prevent scattering of the electron beam by air. Thus, the interior of the microscope is incompatible with solutions prepared with volatile solvents. Second, diffusive motion of particles in a solution based sample would ultimately result in blurring of the microscopic images. With cryo-TEM, these issues are resolved by vitrification of the solution via cryogenic fixation.

Cryo-TEM has been established as a powerful technique for the investigation of amphiphilic block copolymer aggregates in solution. Typically, most studies have employed aqueous solutions due to the solubility of many organic solvents in commonly used cryogens (*e.g.* liquid ethane or liquid nitrogen).[19,20] However, some cryo-TEM investigations of block copolymer aggregates in organic solvents have been reported.[21,22] Additionally, block copolymer solutions prepared with ionic liquid solvents have been investigated via cryo-TEM.[23] The dilute block copolymer/ionic liquid solution studies reported in this thesis (Chapter 3) represent some of the first cryo-TEM investigations of solutions with ionic liquids as the solvent.

One particular requirement for the preparation of solution samples for cryo-TEM, particularly for aqueous solutions, is the need for extremely rapid sample cooling in order to achieve solution vitrification rather than crystallization. Cooling rates on the order of 10^5 K/s are necessary for the vitrification of aqueous samples.[24] This highlights one of the benefits of cryo-TEM investigations of solutions prepared with ionic liquids. Due to the large size and asymmetry of their constituent ions, many ionic liquids readily

undergo supercooling, often with a glass transition preempting crystallization.[6] Thus, vitrification of ionic liquid solutions is easily achieved. Additionally, the nonvolatility of ionic liquids eliminates the need to guard against solvent evaporation that can occur during addition of solutions to TEM grids prior to vitrification. However, in addition to these benefits, there are also negative aspects associated with the preparation of cryo-TEM samples using solutions with ionic liquid solvents. Thin solution films for cryo-TEM analysis, ideally $\leq$ 300 nm thick, are necessary to allow sufficient electron transmission through the sample. Thin solution films are typically obtained by addition of the solution to a TEM specimen grid coated with a perforated support film. Excess solution is typically wicked away to obtain thin solution films which span the holes in the support film of the TEM grid. The low viscosity of aqueous solutions allows them to be easily wicked away from the grid, and thin solution films are readily obtained. However, ionic liquids typically possess relatively high viscosities, usually in the range from several tens to several hundreds in units of cP at room temperature. The high ionic liquid viscosity makes obtaining thin solution films via wicking away excess solution fairly difficult. Fortunately, the viscosity of many ionic liquids is strongly dependent on temperature,[6] thus heating the samples can reduce the solution viscosity enough to allow thin solution films to be obtained via blotting. Additionally, most ionic liquids are fairly hygroscopic, and can absorb significant amounts of atmospheric moisture. Thus, absorption of moisture must be guarded against during cryo-TEM sample preparation.

Cryo-TEM was used in this thesis project to directly characterize the morphology of amphiphilic block copolymer micelles in ionic liquids. The dilute

solutions of copolymers in ionic liquid solvents used in cryo-TEM experiments were prepared as described in Section 2.4. Cryo-TEM specimens were prepared using a controlled environment vitrification system (CEVS), which was first developed by Bellare.[25] The CEVS basically consists of a polycarbonate chamber, inside which TEM sample grids can be suspended from a tweezers in order to apply and blot solution samples. Temperature is controlled inside the CEVS by a high power light bulb, regulated by an on-off temperature sensor. The tweezers which hold the sample grid are spring–loaded, and are connected to a switch that quickly plunges the tweezers from inside the CEVS chamber into the cryogen reservoir below. Schematic illustrations of the sample blotting procedure and the CEVS are shown in Figures 2.7 and 2.8, respectively. Samples for cryo-TEM were prepared by first placing a small drop of solution on a micro-perforated copper TEM grid, coated with a carbon-stabilized lacey formvar support film (Ted Pella, Inc.). The samples were pre-heated at 60 °C for 5 minutes in a sample preparation chamber in order to reduce the viscosity of the ionic liquid solvent. At 60 °C the viscosities for [BMI][PF_6] and [EMI][TFSI] drop to ~46 and ~12 cP, respectively. Excess solution was then blotted away with filter paper in order to obtain a thin solution layer ($\leq$ 300 nm) that spans the holes in the support film of the sample grid and allows sufficient electron transmission. Subsequently, the thin solution layer was vitrified by plunging the grid into liquid nitrogen or liquid ethane. For solutions with [EMI][TFSI] as the solvent, better vitrification results were obtained using liquid ethane as the cryogen rather than liquid nitrogen. This result was not explicitly studied, but could be due to easier crystallization of [EMI][TFSI] resulting

from lower asymmetry of the [EMI] cation. Liquid ethane possess a higher boiling point (190 K) and heat of vaporization (~7.04 kJ/mol) than liquid nitrogen (77 K, 5.82 kJ/mol), and is thus a better cryogen. Liquid ethane maintains good thermal, liquid contact with the solution film, which results in high cooling rates and more consistent sample vitrification. For [BMI][PF_6] good vitrification of the solution films could be accomplished using liquid nitrogen as the cryogen. Once vitrified, the samples were kept under liquid nitrogen until being inserted into the microscope. The samples were examined using a JEOL 1210 TEM and a Gatan 626 cryogenic sample holder, which maintained the samples at a temperature of –177 °C while in the microscope. The microscope was operated at an accelerating voltage of 120 kV, and sample images were recorded with a Gatan 724 multiscan CCD camera. Analysis of the cryo-TEM images was performed using DigitalMicrograph™ software (version 3.3).

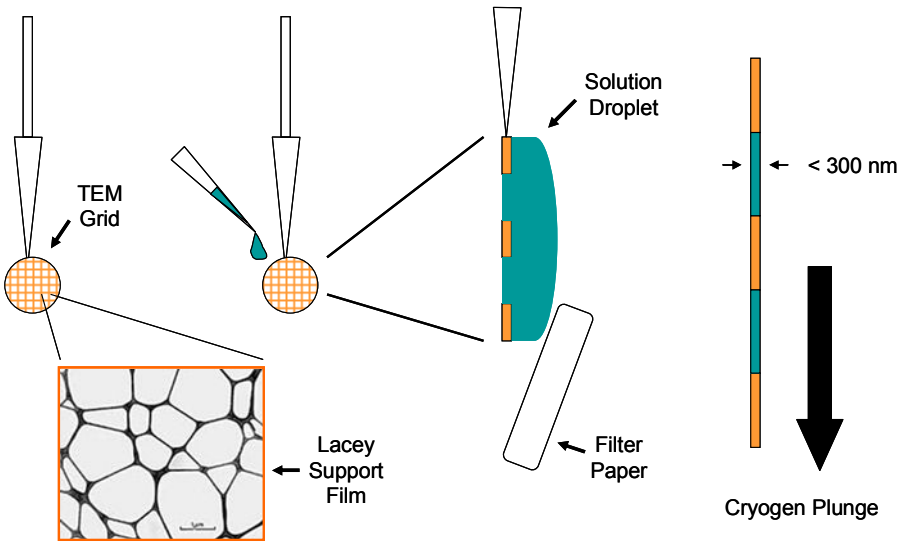

Figure 2.7: Schematic illustration of the blotting procedure for preparing cryo-TEM samples.

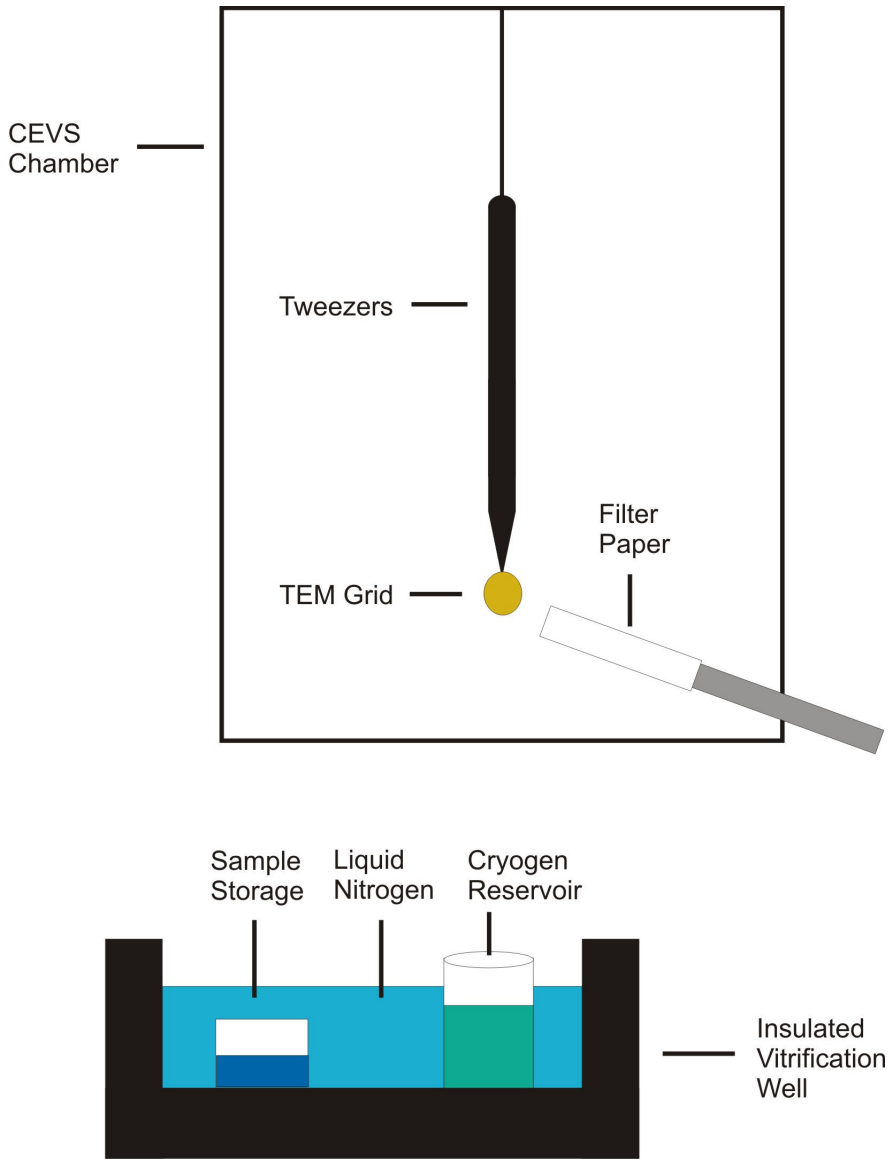

Figure 2.8: Schematic illustration of the controlled environment vitrification system used for preparing cryo-TEM samples.

2.7 Small Angle X-ray Scattering

The microstructures formed by block copolymers possess an ordered, periodic structure. Thus the microstructure domains of the copolymer can act as parallel scattering planes, and X-ray scattering can be used to probe the structure of the self-assembled copolymer.[26] Waves scattered from parallel scattering planes can be described by Bragg's Law, which states that constructive interference between waves scattered from different planes occurs only when the difference in their path length is an integral multiple of the wavelength. Figure 2.9 represents two waves scattered from two parallel scattering planes. The wave scattered from the lower plane must travel a longer distance (represented by the bold segments) than that of the wave scattered by the upper plane. The dotted perpendicular lines between the incident and scattered waves show that each bold segment is equal to $d\sin(\theta/2)$, where d is the distance between scattering planes and θ is the angle between the incident $\left(\vec{k}_i\right)$ and scattered waves $\left(\vec{k}_s\right)$. Thus, in order for there to be constructive interference between scattered waves Bragg's law written as,

$$2d\sin\left(\frac{\theta}{2}\right) = m\lambda \tag{2.12}$$

must be satisfied, where λ is the wavelength of incident radiation and m is an integer. X-ray radiation has wavelengths on the order of Angstroms, and typical domain spacing for self-assembled copolymer microstructures is on the order of several tens of nanometers. Thus, from Equation 2.12, it can be seen that X-ray diffraction from

copolymer microstructures occurs at very small angles, and it is therefore most often referred to as small angle X-ray scattering (SAXS).

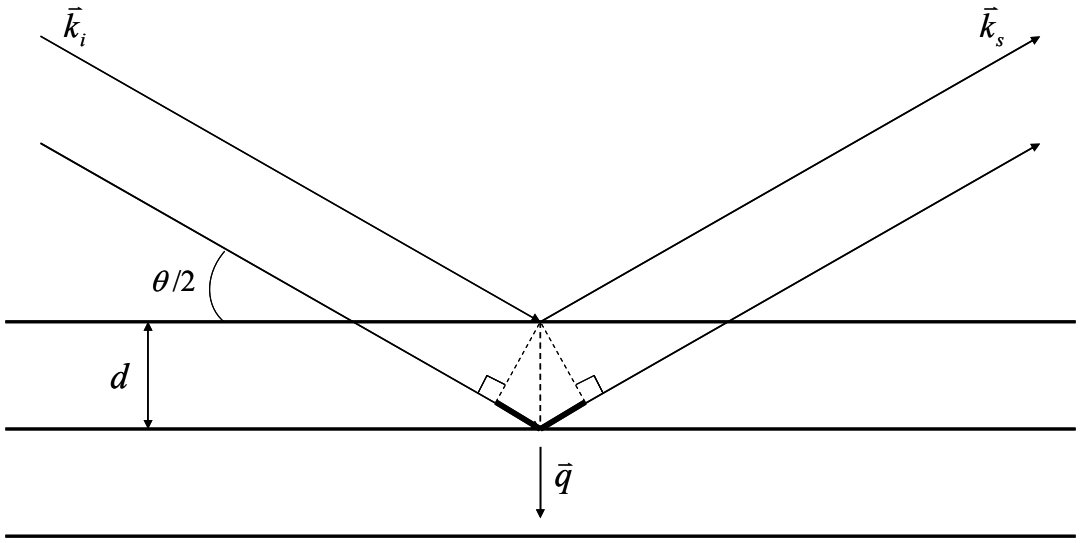

Figure 2.9: Schematic of waves scattered from parallel scattering planes illustrating Bragg's Law for constructive interference.

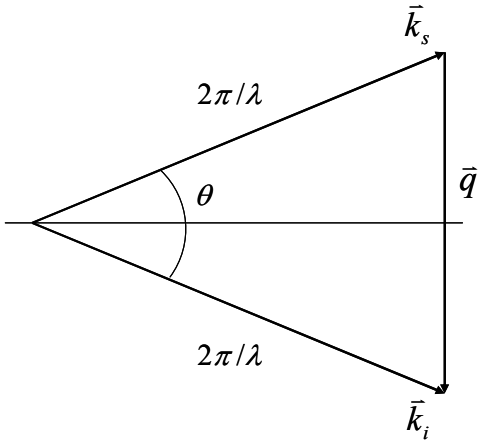

Figure 2.10: Schematic definition of the scattering vector, $\vec{q}$. The incident $(\vec{k}_i)$ and scattered $(\vec{k}_s)$ waves both possess magnitudes of $2\pi/\lambda$., and θ is the scattering angle.

In Figures 2.9 and 2.10, $\vec{q}$ is the scattering vector, which is defined as the difference between the incident and scattered wave vectors. For elastic scattering, the magnitude of the incident and scattered vectors are equal, and thus, the magnitude of $\vec{q}$ is given as

$$q = 2\left(\frac{2\pi}{\lambda}\sin\left(\frac{\theta}{2}\right)\right) = \frac{4\pi}{\lambda}\sin\left(\frac{\theta}{2}\right) \tag{2.13}$$

The self-assembled microstructure of a block copolymer sample can be characterized by referencing its scattering pattern to the scattering intensity maxima allowed by the Bragg criterion for constructive interference. The allowed Bragg reflections for several common block copolymer microstructures are given in Table 2.3. The allowed reflections are given as the ratio (q/q^*), where q^* is the position of the primary scattering peak in the copolymer scattering pattern.

Table 2.3: Allowed Bragg Reflections for Common Block Copolymer Microstructures

Microstructure	Allowed Reflections (q/q^*)
Lamellae	1:2:3:4:5:6…
Hexagonally packed cylinders	1:√3:√4:√7:√9:√12:√13…
Gyroid	√3:√4:√7:√8:√10…
Spheres (bcc symmetry)	1:√2:√3:√4:√5:√6…
Spheres (fcc symmetry)	√3:√4:√8:√11:√12…

Self-assembled block copolymers consist of multiple randomly oriented microscopic grains. This results in scattering patters consisting of multiple concentric rings positioned at q values corresponding to the specific copolymer microstructure. In practice the two dimensional concentric ring pattern is collected and integrated azimuthally to obtain a one dimensional scattering pattern plotted as scattering intensity vs. scattering vector. Figure 2.11 shows a simple schematic illustration of X-ray scattering from a copolymer sample consisting of randomly oriented microstructure grains, and integration of the two dimensional scattering pattern.

Two general procedures were used when preparing concentrated block copolymer/ionic liquid solution samples for SAXS experiments. For the first configuration, a hole was punched in an aluminum DSC pan, and a small piece of Kapton film (DuPont) was placed in the bottom of the pan to cover the hole. Next, a Teflon o-ring was placed in the DSC pan and filled with the copolymer/ionic liquid solution. Finally, a hole was punched in the DSC pan lid, and another piece of Kapton film was placed inside the lid to cover the hole. The DSC pan and lid were then crimped shut to seal the solution inside. After assembly, the SAXS samples were stored in a

vacuum-sealed desiccator. Alternatively, samples were also prepared by simply sealing the block copolymer/ionic liquid solutions in DSC pans without punched holes.

SAXS data was collected at the DuPont-Northwestern-Dow Collaborative Access Team (DND-CAT) beamline at the Advanced Photon Source, Argonne National Laboratory. Two-dimensional scattering patterns were recorded by a Mar CCD area detector, and then azimuthally integrated to give one-dimensional scattering data as intensity (I) vs. scattering wave-vector. The scattering angle (θ) was calibrated with silver behenate. Additionally, some SAXS experiments were conducted on a home-built beamline at the University of Minnesota Characterization Facility. This beamline consisted of a Rigaku RU-200BVH rotating anode generating Cu Kα X-rays (λ = 1.54 Å), Franks mirror optics, a 230 cm sample-to-detector distance, and a multiwire area detector (HI-STAR, Siemens Analytical X-ray Instruments).

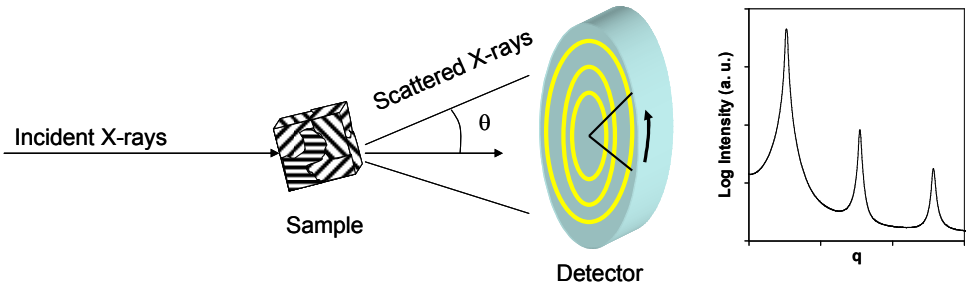

Figure 2.11: Illustration of scattering from a sample consisting of randomly oriented microstructure domains, and azimuthal integration of the two-dimensional scattering pattern.

2.8 Impedance Spectroscopy

Impedance spectroscopy (IS) was used in this thesis project to characterize the ionic conductivity of concentrated block copolymer/ionic liquid solutions. This technique has been used extensively to characterize the ionic conductivity of neat ionic liquids and polymer/ionic liquid composite materials.[27] IS can be used to investigate the electrochemical characteristics of a wide variety of materials, and thorough treatments of methods and theory are available.[28,29]

In practice, IS involves applying an alternating voltage to a sample over a range of frequencies, and measuring the resulting alternating current in order to calculate the sample impedance. The impedance describes the sample's opposition to a sinusoidal alternating current, and relates the amplitudes and phases of the applied voltage and measured current. The impedance (Z) is represented by a complex quantity and is thus often referred to as the complex impedance.

$$Z = Z' + iZ'' \tag{2.14}$$

In Equation (2.14) Z' and Z'' represent the real and imaginary components of the complex impedance, respectively. For a simple circuit model of a resistor and capacitor in series, Z' is the resistance and Z'' is the capacitive reactance, which is given as $-1/\omega$C, where ω is the angular frequency and C is the capacitance. The impedance can also be represented on a complex plane as shown in Figure 2.12. Several relations can be obtained from the plot in Figure 2.12.

$$Z' = |Z|\cos(\theta) \tag{2.15}$$

$$Z'' = |Z|\sin(\theta) \tag{2.16}$$

$$\theta = \tan^{-1}(Z''/Z') \tag{2.17}$$

$$|Z| = \left[(Z')^2 + (Z'')^2\right]^{1/2} \tag{2.18}$$

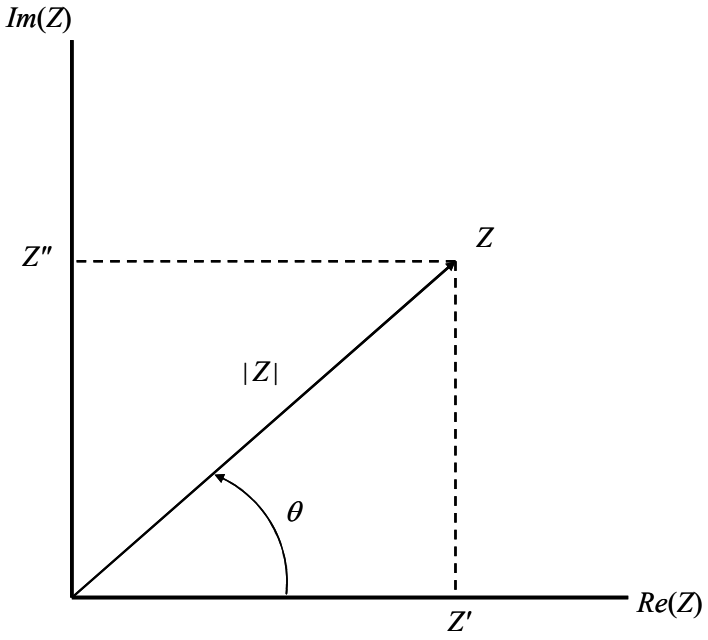

Figure 2.12: Complex impedance plane.

In Equations 2.15–2.17 and Figure 2.12, θ is the phase difference, or phase angle, between the applied voltage and measured current.

Purely resistive behavior occurs when θ, and thus Z'', equal zero. In this case $|Z| = Z' = \text{sample resistance } (R)$, and the conductivity of the sample (σ) can be calculated as,

$$\sigma = \frac{1}{Z'}\left(\frac{l}{A}\right) \tag{2.19}$$

where l is the sample thickness and A is the cross-sectional area of the sample.

Impedance spectroscopy experiments were performed using a Solartron 1255B frequency response analyzer connected to a Solartron SI 1287 electrochemical interface. The block copolymer/ionic liquid solutions were hot-pressed at ~150 °C into a Teflon ring, which held the samples at a constant diameter (7 mm) and thickness (2 mm). The sample disks were sandwiched between two stainless steel blocking electrodes. The applied voltage amplitude was typically 10 mV and the frequency was typically scanned from 10^6–1 Hz. Figure 2.13a shows a schematic illustration of the electrode set-up used for impedance measurements, and Figure 2.13b shows a representative plot of $|Z|$, Z' and Z'' for a concentrated block copolymer/ionic liquid solution (58 wt% SO(20–13)/[EMI][TFSI]). The impedance data shows a plateau in Z' at high frequency, where the sample response is dominated by ionic motion. This plateau value, where Z'' tends toward zero and $|Z|$ is equal to Z', is taken as the bulk resistance of the samples, and used to calculate ionic conductivity, σ, via Equation 2.19.

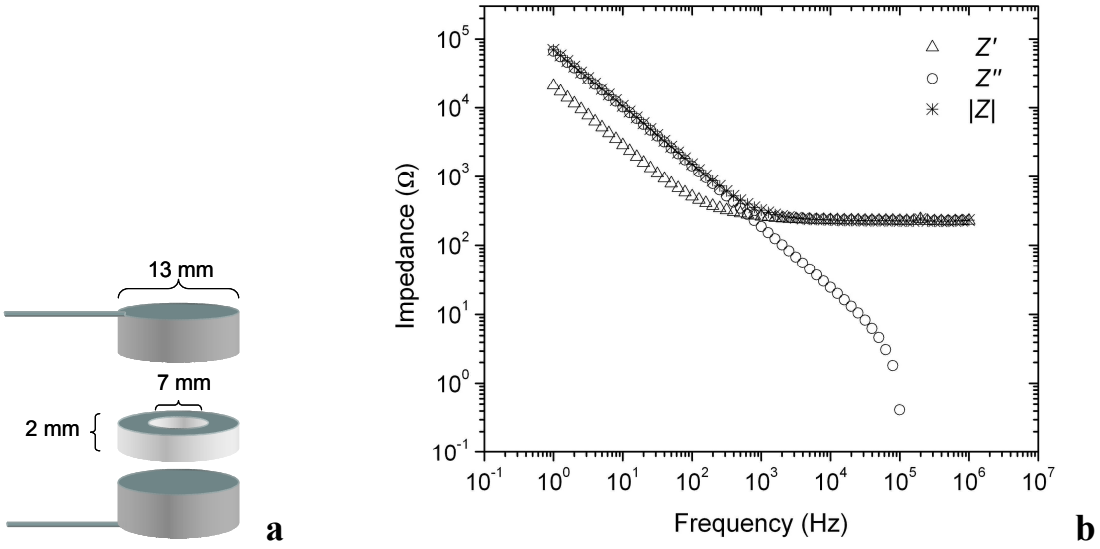

Figure 2.13: a) Schematic illustration of the electrode set-up used for impedance measurements; b) Representative impedance data for a concentrated PS–PEO solution (58 wt% SO(20–13)/[EMI][TFSI]).

2.9 Thin Film Preparation

Thin films of PS–PEO/[EMI][TFSI] solutions were prepared in order to investigate anisotropic alignment of their self-assembled microstructures. The PS–PEO/[EMI][TFSI] solution thin films were prepared by spin-coating, using silicon wafers as the substrate. Dilute solutions for spin coating were prepared by first combining the appropriate amounts of copolymer and ionic liquid, by weight, for the desired thin film copolymer/ionic liquid solution concentration. The block copolymer and ionic liquid were then diluted to a combined 1.0 wt% in dichloromethane. The Si wafers used as substrates for the PS–PEO/[EMI][TFSI] films were approximately one square cm pieces cut from larger (10 cm diameter) wafers using a diamond scribe. The

Si wafers possessed a native oxide layer, and were cleaned by sonication in isopropanol and distilled water for 15 minutes each. The wafers were then dried with blown high purity nitrogen. Finally, the wafers were cleaned under UV generated ozone for 10–15 minutes immediately prior to spin-coating. The copolymer/ionic liquid thin films were spin-coated from the 1.0 wt% dichloromethane solutions at 4000 RPM for 45 seconds. The solution was added to the wafer until the entire surface was just coated (~0.1 mL), and then the spin coater was immediately started. After spin-coating, the films were dried further under vacuum (~10 mtorr) at room temperature for 12 hours.

The block copolymer/ionic liquid film thickness was measured via variable angle spectroscopic ellipsometry (VASE) on a V-VASE Ellipsometer (J.A. Woollam Co., Inc.) with incidence angles of 60° and 70°, and a wavelength range of 250–1100 nm. A model for a thin film Cauchy dielectric material was used to fit the data. Three thickness measurements were made at different locations on the films, and were found to be within ± 10%. In general, the thin film preparation protocol described above produced PS–PEO/[EMI][TFSI] solution films with thicknesses between 100–150 nm.

2.10 Scanning Probe Microscopy

Scanning probe microscopy (SPM) was used in this thesis project to obtain images of the surfaces of block copolymer thin films in order to characterize the orientation of the self-assembled copolymer microstructure. SPM is a well established technique for the investigation of polymeric materials ranging from thin films to single polymer chains.[30,31] In general, SPM consists of measuring the deformation of a microfabricated cantilever as the probe or “tip” of the cantilever is laterally scanned

across the surface of a sample. The cantilever motion is detected by focusing a laser beam on the tip end of the cantilever, and sensing the displacement of the reflected laser spot on a position sensitive photodetector.

Many variations of the general SPM technique exist, which are a result of differences in the types of samples, or the types of sample–probe interactions being investigated. In this thesis dynamic force or "tapping" mode SPM has been used exclusively. In dynamic force SPM, the cantilever tip is oscillated sinusoidally in the vertical direction as it is scanned laterally across the sample surface. Thus, interactions between the cantilever tip and the sample surface result in changes in the oscillation amplitude of the cantilever, which are sensed by a corresponding change in the amplitude of the reflected sinusoidal laser signal at the photodetector. The SPM responds to this change by vertically displacing the sample in order to maintain the operator-selected set point amplitude. Then, essentially, the necessary vertical sample displacement can be translated into a height image of the sample surface topography.

In general, two regimes exist for the interactions between the probe and the sample. The attractive regime describes the situation where the oscillating probe comes within close proximity (within several angstroms) to the sample surface but does not actually touch the surface. In this case the net interaction between the tip and the sample surface is attractive, which results in a decrease in the oscillation frequency at the tip. The repulsive regime describes the situation when the oscillating tip makes contact with the sample surface (*i.e.*, electronic overlap between the tip and sample atoms). In this case the net interaction between the tip and the sample is repulsive, which results in an

increase in the oscillation frequency at the tip. These changes in oscillation frequency result in a corresponding change in the phase lag between the tip oscillation and the driving oscillation supplied by the microscope scanner at the base of the cantilever. Within a particular tip–sample interaction regime, relative differences in the tip oscillation phase indicate areas of differing tip–sample interaction magnitude. Thus phase imaging can be used to differentiate between areas of a sample consisting of materials with differing physicochemical properties that result in differing magnitudes of interaction with the probe tip (*e.g.* modulus, polarity, charge).

For the samples investigated in this thesis, SPM experiments were performed in the repulsive tip–sample interaction regime. Thus, for the PS–PEO/[EMI][TFSI] thin films (Chapter 6), the PS domains of the microstructure appear as lighter contrast areas in the SPM phase images. This can be basically rationalized as resulting from the difference in the stiffness, or modulus, between the glassy PS domains and the soft PEO/ionic liquid domains. Tip interactions with the stiffer PS domains lead to a larger shift of the tip resonant response to higher frequency, and thus lesser phase lag between the tip and the drive at the base of the cantilever. In SPM phase images, regions of lesser phase lag are conventionally assigned with brighter contrast. This simple explanation based on the stiffness, or modulus difference between the domains of the film is sufficient for assigning regions of differing contrast in the PS–PEO/[EMI][TFSI] solution films. However, it is obvious that other sample characteristics (*e.g.*, polarizability, charge, etc.) will have an effect on the tip phase lag, and thus a more in–depth rationalization of the phase contrast based on tapping energy dissipation felt in

the different sample domains is often employed.[32] In this case, regions of the sample that are less dissipative display a lesser phase lag, and thus brighter contrast in the phase images. Further background on the fundamentals of dynamic force mode SPM and theoretical analysis of tip–sample interactions are covered in an extensive review by García and Pérez.[33]

SPM experiments were conducted on a Veeco (DI) Nanoscope III multimode SPM, using tapping mode cantilevers with a force constant of 42 N/m, resonance frequency of 285 kHz, and monolithic silicon probe tips (Arrow NCR, Nano World). Images were analyzed with the Nanoscope v5.31 software package. The drive amplitude and amplitude setpoint for the cantilever were adjusted to maintain tip–surface interactions in the repulsive regime.

2.11 References

1. Morton, M. *Anionic Polymerization: Principles and Practice*; Academic Press: New York, 1983.

2. Odian, G. *Priciples of Polymerization*, 4th ed.; John Wiley & Sons, Inc.: Hoboken, 2004.

3. Hillmyer, M. A.; Bates, F. S. *Macromolecules* **1996**, *29*, 6994–7002.

4. Ndoni, S.; Papadakis, C. M.; Bates, F. S.; Almdal, K. *Rev. Sci. Instrum.* **1995**, *66*, 1090–1095.

5. Pangborn, A. B.; Giardello, M. A.; Grubbs, R. H.; Rosen, R. K.; Timmers, F. J. *Organometallics* **1996**, *15*, 1518–1520.

6. Wasserscheid, P; Welton, T., Eds. *Ionic Liquids in Synthesis*, 2nd ed.; Wiley-VCH: Weinheim, 2008.

7. Fuller, J.; Carlin, R. T.; De Long, H. C.; Haworth, D. *J. Chem. Soc., Chem. Commun.* **1994**, 299.

8. Huddleston, J. G.; Visser, A. E.; Reichert, M.; Willauer, H. D.; Broker, G. A.; Rogers, R. D. *Green Chem.* **2001**, *3*, 156–164.

9. Susan, M. A. B. H.; Kaneko, T.; Noda, A.; Watanabe, M. *J. Am. Chem. Soc.* **2005**, *127*, 4976–4983.

10. Holbrey, J. D.; Reichert, W. M.; Nieuwenhuyzen, M.; Johnston, S.; Seddon, K. R.; Rogers, R. D. *Chem. Commun.* **2003**, 1636–1637.

11. Triolo, A.; Mandanici, A.; Russina, O.; Rodriguez-Mora, V.; Cutroni, M.; Hardacre, C.; Nieuwenhuyzen, M.; Bleif, H.-J.; Keller, L.; Ramos, M. A. *J. Phys. Chem. B* **2006**, *110*, 21357–21364.

12. Tokuda, H.; Hayamizu, K.; Ishii, K.; Susan, M. A. B. H.; Watanabe, M. *J. Phys. Chem. B* **2005**, *109*, 6103–6110.

13. Ngo, H. L.; LeCompte, K.; Hargens, L.; McEwan, A.. B. *Thermochim. Acta* **2000**, *357–358*, 97–102.

14. Abraham, M. A.; Moens, L., Eds. *Clean Solvents: Alternative Media for Chemical Reactions and Processing*; American Chemical Society: Washington, DC, 2002.

15. Chu, B. *Laser Light Scattering: Basic Principles and Practice*, 2nd ed.; Academic Press, Inc.:Boston, 1991.

16. Koppel, D. E. *J. Chem. Phys.* **1972**, *57*, 4814

17. Jakes, J. *Collect. Czech. Chem. Commun.* **1995**, *60*, 1781.

18. Williams, D. B.; Carter, C. B. *Transmission Electron Microscopy: A Textbook for Materials, Science*; Plenum Press: New York, 1996.

19. Won, Y.-Y.; Davis, H. T.; Bates, F. S. *Science* **1999**, *283*, 960.

20. Jain, S.; Bates, F. S. *Science* **2003**, *300*, 460.

21. Lodge, T. P.; Bang, J.; Li, Z.; Hillmyer, M. A.; Talmon, Y. *Faraday Discuss.* **2004**, *128*, 1.

22. Oostergetel, G. T.; Esselink, F. J.; Hadziioannou, G. *Langmuir* **1995**, *11*, 3721.

23. He, Y.; Li, Z.; Simone, P.; Lodge, T. P. *J. Am. Chem. Soc.* **2006**, *128*, 2745.

24. Siegel, D. P.; Green, W. J.; Talmon, Y. *Biophys. J.* **1994**, *66*, 402.

25. Bellare, J. R. Cryo-Electron and Optical Microscopy of Surfactant Microstructures. Ph.D. Thesis, University of Minnesota, 1988.

26. Roe, R.-J. *Methods of X-Ray and Neutron Scattering in Polymer Science*; Oxford University Press: New York, 2000.

27. Ohno, H., Ed. *Electrochemical Aspects of Ionic Liquids*; John Wiley & Sons, Inc.: Hoboken, 2005.

28. Barsoukov, E.; Macdonald, J. R., Eds. *Impedance Spectroscopy: Theory, Experiment, and Applications*; John Wiley & Sons, Inc.: Hoboken, 2005.

29. Orazem, M. E.; Tribollet, B. *Electrochemical Impedance Spectroscopy*; John Wiley & Sons, Inc.: Hoboken, 2008.

30. Magonov, S. N.; Reneker, D. H. *Annu. Rev. Mater. Sci.* **1997**, *27*, 175–222.

31. Sheiko, S. S. *Adv. Polym. Sci.* **2000**, *151*, 61–174.

32. Cleveland, J. P.; Anczykowski, B.; Schmid, A. E.; Elings, V. B. *Appl. Phys. Lett.* **1998**, *72*, 2613.

33. García, R.; Pérez, R. *Surf. Sci. Rep.* **2002**, *47*, 197–301.

Chapter 3

Self-Assembly of Block Copolymers in Ionic Liquids at Low Concentration[1]

3.1 Introduction

Self-assembly into well-defined nanostructures is the characteristic that has motivated much of the research concerning the dilute solution behavior of amphiphilic block copolymers. Analogous to low molar mass amphiphiles, block copolymer molecules can aggregate to form micelles when dissolved in selective solvents. For simple AB diblock copolymers spherical micelles often result, with the less soluble blocks aggregating together to form a dense core surrounded by a shell, or corona, made up of the more soluble blocks. Other morphologies such as cylindrical (wormlike) micelles and bilayer vesicles have also been observed,[1–3] with a natural morphological progression from spheres to cylinders to bilayers occurring as the volume fraction of the soluble copolymer block is reduced.[4] Several potential applications of amphiphilic

[1] Reproduced in part with permission from Macromolecular Chemistry and Physics, Vol. 208, 339–348 (2007). Copyright 2007 Wiley–VCH. Reproduced in part with permission from Macromolecules, Vol. 41, 1753–1759 (2008). Copyright 2008 American Chemical Society.

block copolymers and their resulting aggregate structures in solution include drug delivery,[5–7] chemical separations,[8] and nanoparticle synthesis.[9,10]

Despite the growing number of publications presenting ionic liquids as alternative solvents, relatively little work has been reported on the fundamental self-assembly behavior of dilute solutions of amphiphilic block copolymers dissolved in ionic liquids. In a pioneering study by He *et al*., the dilute solution self assembly behavior of several poly(butadiene-*b*-ethylene oxide) copolymers (PB–PEO) was studied in the ionic liquid 1-butyl-3-methylimidazolium hexafluorophosphate ([BMI][PF_6]).[11] The researchers in this study utilized dynamic light scattering (DLS) and cryogenic transmission electron microscopy (cryo-TEM) to investigate the morphology of the copolymer micelles formed in the ionic liquid. Their results showed well defined micellar structures that followed the universal sequence of spheres→cylinders→bilayer vesicles as the volume fraction of the soluble copolymer block was decreased. This work by He has led to a unique application for block copolymer micelles in ionic liquids know as the "micellar shuttle".[12–14] Upon heating and cooling, transfer of intact copolymer micelles between water and hydrophobic ionic liquids has been observed. This process takes advantage of the unique solvent properties of ionic liquids, where, in this case, they are immiscible with water yet still a good solvent for the PEO blocks of the copolymers. Other unique block copolymer micellization behavior has been recently reported by Ueki and coworkers.[15] In this system the researchers utilized diblock copolymers in which one block has an upper critical solution temperature and the other has a lower critical solution temperature in

the ionic liquid solvent. Thus, the copolymers display doubly thermoresponsive micellization with a transition from spherical micelles, to single polymer chains, to reverse spherical micelles upon heating the solution. Additionally, the dilute solution self-assembly behavior of several poly(ethylene oxide-*b*-propylene oxide-*b*-ethylene oxide) (Pluronic) copolymers has been reported in the ionic liquids [BMI][PF_6] and [BMI] tetrafluoroborate (BF_4).[16]

One of the goals of this thesis has been to expand upon the understanding of the dilute solution self-assembly behavior of amphiphilic block copolymers in ionic liquids. This chapter describes the results of studies on the dilute solution self-assembly behavior of poly(styrene-*b*-methyl methacrylate) copolymers (PS–PMMA) and PB-PEO copolymers dissolved in the ionic liquids [BMI][PF_6] and 1-ethyl-3-methylimidazolium bis(trifluoromethylsulfonyl)imide ([EMI][TFSI]).

3.2 Experimental

This section briefly describes details of the materials and techniques specific to the experiments in this portion of the thesis. A more general account of the synthesis and characterization of materials, and the experimental techniques can be found in Chapter 2.

Table 3.1 shows the molecular characteristics of the PS–PMMA copolymers used in these dilute solution studies. The PS–PMMA copolymers had been prepared previously via anionic polymerization,[17] and were characterized via ^{1}H-NMR and SEC prior to use. The copolymer molecular weights and polydispersities were found to correspond to those reported from their original synthesis. The PS–PMMA copolymers

will be designated as SM(X–Y), where the numbers in parenthesis correspond to the block molecular weights in kg/mol. Thus, the polymers are of almost constant total molecular weight, but differ in composition. A PMMA homopolymer, previously synthesized via anionic polymerization, was also used. It possessed a molecular weight of 100 kg/mol and PDI of 1.07, both determined by SEC with polystyrene standards.

Table 3.2 shows the molecular characteristics of the PB–PEO copolymers used in the following experiments. The PB–PEO copolymers had been prepared previously via anionic polymerization,[18] and were characterized via ^{1}H-NMR and SEC prior to use. These block copolymers were synthesized from the same parent PB block, thus only the PEO block length differs between the various copolymers. The PB blocks of the copolymers consist of 90% 1,2 monomer addition. In a similar manner to the PS–PMMA copolymers, the PB–PEO copolymers will be designated as BO(X–Y), with the numbers in parenthesis again representing the block molecular weights in kg/mol.

Table 3.1: Molecular Characteristics of PS–PMMA Diblock Copolymers.

Copolymer	M_{PS} (kg/mol)	M_{PMMA} (kg/mol)	PDI	f_{PMMA}
SM(1–15)	1.3	15.0	1.05	0.92
SM(3–13)	3.0	13.5	1.05	0.82
SM(7–8)	7.0	7.8	1.04	0.53

Table 3.2: Molecular Characteristics of PB–PEO Diblock Copolymers[a]

Copolymer	M_{PB} (kg/mol)	M_{PEO} (kg/mol)	PDI	f_{PEO}
BO(9–6)	9.2	5.9	1.04	0.33
BO(9–4)	9.2	4.0	1.06	0.25
BO(9–3)	9.2	2.9	1.04	0.20

[a] PB blocks consist of 90% 1,2 addition of butadiene monomer.

[BMI][PF_6] (solvent grade, ≥98%) was purchased from Solvent Innovation GmbH. [EMI][TFSI] was synthesized as described in Chapter 2. Prior to use, the ionic liquids were dried under vacuum (ca. 10 mTorr) at 60-70 °C for 2-3 days to remove absorbed moisture and then stored either in a glove box under argon or in a vacuum-sealed desiccator.

The general procedure used for dissolution of polymers in ionic liquid solvents is described in Chapter 2. Briefly, the dilute polymer in ionic liquid solutions used in the following experiments were prepared with the use of a cosolvent (dichloromethane) which was subsequently removed under N_2 purge and vacuum with heating (ca. 60 °C). This protocol takes advantage of the negligible volatility of the ionic liquid solvents, even under reduced pressure and elevated temperature. Solutions of PMMA homopolymer in acetone were also prepared simply by direct dissolution of the polymer. These solutions were used to make a comparison between the behavior of PMMA in a known good solvent and in [BMI][PF_6].

3.3 Dilute Solutions of Poly(Styrene–Methyl Methacrylate) Diblock Copolymers in Ionic Liquid

Initially, DLS was used to investigate the structural characteristics of the PS–PMMA copolymers dissolved in [BMI][PF_6]. Figure 3.1 shows examples of the squared, normalized electric field correlation functions [$g_1^2(t)$] for the three PS-PMMA block copolymer solutions at concentrations of 1.0 wt%. These functions were fitted by the method of cumulants (Equation 3.1) to obtain an average decay rate $(\overline{\Gamma})$ associated with the diffusion of the block copolymers and/or block copolymer aggregate structures in solution.[19]

$$\ln g_1(t) = -\overline{\Gamma} t + \left(\frac{1}{2!}\right)\mu_2 t^2 - \left(\frac{1}{3!}\right)\mu_3 t^3 + \ldots \tag{3.1}$$

The inset of Figure 3.1 shows the decay rates for the three solutions plotted versus the scattering vector squared (q^2). Using the relation $\overline{\Gamma} = q^2 D_m$, the slopes of the linear plots in Figure 3.1 give the mutual diffusion coefficients (D_m) for the block copolymer aggregates in solution. By assuming that the concentrations of the solutions are sufficiently dilute and that the mutual diffusion coefficients tend towards the infinite dilution tracer diffusion coefficients (D_t), the Stokes-Einstein relation (Equation 3.2) can be used to extract an apparent hydrodynamic radius (R_h) for the solute particles. In Equation (3.2), η_s is the viscosity of the solvent, k_B is the Boltzmann constant, and T is the absolute temperature.

$$R_{\mathrm{h}} = \frac{k_{\mathrm{B}}T}{6\pi\eta_{\mathrm{s}}D_{\mathrm{t}}} \tag{3.2}$$

Values of R_{h} for the three 1.0 wt% PS-PMMA block copolymer solutions are given in Table 3.3. The estimated error in the values of R_{h} obtained from DLS is $\pm 5\%$.

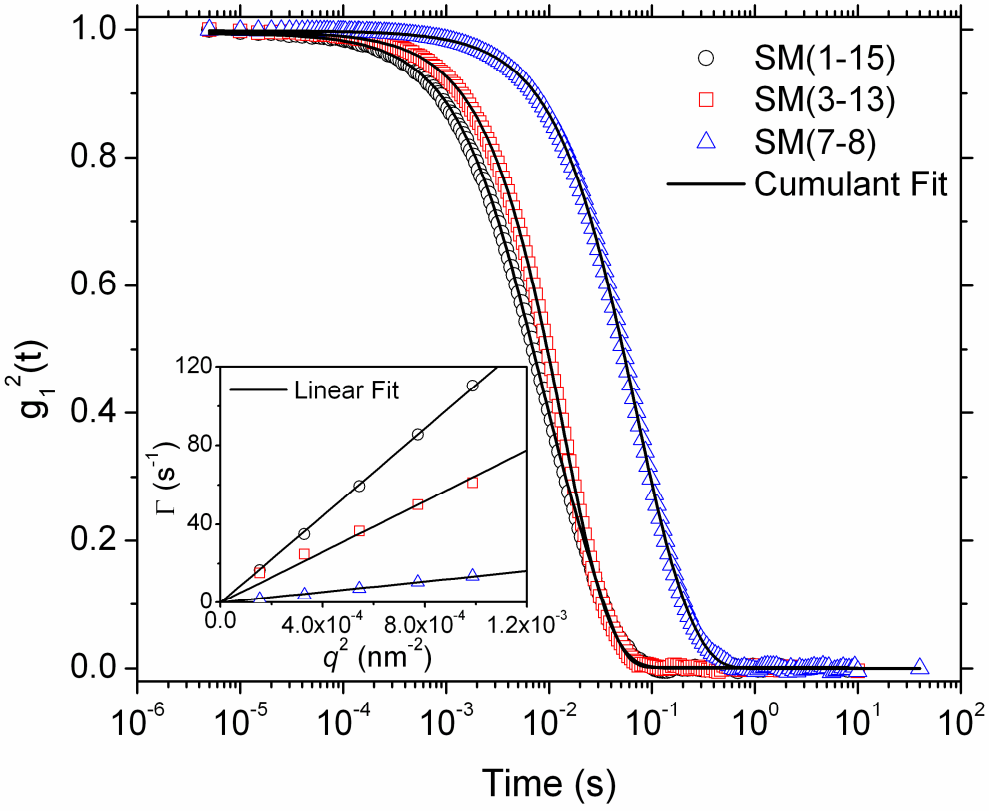

Figure 3.1: Squared electric field correlation functions for 1.0 wt% solutions of the PS–PMMA block copolymers dissolved in [BMI][PF_6]. The correlation functions were measured at $\theta = 80°$ and 25 °C. The inset shows linear fits of the decay rates versus the square of the scattering vector.

Table 3.3: Size and aggregation characteristics for PS–PMMA block copolymer micelles formed at a concentration of 1.0 wt% in [BMI][PF_6].

Copolymer	Time[a] (d)	$\mu_2/\bar{\Gamma}^2$	R_h (nm)[b] cumulant	R_h (nm)[c] double exp.	R_c (nm)	s_{PS}	N_{agg}	a_o (nm^2)
SM(1–15)	3	0.90	13	3, 27				
	137	0.90	9	2, 18				
	251	0.93	8	2, 17	6.9±1.0	2.9	670	0.9
SM(3–13)	6	0.22	14					
	143	0.29	14		7.4±0.8	2.1	360	1.9
SM(7–8)	7	0.49	63	31, 117				
	189	0.44	65	32, 117	10.4±1.9 (S)[d]	1.9	430	3.2
					9.0±1.4 (C)[d]	1.6	20[e]	2.8

[a)]Time between solution preparation and DLS experiments; [b)]R_h obtained via cumulant function (Equation 3.1); [c)]R_h obtained via double exponential function (Equation 3.3); [d)](S) denotes spherical morphology, (C) denotes cylindrical morphology; [e)]N_{agg} for cylindrical SM(7–8) micelles is calculated as the number of copolymer chains per 1 nm cylinder length.

3.3.1 PS–PMMA Copolymer Aggregation Characteristics

For the SM(1-15) copolymer an initial R_h value of 13 nm indicates the formation of molecular aggregate structures, since a simple calculation of the radius of gyration (R_g) of a single, unperturbed SM(1-15) molecule gives a value of approximately 3 nm. Table 3.3 also lists values for the reduced second cumulant ($\mu_2/\overline{\Gamma}^2$), which is used as a measure of the polydispersity of particle size since μ_2 represents the variance of the decay rate distribution. As can be seen, the polydispersity for the SM(1-15) solution is higher than for the other block copolymer solutions in this study. This can be explained by coexistence of single block copolymer molecules (unimers) along with molecular aggregate structures in solution. To test this hypothesis $g_1(t)$ for SM(1-15) was fit with a double exponential function (Equation 3.3), which expresses the electric field correlation function as arising from two distinct size classes of solute particles.

$$g_1(t) = A_1 \exp(-\Gamma_1 t) + A_2 \exp(-\Gamma_2 t) \tag{3.3}$$

In Equation 3.3 Γ_1 and Γ_2 are the decay rates corresponding to the solute particles in the two different size classes. Table 3.3 lists the values of R_h for the SM(1-15) solution, which were calculated using Γ_1 and Γ_2 from the double exponential fit. These values correspond well with the above explanation for the large value of the reduced second cumulant, with 3 nm being consistent with the expected unimer size and 27 nm being a reasonable size for block copolymer micelles. Additionally, it was observed that the R_h values for the SM(1-15) solute particles decreased with time, particularly those obtained from Equation 3.3 for the molecular aggregates. This result could indicate the establishment of equilibrium between the block copolymer unimers and micelles,

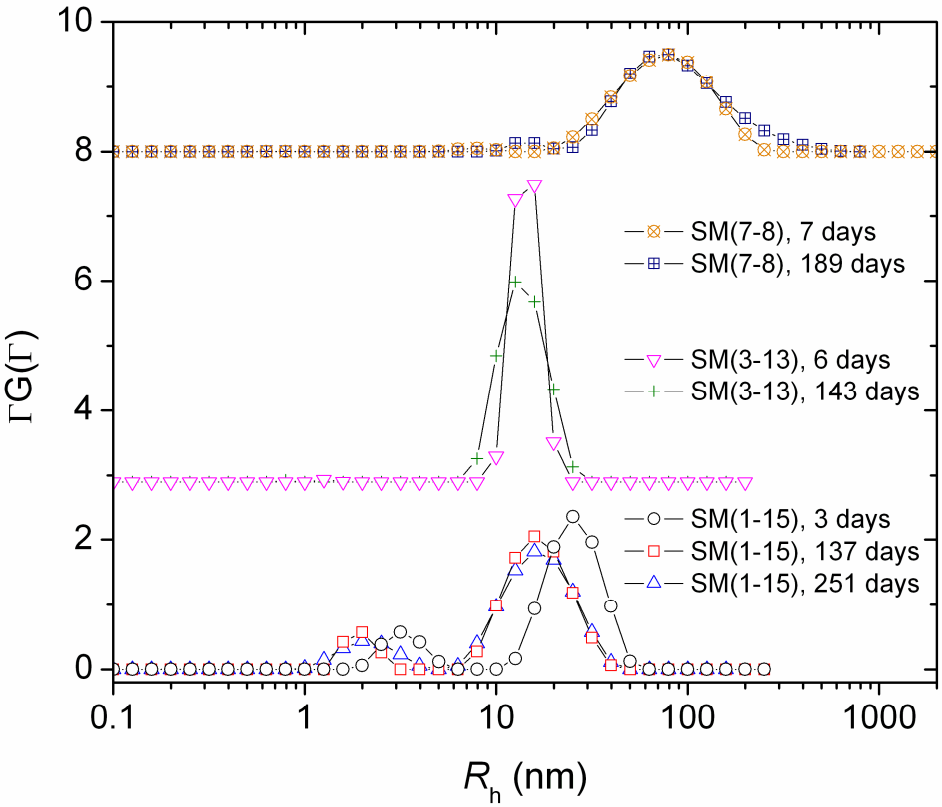

Figure 3.2: R_h distribution for 1.0 wt% solutions of PS–PMMA block copolymers dissolved in [BMI][PF_6]. Plots shifted vertically for clarity.

particularly since R_h did not change considerably between 137 and 251 days after solution preparation.

To investigate the distribution of aggregate size the Laplace inversion routine REPES was applied to the field correlation function data obtained from DLS (Figure 3.2).[20] The R_h distribution shown in Figure 3.2 for the SM(1-15) solution corresponds well with the DLS results and the hypothesis of coexistence of single copolymer chains and molecular aggregate structures. The first peak at R_h~ 2-3 nm is consistent with the size expected for a single SM(1-15) copolymer chain, and the second peak at R_h~ 20-30 nm is consistent with copolymer micelles. The decrease in R_h with time for the SM(1-15) micelles is also seen in Figure 3.2. Additionally, similar results are obtained for the R_h distributions observed at 137 and 251 days after solution preparation.

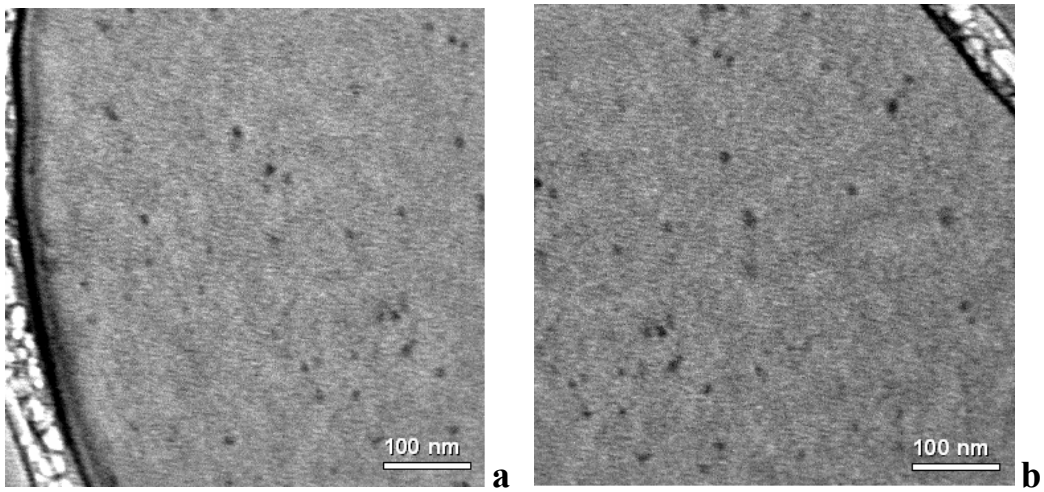

Figure 3.3: Cryo-TEM images of a 1.0 wt% solution of SM(1–15) in [BMI][PF_6].

Representative cryo-TEM images of a 1.0 wt% solution of SM(1-15) in [BMI][PF_6] are shown in Figure 3.3. The small, dark spots that can be seen in the image correspond to the PS cores of the SM(1-15) spherical micelles. Only the densely associated PS blocks that make up the micellar cores appear in the cryo-TEM images because the PMMA blocks that form the micellar coronas are well solvated in the [BMI][PF_6] matrix. Table 3.3 lists the mean core radius (R_c) of the block copolymer micelles, which were determined by measuring the diameters of over 100 micellar cores in a series of cryo-TEM images. For the SM(1-15) copolymer micelles the mean core radius was found to be 6.9±1.0 nm. In addition to the mean core radius, Table 3.3 also lists the stretching factors for the PS chains of the micelle cores (s_{PS}), which were calculated as R_c divided by the root-mean-squared end-to-end distance for an unperturbed Gaussian chain with mean degree of polymerization equal to that of the PS blocks. The aggregation numbers (N_{agg}) in Table 3.3 were calculated for spherical micelles using the volume of the micelle cores, assuming that the density of the PS is equal to that of the bulk (1.05 g/cm^3). Finally, Table 3.3 lists the core-corona interfacial area per chain (a_o), which is simply the core surface area divided by the aggregation number. The formation of spherical micelles by the SM(1-15) copolymer molecules agrees with experimental precedent and theoretical expectation, where spheres are the most common morphology for "hairy micelles" (soluble block longer than insoluble block).[21,22] However, the value of R_c measured from the cryo-TEM images of SM(1-15) micelles is larger than anticipated based on the length of the PS blocks of the copolymer molecules (ca. 3 nm fully stretched). This suggests a possible overestimation of the rest

of the aggregation characteristics listed in Table 3.3 for the SM(1-15) micelles. Recalculating the SM(1–15) aggregation characteristics based on a core radius of 3 nm gives N_{agg} = 52, s_{PS} = 1.3, and a_o = 2.2 nm^2.

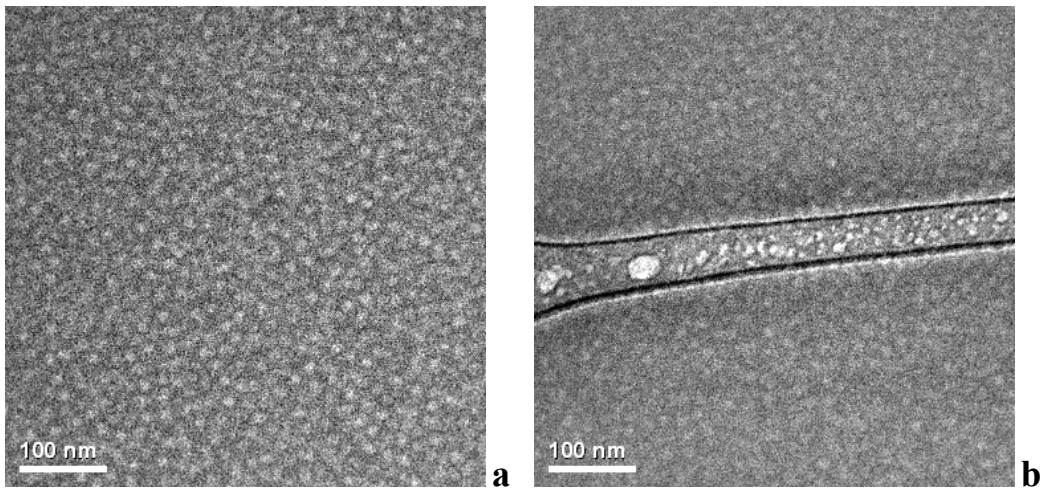

Figure 3.4: Cryo-TEM images of a 1.0 wt% solution of SM(3–13) in [BMI][PF_6].

The formation of SM(3-13) copolymer micelles was also confirmed by both cryo-TEM and DLS. Figure 3.4 shows representative cryo-TEM images of a 1.0 wt% solution of SM(3-13) in [BMI][PF_6], in which the white, circular cores of spherical micelles can be seen. For the SM(3-13) copolymer micelles the mean core radius was measured to be 7.4±0.8 nm (Table 3.3). As would be expected due to an increase in the core PS block length and a decrease in the corona PMMA block length, R_c of the SM(3–13) micelles is larger than that of the SM(1–15) micelles. The reason for the different contrast in the SM(1-15) cryo-TEM images (micelle cores darker than background), as compared to the SM(3-13) images (micelle cores lighter than background), is due to degradation of the SM(1-15) block copolymer micelle cores as a result of overexposure

to the electron beam. Further evidence and discussion of this phenomenon is presented later. DLS measurements produced an apparent R_h of 14 nm for the SM(3-13) micelles. The polydispersity given by the reduced second cumulant in Table 3.3, and the distribution of R_h in Figure 3.2 both show a narrower range of aggregate size than was obtained for the SM(1-15) copolymer solutions. Additionally, the micelles formed by the SM(3-13) copolymers do not change size significantly between the first DLS measurements and those performed several months later (Table 3.3). Thus these micelles either represent a thermodynamically stable morphology for the SM(3-13) molecular aggregates, or they represent aggregates that are metastable.

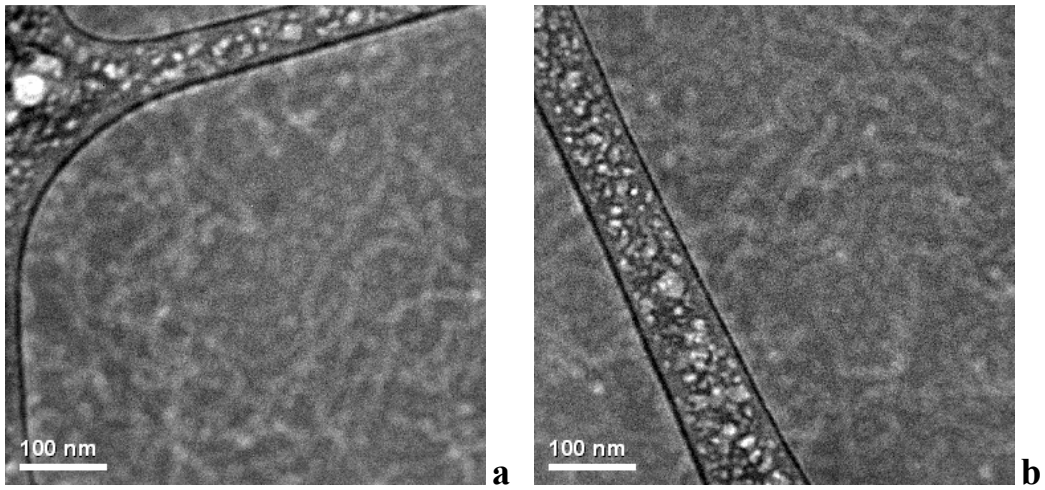

Figure 3.5: Cryo-TEM images of a 1.0 wt% solution of SM(7–8) in [BMI][PF_6].

As the volume fraction of the PS block increases on changing from SM(3-13) to SM(7-8), the radii of the spherical micelle cores also increases (Table 3.3, Figure 3.5). As stated above, this is expected due to the increase in core block length and decrease in

corona block length. Thus, the degree of crowding of the corona chains in the spherical SM(7-8) copolymer micelles is lower than that of the SM(3-13) spherical micelles, as seen in Table 3.3 by the larger value of a_o. This lower degree of corona crowding, along with the larger average core radius, leads to the higher aggregation number observed for the spherical SM(7-8) micelles.

The reduction in the PMMA copolymer volume fraction also leads to the formation of coexisting spherical and cylindrical micelles in the SM(7-8) solution (Figure 3.5). Normally the competition between crowding of the corona chains and the core-corona interfacial tension is the dominant factor in determining the micelle morphology,[22] which, in the case of long corona chains, is predominantly spherical. So as corona crowding is reduced, the drive to ease the interfacial tension causes the copolymer micelles to adopt a morphology that lowers the curvature of the core-corona interface. This lower degree of interfacial curvature, and thus greater crowding of the corona chains, is displayed in Table 3.3 by a lower value of a_o for the cylindrical SM(7-8) micelles as compared to that of the spherical SM(7-8) micelles. Additionally, the cylindrical morphology possesses a lower degree of core chain stretching than the spherical morphology, as shown in Table 3.3 by a lower value of s_{PS} for the cylindrical micelles.

The large apparent R_h measured by DLS for the SM(7-8) solution corresponds to the formation of cylindrical micelles as seen in Figure 3.5. Increased polydispersity in the SM(7-8) micelle size, as shown by the reduced second cumulant (Table 3.3) and REPES analysis (Figure 3.2), is also in agreement with the direct images of the micelles

from cryo-TEM. Additionally, the R_h and its distribution in Figure 3.2 do not show a significant shift with time. So, just as with the SM(3-13) micelles, it is possible that these aggregate structures represent equilibrium morphologies, or long lived metastable morphologies.

3.3.2 Micelle Morphology Equilibrium

There exists the possibility that the micelles present in the PS-PMMA/[BMI][PF_6] solutions represent frozen, non-ergodic morphologies, which are characterized by undetectably slow molecular exchange between micelles that prevents the formation of the lowest energy micelle structure. The main factors that support the expectation of frozen micelles in these solutions are the solution preparation method, the high amphiphilicity of the copolymer, and the high T_g of the PS core blocks. As the dichloromethane is evaporated during solution preparation, the solvent becomes increasingly more selective for the PMMA blocks of the copolymer, initially leading to the formation of micelles. Eventually, the quality of the solvent for the PS blocks becomes so poor that they are essentially locked in the cores of the micelles. The slow removal of dichloromethane by evaporation is similar to removing the cosolvent by dialysis, which has been shown in previous studies to result in frozen micelles.[23,24] Frozen micelles have also been identified mainly in systems where there is high amphiphilicity, [25–29] and/or the core forming blocks possess a high T_g and are thus in a glassy state at room temperature.[23,24,30–32]

DLS evidence for the presence of SM(1-15) unimers in solution, and a decrease in the apparent R_h values for the SM(1-15) micelles suggests the establishment of a

stable, equilibrium micelle size on the time scale of days to weeks. Using the following empirical equation for the decrease in PS T_g with molecular weight,[33]

$$T_g = 373 - 10^5 / M_{PS} \tag{3.4}$$

gives an estimated T_g of 23 °C for the PS block of the SM(1–15) copolymers. So, even at room temperature, the PS cores of the SM(1–15) micelles are at or slightly above T_g, and the copolymer molecules should not be locked in the cores. Thus, an equilibrium micelle size is established, albeit slowly, which presumably occurs via the single chain insertion/expulsion mechanism established by Aniansson and Wall[34,35], and extended to amphiphilic block copolymers by Halperin and Alexander.[36,37]

The size of the micelles formed in the SM(3-13)/[BMI][PF_6] solution did not change over the course of several months, as is shown by the apparent R_h values in Table 3.3 and the R_h distribution obtained from REPES analysis. Thus it is possible that the SM(3-13) spherical micelles represent a thermodynamically stable morphology, or that they represent a morphology that forms during evaporation of the cosolvent and subsequently becomes frozen by the selectivity of the [BMI][PF_6] and/or the glassy nature of the PS cores upon further removal of the dichloromethane. Using Equation 3.4, 67 °C was calculated as an estimate of T_g for the PS cores of the SM(3–13) micelles. Thus it is possible that establishment of an equilibrium micelle size is being inhibited by the glassy micelle cores.

To investigate the effect of glassy micelle cores on the establishment of an equilibrium SM(3-13) copolymer micelle size, DLS measurements were performed while the solution was heated. Figure 3.6 shows the squared, normalized electric field

correlation functions measured for a 1.0 wt% solution of SM(3-13) in [BMI][PF_6], at a scattering angle of 80° and increasing temperature. The inset of Figure 3.6 shows the change in apparent R_h with temperature for the SM(3-13) copolymer micelles and for a 100 kg/mol PMMA homopolymer dissolved in [BMI][PF_6]. The R_h of the copolymer micelles increases from 13.5 nm at 25 °C, to 17.7 nm at 105 °C. Similarly, R_h for the PMMA homopolymer increased upon heating as well, from 7.9 nm at 25 °C to 10.6 nm

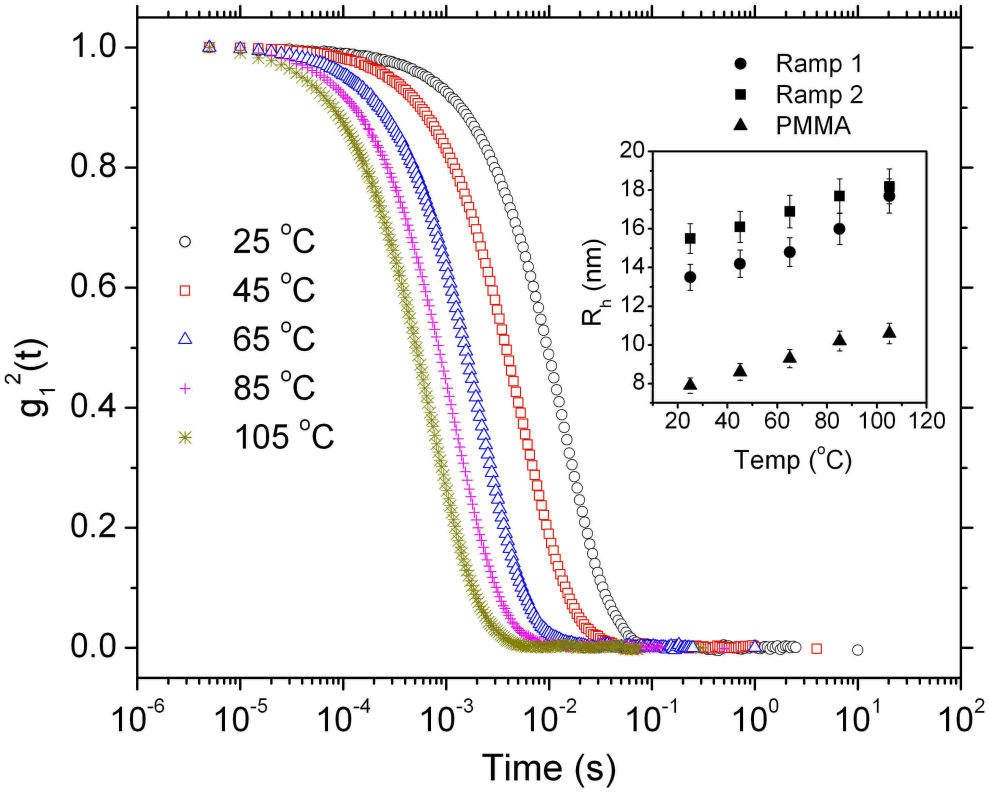

Figure 3.6: Comparison of squared electric field correlation functions measured at θ = 80° for a 1.0 wt% solution of SM(3–13) with increasing temperature. The inset shows R_h versus temperature for the SM(3–13) micelles (Ramp 1 and Ramp 2) and a 100 kg/mol PMMA homopolymer in [BMI][PF_6] at 1.0 wt%. Correlation functions correspond to temperature ramp 1.

at 105 °C. Thus the increase in R_h upon heating the SM(3-13) micelles could be attributed simply to an increase in the PMMA corona thickness, similar to the increase in size seen for the PMMA homopolymer. However, upon repeating the temperature ramp of the SM(3-13) solution, the initial R_h at 25 °C (15.5 nm) was slightly larger than in the previous experiments. Finally, after the second temperature ramp, R_h for the SM(3-13) micelles was re-measured at 25 °C and again found to be 15.5 nm. Thus, it is possible the SM(3-13) micelles have been frozen by the glassy nature of their PS cores, and after heating above the T_g of PS, the micelles undergo a slight rearrangement that is evidenced by a larger R_h at room temperature. This result is similar to that reported for PS-PEO copolymers in aqueous solution,[30] where the PS block length of the copolymers (4.5 kg/mol) was similar to that of the SM(3–13) copolymers used in the present study. Using a fluorescence technique to quantify chain exchange, the researchers found no detectable exchange at ambient temperature over several days, but at 60 °C chain exchange occurred on the time scale of several hours.

As shown in Table 3.3 and Figure 3.2, R_h and its distribution for the SM(7-8) micelles do not change significantly over the span of several months. Thus, as was the case for the SM(3-13) micelles, the molecular aggregate structures seen in the SM(7-8) solution could represent either equilibrium or frozen morphologies. However, the coexistence of spherical and cylindrical micelles may be indicative of non-equilibrium structures, since the micelles would be expected to ultimately adopt whichever morphology was more thermodynamically stable. Initially, DLS measurements were conducted with increasing temperature to test if the SM(7-8) micelle morphology was

frozen by the T_g of the PS cores. However, upon heating the SM(7-8) solution, the copolymer began to visibly precipitate at 65-75 °C. So, rather than DLS, cryo-TEM was used to study the behavior of the SM(7-8) micelles with heating. A 1.0 wt% solution of SM(7-8) in [BMI][PF_6] was heated in a closed vial at 120 °C, and portions were removed after 1, 3, 6, and 9 hours. Figure 3.7a shows that prior to heating, the SM(7-8) solution contains coexisting spherical and cylindrical micelles. It should be noted that since the micelles appear darker than the ionic liquid matrix, some damage from the electron beam has occurred. However, the coexisting spherical and cylindrical morphologies that were present in undamaged samples (Figure 3.5) are still distinguishable. After approximately 1-2 hours of heating, the copolymer solution became increasingly cloudy-white in appearance, and after 9 hours the solution was completely opaque. Figure 3.7b is a cryo-TEM image taken of the solution after 3 hours of heating, and shows that the copolymer remaining in solution has aggregated into large particles with an average diameter of approximately 60-70 nm. Similar images were obtained for all lengths of heating time. Subsequently, the copolymer solutions that had been heated were redissolved in dichloromethane and stirred for several hours. The cosolvent was then removed using the same procedure as in the initial solution preparation. Figure 3.7c is a cryo-TEM image taken of the solution that had been heated for 3 hours and then redissolved in dichloromethane. As can be seen, the cylindrical and spherical SM(7-8) micelles have reformed. These results indicate that not only is the morphology of the SM(7-8) micelles frozen, but that the SM(7-8) copolymer molecules are insoluble in [BMI][PF_6] alone, and will precipitate from solution if heated above the

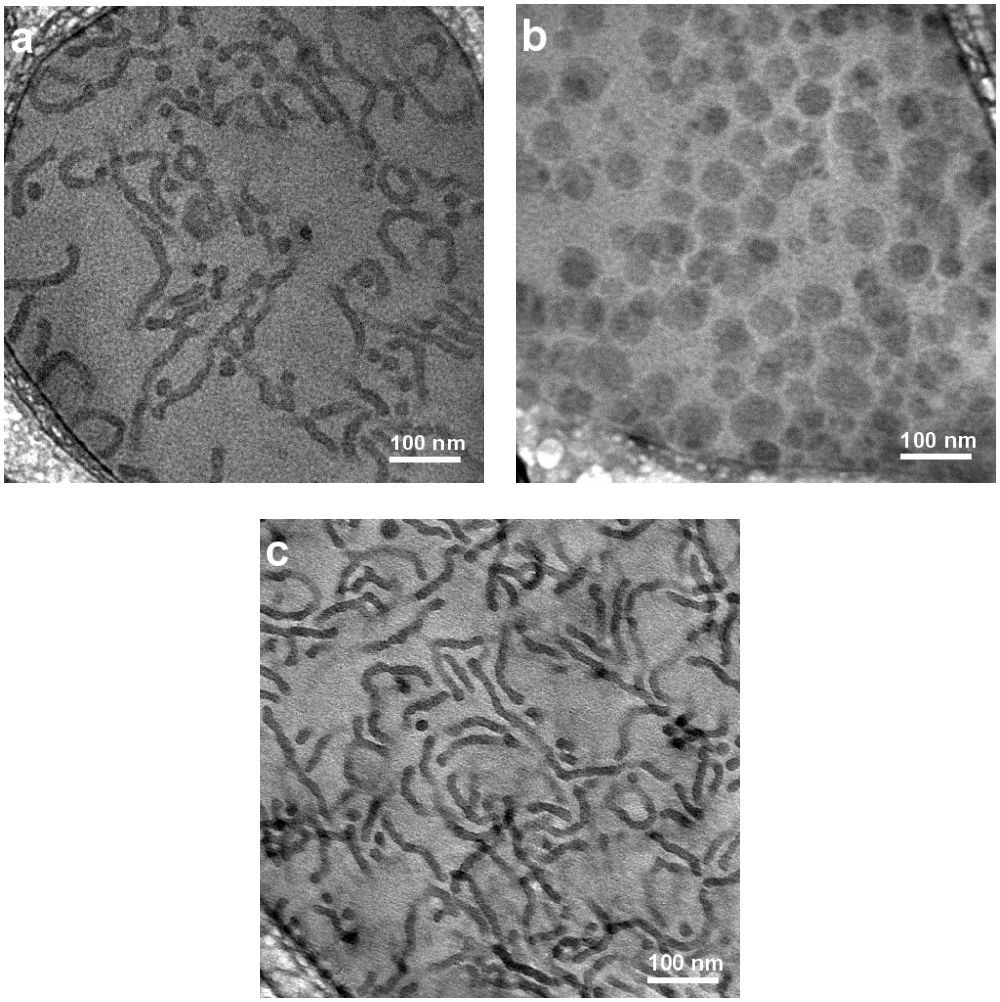

Figure 3.7: Cryo-TEM images of copolymer aggregates present in a 1.0 wt% SM(7-8)/[BMI][PF_6] solution: (a) solution prepared by standard procedure, before heating; (b) solution after heating at 120 °C for 3 h; (c) heated solution after being redissolved in CH_2Cl_2 followed by evaporation of the cosolvent.

T_g of PS. Similar behavior has been reported in other systems, where a specific block copolymer is insoluble in a desired selective solvent alone, but stable micelles can be formed by dissolution of the copolymer in a good solvent followed by dialysis against the selective solvent.[23,38]

To gauge the solvent quality of [BMI][PF_6] for PMMA, DLS was used to measure R_h values for a 100 kg/mol PMMA homopolymer dissolved in both [BMI][PF_6] and a known good solvent, acetone, at 1.0 wt%. R_h values of 7.9 nm and 8.0 nm were obtained at 25 °C for the homopolymer in [BMI][PF_6] and acetone, respectively. These two values suggest similar solvent quality towards PMMA for both [BMI][PF_6] and acetone. Additionally, an increase in R_h of the PMMA homopolymer in [BMI][PF_6] with temperature, as seen in Figure 3.6, suggests increasing PMMA solubility with temperature. Thus, the precipitation of the SM(7–8) micelles observed with heating is not a result of a decrease in solubility of the PMMA corona blocks.

3.3.3 Micelle Damage in Cryo-TEM

As mentioned above, several of the cryo-TEM images of the PS-PMMA solutions presented thus far possess opposite contrast. In Figures 3.3, 3.7a and 3.7c, the micelles are darker than the ionic liquid matrix, and in Figures 3.4 and 3.5 the micelles are lighter than the ionic liquid matrix. Contrast in TEM images arises mainly from differences in electron density between the various materials in the sample. In other words, regions of a sample with high electron density will allow fewer electrons to pass through, and thus appear darker than regions with lower electron density. The electron density of [BMI][PF_6] (0.699 mol e^-/cm^3) is higher than that of PS (0.565 mol e^-/cm^3),

so the cores of the copolymer micelles should appear lighter than the background in the images. However, it has been observed that damage to the PS-PMMA micelles occurs as the time length of exposure to the electron beam of the microscope increases. Similar contrast reversal has also been observed in cryo-TEM images of polystyrene-polyisoprene (PS-PI) copolymer aggregates in dialkyl phthalate solvents.[3,39] Figure 3.8 shows a representative progression of the electron beam damage that occurs in the PS-PMMA/[BMI][PF_6] samples. The arrows in Figures 3.8a and 3.8c point to two micelles that are distinguishable both before and after beam damage.

As can be seen in Figure 3.8, not only does the contrast of the images change upon beam damage, but the micelle core radii increase slightly as well. This is possibly the source of the larger than anticipated average core radius measured from the SM(1-15) cryo-TEM images (Figure 3.3). For example, the PS blocks of the SM(1-15) copolymer molecules contain approximately 13 styrene monomers, or about 26 carbon-carbon single bonds. Thus even if the PS blocks were fully extended, a situation that is highly unlikely, they would only be approximately 3 nm in length. Therefore, the measured core radius is more than twice the maximum possible length of the SM(1-15) PS blocks. The beam damaged image in Figure 3.3 was used because the non-damaged SM(1-15) micelles proved to be difficult to locate due to small core size. Assuming that the PS blocks are fully extended, the non-damaged SM(1-15) micelle cores would appear as less than half the size of the SM(3-13) cores seen in Figure 3.4. Since the overall morphology of the copolymer micelles is preserved after beam damage has occurred, inducing contrast reversal could potentially be utilized as a technique for

observing small micelles or micelles that possess an electron density similar to that of the ionic liquid and thus show low initial contrast with the vitrified solvent matrix.

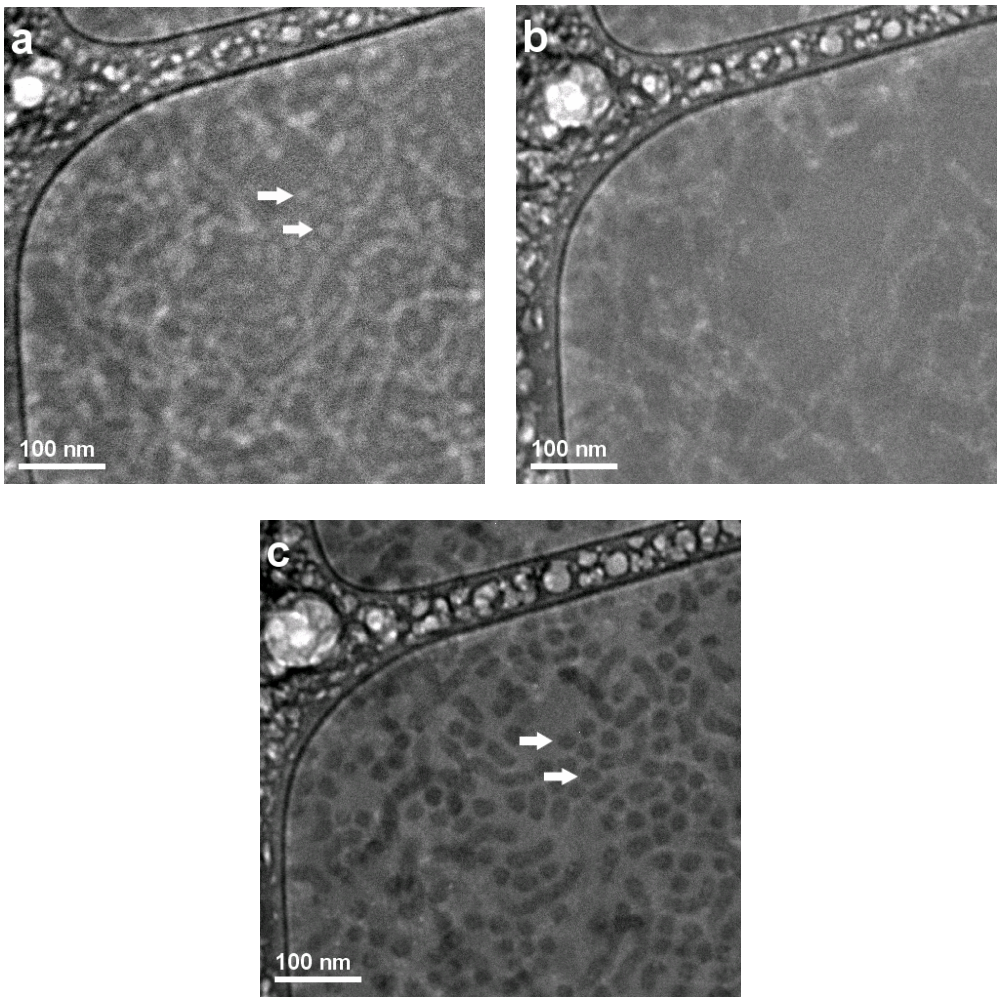

Figure 3.8: Cryo-TEM images showing progression of electron beam damage to micelles in a 1.0 wt% SM(7–8) solution. Arrows in (a) and (c) correspond to specific micelles that are distinguishable both before and after beam damage has occurred.

3.4 Dilute Solutions of Poly(Butadiene–Ethylene Oxide) Diblock Copolymers in Ionic Liquid

The dilute solution self-assembly behavior for several PB–PEO copolymers (Table 3.2) dissolved in [BMI][PF_6] and [EMI][TFSI] was also studied via DLS and cryo-TEM. Both ionic liquids are selective solvents for the PEO blocks of the copolymers. One of the main thrusts of these experiments was to investigate the solvation characteristics of the two ionic liquids by characterizing the PB–PEO micelle morphology. The dilute solution copolymer aggregates formed by the PB–PEO copolymers in these ionic liquids suggest that [BMI][PF_6] behaves as a more selective solvent than [EMI][TFSI].

Table 3.4: Size and aggregation characteristics for PB–PEO block copolymer micelles formed at a concentration of 1.0 wt% in [EMI][TFSI].

Copolymer	R_h[a] (nm)	$\mu_2/\bar{\Gamma}^2$	Micelle Morphology[b]	R_c (nm)	N_{agg}	s_{PB}	a_o (nm^2)
BO(9–6)	18	0.24	S	12.1±1.5	420	1.6	4.4
BO(9–4)	20	0.18	S	14.7±2.1	760	1.9	3.6
BO(9–3)	59	0.11	B	11.9±1.1[c]	1.4[d]	1.5	0.7

[a] R_h obtained via cumulant function (Equation 3.1). [b]Morphology from cryo-TEM, S denotes spherical micelles, B denotes bilayer vesicles. [c]R_c corresponds to half-thickness for bilayer vesicle. [d]N_{agg} for bilayer vesicles corresponds to number of chains per 1 nm^2 bilayer surface area.

3.4.1 PB–PEO Copolymer Aggregation Characteristics

Structural characteristics of the copolymer micelles, obtained from DLS and cryo-TEM, are shown in Table 3.4 for the BO copolymers in [EMI][TFSI]. Analysis of the electric field correlation functions obtained from DLS experiments was the same as described above for the PS–PMMA solutions. The cumulant expansion (Equation 3.1) was used to fit the electric field correlation functions obtained for all the BO/[EMI][TFSI] solutions. The double exponential expression (Equation 3.3) did not fit the BO/[EMI][TFSI] solution data well. For a 1.0 wt% solution of BO(9–6) in [EMI][TFSI], the R_h obtained from DLS for the molecular aggregate structures is 18 nm. From the cryo-TEM images (Figure 3.9), it can be seen that this radius corresponds to spherical BO(9–6) micelles in [EMI][TFSI]. The radii of over 100 BO(9–6) micelle cores were measured from the cryo-TEM images and were averaged to give an R_c of 12.1±1.5 nm.

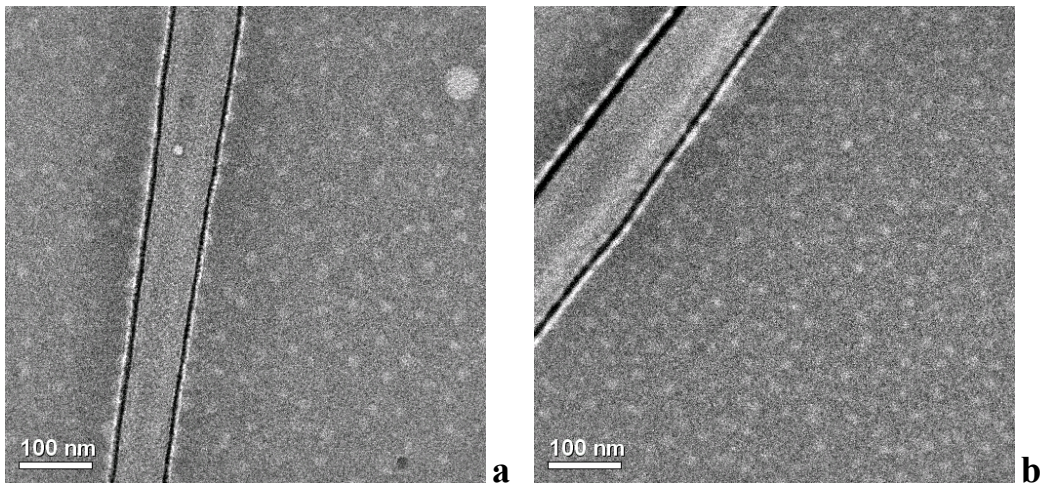

Figure 3.9: Cryo-TEM images of a 1.0 wt% solution of BO(9–6) in [EMI][TFSI].

For 1.0 wt% solutions of BO(9–4) in [EMI][TFSI] the hydrodynamic radius for the copolymer micelles was found to be 20 nm. Figure 3.10 shows representative cryo-TEM images of the BO(9–4)/[EMI][TFSI] solutions. The predominant morphology for the BO(9–4) micelles is spheres, with some short cylindrical micelles also observed in some images. The average core radius for the spherical BO(9–4) micelles was found to be 14.7±2.1 nm. A value of R_c for the short cylindrical BO(9–4) micelles was not obtained due to the relatively small number that were able to be observed in the cryo-TEM images.

A much larger R_h of 59 nm was observed for the 1.0 wt% solutions of BO(9–3) in [EMI][TFSI]. From the cryo-TEM images for these solutions (Figure 3.11), it can be seen that the large hydrodynamic radius corresponds to that of bilayer vesicles. In Table 3.4, R_c of 11.9±1.1 nm corresponds to the half bilayer thickness, which was measured from the cryo-TEM images.

Additionally, the distribution of hydrodynamic radii was obtained by applying the Laplace inversion routine REPES to the electric field correlation functions for the BO/[EMI][TFSI] solutions. The results are shown in Figure 3.12, and they correspond well with the results of DLS and cryo-TEM. For both BO(9–6) and BO(9–4) solutions there is a peak in the R_h distribution at ~20 nm, which corresponds to the size of the spherical micelles observed in these solutions. Further more, the peak in the R_h distribution obtained for the BO(9–3) solution at ~60 nm corresponds well to the size of the bilayer vesicles observed in this solution.

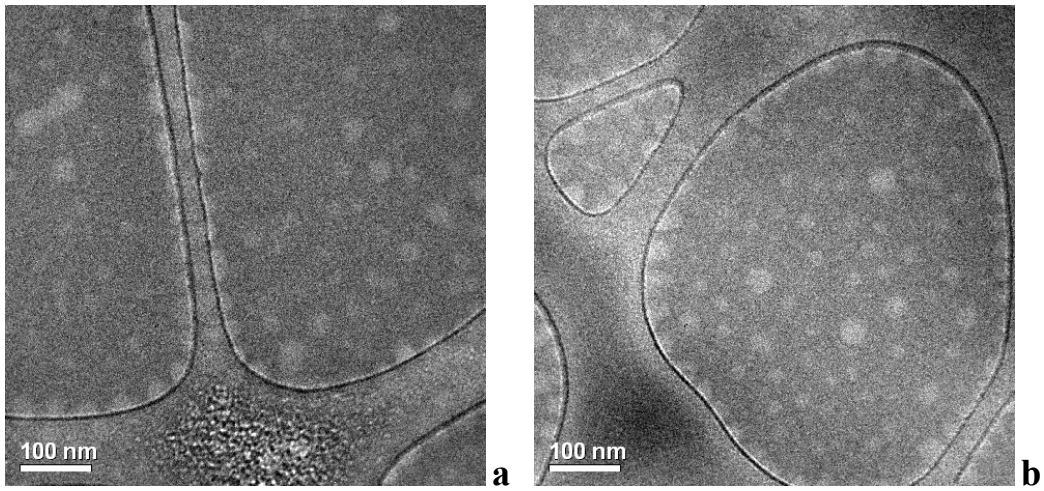

Figure 3.10: Cryo-TEM images of a 1.0 wt% solution of BO(9–4) in [EMI][TFSI].

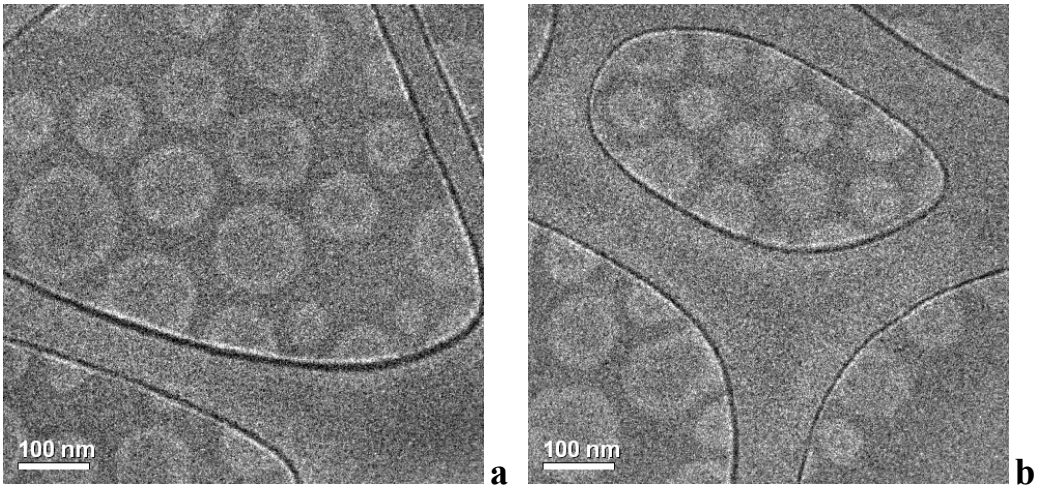

Figure 3.11: Cryo-TEM images of a 1.0 wt% solution of BO(9–3) in [EMI][TFSI].

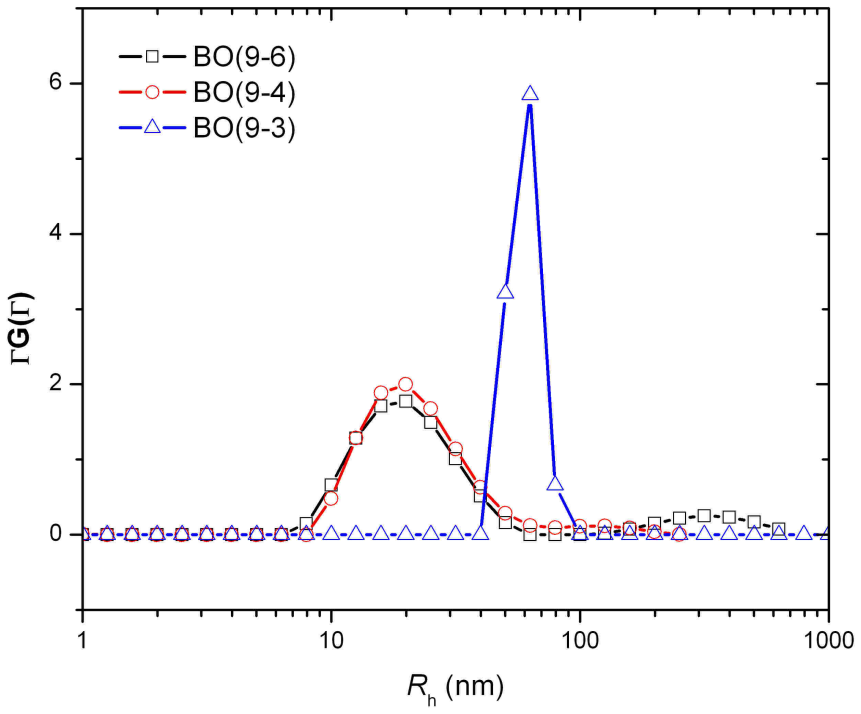

Figure 3.12: R_h distribution for 1.0 wt% solutions of PB–PEO copolymers dissolved in [EMI][TFSI].

For the PB–PEO/[EMI][TFSI] solutions there is a progression from spherical micelles for BO(9-6), to larger spherical micelles with some short cylindrical micelles for BO(9-4), to bilayer vesicles for BO(9-3). This is consistent with the expected morphological progression upon decreasing the soluble block volume fraction of the copolymer. The aggregation number (N_{agg}), core block degree of stretching (s_{PB}), and core/corona interfacial area per chain (a_o) were calculated as described above in Section 3.3, and are listed in Table 3.4. The trends observed in the aggregation characteristics are consistent with expectation for the particular micelle morphologies observed. For example, a larger aggregation number for the BO(9–4) micelles than for the BO(9–6) micelles would be expected due to the decrease in the soluble block length of the copolymer. Additionally, the large decrease in a_o between the BO(9–4) spherical micelles and the BO(9–3) vesicles is expected due to the much lower interfacial curvature of the bilayer vesicle morphology.

However, some aspects of the copolymer aggregation in [EMI][TFSI] are difficult to explain. For example, it is peculiar that the cylindrical micelle morphology is not more predominant. Instead, an abrupt change is observed from predominantly spherical micelles in the BO(9–4) solution to predominantly vesicles in the BO(9–3) solution. However, theory and experiments have shown that the copolymer composition window corresponding to cylindrical micelles is typically fairly narrow.[18,21,22] Alternatively, an explanation for the absence of cylindrical micelles could be that the micelles present in solution represent metastable morphologies that form during solution preparation with the dichloromethane cosolvent and are subsequently frozen by

the low solubility of the core PB blocks in the ionic liquid. Formation of metastable PB–PEO micelles in [EMI][TFSI] has been reported recently by Meli *et al*.,[40] where heating the solution for extended periods resulted in micelle size equilibration. A limited number of DLS experiments at elevated temperatures were performed with the BO(9–4)/[EMI][TFSI] solution in the present study. After 30 min at 50 °C there was no change observed in the size or polydispersity of the BO(9–4) micelles (R_h = 20 nm, $\mu_2/\overline{\Gamma}^2$ = 0.15). Heating at 100 °C for 30 min results in a slight increase in the size of the BO(9–4) micelles (R_h = 23nm, $\mu_2/\overline{\Gamma}^2$ = 0.19). These results are consistent with those reported by Meli, where micelles solutions prepared using dichloromethane cosolvent did not display a large change in R_h with heating. Alternatively, Meli reported that micelle solutions prepared using two different methods for directly dissolving the copolymer in ionic liquid without cosolvent displayed a large decrease in R_h (≥ 50%) with heating. Moreover, the micelles prepared via the direct dissolution methods equilibrated to an R_h that was approximately twice that of the micelles prepared using the cosolvent. The authors concluded that the larger micelles obtained after thermal annealing of the directly dissolved copolymer solutions represent the equilibrium micelle structure, and that the micelles prepared with cosolvent are unable to equilibrate to the larger size since the most likely mechanism for size equilibration (chain expulsion and micelle dissolution) is in opposition to the drive for micelle growth. Thus we assume similar micelle formation and size equilibration mechanisms for our solutions which were prepared using dichloromethane cosolvent. However, it isn't possible to make a definitive conclusion as to the thermodynamic stability of the PB–

PEO micelles observed in the present study without further thermal annealing of the solutions and experimentation with alternative solution preparation procedures.

Table 3.5 lists the aggregation characteristics for the BO copolymer micelles in [BMI][PF_6]. From DLS an R_h of 39 nm was obtained for the 1.0 wt% solution of BO(9–6) in [BMI][PF_6]. From the cyro-TEM images in Figure 3.13 it can be seen that the BO(9–6) solutions contained a mix of spherical and short cylindrical micelles. The core radii for both morphologies were measured, and found to be 17.9±2.9 nm and 13.8±1.3 nm for spheres and cylinders, respectively.

For 1.0 wt% solutions of BO(9–4) in [BMI][PF_6], a much larger R_h of 95 nm was obtained. In Figure 3.14, the cryo-TEM images show that the predominant aggregate morphology in the BO(9–4) solutions is that of bilayer vesicles, along with long cylindrical micelles. The bilayer half-thickness was measured to be 12.1±0.9 nm, and core radius of the cylindrical micelles was 16.5±1.1 nm.

Table 3.5: Size and aggregation characteristics for PB–PEO block copolymer micelles formed at a concentration of 1.0 wt% in [BMI][PF_6].

Copolymer	R_h[a] (nm)	$\mu_2/\bar{\Gamma}^2$	Micelle Morphology[b]	R_c (nm)	N_{agg}	s_{PB}	a_o (nm^2)
BO(9–6)	39	0.27	S	17.9±2.9	1370	2.3	2.9
			C	13.8±1.3	34[d]	1.8	2.6
BO(9–4)	95	0.10	C	16.5±1.1	49[d]	2.1	2.1
			B	12.1±0.9[c]	1.4[e]	1.6	0.7
BO(9–3)	112	0.10	B	11.5±0.9[c]	1.3[e]	1.5	0.8

[a] R_h obtained via cumulant function (Equation 3.1). [b]Morphology from cryo-TEM, S denotes spherical micelles, C denotes cylindrical micelles, B denotes bilayer vesicles. [c]R_c corresponds to half-thickness for bilayer vesicle. [d]N_{agg} for cylindrical micelles corresponds to number of chains per 1 nm cylinder length. [e]N_{agg} for bilayer vesicles corresponds to number of chains per 1 nm^2 bilayer surface area.

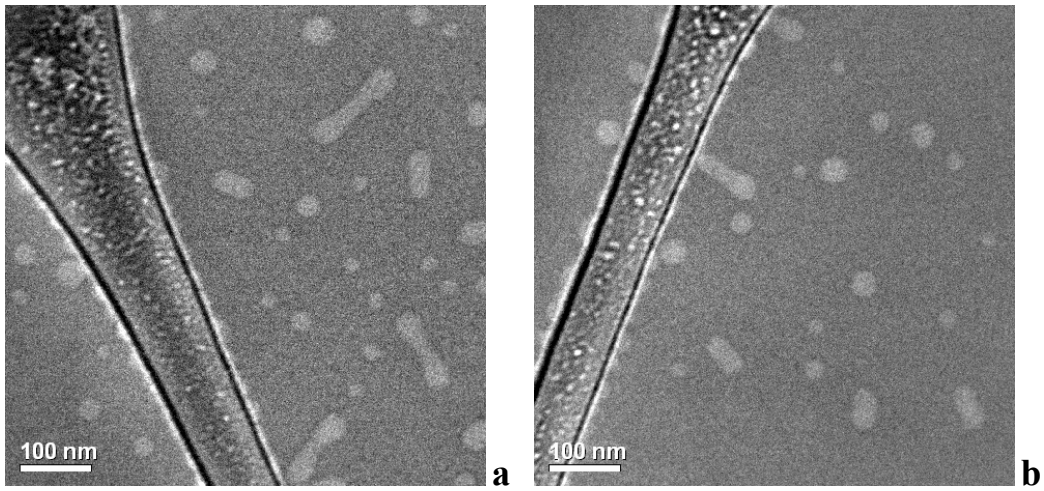

a **b**

Figure 3.13: Cryo-TEM images of a 1.0 wt% solution of BO(9–6) in [BMI][PF_6].

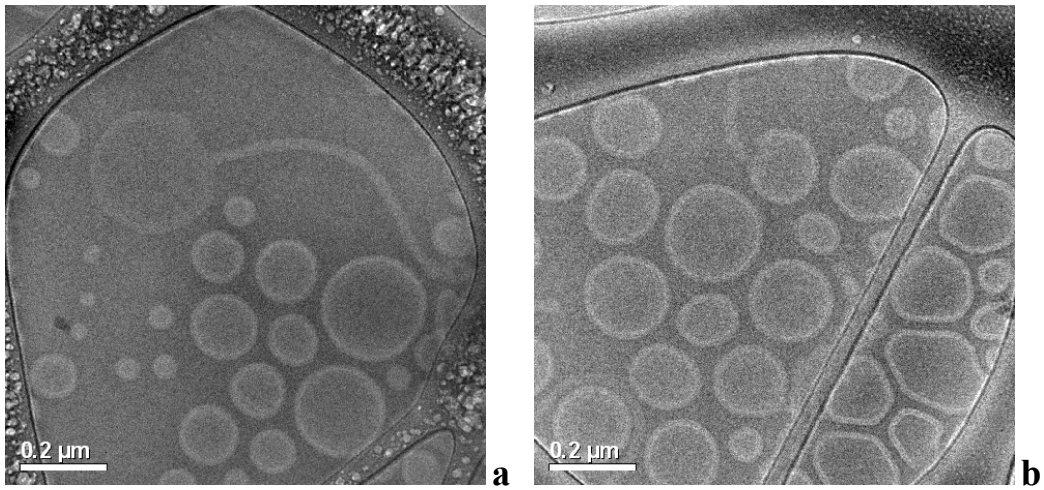

a **b**

Figure 3.14: Cryo-TEM images of a 1.0 wt% solution of BO(9–4) in [BMI][PF_6].

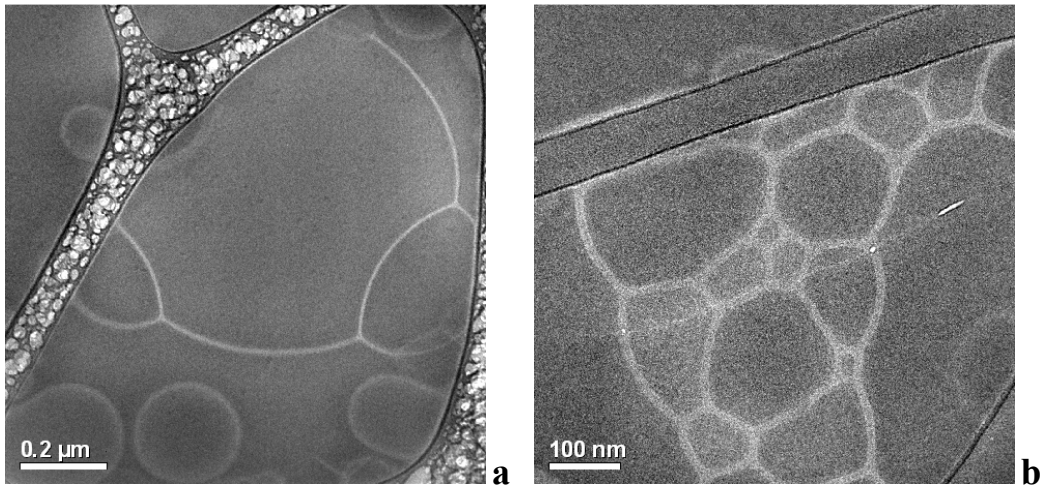

Figure 3.15: Cryo-TEM images of a 1.0 wt% solution of BO(9–3) in [BMI][PF_6].

Finally, R_h for the 1.0 wt% BO(9–3) solutions was 112 nm, and the predominant micelle morphology observed in the cryo-TEM images (Figure 3.15) was bilayer vesicles. Interestingly, the cryo-TEM images of the BO(9–3)/[BMI][PF_6] solutions also showed large structures that appear to possibly be aggregates of multiple bilayer vesicles. However, the R_c value for the bilayer aggregates was measured to be 9.1±0.4 nm, which is slightly smaller than that measured for solitary vesicles (11.5±0.9 nm).

The R_h and $\mu_2/\overline{\Gamma}^2$ values for the BO(9–4) and BO(9–3) solutions given in Table 3.5 seem inconsistent with the micellar structures observed via cryo-TEM. This is most likely a result of an inconsistency in sample preparation between the two techniques. Prior to DLS experiments, the copolymer solutions are passed through 0.45 µm filters to remove dust particles which can scatter light and lead to skewed results. The solutions were not filtered prior to preparing cryo-TEM samples. Thus, many of the large vesicles and bilayer aggregate structures, which from the cryo-TEM images

appear to be on the same size scale as 0.45 μm, were most likely filtered from the solutions prior to DLS. This would lead to the smaller and less polydisperse hydrodynamic radii than would be expected from the micellar structures observed with cryo-TEM. These results are a prime example of the benefits of employing the complimentary dilute solution characterization techniques of DLS and cryo-TEM.

The distribution of hydrodynamic radii was obtained for the PB–PEO/[BMI][PF_6] solutions using REPES analysis, and the results are shown in Figure 3.16. The distributions for the BO(9–3) and BO(9–4) solutions correspond well with R_h obtained from cumulant analysis and with the cryo-TEM results, with a peak in R_h distribution at ~100 nm corresponding to the large bilayer vesicles in solution. The R_h distribution for the BO(9–6) solution shows two peaks, which potentially correspond to the spherical and cylindrical micelles observed via cryo-TEM. Thus, the electric field correlation functions for the BO(9–6) solution were also fit with the double exponential function, Equation 3.3. The R_h values obtained from the two decay rates (Γ_1 and Γ_2) were 21 nm and 60 nm. These values correspond well with the maxima in the R_h distribution obtained from REPES, and represent the two different micelle size classes (spheres and short cylinders) observed in the BO(9–6) cryo-TEM images.

Again, the morphologies of the copolymer micelles in [BMI][PF_6] are consistent with the expected progression of spheres to cylinders to bilayer vesicles, as the soluble copolymer block length is reduced. Additionally, the values calculated for the other aggregate characteristics listed in Table 3.5 (N_{agg}, s_{PB}, a_o) are also consistent with expectation for the morphologies observed. For example, the increase in N_{agg} between

cylindrical BO(9–6) and BO(9–4) micelles is consistent with the decrease in soluble PEO block length. Moreover, there is also a large decrease in core/corona interfacial area per chain between BO(9–4) cylindrical micelles and bilayer vesicles, which corresponds to the lower degree of interfacial curvature for the bilayer structure.

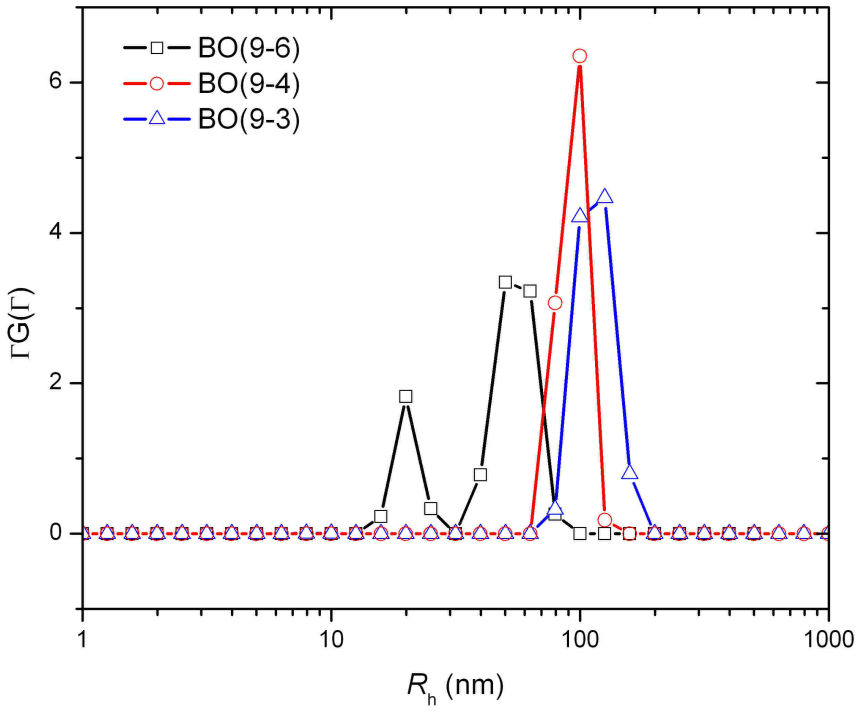

Figure 3.16: R_h distribution for 1.0 wt% solutions of PB–PEO copolymers dissolved in [BMI][PF_6].

Just as discussed above with the PB–PEO/[EMI][TFSI] solutions, it is difficult to say whether the micelles observed in [BMI][PF_6] represent stable, equilibrium morphologies. For example, there is again an abrupt change from spherical and short cylindrical micelles in the BO(9–6) solutions, to predominantly large vesicles in the BO(9–4) solution. Here, it is interesting to note that the morphology observed in this study for the BO(9–4) copolymers in [BMI][PF_6] is consistent with that reported by He *et al*.[11] for the same copolymer dissolved in [BMI][PF_6] using dichloromethane cosolvent. Conversely, He reported the formation of spheres, cylinders and vesicles in the BO(9–4)/[BMI][PF_6] solutions prepared via direct dissolution of the copolymers without the use of a cosolvent. While the predominance of a single micelle morphology in the solutions prepared using a cosolvent suggests this to be the stable, equilibrium micelle structure, a definitive conclusion cannot be made with out further experiments involving thermal annealing of the solutions, as discussed above by comparison with results of Meli *et al*.[40] In any case, it is at least encouraging that the resulting micelle morphologies are consistent for a single solution preparation procedure, as is shown by comparison with the work of He.

3.4.2 Solvent Selectivity

Comparison of the PB–PEO copolymer self-assembly behavior in the two ionic liquid solvents allows a qualitative measure of their solvation characteristics. The dominant factor in determining the morphology of dilute solution block copolymer aggregates is the core/corona interfacial tension. Increasing the selectivity of the solvent (*i.e*., increasing interfacial tension) will drive the aggregates toward morphologies with

lower interfacial curvature. Comparing the morphologies of the same copolymer in the two ionic liquids shows BO(9–6) forming spherical micelles in [EMI][TFSI] and spheres coexisting with cylinders in [BMI][PF_6]. BO(9–4) forms spheres in [EMI][TFSI] and cylinders coexisting with vesicles in [BMI][PF_6]. Finally, BO(9–3) forms vesicles in both ionic liquids. Thus the formation of aggregates with lower interfacial curvature for a given copolymer in [BMI][PF_6] than in [EMI][TFSI], suggests [BMI][PF_6] acts as the more selective solvent.

Comparing the dilute solution aggregate behavior for the PB-PEO copolymers in ionic liquids to that observed by Jain *et al*.[41] for aqueous solutions of these same PB–PEO copolymers suggests that water is more selective than [EMI][TFSI] and, at least, equally as selective as [BMI][PF_6]. In aqueous solution BO(9–6) forms cylindrical micelles possessing Y-junctions, BO(9–4) forms coexisting Y-junction cylinders and bilayer vesicles, and BO(9–3) forms bilayer vesicles.

It is not surprising that the ionic liquids display less selective solvent behavior than water, since their molecular constituent ions allow them to participate in multiple solvent–solute interactions. It has been shown that various ionic liquids are capable of participating in both polar and nonpolar solvent–solute interactions.[42,43] If it is assumed that both [BMI][PF_6] and [EMI][TFSI] behave as equally good solvents for PEO, then it might be expected that [BMI][PF_6] should behave as a less selective solvent based on the increased possibility of dispersion interactions between the PB blocks and the butyl groups of the [BMI] cations, as compared to the ethyl group of the [EMI] cations. This hypothesis is supported by the results of Favre *et al.*, who found that the solubility of 1-

hexene in an ionic liquid with a constant anion increased along with the alkyl chain length of the 1-alkyl-3-methylimidazolium cation.[44] However, since [EMI][TFSI] displays less selective solvent behavior, this suggests that the solvent–solute interactions between the ionic liquid and the PB blocks are dependent upon the anion identity as well as the cation. Indeed, Farve also observed greater 1-hexene solubility with the [TFSI] anion than with the [PF_6] anion in combination with [BMI]. This could be a result of the higher degree of charge delocalization present in the [TFSI] anion, which would result in a less unfavorable environment for the nonpolar PB blocks.

3.5 Summary

The dilute solution self-assembly behavior of several PS–PMMA and PB–PEO block copolymers in ionic liquid solvents has been investigated using the complimentary techniques of DLS and cryo-TEM. The ionic liquids solvents selectively solvated the PMMA and PEO blocks of the copolymers, which led to the formation of block copolymer micelles in solution. From DLS experiments an average R_h, as well as the distribution of R_h could be obtained for the copolymer micelles, while direct images of the copolymer micelle cores from cryo-TEM allowed calculation of other micelle characteristics (R_c, N_{agg}, s, a_o).

For the PS–PMMA copolymer solutions a progression from spherical micelles to coexisting spherical and cylindrical micelles was observed upon reduction of the volume fraction of the soluble PMMA copolymer block. The size of SM(1–15) micelles, measured as R_h obtained from DLS, decreased over the course of several months, indicating establishment of equilibrium between the copolymer micelles and

copolymer unimers in solution. The size of the SM(3–13) and SM(7–8) micelles did not change over the course of several months. DLS experiments conducted at elevated temperature were performed to determine if the glassy nature of the PS cores was inhibiting micellar size equilibration. For the SM(3–13) micelles a slight increase in R_h at room temperature was observed after heating the solution above T_g of PS, which could potentially be attributed to equilibration of micelle size. The SM(7–8) copolymer was observed to precipitate from solution upon heating. Re-dissolution of the copolymer in the ionic liquid using dichloromethane resulted in a restoration of the copolymer micelles observed prior to heating. These results indicate the SM(7–8) is actually insoluble in the ionic liquid, but does not precipitate due to formation of frozen copolymer micelles during solution preparation with a cosolvent. Finally, degredation of the micelle cores was observed in the cryo-TEM images.

The PB–PEO copolymers formed different micelle morphologies in [EMI][TFSI] and [BMI][PF_6]. For the same copolymer in the two different ionic liquids, the formation of micelle morphologies with a lower degree of interfacial curvature in [BMI][PF_6] indicates it behaves as a more selective solvent than [EMI][TFSI]. Comparing the dilute solution behavior of the PB–PEO copolymers in ionic liquids with that reported for aqueous solutions indicates water is a more selective solvent than [EMI][TFSI] and is at least as selective as [BMI][PF_6]. The lower solvent selectivity for [EMI][TFSI] than for [BMI][PF_6] was attributed to a greater degree of charge delocalization in the [TFSI] anion resulting in a less unfavorable environment for the PB blocks of the copolymers.

3.6 References

1. Won, Y.-Y.; Davis, H. T.; Bates, F. S. *Science* **1999**, *283*, 960.
2. Zhang, L.; Eisenberg, A. *Science* **1995**, *268*, 1728.
3. Bang, J.; Jain, S.; Li, Z.; Lodge, T. P.; Pedersen, J. S.; Kesselman, E.; Talmon, Y. *Macromolecules* **2006**, *39*, 1199.
4. Hamley, I. W.; *The Physics of Block Copolymers*, Oxford University Press, New York 1998.
5. Kataoka, K.; Harada, A.; Nagasaki, Y. *Adv. Drug Deliver. Rev.* **2001**, *47*, 113.
6. Savic, R.; Luo, L.; Eisenberg, A.; Maysinger, D. *Science* **2003**, *300*, 615.
7. Allen, C; Maysinger, D.; Eisenberg, A. *Colloids and Surfaces B* **1999**, *16*, 3–27.
8. Alexandridis, P.; Lindman, B. Eds. *Amphiphilic Block Copolymers: Self-Assembly and Applications*, Elsevier, Amsterdam 2000.
9. Glass, R.; Moeller, M.; Spatz, J. P. *Nanotechnology* **2003**, *14*, 1153.
10. Lu, J.; Yi, S. S.; Kopley, T.; Qian, C.; Liu, J.; Gulari, E. *J. Phys. Chem. B* **2006**, *110*, 6655.
11. He. Y.; Li, Z.; Simone, P.; Lodge, T. P. *J. Am. Chem. Soc.* **2006**, *128*, 2745–2750.
12. He, Y.; Lodge, T. P. *J. Am. Chem. Soc.* **2006**, *128*, 12666–12667.
13. Bai, Z.; He. Y.; Lodge, T. P. *Langmuir* **2008**, *24*, 5284–5290.
14. Bai, Z.; He, Y.; Young, N. P.; Lodge, T. P. *Macromolecules* **2008**, *41*, 6615–6617.
15. Ueki, T.; Watanabe, M.; Lodge, T. P. *Macromolecules* **2009**, *42*, 1315–1320.
16. Zhang, S.; Li, N.; Zheng, L.; Li, X.; Gao, Y.; Yu, L. *J. Phys. Chem. B* **2008**, *112*, 10228–10223.
17. Milhaupt, J. M.; Lodge, T. P.; Smith, S. D.; Hamersky, M. W. *Macromolecules* **2001**, *34*, 5561–5570.
18. Jain, S.; Bates, F. S. *Macromolecules* **2004**, *37*, 1511–1523.
19. Koppel, D. E. *J. Chem. Phys.* **1972**, *57*, 4814.

20. Jakes, J. *Collect. Czech. Chem. Commun.* **1995**, *60*, 1781.

21. Won, Y.-Y.; Brannan, A. K.; Davis, H. T.; Bates, F. S. *J. Phys. Chem. B* **2002**, *106*, 3354.

22. Zhulina, E. B.; Adam, M.; LaRue, I.; Sheiko, S. S.; Rubinstein, M. *Macromolecules* **2005**, *38*, 5330.

23. Zhang, L.; Barlow, R. J.; Eisenberg, A. *Macromolecules* **1995**, *28*, 6055.

24. Jada, A.; Hurtrez, G.; Siffert, B.; Riess, G. *Macromol. Chem. Phys.* **1996**, *197*, 3697.

25. Won, Y.-Y.; Davis, H. T.; Bates, F. S. *Macromolecules* **2003**, *36*, 953.

26. Rager, T.; Meyer, W. H.; Wegner, G. *Macromol. Chem. Phys.* **1999**, *200*, 1672–1680.

27. Schillén, K.; Yekta, A.; Ni, S.; Winnik, M. A. *Macromolecules* **1998**, *31*, 210–212.

28. Willner, L.; Poppe, A.; Allgaier, J.; Monkenbusch, M.; Richter, D. *Europhys. Lett.* **2001**, *55*, 667–673.

29. Lund, R.; Willner, L.; Richter, D.; Dormidontova, E. E. *Macromolecules* **2006**, *39*, 4566–4575.

30. Wang, Y.; Balaji, R.; Quirk, R. P.; Mattice, W. L. *Polym. Bull.* **1992**, *28*, 333–338.

31. Tian, M.; Qin, A.; Ramireddy, C.; Webber, S. E.; Munk, P. *Langmuir* **1993**, *9*, 1741–1748.

32. Pacovská, M.; Procházka, K.; Tuzar, Z.; Munk, P. *Polymer* **1993**, *34*, 4585–4588.

33. Fox, T. G.; Flory, P. J. *J. Polym. Sci.* **1954**, *14*, 315–319.

34. Aniansson, E. A. G.; Wall, S. N. *J. Phys. Chem.* **1974**, *78*, 1024–1030.

35. Aniansson, E. A. G.; Wall, S. N.; Almgren, M.; Hoffmann, H.; Kielmann, I.; Ulbricht, W.; Zana, R.; Lang, J.; Tondre, C. *J. Phys. Chem.* **1976**, *80*, 905–922.

36. Halperin, A. *Macromolecules* **1987**, *20*, 2943–2946.

37. Halperin, A.; Alexander, S. *Macromolecules* **1989**, *22*, 2403–2412.

38. Štěpánek, M.; Procházka, K.; Brown, W. *Langmuir* **2000**, *16*, 2502–2507.

39. Kesselman, E.; Talmon, Y.; Bang, J.; Abbas, S.; Li, Z.; Lodge, T. P. *Macromolecules* **2005**, *38*, 6779.

40. Meli, L.; Lodge, T. P. *Macromolecules* **2009**, *42*, 580–583.

41. Jain, S.; Bates, F. S. *Science (Washington, DC, United States)* **2003**, *300*, 460-464.

42. Armstrong, D. W.; He, L.; Liu, Y.-S. *Anal. Chem.* **1999**, *71*, 3873–3876.

43. Anderson, J. L.; Ding, J.; Welton, T.; Armstrong, D. W. *J. Am. Chem. Soc.* **2002**, *124*, 14247–14254.

44. Favre, F.; Olivier-Bourbigou, H.; Commereuc, D.; Saussine, L. *Chem. Commun.* **2001**, 1360–1361.

Chapter 4

Phase Behavior of Concentrated Solutions of Block Copolymers in Ionic Liquids[1]

4.1 Introduction

Concentrated solutions of block copolymers possess self-assembled microstructures akin to those in the bulk state.[1] For simple AB diblocks the common microstructures observed include spherical domains situated on a cubic lattice (either bcc or fcc), hexagonally packed cylindrical domains, the bicontinuous gyroid, and lamellae. If the solvent used to prepare the solution is selective, the majority will partition into one of the block microdomains. This is analogous to a change in the block volume fraction of the copolymer (f), which drives the domain interfacial curvature toward the less soluble block domains. Additionally, the unfavorable interactions between the insoluble block and the selective solvent can increase the effective degree of segregation (χN) between the microstructure domains, where χ is the Flory-Huggins interaction parameter between the (solvated) copolymer blocks and N is the degree of

[1] Reproduced in part with permission from Macromolecules, Vol. 41, 1753–1759 (2008). Copyright 2008 American Chemical Society.

polymerization. These changes in the effective copolymer volume fraction and degree of segregation drive lyotropic mesophase transitions as the solution concentration is varied.

The behavior of many block copolymers upon addition of common organic and aqueous solvents has been extensively studied.[2–12] This chapter describes studies of the self-assembled copolymer microstructure phase behavior of concentrated solutions with ionic liquids as the solvent. The specific systems consist of PB–PEO in the ionic liquids [BMI][PF_6] and [EMI][TFSI], and PS–PEO in [EMI][TFSI]. The concentrated PB–PEO solution studies represent an extension of the dilute PB–PEO solution studies described in Chapter 3. For both classes of copolymers, the ionic liquids behave as selective solvents for the PEO blocks, and thus lyotropic transitions in the copolymer microstructure are observed as the concentration of the solutions is varied. Characterization of the copolymer microstructure in the concentrated solutions was performed via small angle X-ray scattering (SAXS).

4.2 Experimental

This section briefly describes details of the materials and techniques specific to the experiments in this chapter. A more general account of the synthesis and characterization of materials, and the experimental techniques, can be found in Chapter 2.

The PB–PEO copolymers are the same as those used for the dilute solution experiments described in Chapter 3, and Table 3.2 shows their molecular characteristics. The PS–PEO copolymers were synthesized via anionic polymerization,

and characterized using SEC and ^{1}H-NMR. The synthesis and characterization procedures are described in Chapter 2. The molecular characteristics of the PS–PEO copolymers are listed in Table 2.1. The PS–PEO copolymers were prepared from the same parent PS block, thus the copolymers differ only in length of the PEO blocks. The PS–PEO copolymers will be abbreviated as SO(X-Y), where the numbers in parenthesis correspond to the block molecular weights in kg/mol.

[BMI][PF_6] (solvent grade ≥ 98%) was purchased from Solvent Innovation GmbH. [EMI][TFSI] was synthesized as described in Chapter 2. Prior to use, the ionic liquids were dried under vacuum (ca. 10 mTorr) at 60–70 °C for 2–3 days to remove absorbed moisture, and then stored either in a glove box under argon or in a vacuum-sealed desiccator.

The general procedure used for dissolution of polymers in ionic liquid solvents is described in Chapter 2. All of the concentrated solutions used in the following experiments were prepared with the use of a cosolvent (dichloromethane). The cosolvent was subsequently removed under a dry N_2 purge, followed by drying under vacuum with heating (ca. 60 °C) until constant weight was reached.

The general procedure followed for preparation of copolymer solution samples for SAXS experiments is described in Chapter 2. Specifically, the PB–PEO solutions were sealed in aluminum DSC sample pans with Kapton windows, and then annealed under vacuum at ~80 °C for 3 days. The PS–PEO solutions were annealed under vacuum at 150 °C for 1 hour prior to sealing in DSC pans.

SAXS experiments were performed at the DuPont-Northwestern-Dow

Collaborative Access Team (DND-CAT) beamline at the Advanced Photon Source, Argonne National Laboratory. Two-dimensional scattering patterns were recorded by a Mar CCD area detector and then azimuthally integrated to give one-dimensional scattering data as intensity (I) versus wave vector ($q = 4\pi \sin(\theta/2)/\lambda$), where θ is the scattering angle (calibrated with silver behenate) and λ is the X-ray wavelength. The SAXS data used to characterize the concentrated copolymer solutions were collected over multiple trips to the DND-CAT beamline. For the experiments with PB–PEO solutions, the sample-to-detector distances used were 869, 603, and 201 cm, and the X-ray wavelengths were 1.03, 0.827, and 1.03 Å, respectively. For the PS–PEO solutions, the sample-to-detector distances were 650 and 850 cm, and the X-ray wavelengths were 0.886 and 0.729 Å. Additionally, some SAXS experiments were conducted on a home-built beamline at the University of Minnesota Characterization Facility. This beamline consisted of a Rigaku RU-200BVH rotating anode generating Cu Kα X-rays (λ = 1.54 Å), Franks mirror optics, a 230 cm sample-to-detector distance, and a multiwire area detector (HI-STAR, Siemens Analytical X-ray Instruments).

SAXS patterns for the PB–PEO/ionic liquid solutions were collected at 25 °C. The thermotropic behavior of the solutions was not extensively studied. However, SAXS patterns were collected at 70 °C and/or 100 °C for most of the solutions, particularly those displaying coexisting microstructures.

For SAXS experiments with the PS–PEO solutions, the samples were initially heated to 250 °C, and scattering patterns were collected at various temperatures upon cooling.

4.3 PB–PEO Solutions

4.3.1 [BMI][PF_6] Solution Results

This section contains the microstructure phase characterization results for the concentrated PB–PEO solutions with [BMI][PF_6] as the solvent. Figure 4.1 shows the phase map that was assembled based on the SAXS patterns obtained for the PB–PEO/[BMI][PF_6] solutions. The phase map is plotted as solution concentration (in wt% copolymer) vs. volume fraction of PEO (f_{PEO}) in the bulk copolymers. Thus, each vertical series of points represents the lyotropic phase behavior of a single copolymer, with increasing ionic liquid content. The subscripts of the microstructure domain labels designate which copolymer block forms the minor domain of the copolymer microstructure (spherical domains for S, and cylindrical domains for C). The phase boundaries in Figure 4.1 are estimated based on the experimentally observed phase behavior, and are included to help guide the eye. The shaded regions of Figure 4.1 represent regions of the phase map where the SAXS patterns were assigned to coexisting microstructure phases. One-dimensional scattering patterns for solutions of the three PB–PEO copolymers in [BMI][PF_6] at 25 °C are presented below.

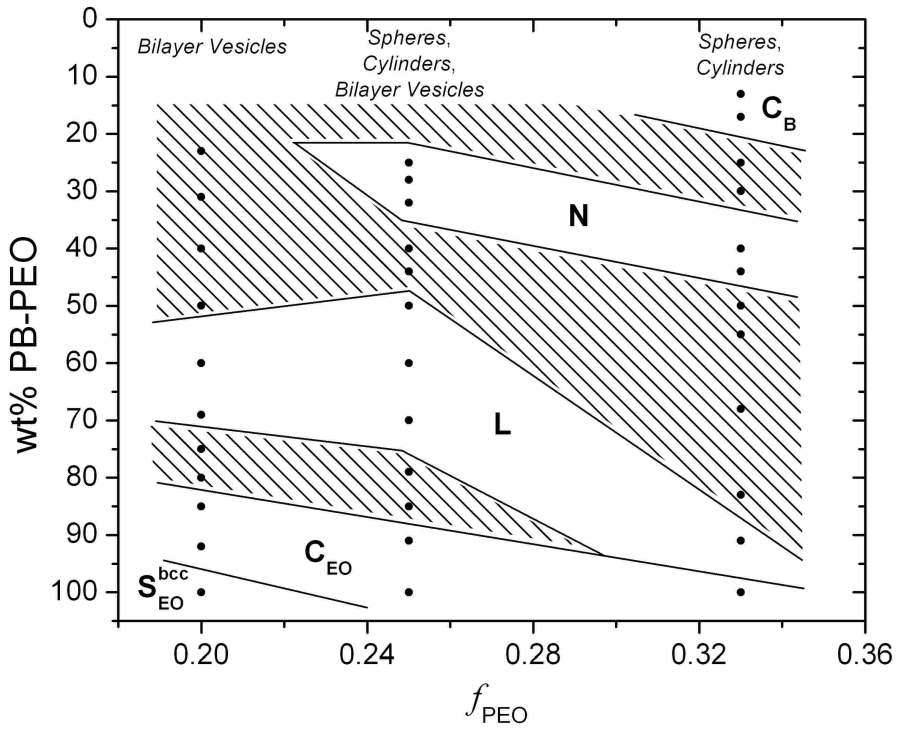

Figure 4.1: Microstructure phase map for PB–PEO/[BMI][PF_6] solutions at 25 °C. The *x*-axis corresponds to volume fraction of PEO in the bulk copolymers. The *y*-axis is the solution concentration in weight % copolymer. The microstructure labels correspond to bcc packed spheres (S^{bcc}), hexagonally packed cylinders (C), lamellae (L) and a random cylindrical network (N). The subscripts of the S and C microstructure labels correspond to the blocks forming the minor domain (spheres and cylinders) of the microstructure. Filled areas of the phase map correspond to regions of coexisting copolymer microstructures. Bilayer vesicles, cylinders, and spheres refer to the dilute solution copolymer micelle structures determined via cryo-TEM (see Chapter 3).

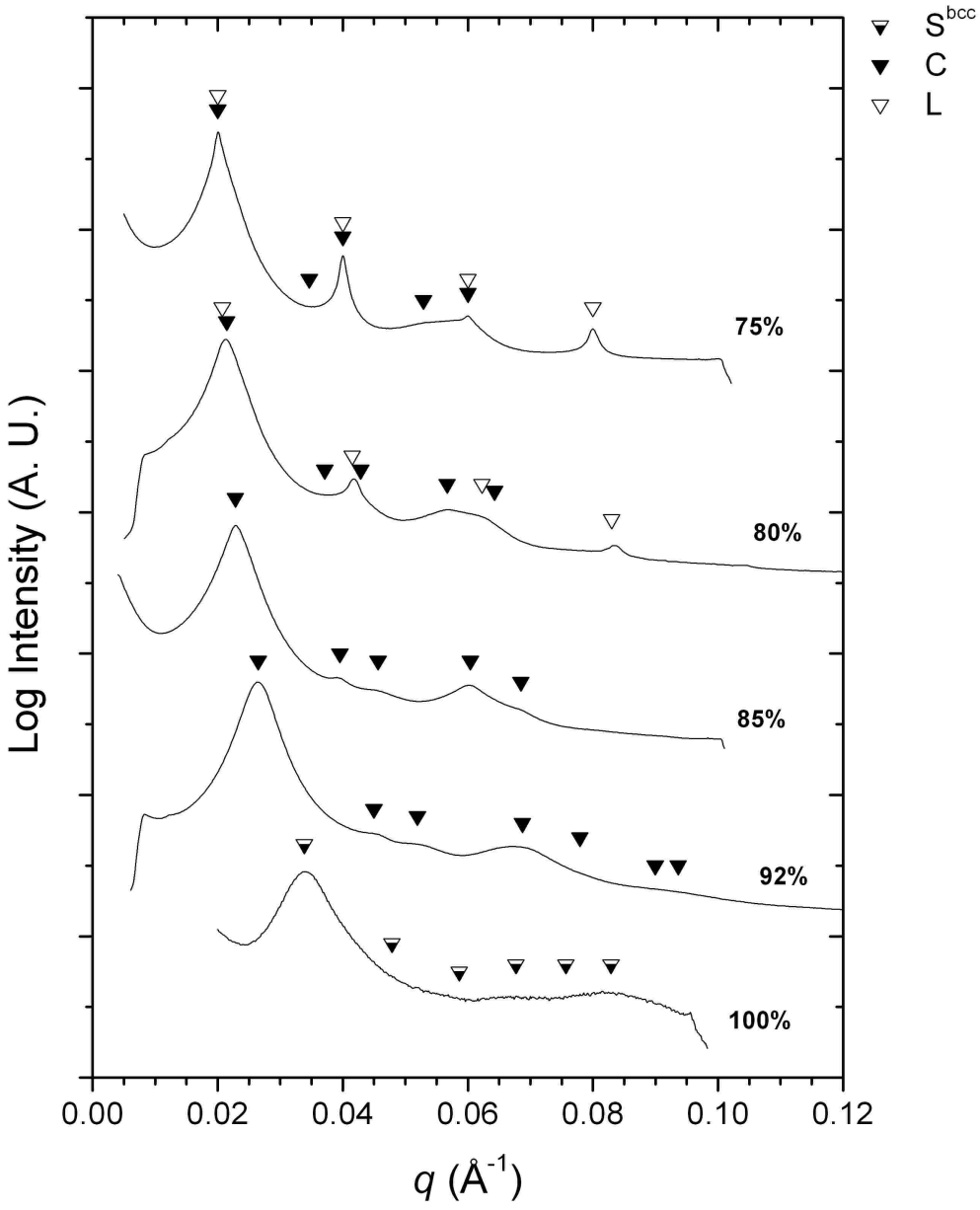

Figure 4.2: 1D X-ray scattering plots for BO(9–3)/[BMI][PF_6] solutions. Arrowheads mark allowed scattering intensity peaks for the assigned microstructures: 100 wt% (S_{EO}^{bcc}, √1:√2:√3:√4:√5:√6); 92 wt% and 85 wt% (C_{EO}, √1:√3:√4:√7:√9); 80 wt% and 75 wt% (C_{EO}, √1:√3:√4:√7:√9) and (L, 1:2:3:4).

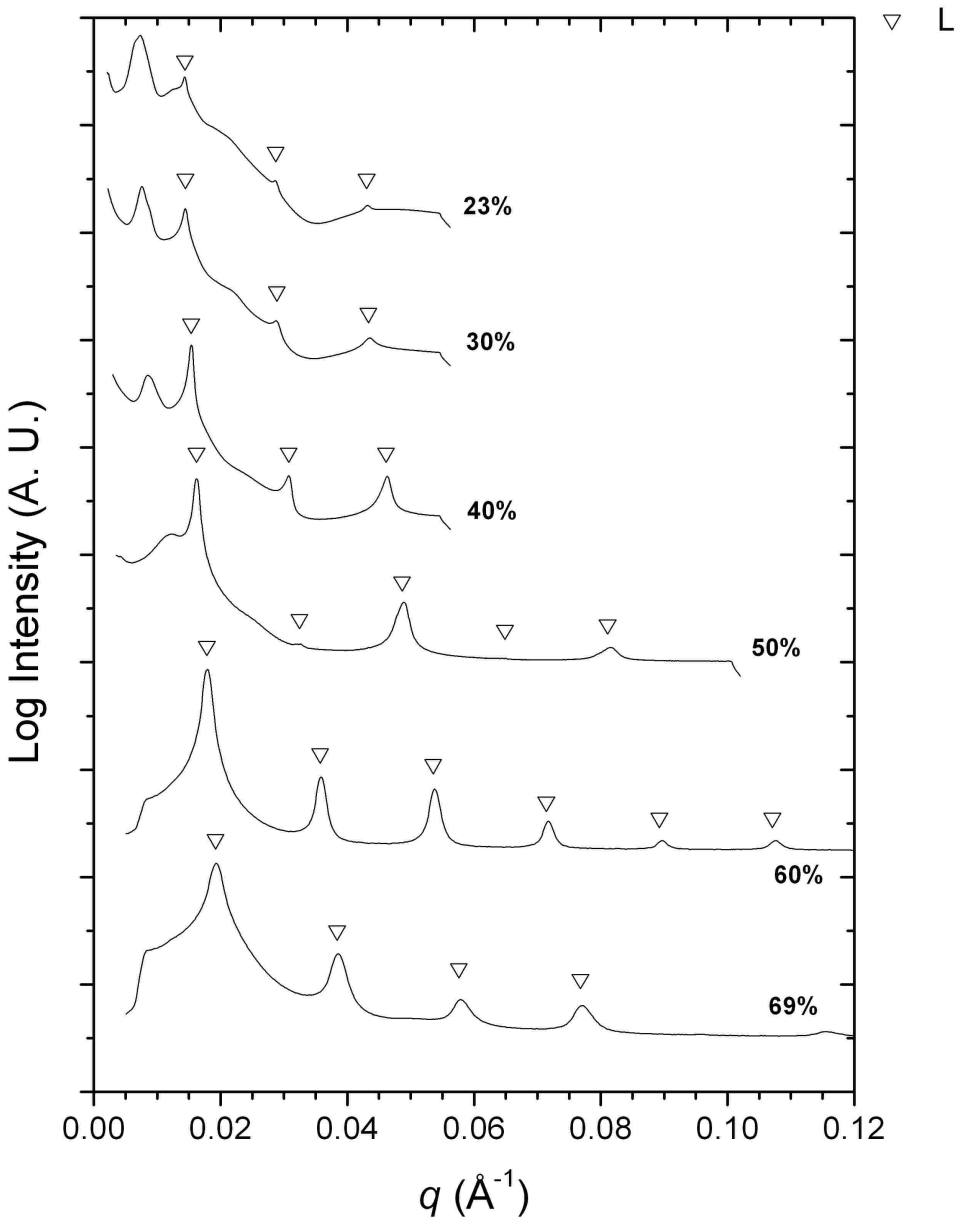

Figure 4.3: 1D X-ray scattering plots for BO(9–3)/[BMI][PF_6] solutions. Arrowheads mark allowed scattering intensity peaks for the L microstructure: q/q^* = 1:2:3:4:5:6.

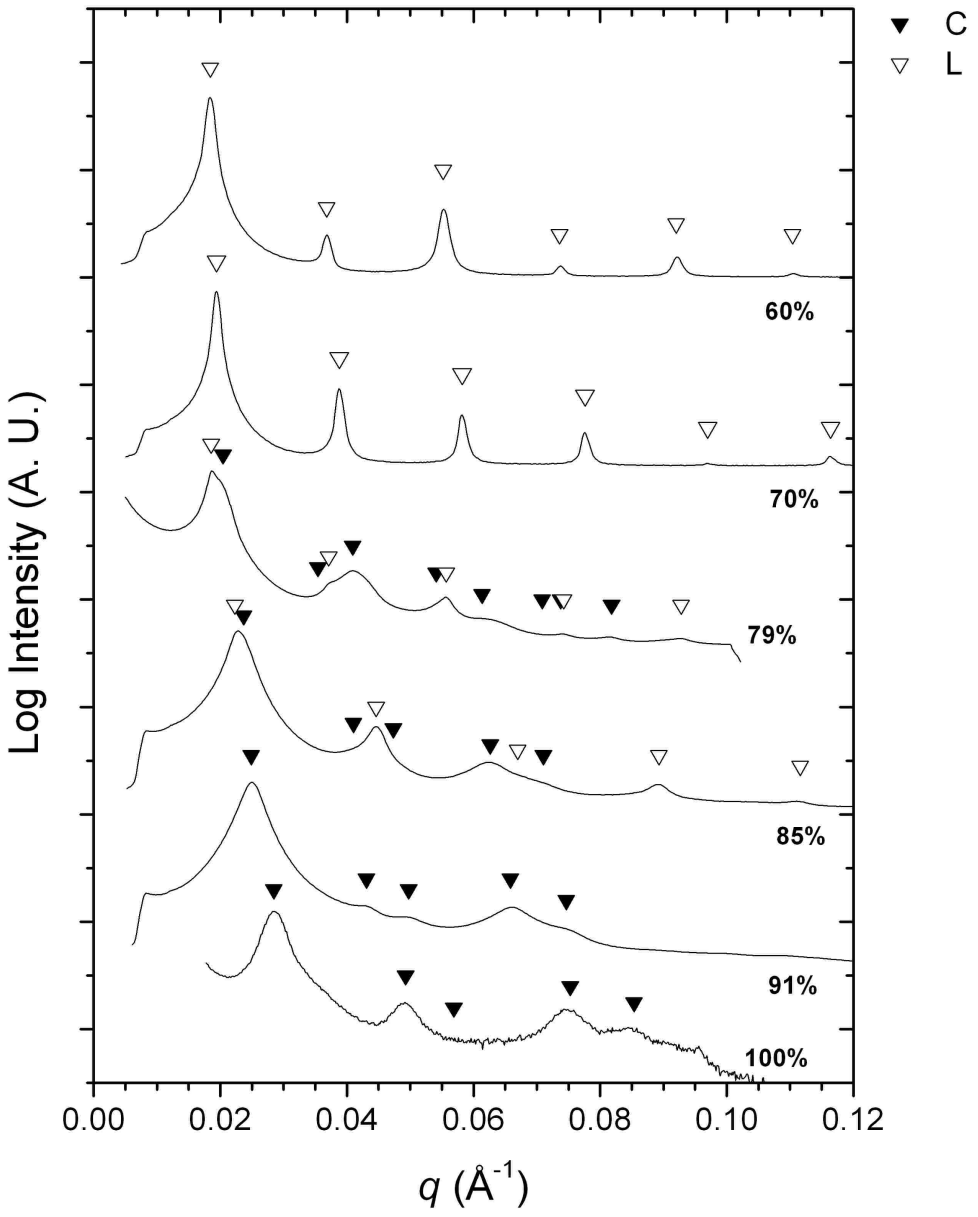

Figure 4.4: 1D scattering plots for BO(9–4)/[BMI][PF_6] solutions. Arrowheads mark allowed scattering intensity peaks for the assigned microstructures: 100 wt% and 91 wt% (C_{EO}, √1:√3:√4:√7:√9); 85 wt% and 79 wt% (C_{EO}, √1:√3:√4:√7:√9:√12: √13:√16) and (L, 1:2:3:4:5); 70 wt% and 60 wt% (L, 1:2:3:4:5:6).

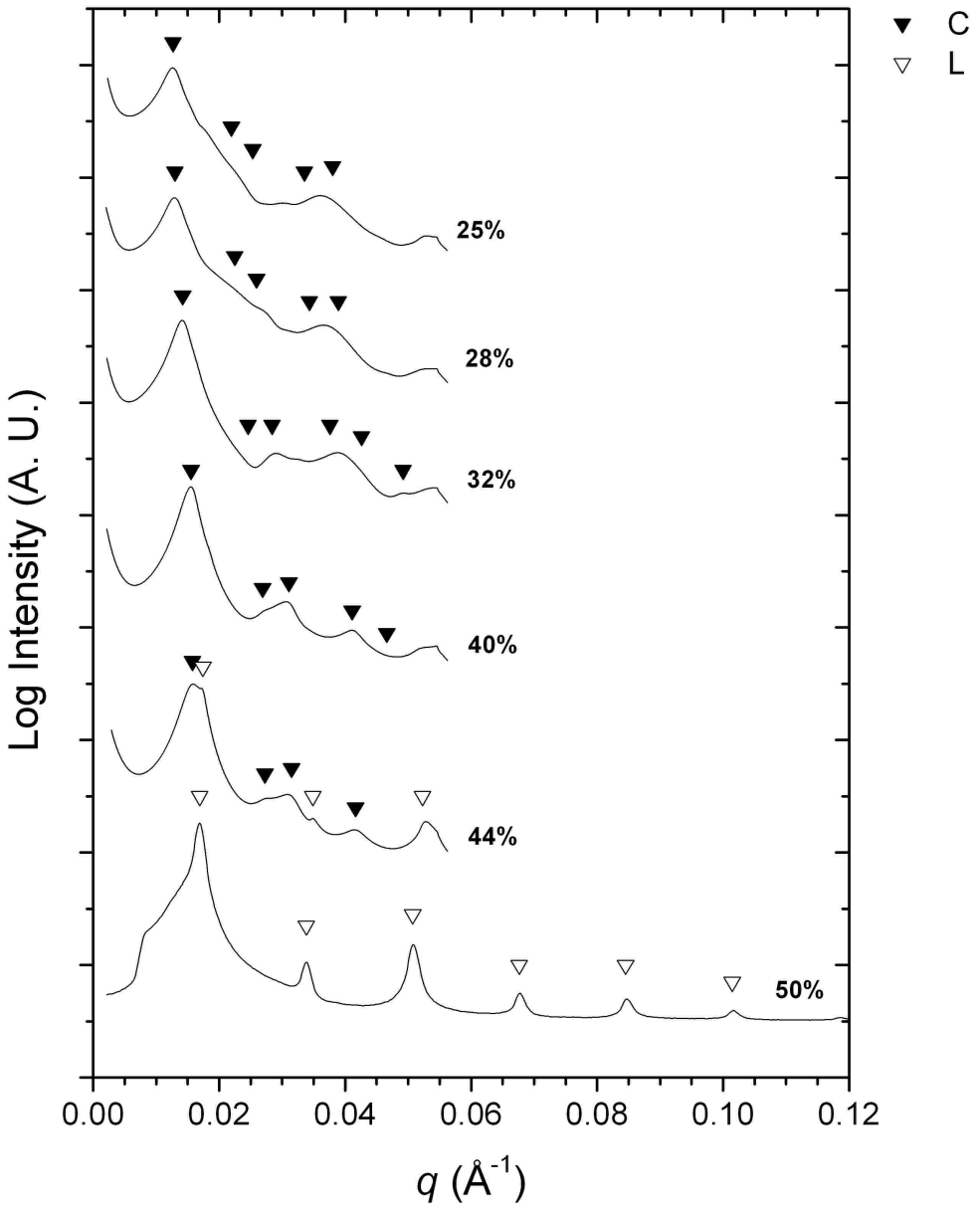

Figure 4.5: 1D scattering plots for BO(9–4)/[BMI][PF_6] solutions. Arrowheads mark allowed scattering intensity peaks for the assigned microstructures: 50 wt% (L 1:2:3:4:5:6); 44 wt% (L, 1:2:3) and (C_B, √1:√3:√4:√7); 40 wt%, 32 wt%, 28 wt% , and 25 wt% peak ratios for C_B are shown (√1:√3:√4:√7:√9), random cylindrical network morphology (N) also speculated to be present.

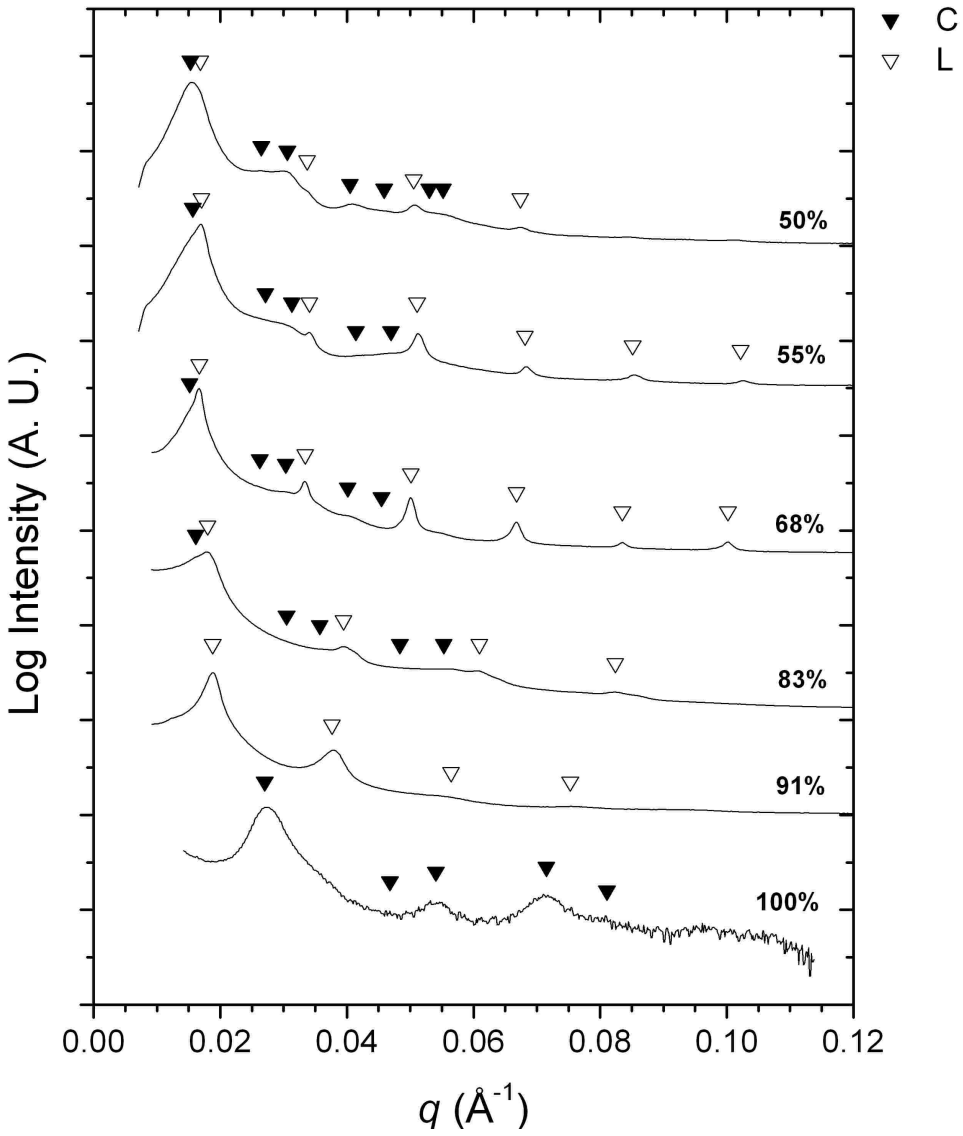

Figure 4.6: 1D scattering plots for BO(9–6)/[BMI][PF_6] solutions. Arrowheads mark allowed scattering intensity peaks for the assigned microstructures: 100 wt% (C_{EO}, √1:√3:√4:√7:√9); 91 wt% (L, 1:2:3:4); 83 wt%, 68 wt%, 55 wt%, and 50 wt% (L, 1:2:3:4:5:6) and (C_B, √1:√3:√4:√7:√9:√12:√13);

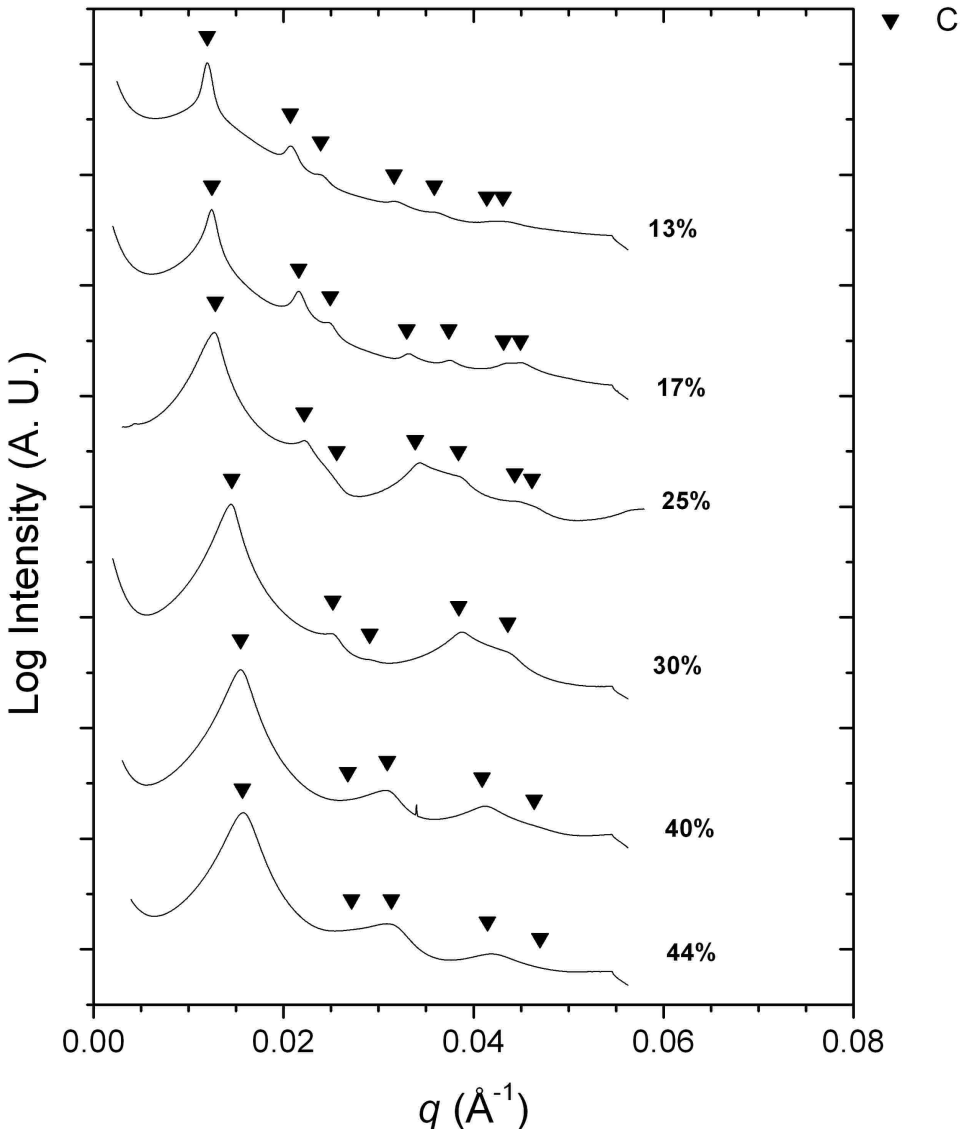

Figure 4.7: 1D scattering plots for BO(9–6)/[BMI][PF_6] solutions. Arrowheads mark allowed scattering intensity peaks for the assigned microstructures: 44 wt% and 40 wt%, N (C_B referenced, √1:√3:√4:√7:√9); 30 wt% and 25 wt%, N and (C_B, √1:√3:√4:√7:√9); 17 wt% and 13 wt%, (C_B, √1:√3:√4:√7:√9:√12:√13).

BO(9–3)

Figures 4.2 and 4.3 show 1D scattering patterns for solutions of BO(9–3) in [BMI][PF_6]. The arrowheads in Figures 4.2 and 4.3 are positioned at the ratios, q/q^*, (q^* is the position of the primary scattering peak) which characterize the allowed scattering intensity peaks for the assigned microstructures. The microstructure of the bulk BO(9–3) copolymer is a bcc packed lattice of spherical PEO domains $\left(S_{EO}^{bcc}\right)$. The scattering pattern shown for bulk BO(9–3) in Figure 4.2 is not completely conclusive, but Jain, *et al.* have characterized the bulk microstructure for this same copolymer as $\left(S_{EO}^{bcc}\right)$ as well.[8] Upon addition of [BMI][PF_6] the microstructure transitions to hexagonally packed cylinders (Figure 4.2, 92 wt% and 85 wt%), where the cylinder domains are formed by the PEO blocks plus ionic liquid. Here it is important to note that SAXS does not provide direct evidence of the partitioning of the ionic liquid into the PEO domains of the copolymer microstructure. However, as presented in Chapter 1, most ionic liquids behave as polar solvents, which, from a simple "like dissolves like" standpoint, would give them a higher affinity toward PEO. Additionally, the dilute solution micelle morphology behavior described in Chapter 3, and the concentrated solution phase behavior described below for the PB–PEO copolymers is consistent with the ionic liquids behaving as very selective solvents for the PEO blocks of the copolymers. Further addition of ionic liquid results in solutions with coexisting hexagonally packed cylinders and lamellae. These solutions were characterized by the emergence of X-ray scattering peaks corresponding to a lamellar microstructure, along with peaks corresponding to hexagonally packed cylinders. The 80 wt% and 75 wt%

solution scattering patterns in Figure 4.2 display coexisting microstructures. For the 75 wt% solution, the primary domain spacing (~1/q^*) for the C and L microstructures is the same, however, the persistence of the √7 peak signifies the presence of hexagonally packed cylinders. From concentrations of approximately 70–55 wt% the solutions display well ordered lamellar microstructure, as shown by the 69 wt% and 60 wt% scattering patterns in Figure 4.3. Finally, at concentrations of approximately 50 wt% copolymer and below, the scattering patterns can be characterized with a lamellar microstructure coexisting with the emergence of a broad, ambiguous peak at a larger domain length scale (lower q), as shown by the 50 wt%, 40 wt%, 30 wt%, and 23 wt% solution patterns in Figure 4.3. The broad peak observed in the scattering patterns for the moderate concentration (≤ 50wt%) BO(9–3)/[BMI][PF_6] solutions could potentially be a result of the formation of a diffuse cylinder microstructure, possibly related to the random cylindrical network microstructure (N) characterized by Jain, *et al*. for PB–PEO copolymers in aqueous solution.[8,9]

BO(9–4)

Figures 4.4 and 4.5 show 1D scattering patterns for solutions of BO(9–4) in [BMI][PF_6]. The C_{EO} microstructure was observed for samples from the bulk to approximately 90 wt% copolymer (Figure 4.4, 100 wt% and 91 wt%). A region of the phase map characterized by coexisting C_{EO} and L exists between solution concentrations of approximately 90–75 wt %. The 85 wt% and 79 wt% scattering patterns shown in Figure 4.4 display coexisting microstructure. Upon further addition of ionic liquid, the phase map displays a fairly wide region of solution concentration with

well ordered lamellae (Figures 4.4 and 4.5, 70 wt%, 60 wt%, and 50 wt%), followed by another region of coexisting lamellae and hexagonally packed cylinders. The reemergence of the hexagonal cylinder microstructure corresponds to addition of sufficient ionic liquid, to the point where the analogous increase in f_{PEO} drives the microstructure interfacial curvature toward the insoluble PB blocks, which now form the cylindrical regions of the microstructure. The scattering pattern for the 44 wt% solution in Figure 4.5 shows coexisting L and C_B microstructures. Finally, a region of the phase map exists where the BO(9–4)/[BMI][PF_6] solutions are characterized by scattering patterns consisting of broad peaks that cannot be directly referenced to any of the commonly observed block copolymer self-assembled microstructures. The scattering patterns shown in Figure 4.5 for the 40 wt%, 32 wt%, 28 wt%, and 25 wt% solutions are from this region of the phase map. The arrowheads represent the positions of the expected intensity peaks for a hexagonal cylinder microstructure. As can be seen, there is only moderate agreement between the observed scattering pattern and the expected scattering peaks for a hexagonal cylinder microstructure. Thus, it is again speculated that solutions in this region of the phase map possess a poorly ordered cylinder microstructure, possibly the N phase.

BO(9–6)

Figures 4.6 and 4.7 show 1D scattering patterns for solutions of BO(9–6) in [BMI][PF_6]. The bulk BO(9–6) copolymer possess the C_{EO} microstructure. Upon addition of ionic liquid, a narrow region of lamellar microstructure is observed (91 wt%, Figure 4.6). At moderate concentrations, the phase map is characterized by a wide

region of solutions with coexisting C_B and L microstructure. The scattering patterns for the 83 wt%, 68 wt%, 55 wt%, and 50 wt% solutions shown in Figure 4.6 are from this wide microstructure coexistence region of the phase map. As observed for the BO(9–4) solutions above, the coexisting C_B and L region of the phase map is followed by a region characterized by solutions which display broad, ambiguous X-ray scattering patterns (44 wt% and 40 wt%, Figure 4.7), which resemble form factor scattering. Upon further addition of ionic liquid, clear peaks corresponding to the C_B microstructure begin to reemerge in the scattering patterns, as shown in Figure 4.7 by the pattern for the 30 wt% solution. However, the scattering pattern for the 30 wt% solution still possesses the broad underlying form factor shape observed for the 40 wt% solution, potentially indicative of the N microstructure. Thus, the solutions in this region of the phase map are referenced to coexisting C_B and N. Finally, a region of the phase map emerges in which the BO(9–6)/[BMI][PF_6] solutions can be characterized by a well ordered C_B microstructure. The scattering patterns for the 17 wt% and 13 wt% solutions shown in Figure 4.7 are representative of the solutions in this region, where up to seven peaks in the scattering pattern can be resolved.

4.3.2 [EMI][TFSI] Solution Results

This section contains the microstructure phase characterization results for the concentrated PB–PEO solutions with [EMI][TFSI] as the solvent. Figure 4.8 shows the phase map for the PB–PEO solutions, which is plotted in the same fashion as Figure 4.1. One-dimensional SAXS patterns used to characterize the PB–PEO/[EMI][TFSI] solution microstructures are presented below.

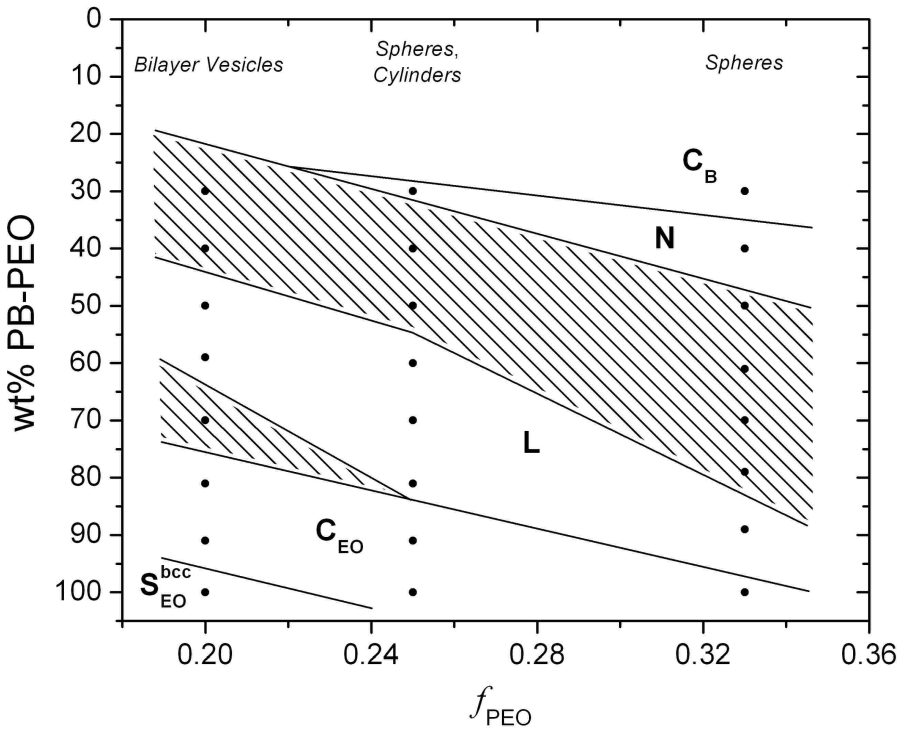

Figure 4.8: Microstructure phase map for PB–PEO/[EMI][TFSI] solutions at 25 °C. The *x*-axis corresponds to volume fraction of PEO in the bulk copolymers. The *y*-axis is the solution concentration in weight % copolymer. The microstructure labels correspond to bcc packed spheres (S^{bcc}), hexagonally packed cylinders (C), lamellae (L) and a random cylindrical network (N). The subscripts of the S and C microstructure labels correspond to the blocks forming the minor domain (spheres and cylinders) of the microstructure. Filled areas of the phase map correspond to regions of coexisting copolymer microstructures. Bilayer vesicles, cylinders, and spheres refer to the dilute solution copolymer micelle structures determined via cryo-TEM (see Chapter 3).

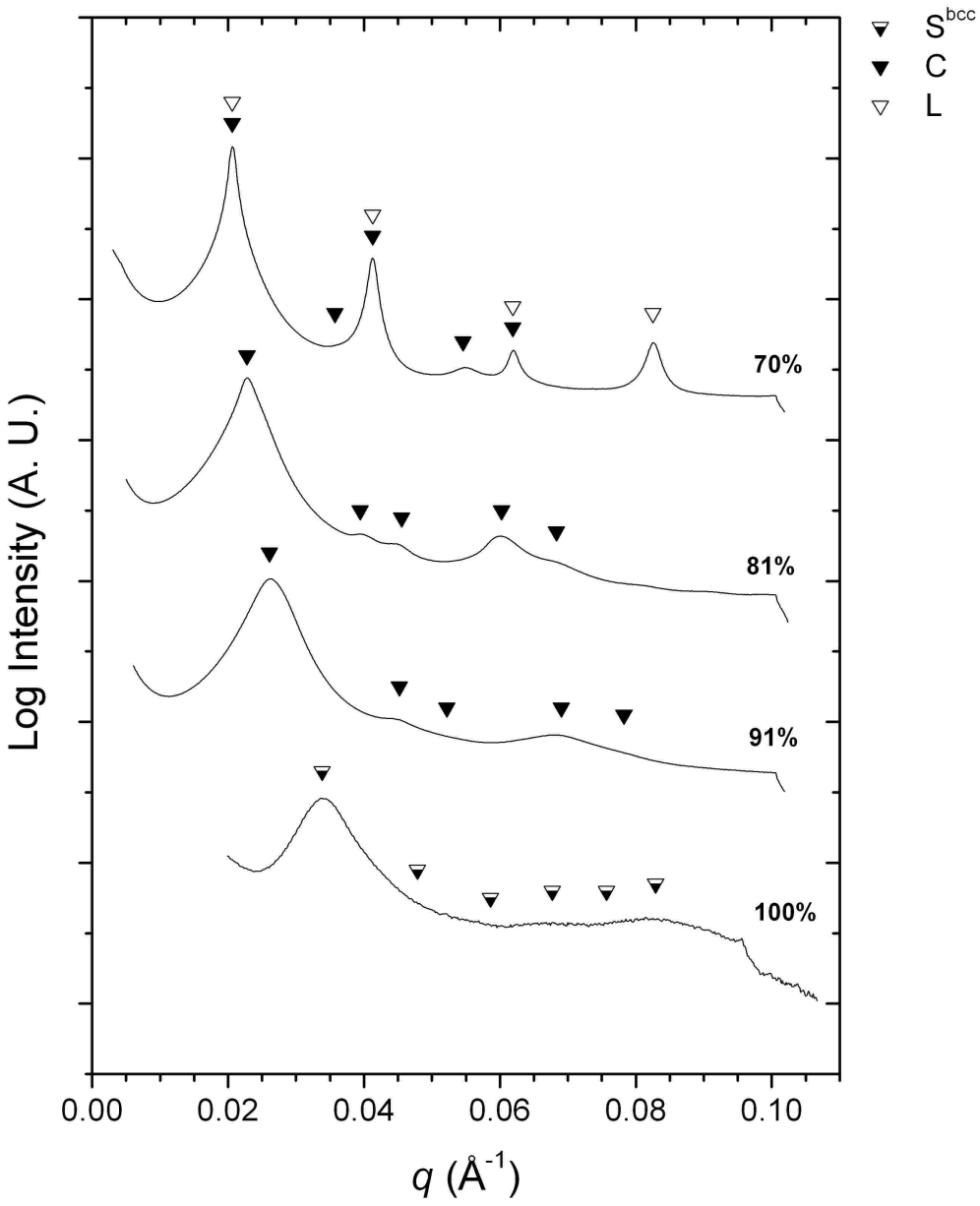

Figure 4.9: 1D scattering plots for BO(9–3)/[EMI][TFSI] solutions. Arrowheads mark allowed scattering intensity peaks for the assigned microstructures: 100 wt% (S_{EO}^{bcc}, √1:√2:√3:√4:√5:√6); 91 wt% and 81 wt% (C_{EO}, √1:√3:√4:√7:√9); 70 wt% (C_{EO}, √1:√3:√4:√7:√9) and (L, 1:2:3:4).

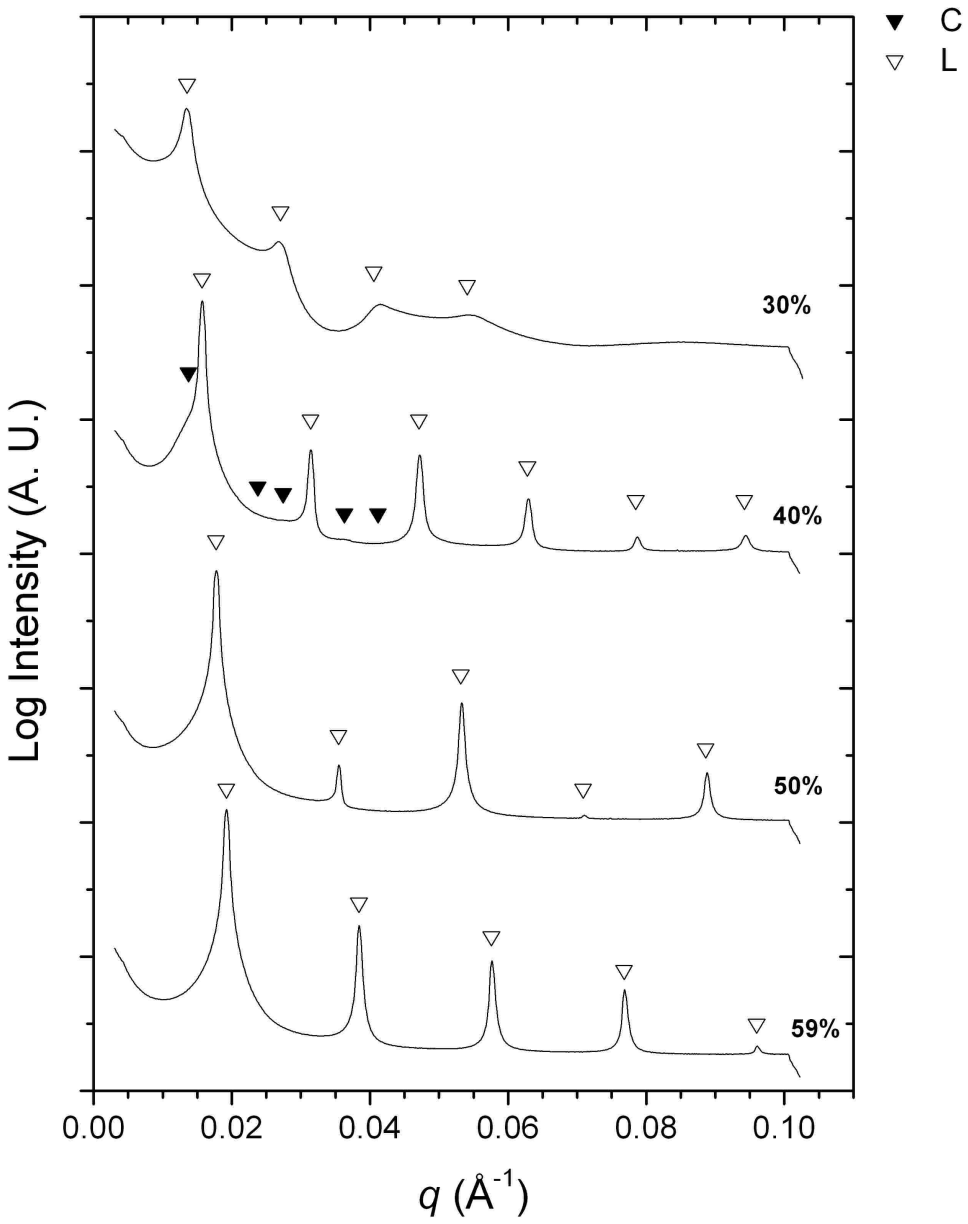

Figure 4.10: 1D scattering plots for BO(9–3)/[EMI][TFSI] solutions. Arrowheads mark allowed scattering intensity peaks for the assigned microstructures: 59 wt% and 50 wt% (L, 1:2:3:4:5); 40 wt% (L, 1:2:3:4:5:6) and (C_B, √1:√3:√4:√7:√9); 30 wt% (L, 1:2:3:4) and possible N.

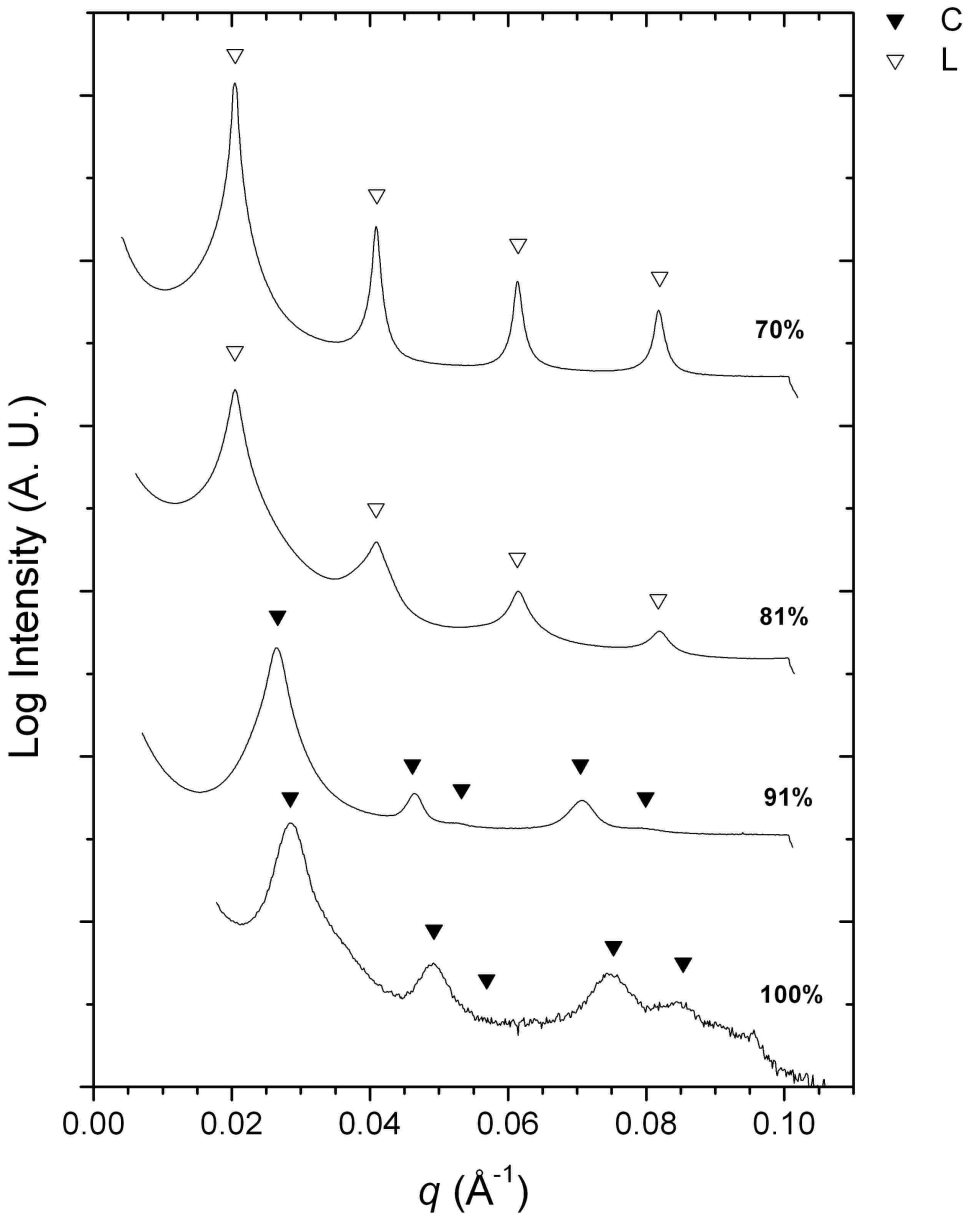

Figure 4.11: 1D scattering plots for BO(9–4)/[EMI][TFSI] solutions. Arrowheads mark allowed scattering intensity peaks for the assigned microstructures: 100 wt% and 91 wt% (C_{EO}, √1:√3:√4:√7:√9); 81 wt% and 70 wt% (L, 1:2:3:4).

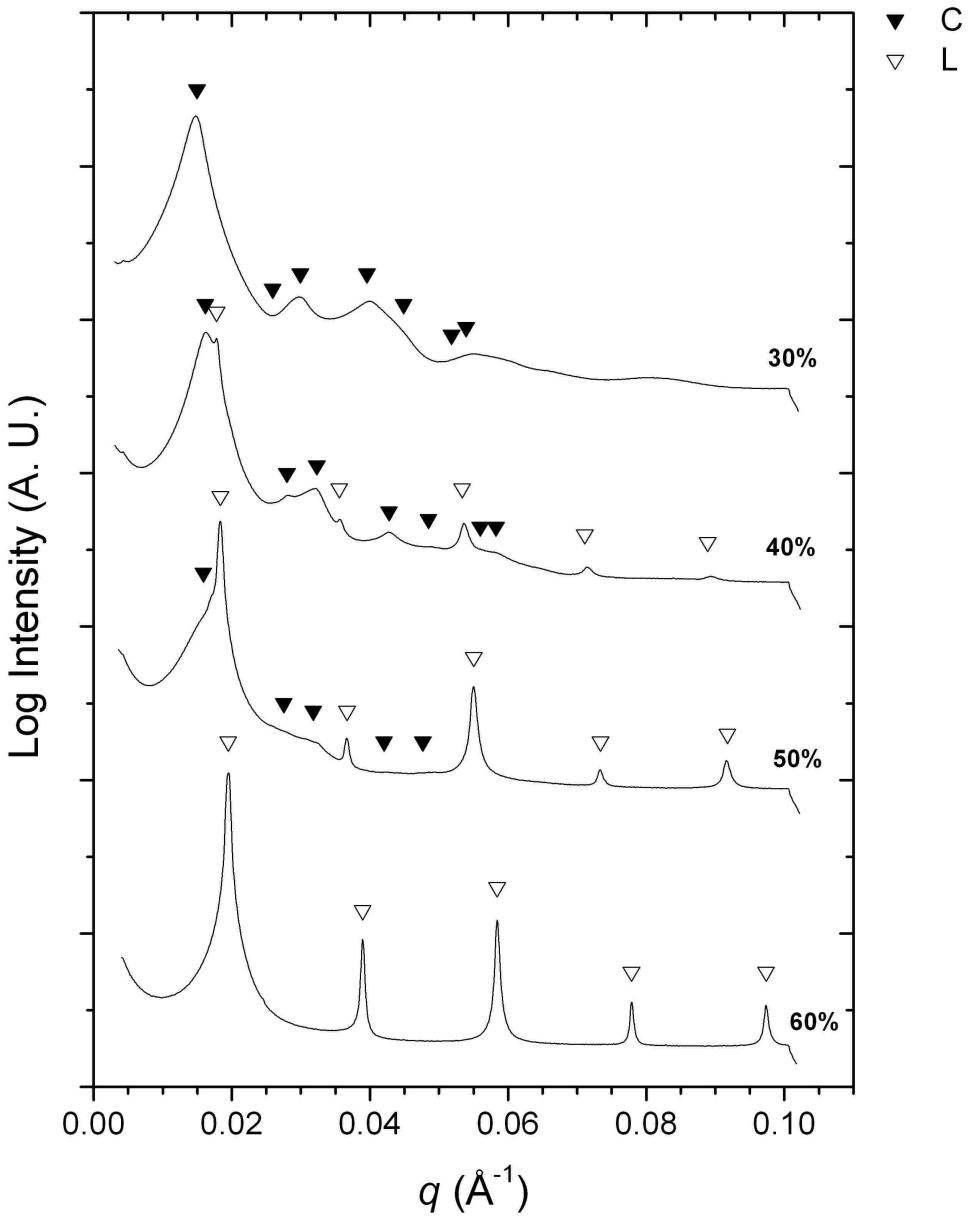

Figure 4.12: 1D scattering plots for BO(9–4)/[EMI][TFSI] solutions. Arrowheads mark allowed scattering intensity peaks for the assigned microstructures: 60 wt% (L, 1:2:3:4:5); 50 wt% and 40 wt% (L, 1:2:3:4:5) and (C_B, √1:√3:√4:√7:√9:√12:√13); 30 wt% N (C_B referenced √1:√3:√4:√7:√9:√12:√13:√16).

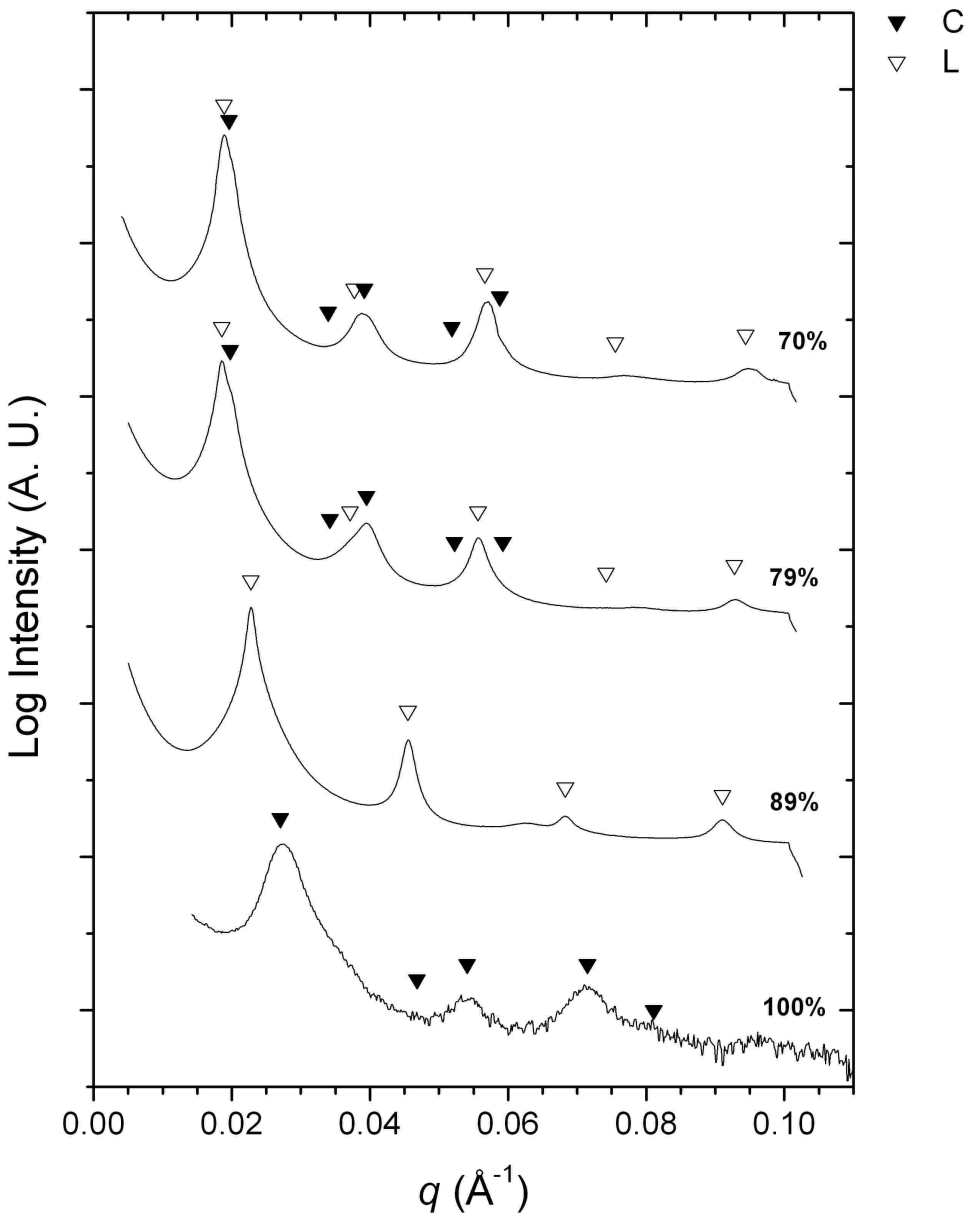

Figure 4.13: 1D scattering plots for BO(9–6)/[EMI][TFSI] solutions. Arrowheads mark allowed scattering intensity peaks for the assigned microstructures: 100 wt% (C_{EO}, √1:√3:√4:√7:√9); 89 wt% (L, 1:2:3:4); 79 wt% and 70 wt% (L, 1:2:3:4:5) and (C_B √1:√3:√4:√7:√9).

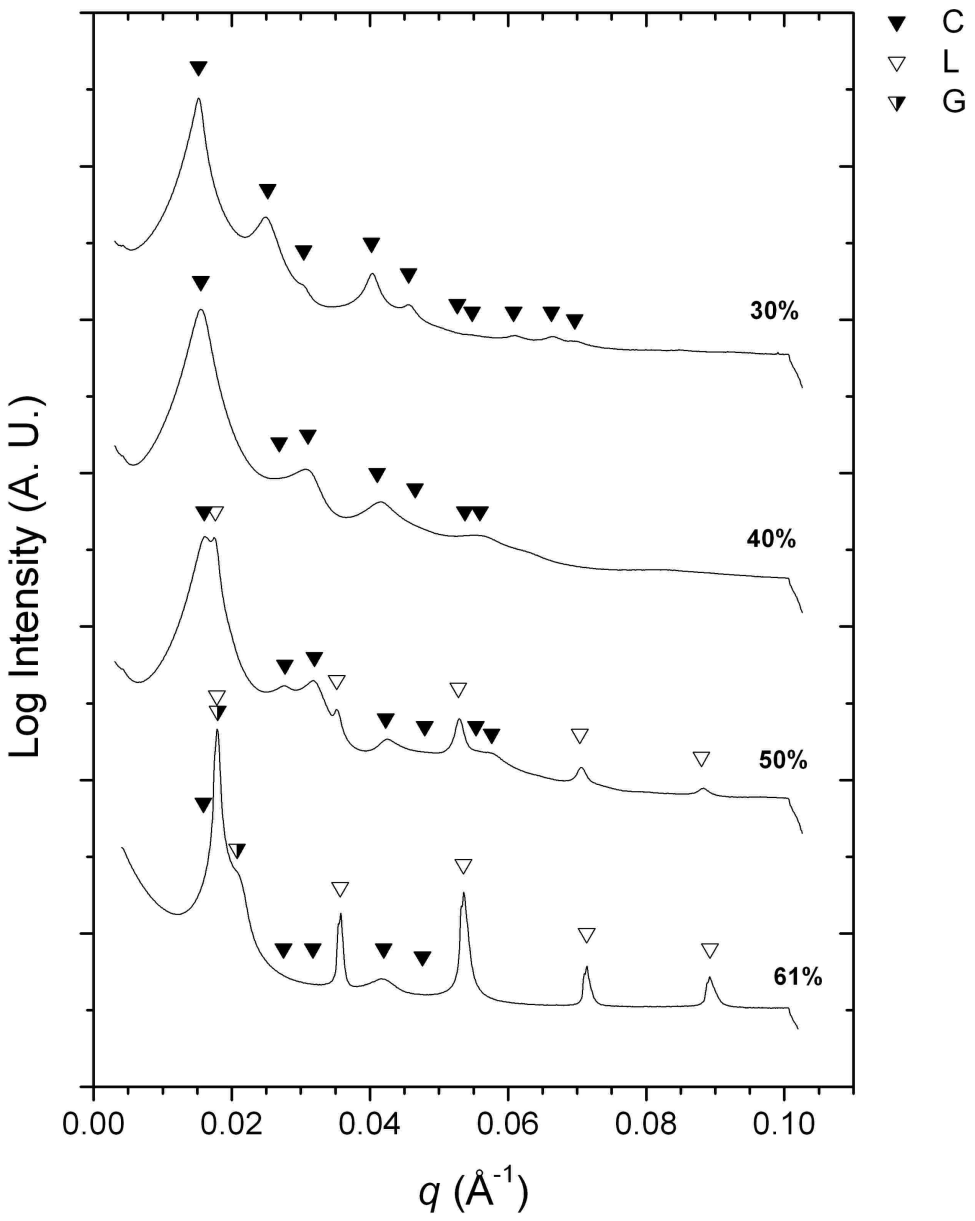

Figure 4.14: 1D scattering plots for BO(9–6)/[EMI][TFSI] solutions. Arrowheads mark allowed scattering intensity peaks for the assigned microstructures: 61 wt% (L, 1:2:3:4:5), (C_B, √1:√3:√4:√7:√9), and (G, √3:√4); 50 wt% (L, 1:2:3:4:5) and (C_B, √1:√3:√4:√7:√9:√12:√13); 40 wt% N (C_B referenced, √1:√3:√4:√7:√9:√12:√13); 30 wt% (C_B, √1:√3:√4:√7:√9:√12:√13:√16:√19:√21).

BO(9–3)

Figures 4.9 and 4.10 show 1D X-ray scattering patterns for the BO(9–3)/[EMI][TFSI] solutions. The bulk BO(9–3) scattering pattern is the same as that shown in Figure 4.2. Upon addition of ionic liquid the solutions display C_{EO} microstructure in the concentration region from approximately 95–75 wt%. A region of coexisting C_{EO} and L microstructures is observed between the C_{EO} and L phase windows. The scattering pattern for the 70 wt% solution shown in Figure 4.9 shows the persistence of the √7 peak, indicating the presence of hexagonal cylinder microstructure along with lamellae. Following the coexisting C_{EO} and L region is a well–defined lamellar region shown by the 59 wt% and 50 wt% solution SAXS patterns in Figure 4.10. The 40 wt% scattering pattern in Figure 4.10 displays well resolved peaks corresponding to L, as well as the emergence of weak scattering peaks indicating coexisting C_B. Finally, the scattering pattern shown in Figure 4.10 for the 30 wt% solution is characterized by broad peaks that could be referenced to the first four intensity maxima for the lamellar microstructure. However, there appears to be an underlying form factor present in the 30 wt% scattering pattern, which is potentially the result of a poorly ordered cylinder phase or the N phase coexisting with the lamellar microstructure.

BO(9–4)

Figures 4.11 and 4.12 show 1D SAXS patterns for the BO(9–4)/[EMI][TFSI] solutions. The initial C_{EO} phase region is represented in Figure 4.11 by the scattering patterns for the 100 wt% and 91 wt% samples. The copolymer solution microstructures

transition to a region characterized by the L phase upon further addition of ionic liquid, as shown by the 81wt%, 70 wt%, and 60 wt% solution scattering patterns. Coexisting C_{EO} and L microstructures were not observed for any of the BO(9–4)/[EMI][TFSI] solutions investigated. However, a region of coexisting L and C_B microstructures was observed and is represented by the 50 wt% and 40 wt% solution scattering patterns, in which the scattering peaks corresponding to both microstructures are well–defined. Finally, the scattering pattern for the 30 wt% solution is shown in Figure 4.12. Similar to other BO/ionic liquid solutions in this concentration range, the scattering pattern consists of broad peaks that can only be vaguely referenced to the C_B microstructure. Thus, again, it is possible that this microstructure corresponds to a poorly ordered cylindrical microstructure similar to the N phase.

BO(9–6)

Figures 4.13 and 4.14 show 1D X-ray scattering patterns for the BO(9–6)/[EMI][TFSI] solutions. The bulk BO(9–6) scattering pattern is the same as that shown in Figure 4.6. Upon addition of ionic liquid, a narrow region of lamellar microstructure is observed, represented by the scattering pattern for the 89 wt% solution in Figure 4.13. Further addition of ionic liquid results in a wide region of solution concentrations displaying coexisting L and C_B microstructure. This region is represented by the 79 wt%, 70 wt%, 61 wt%, and 50 wt% solutions in Figures 4.13 and 4.14, in which the peaks for both the lamellar and hexagonal cylinder microstructures are observed. Additionally, the shoulder on the primary scattering peak for the 61 wt% sample could indicate the presence of a coexisting bicontinuous gyroid microstructure

as well. The G microstructure is referenced by its first two allowed q/q^* ratios ($\sqrt{3}$ and $\sqrt{4}$) in Figure 4.14. A region speculated to correspond to the N microstructure is also observed, as shown by the broad peaks of the 40 wt% solution scattering pattern in Figure 4.14. Finally, a region of well ordered C_B microstructure is also observed, as shown by the scattering pattern for the 30 wt% BO(9–6)/[EMI][TFSI] solution.

4.3.3 Discussion

In general, the phase behavior of the PB–PEO/ionic liquid solutions displayed in Figures 4.1 and 4.8 is consistent with that expected for an analogous increase in f_{PEO} of the bulk copolymers. The common microstructure phase sequence of S_{EO}^{bcc}, to C_{EO}, to L, and ultimately to C_B displays a drive of the interfacial curvature toward the insoluble PB blocks as the effective PEO volume fraction is increased by an increase in the PEO block length of the copolymers, and/or addition of increasing amounts of ionic liquid. Furthermore, a general shift in the estimated phase boundaries to higher solution concentrations with increasing PEO block length is observed in the phase maps. This is also consistent with the analogy between the lyotropic phase behavior and a simple increase in f_{PEO}, where at higher PEO block lengths, less ionic liquid would be necessary to drive the lyotropic phase transitions.

One method for qualitatively explaining the phase behavior for a copolymer/solvent system is to consider "trajectories" across the melt phase diagram for the copolymer. By assuming that a selective solvent completely partitions into the compatible block microdomain, then, as mentioned above, the addition of solvent can be converted to an increase in the soluble block volume fraction. This assumption was

first introduced by Sadron and Gallot in the early 1970s,[5] and was considered in more detail by Hanley, *et al*.[3,13,14] Figure 4.15 shows the experimentally observed block copolymer microstructures for the PB-PEO/ionic liquid solutions, plotted by their effective PEO volume fractions, where effective f_{PEO} = (vol_{PEO} + vol_{IL}/total solution vol). The phase boundaries shown in Figure 4.15 correspond to the theoretical phase boundaries determined for a bulk AB diblock copolymer by Cochran and coworkers.[15] The large degree of segregation between the PB and PEO blocks results in $\chi N > 100$ for the three copolymers,[16] which is in the region of the theoretical phase map where the boundaries are essentially vertical lines. Qualitatively, the experimental copolymer microstructures agree fairly well with the phase regions predicted by the theoretical boundaries. Thus, a horizontal trajectory across the phase diagram, corresponding to an increase in f_{PEO} upon addition of ionic liquid, provides an estimate of the lyotropic phase behavior for the PB–PEO/ionic liquid solutions. It can be noted that since the ionic liquids behave as selective solvents, the estimated trajectories should also include a vertical component corresponding to an increase in effective χ upon addition of the ionic liquid. However, since the χN of the PB-PEO copolymers places them in a region of the theoretical phase map where there is essentially no curvature of the phase boundaries, the vertical trajectory components are ignored.

In addition to the classical S, C, and L block copolymer microstructures, the PB–PEO/ionic liquid solution phase maps include regions that are not anticipated based simply on a lyotropic progression of melt-phase block copolymer microstructures upon addition of solvent. First, wide regions of coexisting microstructures occur in the phase

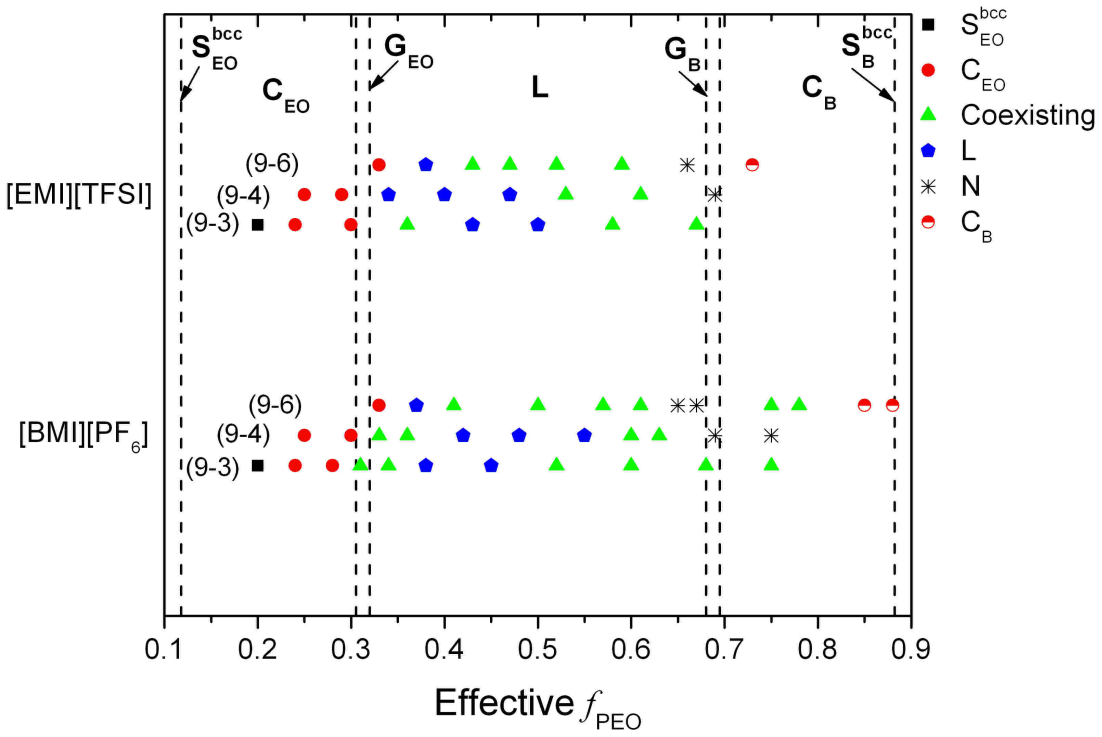

Figure 4.15: Experimentally observed microstructures for PB–PEO/ionic liquid solutions. Effective volume fractions of PEO calculated assuming the ionic liquid completely partitions into the PEO domains of the copolymer microstructure, and using densities of 1.13, 0.87, 1.52, and 1.36 g/cm^3 for PEO, PB, [EMI][TFSI], and [BMI][PF_6], respectively. Vertical lines represent theoretical phase boundaries determined by Cochran *et al.*[15] There are no units corresponding to the *y*-axis. The microstructures for the solutions are shifted vertically for clarity.

diagram where the gyroid microstructure might be expected to appear (*i.e.*, between regions of C and L microstructure in the phase map). Here, we note that the shoulder on the primary scattering peak for the BO(9–6)/[EMI][TFSI] 61 wt% solution (Figure 4.14) could be referenced to the √4 peak of the gyroid scattering pattern. This provides some evidence for the coexistence of the G microstructure in this sample. The PB–PEO/ionic liquid solutions were annealed at ~80 °C for 3 days prior to collecting the room temperature SAXS patterns, which suggests at least long term metastability of the microstructure observed for the 61 wt% sample. However, SAXS patterns were only collected for this sample at 25 °C. So, in the absence of more extensive thermotropic characterization, it is difficult to make any solid conclusions as to the ultimate thermodynamic stability of the G microstructure in the BO(9–6)/[EMI][TFSI] 61 wt% sample. Coexisting microstructures are a result of the high degree of segregation between the blocks of the copolymers, and the addition of solvent. The large interaction parameter χ (~0.4) between PB and PEO,[16] and the increased effective χ upon addition of a very selective solvent, apparently makes the frustrated packing of the gyroid phase less thermodynamically favorable. This is attributed to an intensification of the molecular packing frustration with increasing degree of segregation.[17] The solvent adds another degree of freedom to the system, allowing the copolymers to rearrange in order to alleviate the packing frustration involved with the gyroid microstructure. The same phenomenon was reported by Hanley, *et al.* for poly(styrene-*b*-isoprene) copolymers (PS-PI) in styrene-selective dialkyl phthalate solvents.[3,14] In these systems, the gyroid phase window yields to coexisting C and L microstructures upon increasing the solvent

selectivity, either by decreasing temperature or by shortening the alkyl chains of the phthalate solvents. The absence of the gyroid phase and the occurrence of coexisting C and L microstructures was also reported by Jain, *et al*.[8,9] and Förster, *et al.*[18] for aqueous PB–PEO solutions. It should be noted that recent theoretical[15] and experimental[19] results show that the gyroid phase can persist at strong segregation. However, these results were for block copolymers in the melt phase, not solution.

Second, there exist regions of the PB–PEO/ionic liquid phase maps characterized by scattering patterns containing broad peaks that cannot be referenced to the allowed reflections for any of the classic AB diblock copolymer microstructures. We speculate that these regions of the PB–PEO/ionic liquid phase maps (labeled N) are analogous to the random cylindrical network microstructure characterized by Jain, *et al*. in PB–PEO/H_2O solutions.[8,9] In the N microstructure, the PB domain consists of branched, cylindrical struts, forming an irregular, three-dimensional network. The matrix is formed by the PEO blocks along with the ionic liquid. This hypothesis of the existence of the N microstructure in the present study is based on several comparable characteristics between the PB–PEO/ionic liquid solutions and the aqueous PB–PEO solutions reported by Jain. First, identical PB–PEO block copolymers are used to prepare the aqueous and ionic liquid solutions. Second, the one-dimensional scattering patterns obtained for the random network microstructure in aqueous solutions are very similar to those obtained for the ionic liquid solutions speculated to possess the N microstructure (Figure 4.5: 40 wt%, 32 wt%, 28 wt%, and 25 wt%; Figure 4.7: 44 wt%, 40 wt%, 30 wt% and 25 wt%; Figure 4.12: 30 wt%; Figure 4.14: 40 wt%). They are

characterized by broad peaks that cannot be fully referenced to any of the commonly observed block copolymer microstructures, and resemble cylindrical form factor scattering. Third, the network microstructure appears in similar regions of the aqueous and ionic liquid solution phase maps. Figure 4.16 is the microstructure phase map for the aqueous PB–PEO solutions, adapted from reference 8. As can be seen, the random network microstructure begins to appear in both aqueous and ionic liquid solutions (Figures 4.1 and 4.8) at approximately 50 wt% for BO(9–6) and approximately 40wt% for BO(9–4). Finally, the reemergence of a well ordered C_B phase, as shown by SAXS patterns for the 17 wt% and 13 wt% solutions in Figure 4.7 and the 30 wt% solution in Figure 4.14, provide some evidence that the broad, ambiguous peaks of the scattering patterns assigned to the N phase do not simply represent disordering of the PB–PEO/ionic liquid solutions as the concentration is decreased. Ultimately, however, the assignment of the random network microstructure for the PB–PEO/ionic liquid solutions is speculative. In the case of aqueous PB–PEO solutions, Jain was able to visually characterize the N microstructure using cryogenic scanning electron microscopy (cryo-SEM). Attempts at characterizing the N microstructure in the PB–PEO/ionic liquid solutions with cryo-SEM were made, but were unsuccessful. In cryo-SEM, topographical contrast of the solid polymer structure is obtained by sublimation of the solvent from the vitrified sample surface that is to be imaged. For the block copolymers in ionic liquids, sublimation of the solvent was impossible. Thus, cryo-SEM experiments with the PB–PEO/ionic liquid solutions were plagued by poor topographical contrast in the sample images, and were ultimately inconclusive.

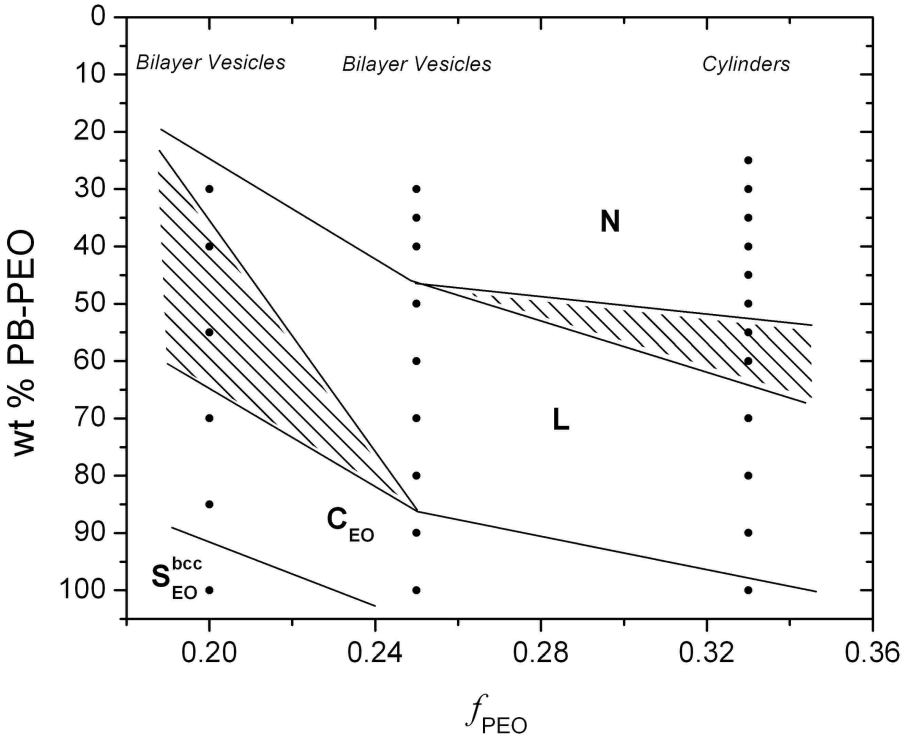

Figure 4.16: Microstructure phase map for aqueous PB–PEO solutions at 25 °C (adapted from ref 8). The *x*-axis corresponds to volume fraction of PEO in the bulk copolymers. The *y*-axis is the sample concentration in weight % copolymer. S is a cubic lattice of spheres, C is hexagonally packed cylinders, L is lamellae, and N is the random cylindrical network. The subscripts of the S and C microstructure labels correspond to the blocks forming the minor domain (spheres and cylinders) of the microstructure. Filled areas of the phase map correspond to regions of coexisting copolymer microstructures. Bilayer vesicles and cylinders refer to the dilute solution copolymer micelle structures.

The samples displaying coexisting microstructures and those presumed to display the random cylindrical network microstructure appear to be thermodynamically stable, or at least deeply metastable. This is based on the fact that all the samples were annealed for extended time (3 days) at 80 °C prior to SAXS experiments, and that no significant changes in the SAXS patterns were observed at elevated temperature (70 and 100 °C). These results are consistent with those reported by Jain for aqueous solutions of the same PB–PEO copolymers.[8,9]

A general comparison of the phase maps for the solutions prepared with the two different ionic liquids shows very similar phase behavior, with some small differences. One, there are somewhat wider regions of coexisting microstructure in the [BMI][PF_6] phase map. Particularly, a region of coexisting C_{EO} and L microstructures is observed for BO(9–4) in [BMI][PF_6], while in [EMI][TFSI] this region does not exist, or is at least much more narrow based on the phase behavior of the samples near the estimated C_{EO}/L phase boundary. Additionally, the region hypothesized to be characterized by the N phase is somewhat lager for the [BMI][PF_6] solutions than for [EMI][TFSI].

A general comparison between the microstructure phase behavior reported for the aqueous PB–PEO solutions (Figure 4.16) and that of the PB–PEO/ionic liquid solutions (Figures 4.1 and 4.8) can also be made. The main differences include a much wider N phase region, and less prevalent coexisting phase regions for the aqueous solutions as compared to those with ionic liquid solvent.

The differences in phase behavior could be a result of the differences in solvent selectivity that were deduced from the dilute solution micelle morphology behavior,

presented in Chapter 3 for these same PB–PEO block copolymers in water,[20] [BMI][PF_6], and [EMI][TFSI]. From these studies it was concluded that the order of selectivity for the three solvents was [EMI][TFSI] < [BMI][PF_6] ≤ H_2O. Thus, the size of the N phase region in the PB–PEO solution phase maps seems to increase with increasing solvent selectivity.

Additional supporting evidence for the higher selectivity of [BMI][PF_6] than [EMI][TFSI] comes from comparing how the structural length scale, taken as $d = 2\pi/q^*$ from the primary 100 scattering peak for the lamellar microstructure, differs based on ionic liquid. Figure 4.17 compares the lamellar structural length scale vs. copolymer concentration (given as copolymer volume fraction, ϕ) for samples prepared with the two ionic liquids. Addition of a neutral solvent (*i.e.*, one that solvates both copolymer blocks equally) will result in a decrease in structural length scale due to a general shielding of the unfavorable interactions between copolymer blocks, which allows increased lateral relaxation of the blocks near the interface.[2,14,21] Conversely, the addition of a selective solvent will cause an increase in structural length scale. This is due to a drive to decrease the interfacial area between block domains in order to reduce the unfavorable interactions between the solvent and the insoluble blocks, which results in increased chain stretching normal to the interface.[7,14,22]

The overall result of larger domain spacing for [BMI][PF_6] samples, shown in Figure 4.17, indicates [BMI][PF_6] behaves as a more selective solvent than [EMI][TFSI]. Additionally, the more negative slope for the power law fit ($d \sim \phi^a$) of the [BMI][PF_6] domain spacing is another indicator of greater solvent selectivity. For

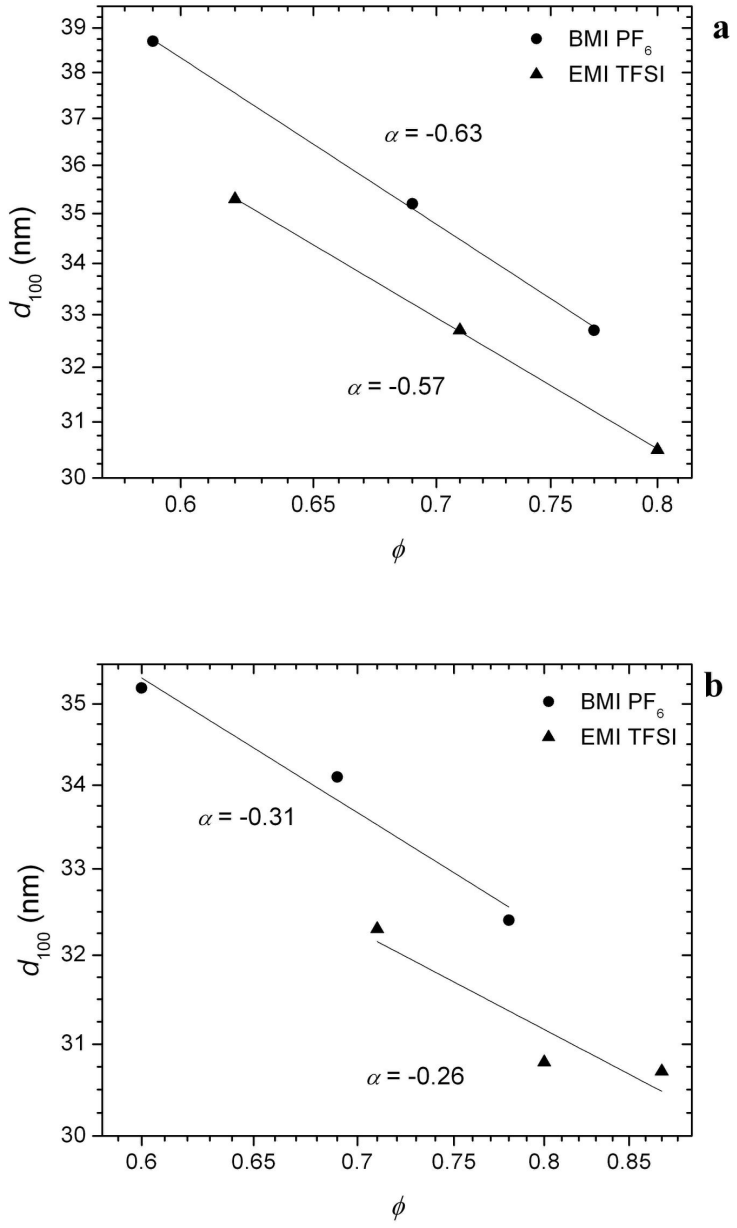

Figure 4.17: Dependence of lamellar domain spacing (d_{100}) on ionic liquid. Double-logarithmic plots, data fit with $d \sim \phi^{\alpha}$. (a) BO(9–3) and (b) BO(9–4).

comparison, theoretical self-consistent mean-field analysis of a lamellar forming system produced a power law exponent of –0.20 for a highly selective solvent (interaction parameter χ between solvent and insoluble block equal to 1).[14] In addition these results compare favorably with the experimental results of Hanley, *et al.* for a lamellar system consisting of a poly(styrene-*b*-isoprene) diblock copolymer (PS–PI) in diethyl phthalate (DEP) and dimethyl phthalate (DMP), which behave as selective and strongly selective PS solvents, respectively. In DEP α = –0.16, and in DMP α = –0.61.[14,23] Additionally, Lai, *et al*. report $\alpha = -1.03$ for PS–PI in the isoprene selective solvent squalane.[22] Based on these results it can be concluded that both ionic liquids behave as strongly selective solvents for the PEO blocks of the PB–PEO copolymers. Moreover, in a recent report closely related to the present study, Virgili, *et al*. investigated the microstructure domain spacing vs. solution concentration for a poly(styrene-*b*-2-vinylpyridine) diblock copolymer (PS–P2VP) dissolved in the ionic liquid imidazolium bis(trifluoromethylsulfonyl)imide ([Im][TFSI]).[24] The researchers report large, negative exponential α values of −2.31 and −3.16 at 145 °C and 225 °C, respectively. However, they do not comment on the nature of the polymer/solvent interactions that lead to the remarkably large, negative α values. The large, negative α values reported by Virgili, *et al.*, could be a result of the limited range in solution concentrations investigated ($1.0 \geq \phi \geq 0.93$), or the result of strongly unfavorable interactions between the solvent and the insoluble PS blocks. In the limit of affine swelling of the soluble domains, $d \sim \phi^{-1/n}$, where n is the dimensionality of the lattice (n = 1 for lamellae, 2 for cylinder, and 3 for spheres). However, α could potentially exceed the affine swelling limit if the solvent is

poor enough for the insoluble block that increased chain stretching is less energetically costly than additional contacts between the solvent and insoluble block.[22]

4.4 PS–PEO Solutions

4.4.1 Results

This section contains the results from SAXS experiments performed in order to characterize the lyotropic phase behavior of concentrated PS–PEO/[EMI][TFSI] solutions. Figure 4.18 shows the microstructure phase map that has been assembled for the PS–PEO/[EMI][TFSI] solutions. This phase map is assembled in a similar fashion to those presented for the PB–PEO/ionic liquid solutions. One-dimensional SAXS patterns used to characterize the copolymer solution microstructure at 150 °C are presented below.

SO(20–5)

Figures 4.19 and 4.20 show 1D SAXS patterns for the SO(20–5) copolymer solutions. The bulk SO(20–5) scattering pattern shown in Figure 4.19 was obtained at 25 °C. The low intensity of the scattering pattern is a result of the low degree of segregation for the SO(20–5) copolymer. Using the following equation for χ between PS and PEO,[25]

$$\chi = \frac{29.8}{T} - 0.0229 \qquad 4.1$$

where T is absolute temperature, χN for the SO(20–5) copolymer is ~23 at 25 °C, and ~14 at 150 °C. Thus, at 25 °C the SO(20-5) copolymer is only weakly ordered, and at 150 °C it is most likely disordered. The order-disorder-transition temperature for the bulk SO(20-5) copolymer was not explicitly characterized. Additionally, the difference

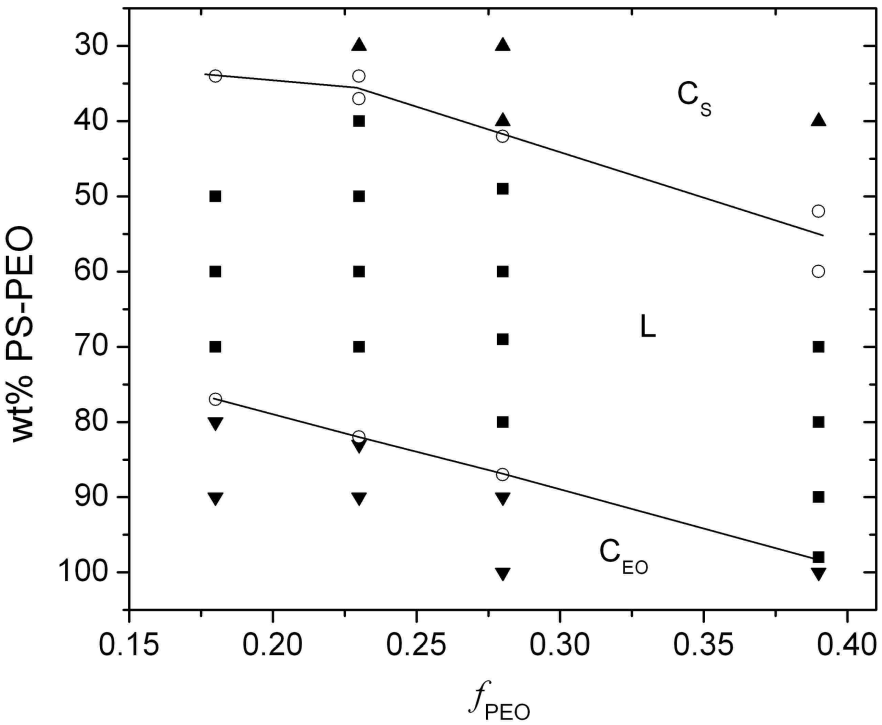

Figure 4.18: Microstructure phase map for PS–PEO/[EMI][TFSI] solutions at 150 °C. The *x*-axis corresponds to volume fraction of PEO in the bulk copolymers. The *y*-axis is the solution concentration in weight % copolymer. The microstructure labels correspond to hexagonally packed cylinders (C), and lamellae (L). The subscripts of the C microstructure labels correspond to the blocks forming the minor domain (spheres and cylinders) of the microstructure. Open symbols correspond to solutions displaying coexisting copolymer microstructures.

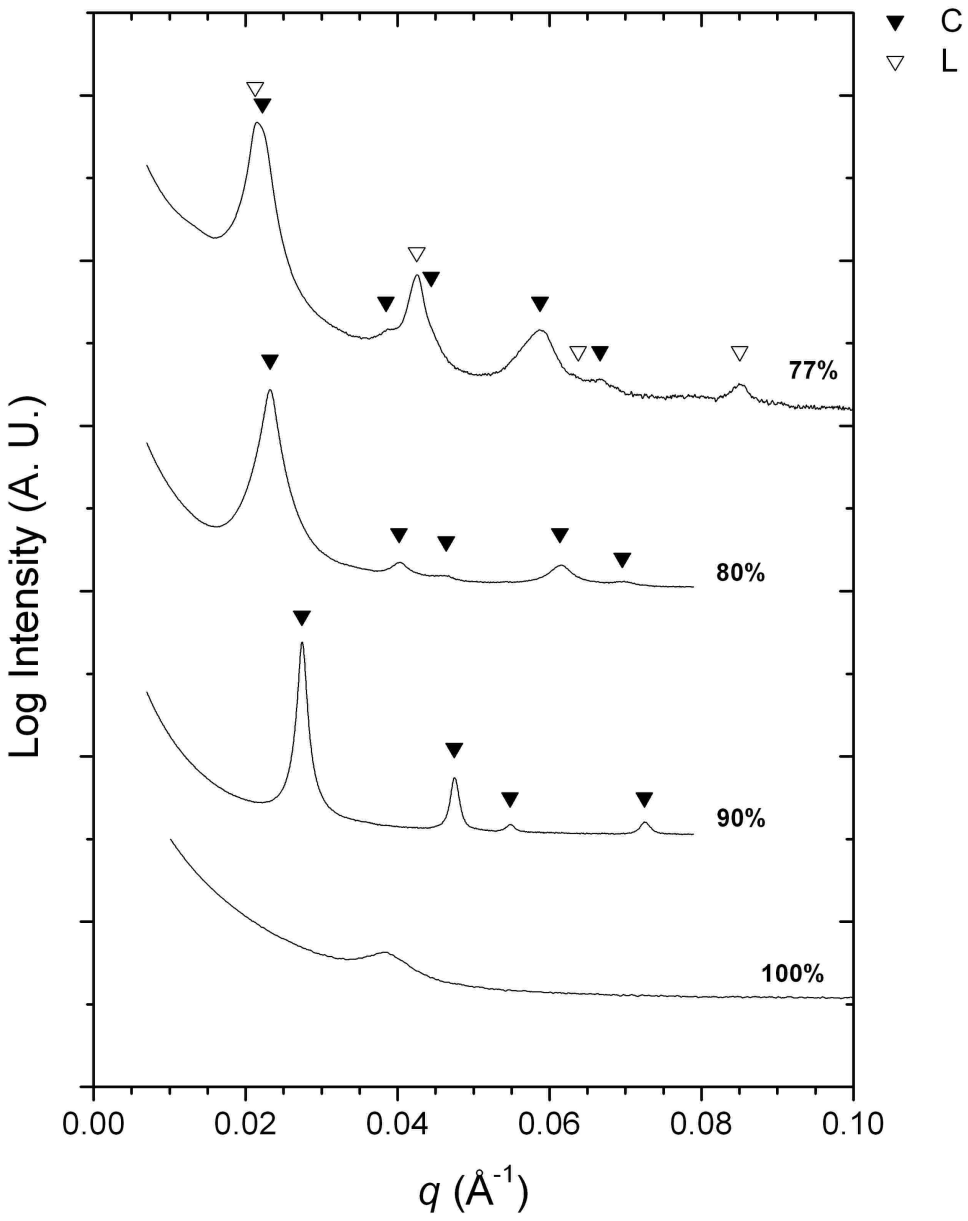

Figure 4.19: 1D scattering plots for SO(20–5)/[EMI][TFSI] solutions. Arrowheads mark allowed scattering intensity peaks for the assigned microstructures: 100 wt% pattern obtained at 25 °C; 90 wt% and 80 wt% (C_{EO}, √1:√3:√4:√7); 77 wt% (C_{EO}, √1:√3:√4:√7:√9) and (L, 1:2:3:4).

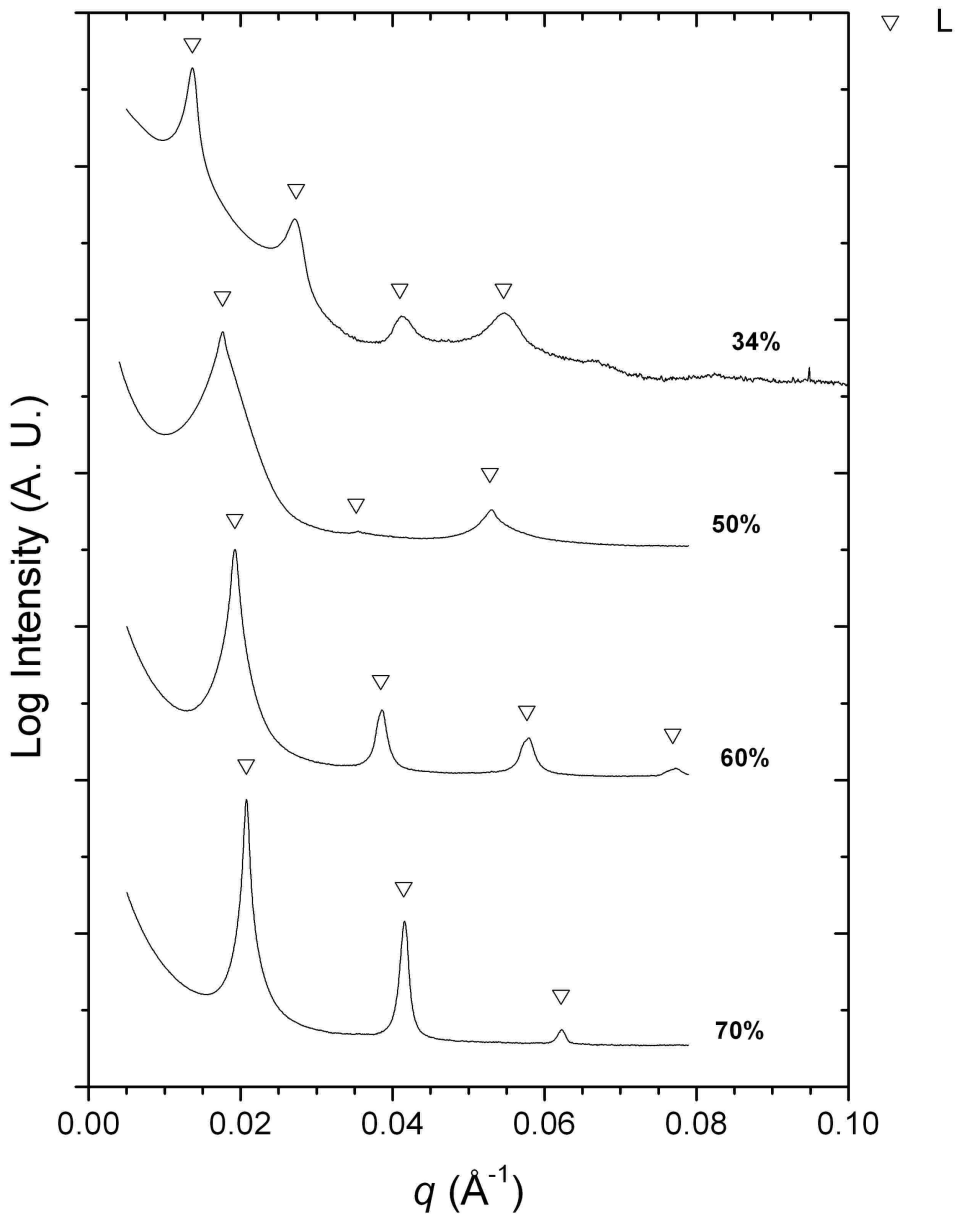

Figure 4.20: 1D scattering plots for SO(20–5)/[EMI][TFSI] solutions. Arrowheads mark allowed scattering intensity peaks for the assigned microstructures: 70 wt%, 60 wt%, 50 wt%, and 34 wt% (L, 1:2:3:4).

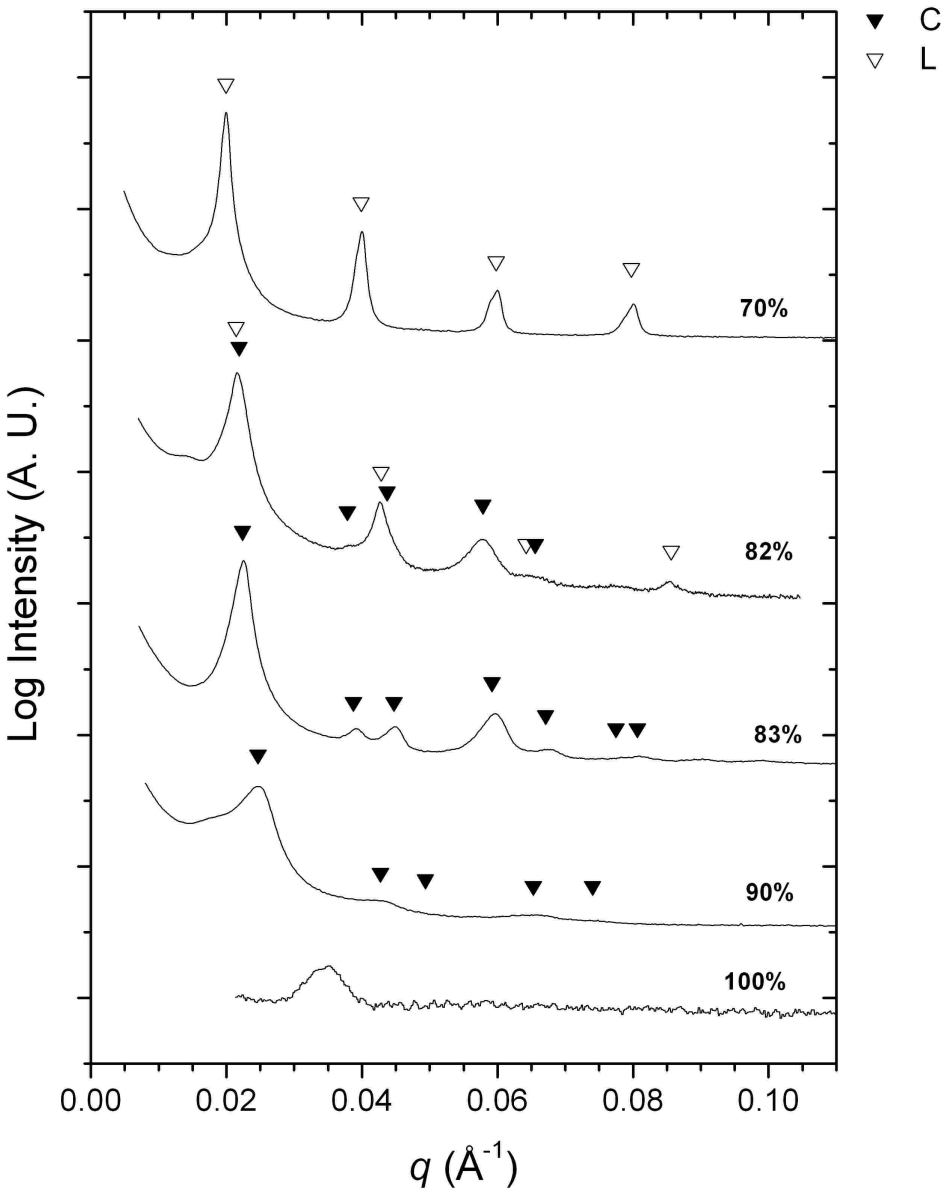

Figure 4.21: 1D scattering plots for SO(20–6)/[EMI][TFSI] solutions. Arrowheads mark allowed scattering intensity peaks for the assigned microstructures: 100 wt% pattern at 150 °C, at room temp bulk SO(20–6) displays C_{EO}; 90 wt% and 83 wt% (C_{EO}, √1:√3:√4:√7:√9); 82 wt% (C_{EO}, √1:√3:√4:√7:√9) and (L, 1:2:3:4); 70 wt% (L, 1:2:3:4).

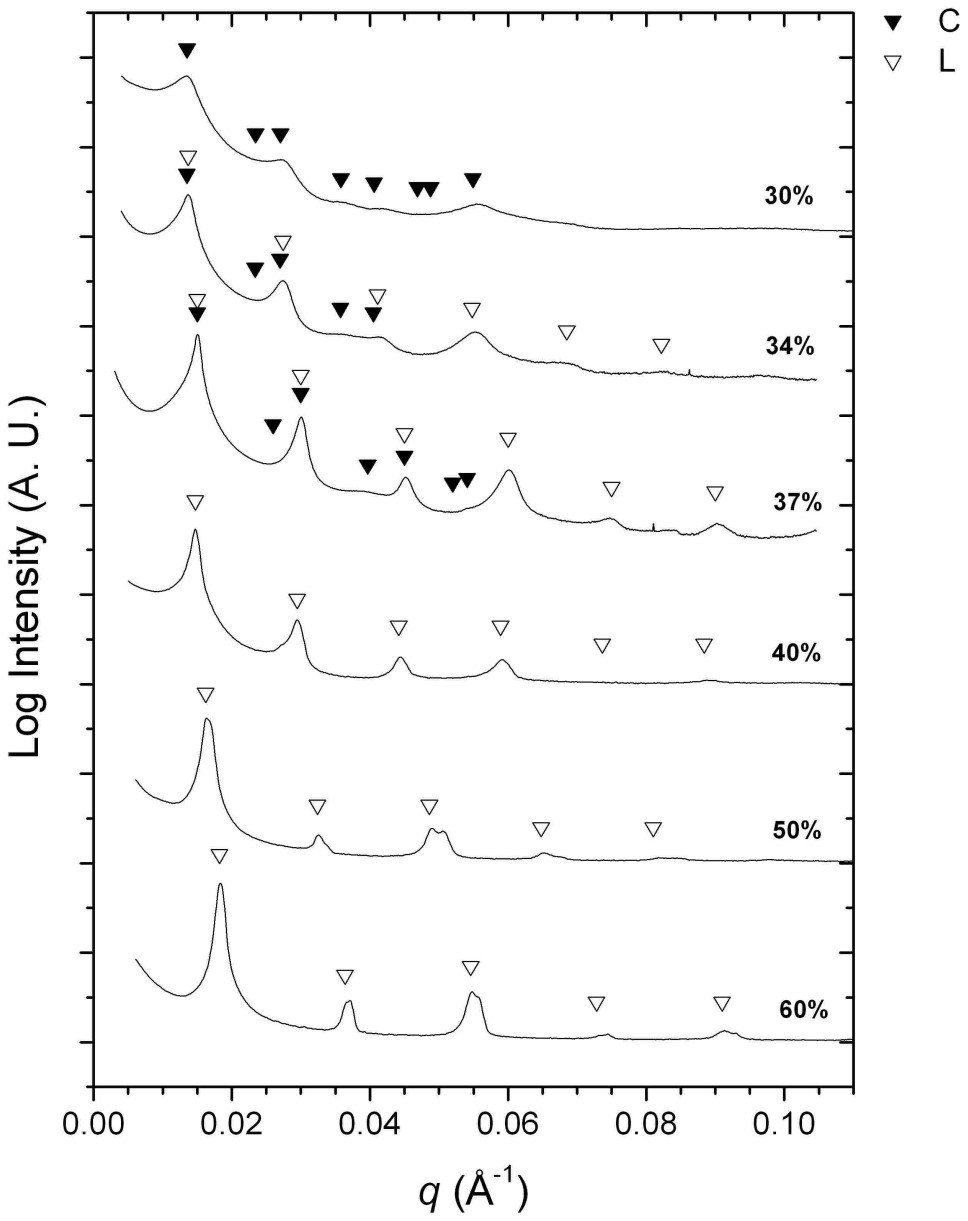

Figure 4.22: 1D scattering plots for SO(20–6)/[EMI][TFSI] solutions. Arrowheads mark allowed scattering intensity peaks for the assigned microstructures: 60 wt%, 50 wt%, and 40 wt% (L, 1:2:3:4:5); 37 wt% and 34 wt% (L, 1:2:3:4:5:6) and (C_S, √1:√3:√4:√7:√9); 30 wt% (C_S, √1:√3:√4:√7:√9:√12:√13:√16).

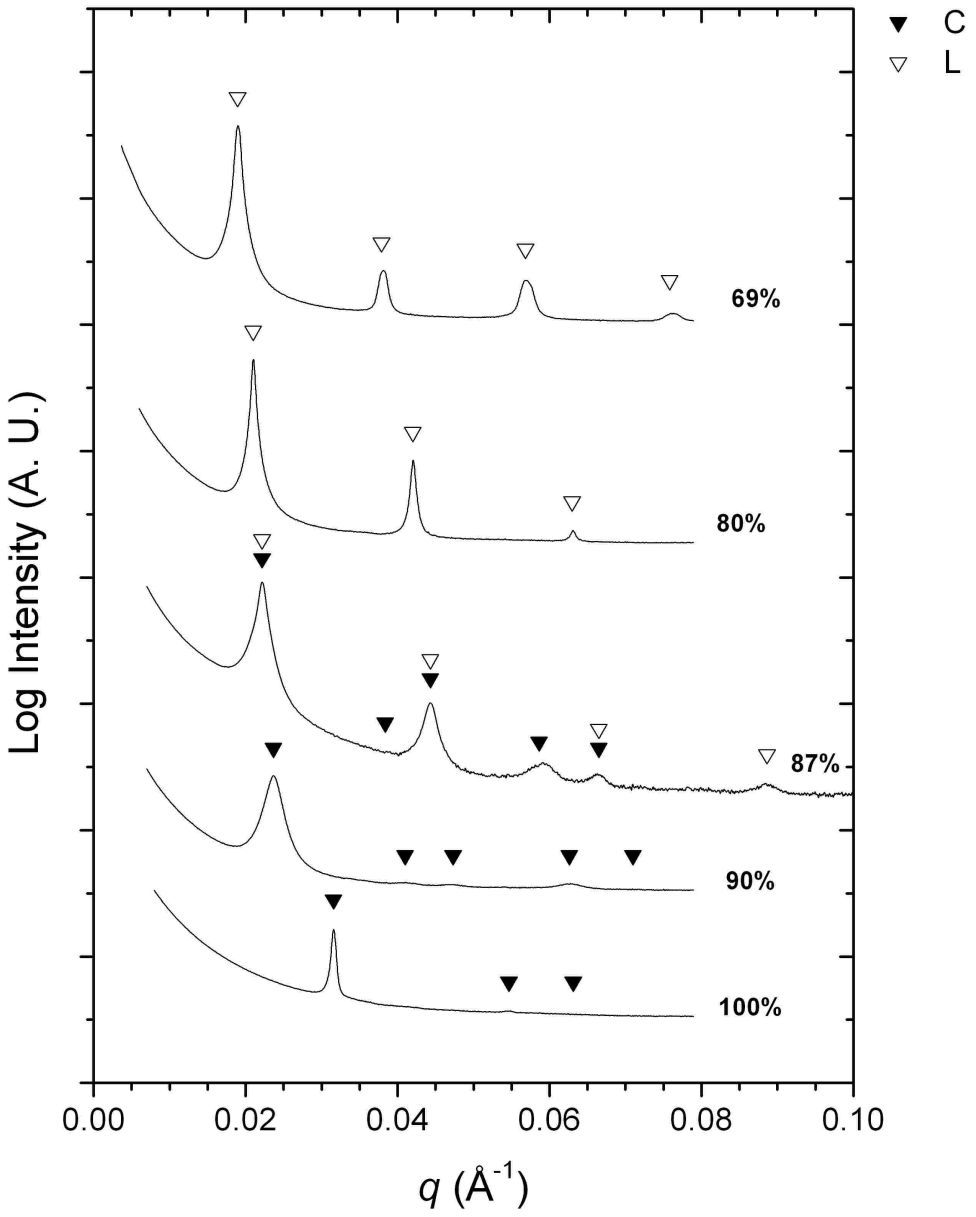

Figure 4.23: 1D scattering plots for SO(20–8)/[EMI][TFSI] solutions. Arrowheads mark allowed scattering intensity peaks for the assigned microstructures:100 wt% and 90wt% (C_{EO}, √1:√3:√4:√7:√9); 87 wt% (C_{EO}, √1:√3:√4:√7:√9) and (L, 1:2:3:4); 80 wt% and 69 wt% (L, 1:2:3:4).

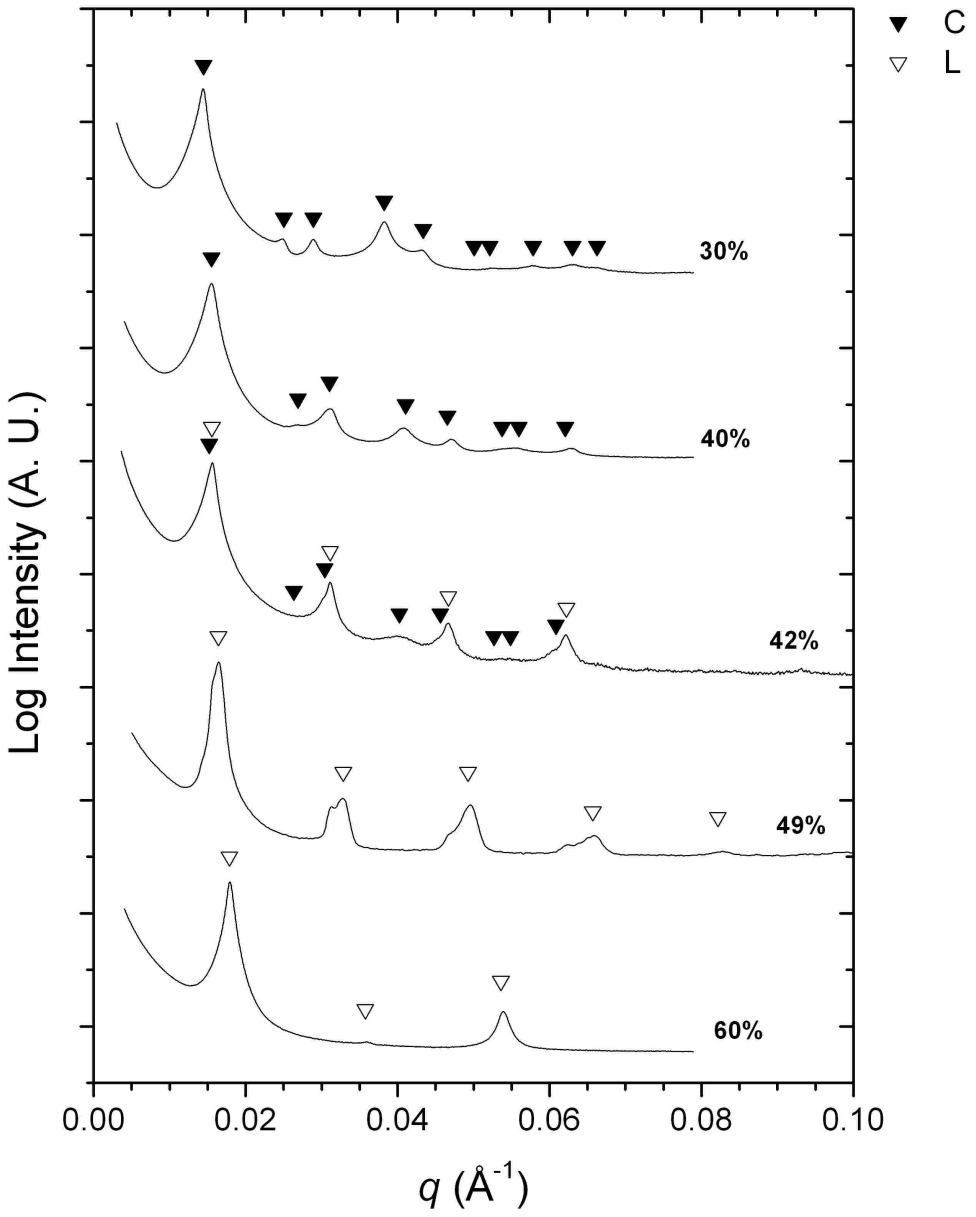

Figure 4.24: 1D scattering plots for SO(20–8)/[EMI][TFSI] solutions. Arrowheads mark allowed scattering intensity peaks for the assigned microstructures: 60 wt% and 49 wt% (L, 1:2:3:4:5); 42 wt% (L, 1:2:3:4) and (C_S, √1:√3:√4:√7:√9:√12:√13:√16); 40 wt% and 30 wt% (C_S, √1:√3:√4:√7:√9:√12:√13:√16:√19:√21).

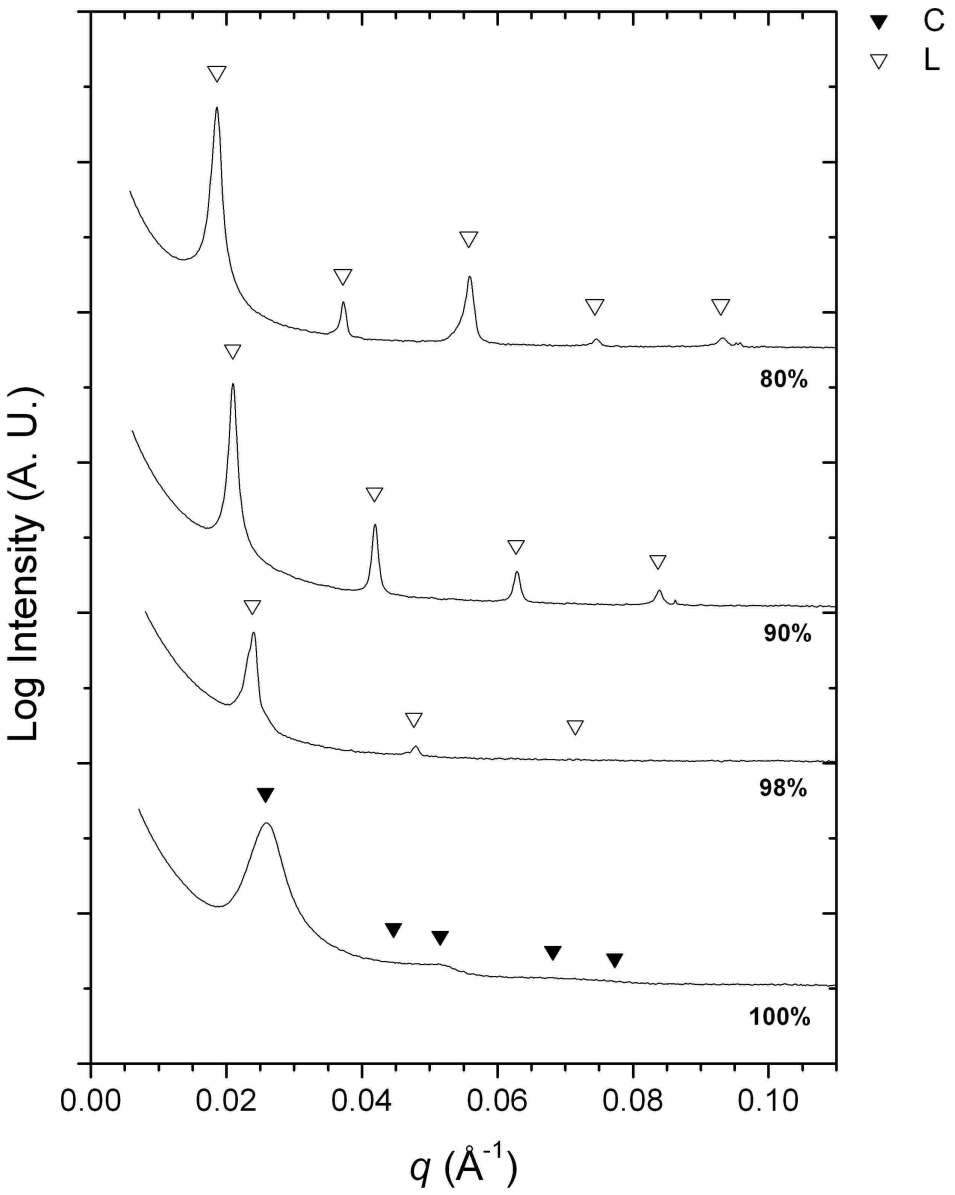

Figure 4.25: 1D scattering plots for SO(20–13)/[EMI][TFSI] solutions. Arrowheads mark allowed scattering intensity peaks for the assigned microstructures: 100 wt% (C_{EO}, √1:√3:√4:√7:√9); 98 wt%, 90 wt%, and 80 wt% (L, 1:2:3:4:5).

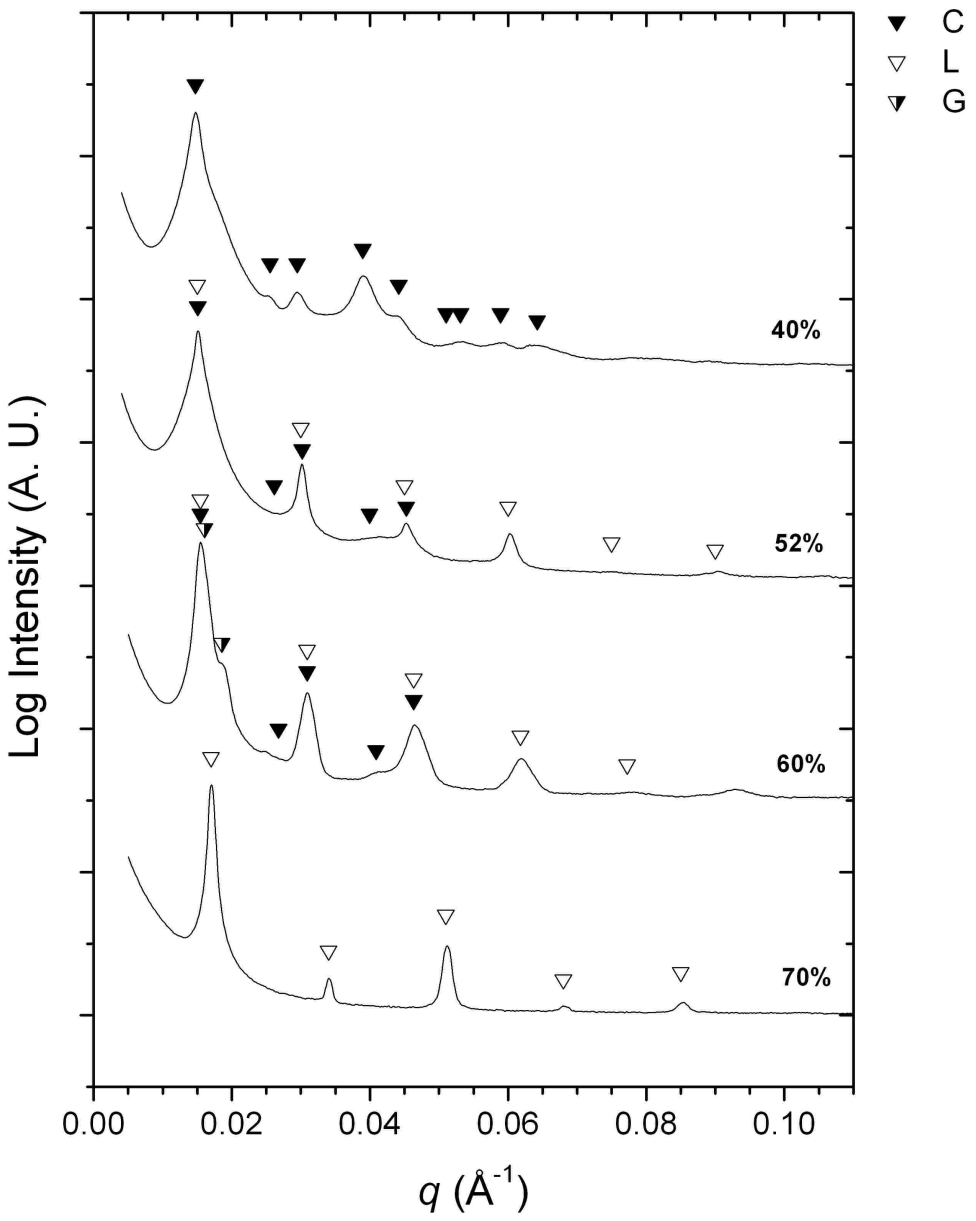

Figure 4.26: 1D scattering plots for SO(20–13)/[EMI][TFSI] solutions. Arrowheads mark allowed scattering intensity peaks for the assigned microstructures: 70 wt% (L, 1:2:3:4:5); 60 wt% (L, 1:2:3:4:5), (C_S, √1:√3:√4:√7:√9), (G, √3:√4); 52 wt% (L, 1:2:3:4:5:6) and (C_S, √1:√3:√4:√7:√9); 40 wt% (C_S, √1:√3:√4:√7:√9:√12:√13:√16:√19).

in electron density (ρ_e), which is proportional to the contrast for X-ray scattering, is relatively low for PS and PEO. At 25 °C, ρ_e is equal to 0.565 $\mathrm{mol\,e^-/cm^3}$ and 0.615 $\mathrm{mol\,e^-/cm^3}$ for PS and PEO, respectively. The addition of the selective [EMI][TFSI] solvent increases both the effective degree of segregation and the electron density difference between the microstructure domains. This is due to preferential solvation of the PEO blocks, and fairly high electron density for [EMI][TFSI] (ρ_e = 0.708 $\mathrm{mol\,e^-/cm^3}$ at 140 °C). The scattering patterns for the 90 wt% and 80 wt% solutions in Figure 4.19 represent the C_{EO} phase, which is observed for solution concentrations greater than ~80 wt%. The 77 wt% solution represents a narrow region of the phase map characterized by coexisting C_{EO} and L microstructure. The scattering pattern for this sample contains scattering peaks corresponding to both hexagonally packed cylinders and lamellae, as shown in Figure 4.19 by the filled and open arrow heads, respectively. Upon further addition of ionic liquid, the solutions are characterized by lamellar microstructure (Figure 4.20, 70 wt%, 60 wt%, 50 wt%, and 34 wt%). As copolymer concentration is further decreased, the lamellar microstructure begins to lose some long range order, as show by broadening of the higher order scattering peaks (Figure 4.20, 50 wt% and 34 wt%). Additionally, there appears to be underlying form factor scattering in the 34 wt% solution pattern, thus this sample is classified in the phase map as possessing coexisting microstructures.

SO(20–6)

Figures 4.21 and 4.22 show 1D SAXS patterns for the different microstructures observed for the SO(20–6) copolymer solutions. The bulk SO(20-6) scattering pattern in

Figure 4.21 was collected at 150 °C, and the low scattering intensity is again a result of the low degree of segregation for the bulk copolymer. Using equation 4.1, χN for the bulk SO(20-6) is ~16 at 150 °C. At room temperature χN is ~26, and the bulk SO(20-6) copolymer possess a C_{EO} microstructure. Regions of C_{EO} (Figure 4.21, 90 wt% and 83 wt%) and L (Figures 4.21 and 4.22, 70 wt%, 60 wt%, 50 wt%, and 40wt%) in the phase map are separated by a narrow region of solution concentration characterized by coexisting C_{EO} and L microstructures (Figure 4.21, 82 wt%). Further decreasing solution concentration results in the emergence of another region of coexisting C and L microstructures, where the PS blocks of the copolymer now form the cylinders of the C microstructure (Figure 4.22, 37 wt% and 34 wt%). Finally, at 30 wt% the C_S microstructure is observed.

SO(20–8)

Figures 4.23 and 4.24 show 1D SAXS patterns for the SO(20–8) solutions. The 100 wt% and 90 wt% solution SAXS patterns shown in Figure 4.23 represent the C_{EO} region observed in the phase map. As was the case for the other PS–PEO copolymer solutions, L (Figures 4.23 and 4.24, 80 wt%, 69 wt%, 60 wt%, and 49 wt%) and C_S (Figure 4.24, 40 wt% and 30 wt%) are observed for the SO(20–8) solutions upon addition of increasing amounts of ionic liquid. Additionally, solutions displaying coexisting C and L are observed at concentrations near the boundaries between the C and L regions of the phase map. In Figure 4.23, the 87 wt% scattering pattern shows C_{EO} + L, and in Figure 4.24, the 42 wt% scattering pattern shows L + C_S.

SO(20–13)

Figures 4.25 and 4.26 show 1D SAXS patterns for the SO(20–13) copolymer solutions. The bulk SO(20–13) is the only sample that displayed the C_{EO} morphology. Solutions that contained only 2 wt% ionic liquid already displayed a lyotropic transition to a lamellar microstructure. The scattering patterns shown in Figures 4.25 and 4.26 for the 98 wt%, 90 wt%, 80 wt%, and 70 wt% solutions all display lamellar microstructure. Again, a region of solutions with coexisting hexagonal cylinder and lamellar microstructure was observed between the L and C_S regions of the phase map (Figure 4.26, 60 wt% and 52 wt%). Additionally, the 60 wt% solution pattern displays a shoulder on the primary scattering peak that could be referenced to the √4 peak for the G microstructure. Finally, fairly well defined C_S microstructure was observed for the 40 wt% solution.

4.4.2 Discussion

The lyotropic microstructure phase behavior displayed in the phase map for the PS–PEO/[EMI][TFSI] solutions (Figure 4.18) is consistent with an analogous increase in f_{PEO} of the copolymers. For example, the general microstructure sequence observed for the solutions, C_{EO} to L to C_S, is representative of increasing curvature of the microstructure interface toward the insoluble PS domains, which would be the expected behavior for a simple increase in f_{PEO} of the copolymers. Additionally, the estimated phase boundaries in Figure 4.18 shift to higher solution concentration with increasing PEO volume fraction in the bulk copolymer. This is also consistent with a simple increase in f_{PEO}, since a smaller amount of added ionic liquid would be necessary to

affect a lyotropic order-order-transition as the initial PEO volume fraction in the bulk copolymer is increased. Using the trajectory approach described above for the PB–PEO solutions, starting in the region of C_{EO} on the theoretical phase diagram and moving horizontally to the C_S region, the anticipated microstructure progression would be $C_{EO}\rightarrow G_{EO}\rightarrow L\rightarrow G_S\rightarrow C_S$. Figure 4.27 shows the experimentally observed microstructures for the PS–PEO/[EMI][TFSI] solutions overlaid on the theoretical phase boundaries for an AB diblock.[15] The effective PEO volume fractions for the solutions were calculated as effective f_{PEO} = (vol_{PEO} + vol_{IL}/total solution vol), which assumes the ionic liquid completely partitions into the PEO domains of the copolymer microstructure. The densities of PS, PEO, and [EMI][TFSI] at 140 °C were used to calculate the volumes of the copolymer and ionic liquid.[26,27] As can be seen, there is good qualitative agreement between the experimentally observed microstructures and the theoretical phase regions.

In general, the gyroid microstructure is not definitively observed for any of the PS–PEO solutions investigated. Evidence for the possible coexistence of the gyroid along with lamellae and hexagonally packed cylinders is seen in the scattering pattern obtained for the 60 wt% SO(20-13)/[EMI][TFSI] solution (Figure 4.26). The shoulder on the primary scattering peak in the 60 wt% pattern could be referenced to the √4 scattering peak consistent with the gyroid, and was persistent at all temperatures investigated (250, 200, 150, and 100 °C). The solutions were annealed at 150 °C for one hour prior to preparation of the SAXS samples (see Section 4.2), and for approximately 10 minutes at each temperature before collecting SAXS patterns. Thus, the coexisting

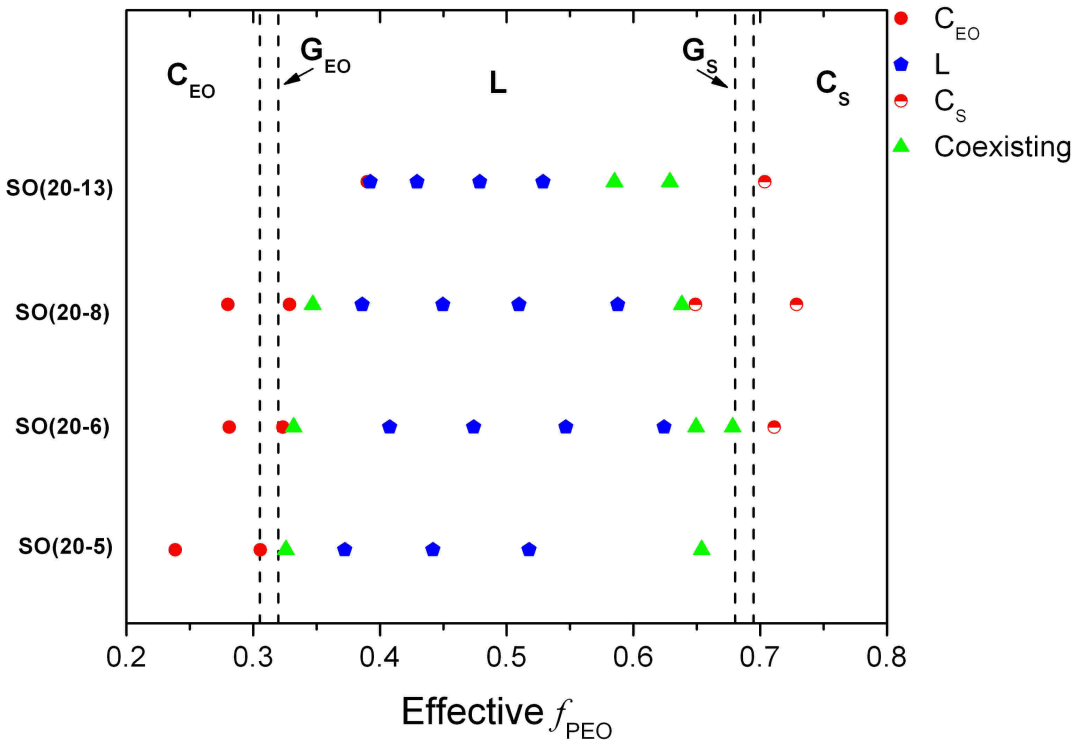

Figure 4.27: Experimentally observed microstructures for PS–PEO/[EMI][TFSI] solutions. Effective volume fractions of PEO calculated assuming the ionic liquid completely partitions into the PEO domains of the copolymer microstructure, and using densities of 1.06, 0.97, and 1.40 g/cm^3 for PEO, PS, and [EMI][TFSI] at 140 °C, respectively. Vertical lines represent theoretical phase boundaries determined by Cochran *et al.*[15] There are no units corresponding to the *y*-axis. The microstructures for the solutions are shifted vertically for clarity.

L, C, and G microstructures appear to be at least metastable. However, longer term annealing experiments are necessary before solid conclusions can be made about the thermodynamic stability of these microstructures. For the majority of the PS–PEO/[EMI][TFSI] solutions, coexisting C and L microstructures were observed for solutions in the region of the phase map where the gyroid would be expected (*i.e.*, between regions of C and L). As discussed previously with the PB–PEO/ionic liquid solutions, this behavior is attributed to destabilization of the gyroid microstructure due to an increase in chain packing frustration with increasing degree of segregation upon addition of the selective ionic liquid solvent. The solvent acts as an extra degree of microstructure assembly freedom, allowing the formation of C/L instead of G.

A measure of the degree of segregation for the PS–PEO/[EMI][TFSI] solutions can be obtained by calculating the change in the microstructure domain spacing with solution concentration. As discussed above with the PB–PEO/ionic liquid solutions, addition of a selective solvent to a block copolymer results in a drive to decrease the interfacial area in the microstructure, in order to reduce the number of unfavorable contacts between the insoluble block and the solvent. This brings about increased chain stretching normal to the interface, and thus an increase in the microstructure domain spacing. Figure 4.28 shows double logarithmic plots of the lamellar domain spacing (d_{100}) versus solution concentration, given as copolymer volume fraction (ϕ). The addition of the selective [EMI][TFSI] solvent results in an increase in domain spacing and thus negative values for the power law exponent α. The range in α values was found to be between −0.58 and −0.92 at 150 °C, and −0.58 and −0.94 at 200 °C for the

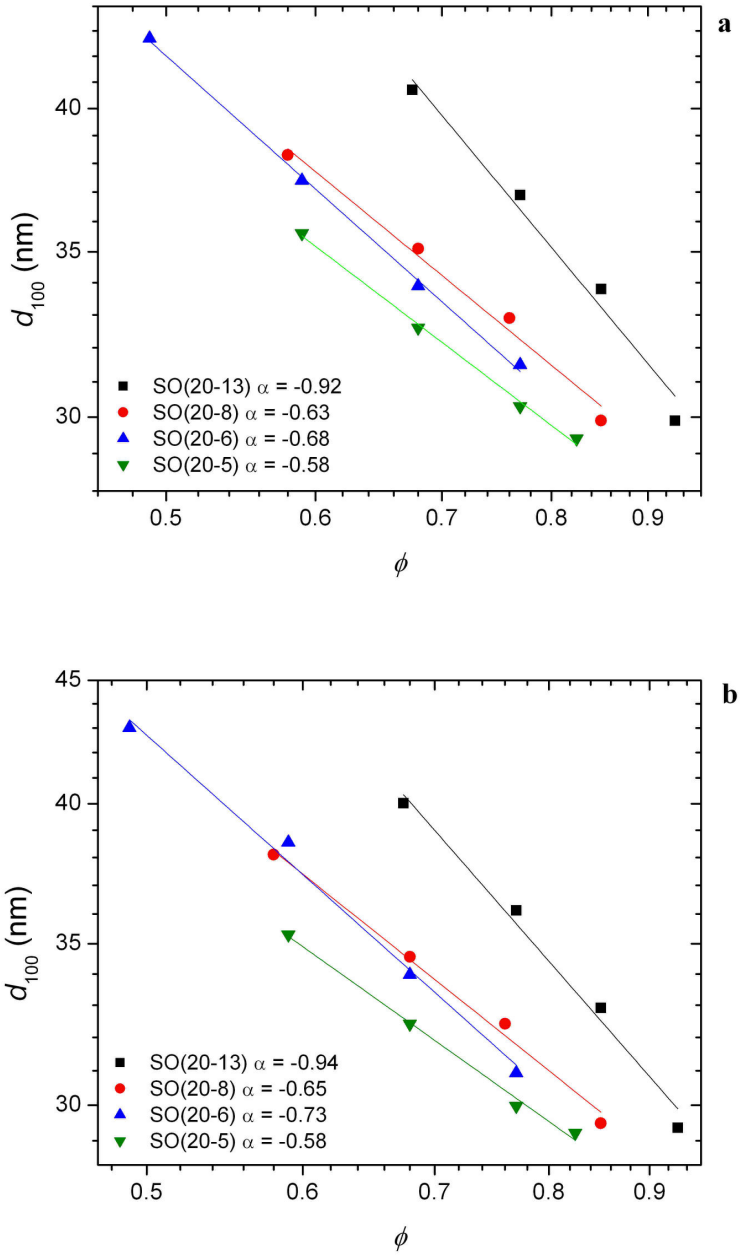

Figure 4.28: Lamellar domain spacing (d_{100}) versus polymer concentration and power law fits ($d \sim \phi^{\alpha}$). (a) 150 °C, (b) 200 °C.

PS–PEO/[EMI][TFSI] solutions. These results are comparable to the α values of −0.61 found by Hanley for PS–PI in dimethyl phthalate,[23] and −1.03 found by Lai for PS–PI in squalane.[22] As mentioned previously, the α values of −2.31 and −3.16 found by Virgili for PS–P2VP in [Im][TFSI] are much more negative than those obtained in the present study.[24] These results show that [EMI][TFSI] behaves as a strongly selective solvent for the PEO blocks of the PS–PEO copolymers. Additionally, there were no thermotropic order transitions observed for any of PS–PEO/[EMI][TFSI] solutions in the temperature range investigated (~100–200 °C), and the microstructure domain spacing for the solutions was found to be fairly independent of temperature as well. For example, Figure 4.29 shows the microstructure domain spacing for the SO(20–8)/[EMI][TFSI] solutions plotted vs. temperature. In general, there is only a slight decrease in domain spacing observed over an 80 °C increase in temperature. However, taking into account the decrease in density of the copolymer and ionic liquid with temperature, the fairly constant domain spacing observed with increasing temperature indicates an overall decrease in the degree of segregation as the temperature is increased. Similar results were observed for all other PS–PEO/[EMI][TFSI] solutions. These results suggest that the selectivity of the [EMI][TFSI] solvent decreases with temperature. This is in contrast to the results of Virgili, who reported increasing selectivity of the [Im][TFSI] ionic liquid with increasing temperature.

Another unique feature of the PS–PEO/[EMI][TFSI] solution phase behavior was the presence of coexisting lamellar microstructures possessing different domain spacing. As shown in Figures 4.30, 4.31, and 4.32, two unique sets of lamellar

scattering peaks are observed for the SO(20-8) 49 wt%, and SO(20-6) 50 wt% and 60 wt% solutions. The heating and annealing procedure employed while collecting the SAXS patterns in Figures 4.30–4.32 is as follows. The solutions were initially heated to 250 °C and annealed for 10 minutes prior to collecting the scattering pattern. The samples were then cooled and annealed for an additional 10 minutes at each subsequent temperature before collecting the scattering patterns. Thus, the total annealing time at elevated temperature (≥ 100 °C) was approximately 40–50 minutes (accounting for 1–2 minutes cooling time between temperatures). For the SO(20–8) 49 wt% solution (Figure 4.30), the lamellar microstructure with larger domain spacing (lower q) begins to yield to the phase possessing lower domain spacing as the sample is annealed. The SO(20–6) 50 wt% and 60 wt% solutions show a smaller change in the relative intensities of the peaks corresponding to the two different lamellar microstructures.

Coexisting lamellar microstructures have also been reported by Virgili, *et al.* for a PS–P2VP/[Im][TFSI] solution,[24] and by Young, *et al.* for PS–PEO copolymers doped with lithium salts.[28,29] Virgili proposed the coexisting lamellar microstructures were a result of two coexisting phases possessing unequal amounts of ionic liquid. Based on DSC experiments showing well defined crystalline melting peaks, Young was able to characterize the coexisting lamellar microstructures as arising from the crystallization of PEO–salt complexes. For Young's systems, the crystallized PEO-salt complexes corresponded to the lamellar microstructure with larger domain spacing.

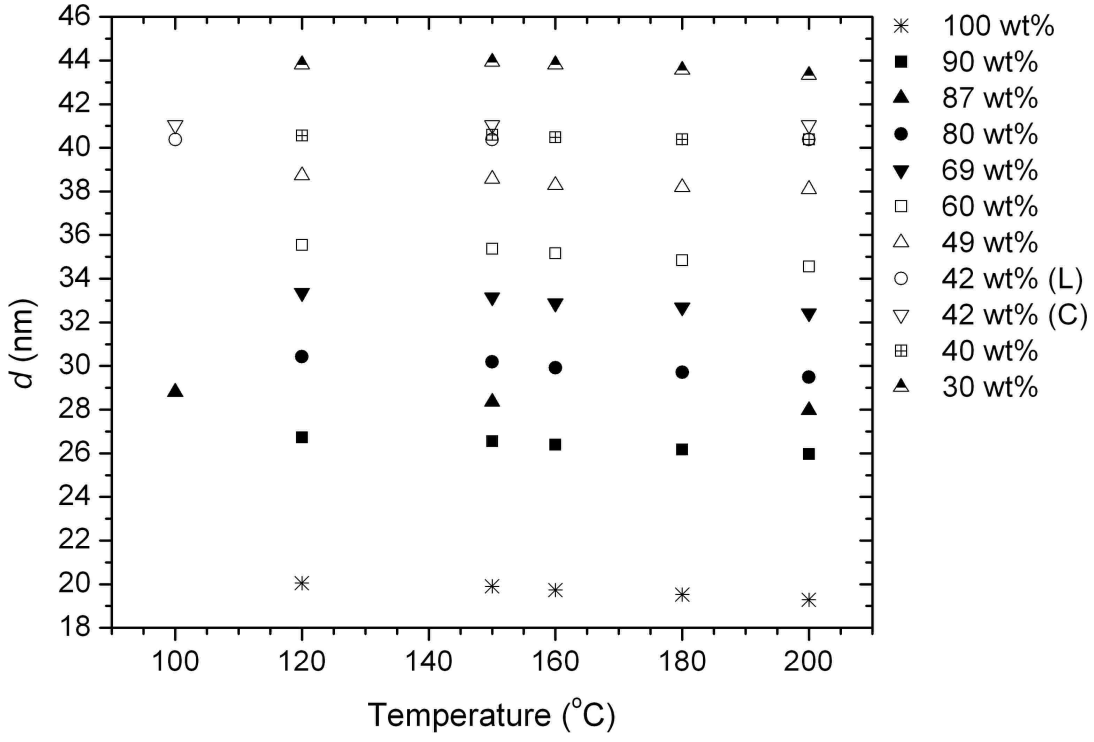

Figure 4.29: Microstructure domain spacing vs. temperature for SO(20-8)/[EMI][TFSI] solutions. d calculated as $2\pi/q^*$.

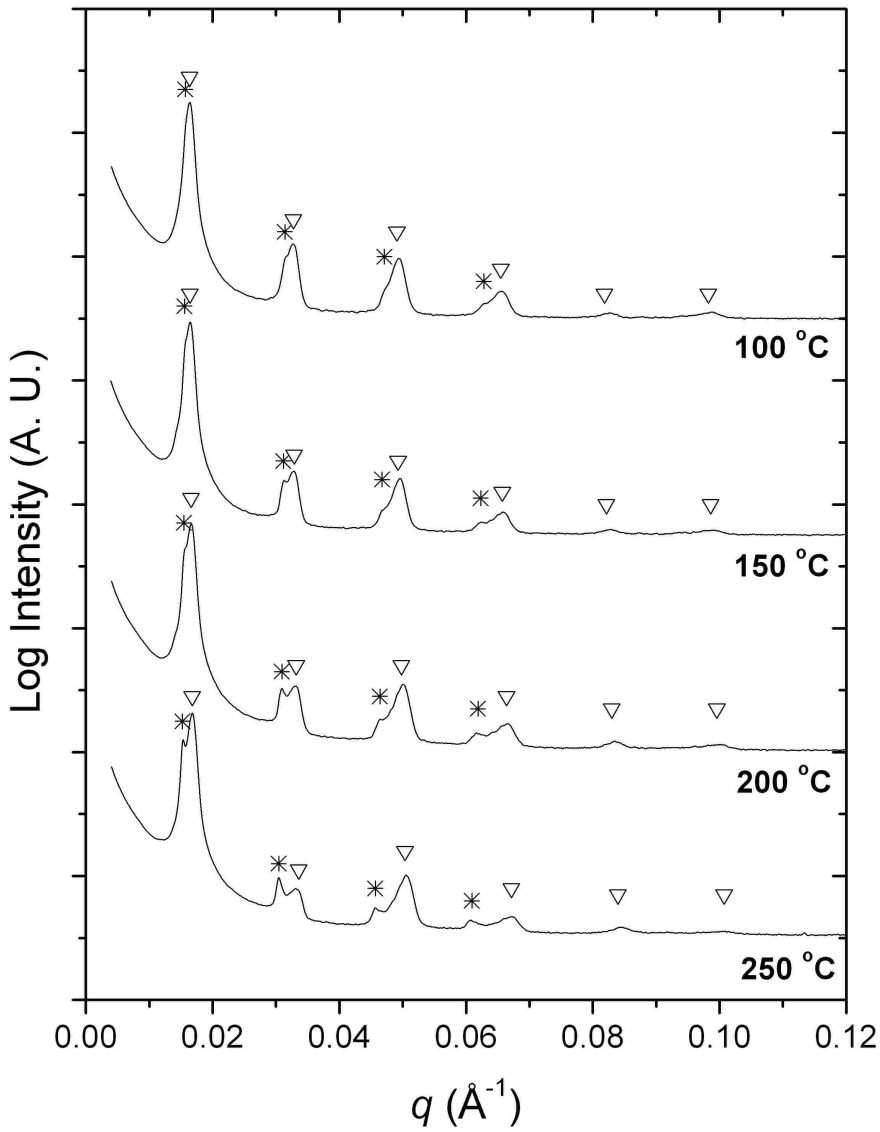

Figure 4.30: 1D SAXS patterns displaying coexisting lamellar microstructure for SO(20-8) 49 wt%/[EMI][TFSI] solution. Patterns collected upon cooling from 250 °C. Annealing time at each temperature was approximately 10 min. Arrowheads and asterisks mark expected intensity peaks for lamellar microstructure (q/q^* = 1:2:3:4...).

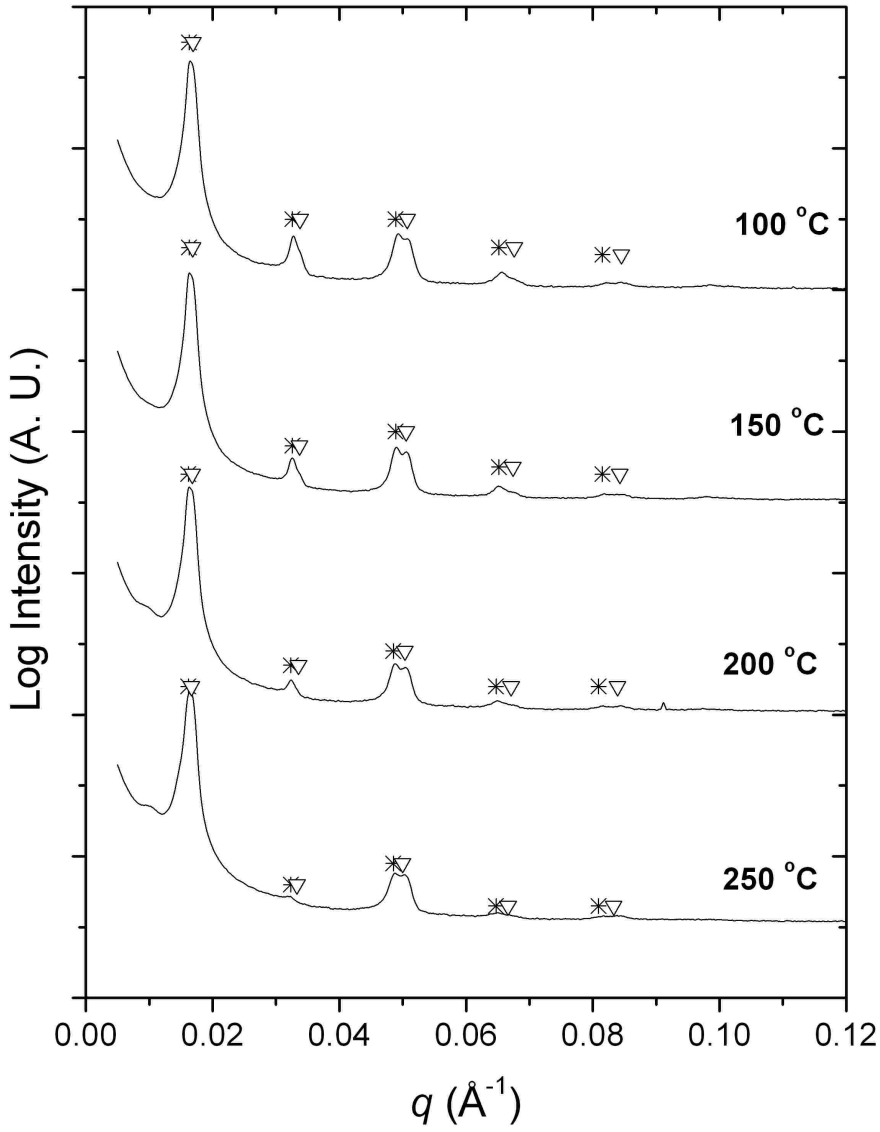

Figure 4.31: 1D SAXS patterns displaying coexisting lamellar microstructure for SO(20-6) 50 wt%/[EMI][TFSI] solution. Patterns collected upon cooling from 250 °C. Annealing time at each temperature was approximately 10 min. Arrowheads and asterisks mark expected intensity peaks for lamellar microstructure (q/q^* = 1:2:3:4...).

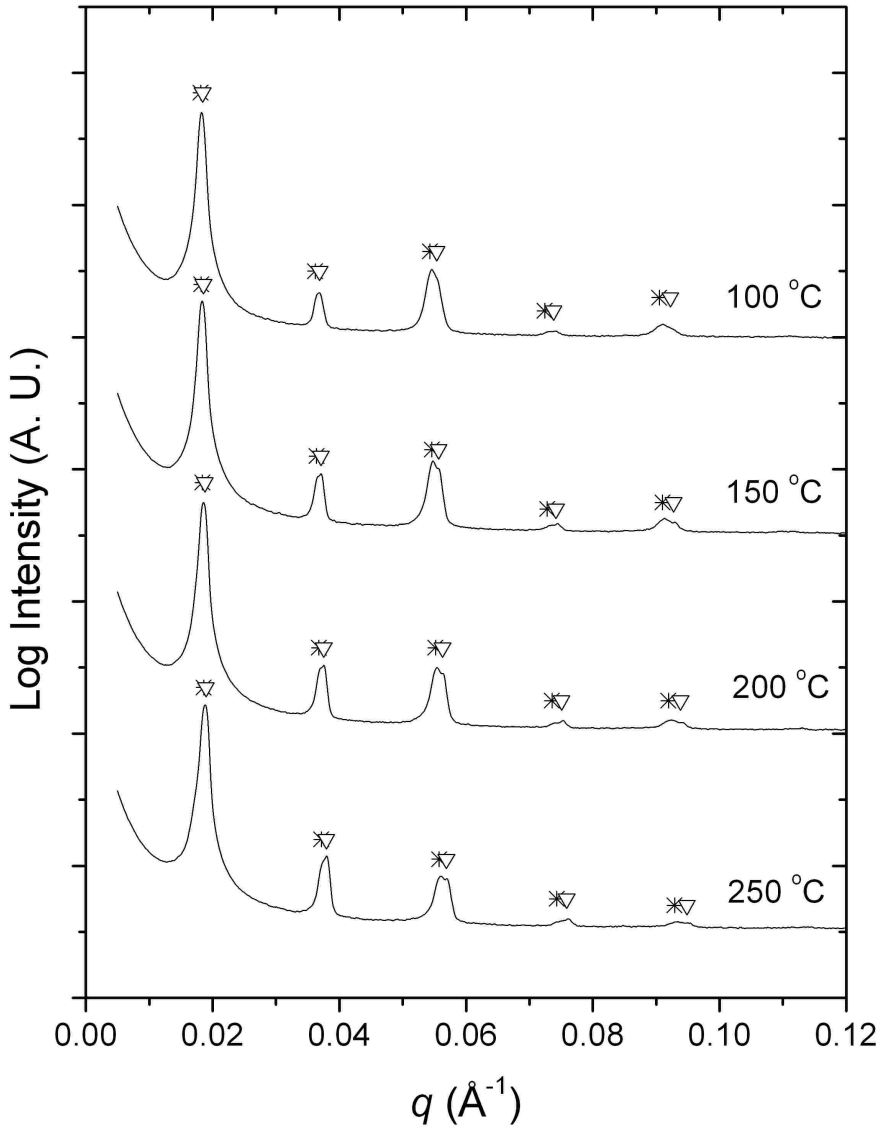

Figure 4.32: 1D SAXS patterns displaying coexisting lamellar microstructure for SO(20-6) 60 wt%/[EMI][TFSI] solution. Patterns collected upon cooling from 250 °C. Annealing time at each temperature was approximately 10 min. Arrowheads and asterisks mark expected intensity peaks for lamellar microstructure (q/q^* = 1:2:3:4...).

DSC experiments were conducted with the three PS–PEO/[EMI][TFSI] solutions that displayed coexisting lamellar microstructures. The DSC thermograms are plotted in Figure 4.33 for the SO(20–8) 49 wt% solution and the SO(20–6) 50 and 60 wt% solutions. DSC traces for the bulk SO(20–8) and SO(20–6) copolymers and for a 31 wt% solution of 9.1 kg/mol PEO homopolymer in [EMI][TFSI] are included in Figure 4.33 for comparison. For the 31 wt% PEO solution, the ion content (r), calculated as the ratio of [EMI] cations to PEO ether oxygen atoms (*i.e.* EO monomer units) in solution, is 0.25. For the SO(20–8) 49 wt% and SO(20–6) 50 wt% and 60 wt% solutions, r is equal to 0.40, 0.46, and 0.31, respectively. Thus the PEO homopolymer solution serves as a close comparison to the solvated state of the PEO blocks of the PS–PEO/[EMI][TFSI] solutions. All of the DSC thermograms in Figure 4.33 were second heating scans, where the heating and cooling rates for all scans were 10 °C/min. The DSC results in Figure 4.33 show no evidence of a crystalline melting peak for the PS–PEO/[EMI][TFSI] solutions or for the PEO homopolymer solution. Only a slight increase in the copolymer T_g is observed for the copolymer solutions, as compared to the neat copolymers. This is consistent with the results of Virgili, who also observed a slight increase in T_g for PS–P2VP/[Im][TFSI] solutions as compared to the bulk PS–P2VP. Thus, we do not observe any evidence that the formation of crystalline PEO–ionic liquid complexes is responsible for the coexisting lamellar microstructures observed via SAXS. However, the formation of crystalline PEO–ionic liquid complexes cannot be completely ruled out based on these results, due to the fact that many ionic liquids are known to undergo slow crystallization.[30] Thus, extremely slow

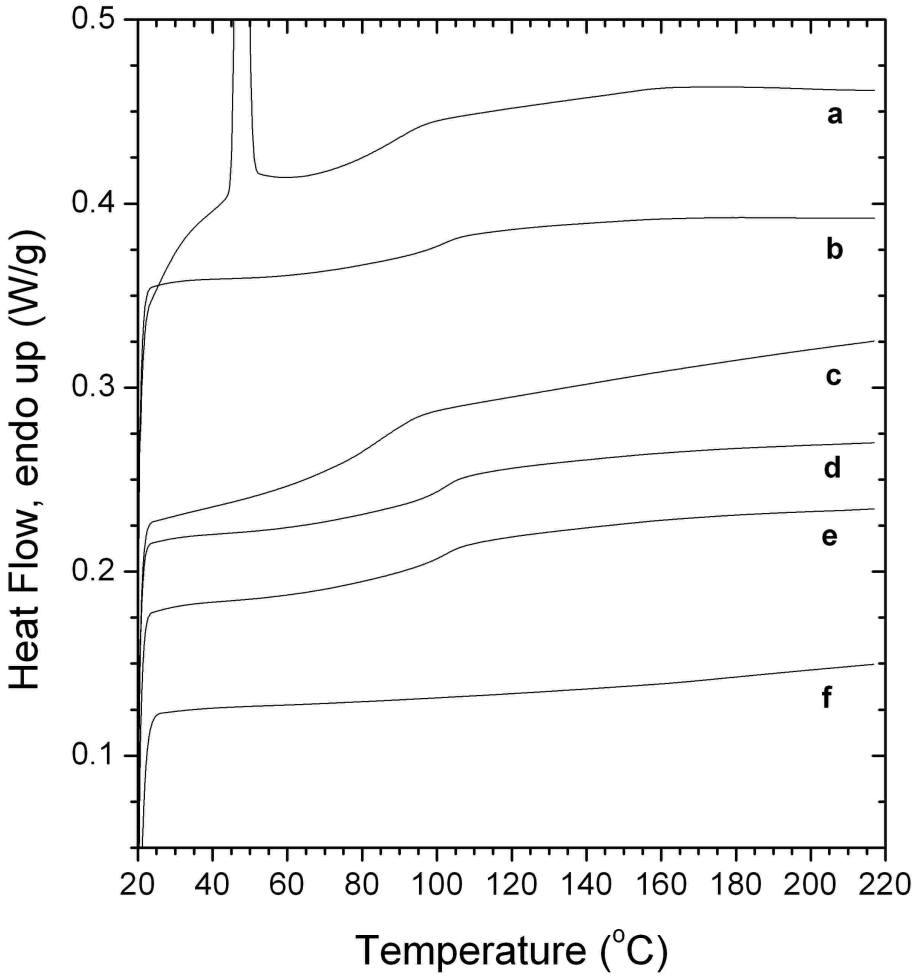

Figure 4.33: DSC thermograms, second heating scans at a heating rate of 10 °C/min. (a) SO(20–8) bulk; (b) SO(20–8) 49 wt%, r = 0.40; (c) SO(20–6) bulk; (d) SO(20–6) 60 wt%, r = 0.31; (e) SO(20–6) 50 wt%, r = 0.46; (f) 9.1 kg/mol PEO homopolymer 31 wt% r = 0.25. Ion content (r) is the ratio of [EMI] cations to EO monomers in solution.

crystallization of PEO–ionic liquid complexes may preclude the observance of crystallization and melting via DSC. It should be noted that the lamellar domain spacing for the three PS–PEO/[EMI][TFSI] solutions displaying coexisting lamellar microstructures were included in the double logarithmic plots of d_{100} vs. ϕ in Figure 4.28. For the SO(20–6) 50 wt% and 60 wt% solutions the difference in the domain spacing for the coexisting lamellar microstructures is small (≤ 1.0 nm). Thus, using either the higher or lower domain spacing value did not change the α value obtained from the power law fits for the SO(20–6) solutions. However, the difference in domain spacing for the coexisting lamellar microstructures in the SO(20–8) 49 wt% solution is ~ 3 nm at 200 °C and ~2 nm at 150 °C. Using the smaller lamellar domain spacing for the SO(20–8) 49 wt% solution results in a power law exponential α value equal to −0.63 and −0.65 at 150 °C and 200 °C, respectively. Using the larger lamellar domain spacing for the SO(20– 8) 49 wt% solution results in a power law exponential α value equal to −0.77 and −0.83 at 150 °C and 200 °C, respectively. In the SAXS patterns collected for the SO(20–8) 49 wt% solution (Figure 4.30), the scattering peaks corresponding to the lamellar microstructure with lower domain spacing become dominant with annealing. Thus, the lower lamellar domain spacing was used in the plots of d_{100} vs. ϕ for the SO(20–8) and SO(20–6) solutions shown in Figure 4.28.

4.5 Summary

The concentrated solution phase behavior has been characterized for PB–PEO copolymers in [BMI][PF_6] and [EMI][TFSI] via SAXS. A general microstructure progression from S_{EO}^{bcc} to C_{EO} to L to C_B was observed for the copolymers in both ionic

liquids, which is consistent with the expected behavior for an analogous increase in f_{PEO} of the bulk copolymers. An increase in the lamellar domain spacing of the microstructured solutions with addition of the ionic liquid solvent was also observed. The values for the exponential term of the power law fits of the log-log plots of d_{100} vs. ϕ for the PB–PEO/ionic liquid solutions were consistent with those reported for other block copolymers in selective solvents. Thus it was concluded that the ionic liquids behave as strongly selective solvents for the PEO blocks of the copolymers. Additionally, large regions of coexisting C and L microstructures exist in the phase maps for the PB–PEO/ionic liquid solutions. This has been attributed to destabilization of the gyroid microstructure with increasing degree of segregation upon addition of the selective ionic liquid solvents. Several of the PB–PEO/ionic liquid solutions also displayed SAXS patterns reminiscent of those obtained for the random cylindrical network microstructure observed by Jain, *et al.* for aqueous PB–PEO solutions.[8,9]

The phase behavior of PS–PEO/[EMI][TFSI] solutions was also characterized via SAXS, and found to be analogous to a simple increase in f_{PEO} of the bulk copolymers upon addition of ionic liquid. The increase in lamellar domain spacing with addition of ionic liquid was also found to be consistent with the behavior reported for other solutions of block copolymers in selective solvents. Additionally, the microstructure domain spacing of the PS–PEO/ionic liquid solutions was found to be independent of temperature, indicating that the selectivity of the [EMI][TFSI] solvent decreases with temperature. Finally, coexisting lamellar microstructures with different domain spacing were observed in several of the PS–PEO/[EMI][TFSI] solutions. DSC experiments did

not show evidence of the formation of crystalline PEO-ionic liquid structures. However, they could not be completely ruled out as a cause for the coexisting lamellar microstructures due to potentially very slow crystallization of such complexes.

4.6 References

1. Hamley, I. W. *The Physics of Block Copolymers*; Oxford University Press: Oxford, 1998.

2. Lodge, T. P.; Hanley, K. J.; Pudil, B.; Alahapperuma, V. *Macromolecules* **2003**, *36*, 816–822.

3. Lodge, T. P.; Pudil, B.; Hanley, K. J. *Macromolecules* **2002**, *35*, 4707–4717.

4. Lai, C.; Russel, W. B.; Register, R. A. *Macromolecules* **2002**, *35*, 841–849.

5. Sadron, C.; Gallot, B. *Makromol. Chem.* **1973**, *164*, 301–332.

6. Hajduk, D. A.; Kossuth, M. B.; Hillmyer, M. A.; Bates, F. S. *J. Phys. Chem. B* **1998**, *102*, 4269–4276.

7. Shibayama, M.; Hashimoto, T.; Kawai, H. *Macromolecules* **1983**, *16*, 16–28.

8. Jain, S.; Gong, X.; Scriven, L. E.; Bates, F. S. *Phys. Rev. Lett.* **2006**, *96*, 138304.

9. Jain, S.; Dyrdahl, M. H. E.; Gong, X.; Scriven, L. E.; Bates, F. S. *Macromolecules* **2008**, *41*, 3305–3316.

10. Wanka, G.; Hoffmann, H.; Ulbricht, W. *Macromolecules* **1994**, *27*, 4145–4159.

11. Messé, L.; Corvazier, L.; Young, R. N.; Ryan, A. J. *Langmuir* **2002**, *18*, 2564–2570.

12. Hamley, I. W.; Mai, S.-M.; Ryan, A. J.; Fairclough, J. P.; Booth, C. *Phys. Chem. Chem. Phys.* **2001**, *3*, 2972–2980.

13. Hanley, K. J.; Lodge, T. P. *J. Polym. Sci., Part B: Polym. Phys.* **1998**, *36*, 3101–3113.

14. Hanley, K. J.; Lodge, T. P.; Huang, C.-I. *Macromolecules* **2000**, *33*, 5918–5931.

15. Cochran, E. W.; Garcia-Cervera, C. J.; Fredrickson, G. H. *Macromolecules* **2006**, *39*, 2449–2451.

16. Jain, S. Aqueous Mixtures of Block Copolymer Surfactants. Ph.D. Thesis, University of Minnesota, 2005.

17. Matsen, M. W.; Bates, F. S. *Macromolecules* **1996**, *29*, 7641–7644.

18. Förster, S.; Berton, B.; Hentze, H.-P.; Krämer, E.; Antonietti, M.; Linder, P. *Macromolecules* **2001**, *34*, 4610–4623.

19. Davidock, D. A.; Hillmyer, M. A.; Lodge, T. P. *Macromolecules* **2003**, *36*, 4682–4685.

20. Jain, S.; Bates, F. S. *Science (Washington, DC, United States)* **2003**, *300*, 460–464

21. Hashimoto, T.; Shibayama, M.; Kawai, H. *Macromolecules* **1983**, *16*, 1093–1101.

22. Lai, C.; Russel, W. B.; Register, R. A. *Macromolecules* **2002**, *35*,4044–4049.

23. Hanley, K. J. Block Copolymers: Phase Behavior in Neutral and Selective Solvents. Ph.D. Thesis, University of Minnesota, 2001.

24. Virgili, J. M.; Hexemer, A.; Pople, J. A.; Balsara, N. P.; Segalman, R. A. *Macromolecules* **2009**, *42*, 4604–4613.

25. Cochran, E. W.; Morse, D. C.; Bates, F. S. *Macromolecules* **2003**, *36*, 782–792.

26. Fetters, L. J.; Lohse, D. J.; Richter, D.; Witten, T. A.; Zirkel, A. *Macromolecules* **1994**, *27*, 4639–4647.

27. Jacquemin, J.; Husson, P.; Mayer, V.; Cibulka, I. *J. Chem. Eng. Data* **2007**, *52*, 2204–2211.

28. Young, W.-S.; Brigandi, P. J.; Epps, T. H. *Macromolecules* **2008**, *41*, 6276–6279.

29. Young, W.-S.; Epps, T. H. *Macromolecules* **2009**, *42*, 2672–2678.

30. Wasserscheid, P.; Welton, T., Eds. *Ionic Liquids in Synthesis*, 2nd ed.; Wiley-VCH: Weinheim, 2008.

Chapter 5

Ionic Conductivity of Concentrated Polymer Solutions

5.1 Introduction

The high level of current research interest in ionic liquids is due to their many appealing properties, including negligible volatility, high thermal and electrochemical stability, and good ionic conductivity, which make them excellent candidates as electrolyte materials.[1–3] Indeed, ionic liquids have been explored as electrolytes in various devices such as lithium ion batteries,[4–10] fuel cells,[11–18] and dye-sensitized solar cells.[19] However, in many cases a solid electrolyte material would be more robust and versatile, and thus there is interest in imparting solid structure to ionic liquids, while still maintaining their good conductivity. One route to a solid structure has been to blend ionic liquids with polymers to form so-called "ion gel electrolytes". Polymeric materials employed include homopolymers,[20–23] typically poly(ethylene oxide) and poly(methacrylates), and copolymers,[24–27] typically poly(vinylidene fluoride-*co*-hexafluoropropylene). Additionally, chemically[28–33] and physically[34–36] cross-linked

polymer networks have been swollen with ionic liquids to form ion gels. Moreover, there have been multiple strategies reported for "gelling" ionic liquids.[37–40] It may also be beneficial if the material used to provide solid structure to the ionic liquid on the macro-scale also possesses an ordered structure on the nano-scale. This has recently been demonstrated by the groups of Ohno and Kato, who utilized liquid crystalline materials that display hexagonal columnar and bicontinuous cubic structures.[41–43] Similarly, block copolymers could also be used to provide nano-scale structure if the ionic liquid selectively partitions into one domain of the copolymer microstructure.

This chapter describes experiments aimed at measuring the ionic conductivity of the concentrated PS–PEO/[EMI][TFSI] solutions described in Chapter 4. It was shown that [EMI][TFSI] behaves as a strongly selective solvent for the PEO blocks of the PS–PEO copolymers. Thus, the majority of the ionic liquid is confined to the nanostructure formed by the self-assembled PEO domains. These concentrated block copolymer solutions therefore represent a simple system for preparing nanostructured electrolyte materials.

5.2 Experimental

The PS–PEO copolymers are the same as those used in Chapter 4, and their molecular characteristics are listed in Table 2.1. PEO homopolymer was ordered from Sigma, and used without further purification. The molecular weight of the PEO homopolymer was determined via SEC calibrated with PS standards. Universal calibration using the Mark–Houwink parameters for PS and PEO in chloroform gave a molecular weight of 9.1 kg/mol for the homopolymer.

[EMI][TFSI] was synthesized as described in Chapter 2. Prior to use, the ionic liquid was dried under vacuum (ca. 10 mTorr) at 60-70 °C for 2-3 days to remove absorbed moisture and then stored either in a glove box under argon or in a vacuum-sealed desiccator.

The general procedure for preparing the concentrated polymer/ionic liquid solutions is described in Chapter 2. Briefly, all the solutions used in the conductivity experiments described in this chapter were prepared with the use of a cosolvent (dichloromethane). After dissolution of the polymer and ionic liquid, the cosolvent was evaporated under a dry N_2 purge, followed by drying under vacuum with heating (ca. 60 °C). Prior to conductivity measurements, the concentrated solutions were annealed at 150 °C for 1 hour. In this chapter the concentrations of the polymer/ionic liquid solutions are given as weight percent copolymer, and as ion content (r). The ion content for a solution is calculated as the molar ratio of [EMI] cations to PEO ether oxygen atoms (*i.e.*, EO monomer units).

The ionic conductivity was measured via impedance spectroscopy, using a Solartron 1255B frequency response analyzer connected to a Solartron SI 1287 electrochemical interface. The solutions were hot-pressed at 150 °C into a teflon ring, which held the samples at a constant diameter (7 mm) and thickness (2 mm). The sample disks were sandwiched between two stainless steel blocking electrodes. The applied voltage amplitude was 10 mV and the frequency was typically scanned from 10^6–1 Hz. The sample temperature was controlled by clamping the electrode assembly inside a copper heating block, which was heated and cooled by a circulating

water/ethylene glycol bath. The samples were initially heated to 100 °C and measurements were taken upon cooling the samples. At each temperature, samples were thermally equilibrated for at least 30 minutes prior to collecting the impedance data. The conductivity of the solutions was calculated from the complex impedance ($Z = Z' + iZ''$). The high frequency plateau in the real impedance (Z') values, where the magnitude of the complex impedance ($|Z|$) is equal to Z', was taken as the bulk resistance (R) of the sample, and the conductivity was calculated as

$$\sigma = \frac{l}{RA} \tag{5.1}$$

where l is the sample thickness and A is the sample cross-sectional area. The conductivity cell constant (l/A) was calibrated using a 3.5 mM aqueous KCl solution standard (Fluka Analytical) with an ionic conductivity of 0.5 mS/cm at 25 °C.

5.3 Results and Discussion

Figure 5.1 shows representative Z', Z'', and $|Z|$ data for a 58 wt% PS–PEO/[EMI][TFSI] solution. The plateau value, where Z'' tends toward zero and $|Z| = Z'$, was taken as the bulk resistance of the samples, and used to calculate ionic conductivity, σ, via Equation 5.1. Ionic conductivity versus temperature for the PS–PEO/[EMI][TFSI] solutions is shown in Figures 5.2–5.4. Additionally, the ionic conductivity for several homopolymer PEO/[EMI][TFSI] solutions is shown in Figure 5.5. The ionic conductivity of the neat [EMI][TFSI] is also shown in Figures 5.2–5.5, and is found to agree well (within ~ 10% at all temperatures) with reported values.[30]

The estimated error in all the ionic conductivity values presented is ±10%, based on experimental reproducibility.

In general, there is good qualitative agreement between the temperature dependence of ionic conductivity for the concentrated block copolymer solutions and for the pure ionic liquid. Here we note that conductivity values are not reported for SO(20–5)/[EMI][TFSI] due to general difficulty in preparing samples for impedance measurements using the hot-pressing method described in the previous section. Samples prepared using the three other PS–PEO copolymers uniformly filled the teflon spacer ring with no visible cracks or bubbles. For the SO(20–5) solutions many samples were prepared and almost all possessed visible cracks and other sample inhomogeneities after hot-pressing, which is potentially due to the higher content of the brittle PS block in the SO(20–5) copolymer.

As expected, the PS–PEO/[EMI][TFSI] solutions display substantially lower conductivity than the neat ionic liquid. However, the solutions still display fairly good ionic conductivity, particularly for the samples with higher ionic liquid content, and at elevated temperature. In general, the PS–PEO/[EMI][TFSI] solution conductivity values ranged from 10^{-8} – 10^{-3} S/cm over the temperature range of 25–100 °C. Additionally, PS–PEO/[EMI][TFSI] solutions display lower ionic conductivity than the PEO/[EMI][TFSI] solutions with the same ion content (r). This is expected due to the randomly oriented copolymer microstructure domains that limit the direct ionic conduction through the material.

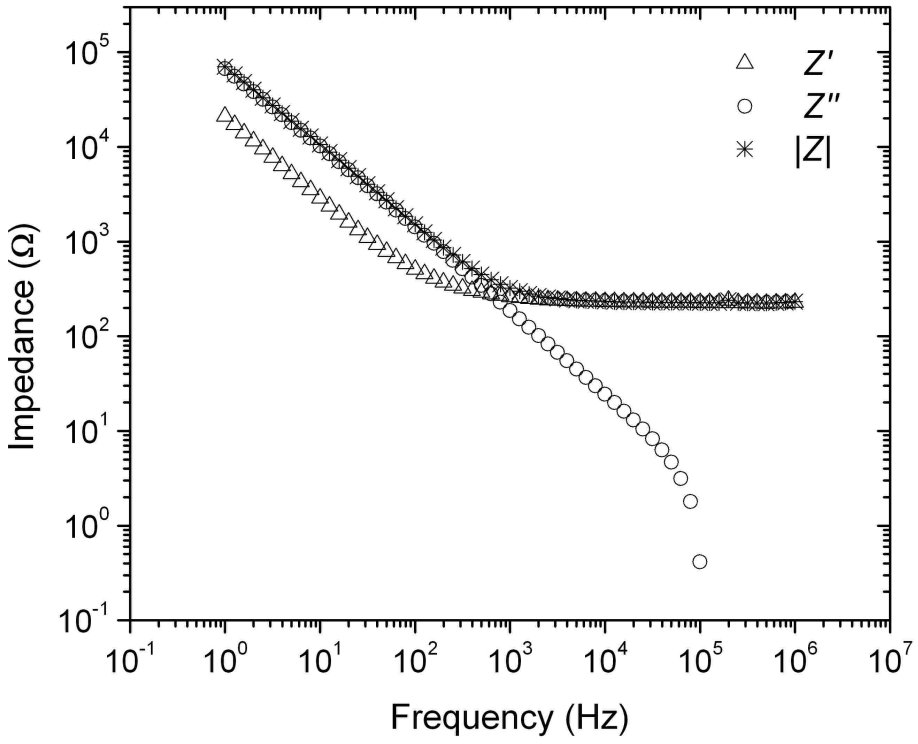

Figure 5.1: Impedance data for a 58 wt% SO(20–13)/[EMI][TFSI] solution. Temperature is 100 °C and the applied voltage amplitude is 10 mV.

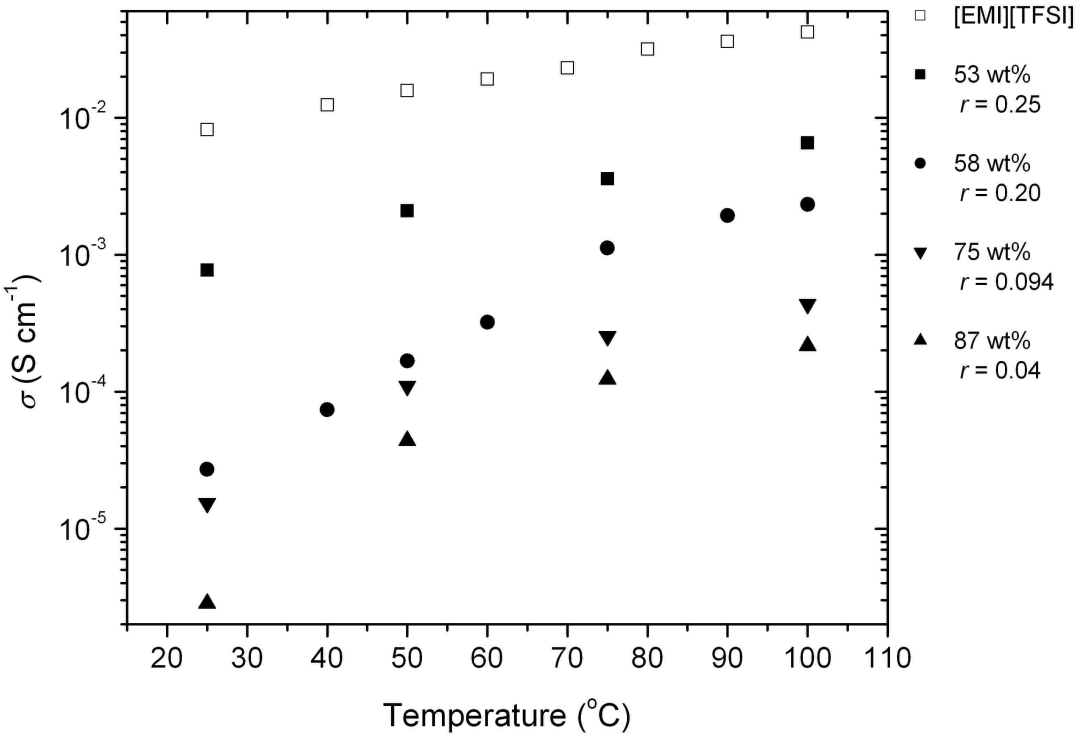

Figure 5.2: Temperature dependence of the ionic conductivity for SO(20–13)/[EMI][TFSI] solutions.

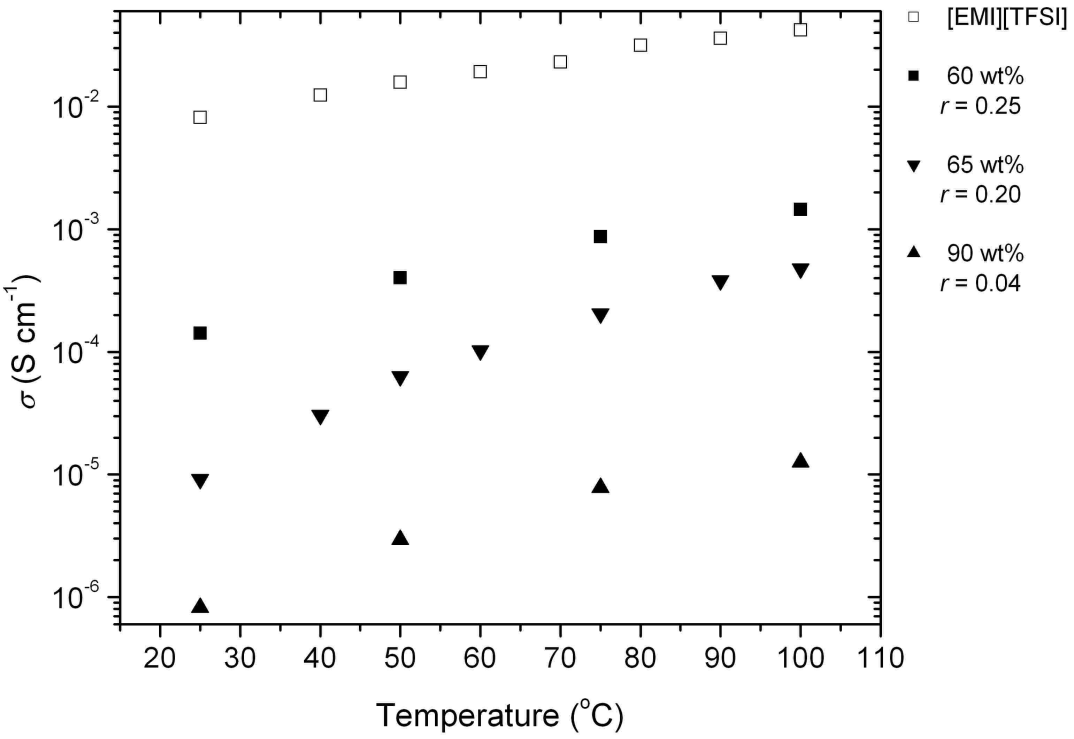

Figure 5.3: Temperature dependence of the ionic conductivity for SO(20–8)/[EMI][TFSI] solutions.

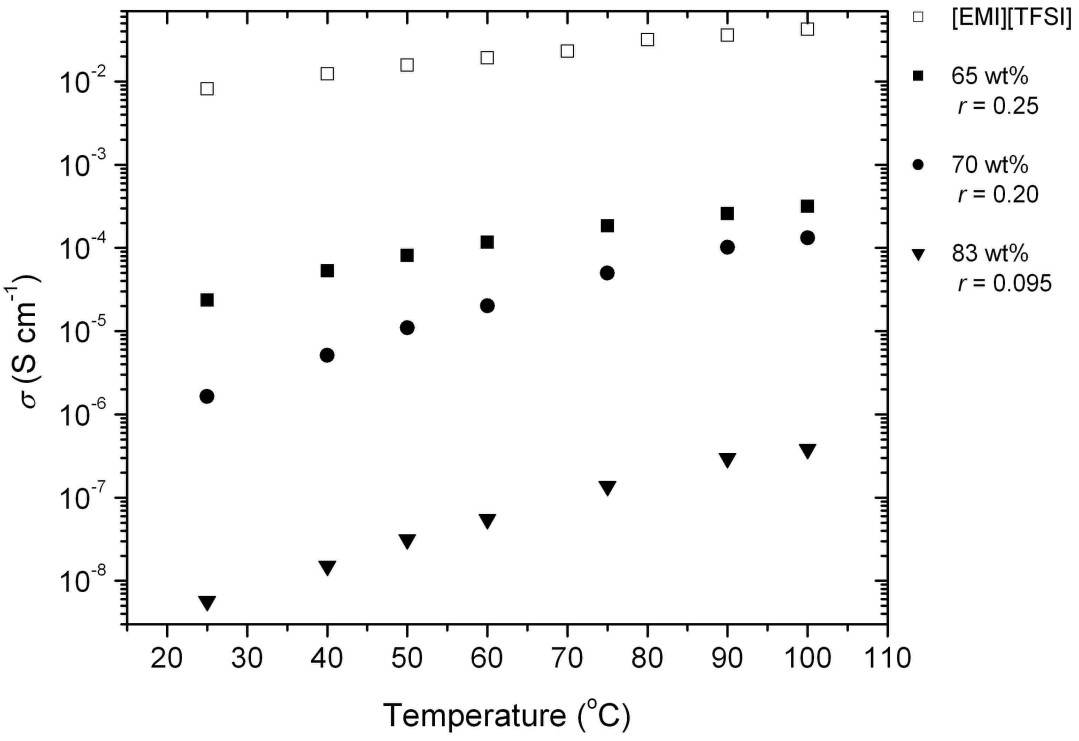

Figure 5.4: Temperature dependence of the ionic conductivity for SO(20–6)/[EMI][TFSI] solutions.

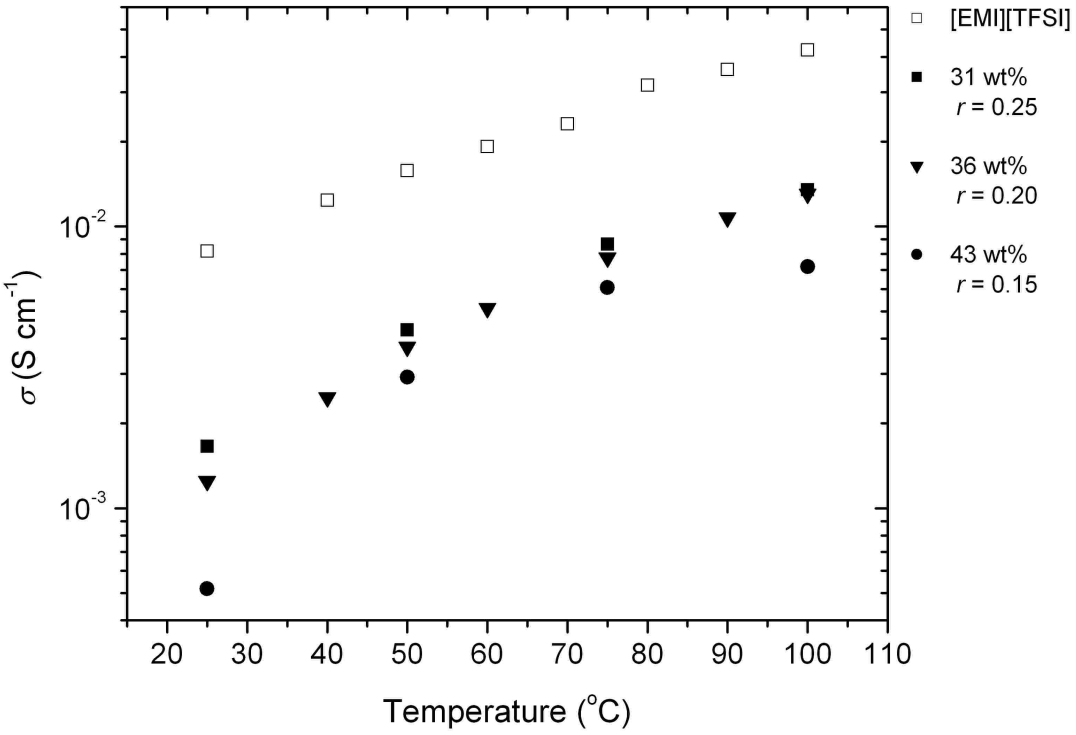

Figure 5.5: Temperature dependence of the ionic conductivity for 9 kg/mol homopolymer PEO/[EMI][TFSI] solutions.

Simple geometric arguments predict for materials with randomly oriented lamellar domains that the ultimate conductivity for the sample is 2/3 of the maximum conductivity for the conducting phase,[44] which is calculated as

$$\sigma_{max} = \phi_{CP}\sigma_{CP} \tag{5.2}$$

where ϕ_{CP} is the volume fraction of the conducting phase (PEO plus ionic liquid) and σ_{CP} is the conductivity of the conducting phase, taken as the measured conductivity of the PEO/[EMI][TFSI] solution. Figure 5.6 shows the normalized ionic conductivity (σ/σ_{max}) at 100 °C vs. molecular weight of the PEO blocks (M_{PEO}) for PS–PEO/[EMI][TFSI] solutions with ion content equal to 0.20 and 0.25. As the molecular weight of the copolymer PEO blocks increases, it can be seen that the normalized conductivity approaches the predicted limit of 2/3. Here it is noted that the SO(20–13)/[EMI][TFSI] solutions with ion content equal to 0.20 and 0.25 fall in a region of the PS–PEO/[EMI][TFSI] solution microstructure phase map (see Section 4.4) characterized by coexisting lamellae and hexagonally packed cylinders. In the hexagonally packed cylinder microstructure the PS blocks form the cylindrical domains, while the majority, matrix domain is formed by the PEO blocks plus the ionic liquid. Thus, the hexagonal cylinder microstructure should display higher ionic conductivity, which is not limited to the predicted 2/3 maximum for the lamellar microstructure. It is likely that the presence of a coexisting hexagonal cylinder phase results in the normalized conductivity above the 2/3 limit for the SO(20–13)/[EMI][TFSI] sample with r equal to 0.25.

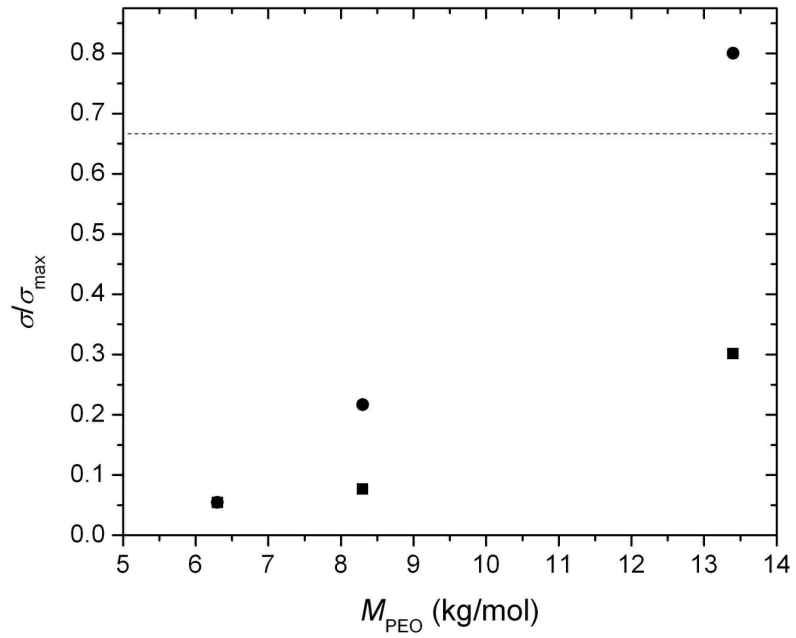

Figure 5.6: Normalized ionic conductivity (σ/σ_{max}) at 100 °C vs. molecular weight of the copolymer PEO block. σ is the measured conductivity of the PS–PEO/[EMI][TFSI] solutions with r = 0.20 (■) and r = 0.25 (●). σ_{max} is calculated from Equation 5.2.

Additionally, we note that a portion of the increase in normalized conductivity for SO(20–13)/[EMI][TFSI] solution with r equal to 0.20 may also be attributed to the presence of a hexagonal cylinder phase coexisting with lamellae. These results can be compared with those of Singh, *et al.* and Panday, *et al.* who have reported on the ionic conductivity of PS–PEO diblocks doped with [Li][TFSI].[45,46] The closest comparison to our SO(20–13) copolymer is an SO(16–16) diblock with r equal to 0.02 and 0.085, where the reported σ/σ_{max} ratio is approximately 0.1–0.15 for both ion content values. However, these researchers showed normalized conductivity values approaching the lamellar 2/3 limit as M_{PEO} increased, with the limit ultimately being reached for copolymers with M_{PEO} > 60 kg/mol. Thus, we expect similar behavior in our PS–PEO/[EMI][TFSI] solutions, where increasing M_{PEO} of the diblocks could lead to higher ionic conductivity and σ/σ_{max} values approaching 2/3 for samples possessing lamellar microstructure.

Figures 5.7a and b show ionic conductivity of the PS–PEO solutions vs. M_{PEO} at r = 0.20 and 0.25, respectively. As can be seen in the figures, the ionic conductivity of the PS–PEO/[EMI][TFSI] solutions increases with increasing M_{PEO}. The studies of Singh and Panday discussed previously also report increasing ionic conductivity with M_{PEO} for PS–PEO diblocks doped with [Li][TFSI]. These authors have attributed the increase in conductivity to an increase in ionic dissociation at the center of the conductive PEO domains. This is reasoned to be a result of a gradient in the dielectric constant of the PEO domains, with the value increasing towards the center of the domains.

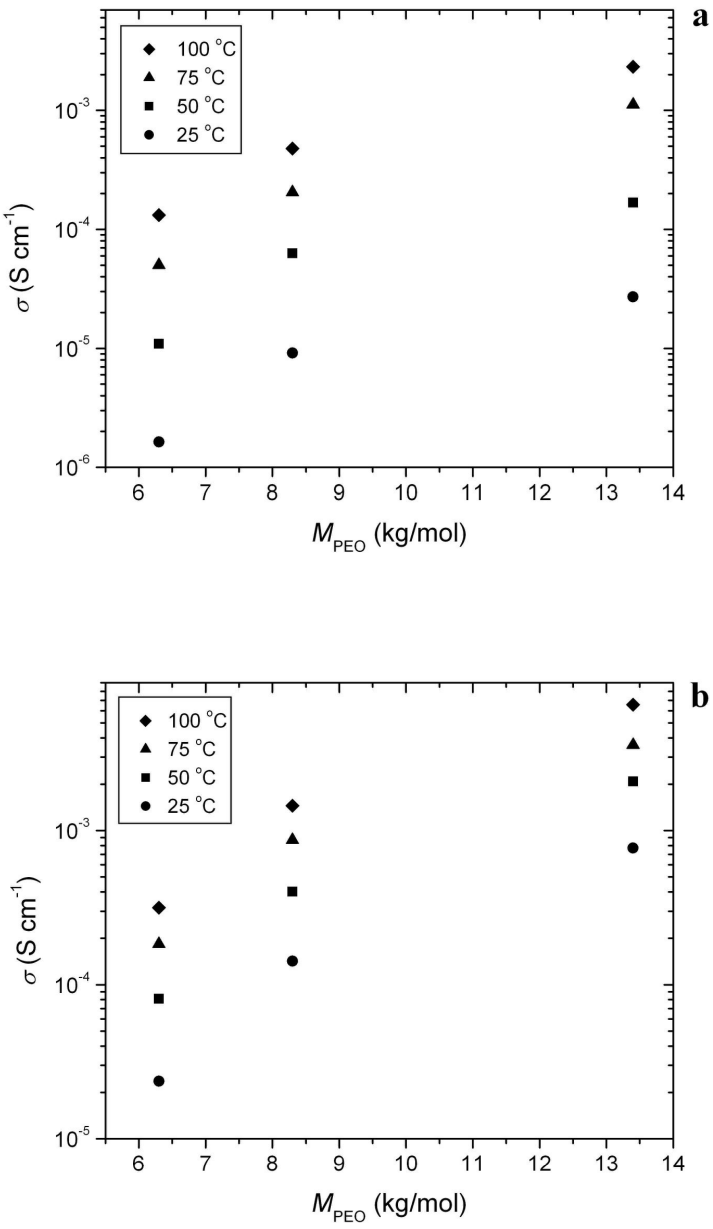

Figure 5.7: Ionic conductivity vs. molecular weight of the copolymer PEO block, a) r = 0.20; b) r = 0.25.

The increase in dielectric constant stems from an increase in chain conformational freedom with increasing distance from the domain interface, where the PEO chains have a more highly stretched conformation. Indeed, Gomez, *et al.* have observed localization of ions at the center of the PEO domains using energy-filtered transmission electron microscopy.[47] It is conceivable that similar effects result in the increase in conductivity with M_{PEO} observed in our PS–PEO/[EMI][TFSI] solutions.

Figures 5.8a–d show σ vs. r for PEO homopolymer, SO(20–13), SO(20–8), and SO(20–6) solutions, respectively. The ionic conductivity for the PEO homopolymer and the PS–PEO copolymers was observed to increase with ion content over all the concentrations measured. In comparison, PEO doped with atomic ions (*e.g.* Li^+ salts) shows a maximum in ionic conductivity with increasing r. This result has been observed in both PEO homopolymers[48,49] and copolymers containing PEO blocks.[45] Initially, at low values of r, increasing ion content leads to higher conductivity due to an increase in the number of charge carriers. However, at higher values of r, a decrease in conductivity is observed due to ion pairing and transient cross-linking of the PEO chains due to strong coordination with the cations. Conversely, the large size, asymmetry, and charge delocalization of the ionic liquid ions potentially leads to weaker ion–dipole interactions with the PEO chains. In other words, the same characteristics that lead to low ionic liquid melting points, allows for increasing ionic conductivity with r. This is supported by recently reported molecular dynamics simulations of electrolytes based on PEO and ionic liquids, where the researchers found decreased interaction strength between PEO and the large ions of ionic liquids,

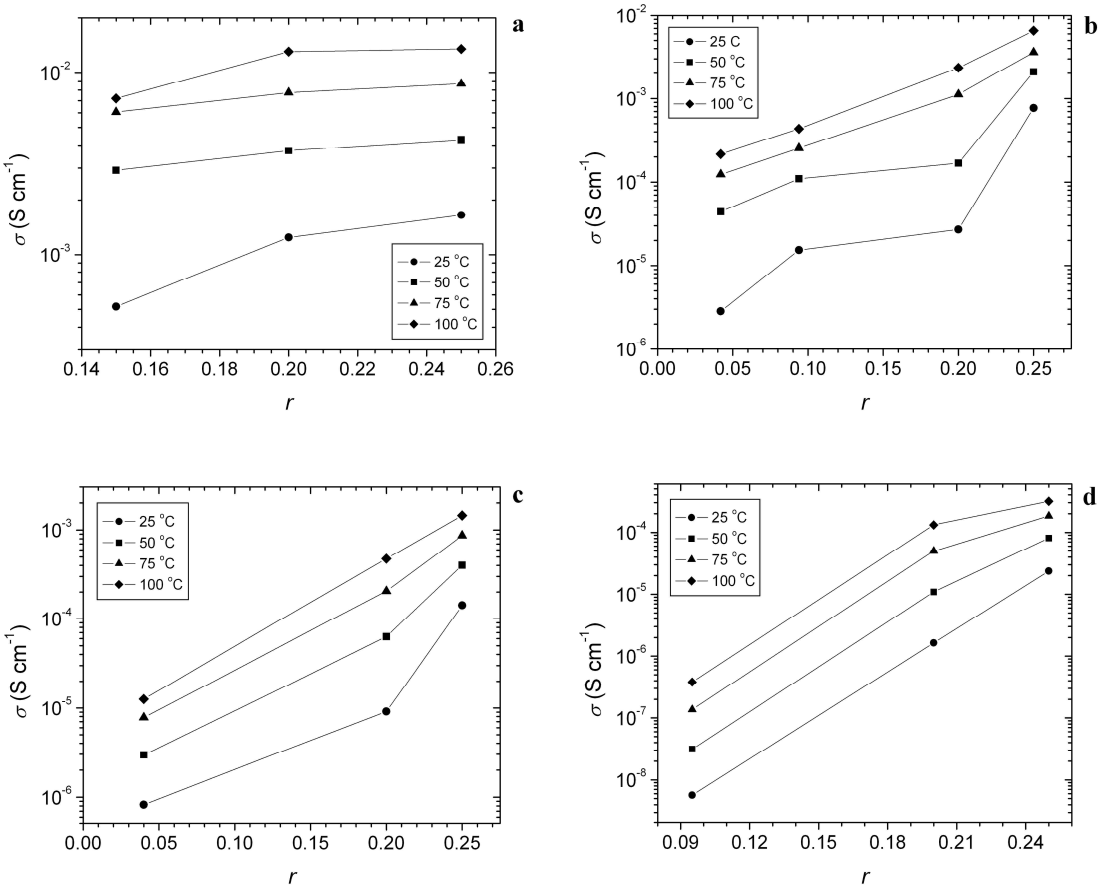

Figure 5.8: Ionic conductivity vs. *r*. a) 9 kg/mol PEO homopolymer; b) SO(20–13); c) SO(20–8); d) SO(20–6).

as compared to Li^+.[50,51] These studies involved the ionic liquids 1,3–dimethylimidazolium hexafluorophosphate [MIM][PF_6] and 1–butyl–3–methylimidazolium hexafluorophosphate [BMI][PF_6]. While these ionic liquids differ from that used in the current study, we believe parallels can safely be drawn since the nature of the interactions depends mostly on the cations and the PEO chains. Thus, we anticipate [EMI] to behave similarly to [MMI] and [BMI].

5.4 Summary

The ionic conductivity of multiple concentrated PS–PEO/[EMI][TFSI] solutions was measured via impedance spectroscopy, and the most conductive samples displayed ionic conductivities in the range of 10^{-3} S/cm at 100 °C. Additionally, the samples showed further promise due to their increasing ionic conductivity with both ion concentration and M_{PEO}. One drawback for these materials is a limit in their ultimate conductivity due to the randomly oriented microstructure domains inherent in the bulk samples. Thus future avenues for research will involve attempts to anisotropically align the electrolyte microstructure in order to improve the ultimate ionic conductivity attainable for these materials.

5.5 References

1. Ohno, H., Ed. *Electrochemical Aspects of Ionic Liquids*; John Wiley & Sons: Hoboken, 2005.

2. Galiński, M.; Lewandowski, A.; Stepniak, I. *Electrochim. Acta* **2006**, *51*, 5567–5580.

3. Fernicola, A.; Scrosati, B.; Ohno, H. *Ionics* **2006**, *12*, 95–102.

4. Seki, S.; Ohno, Y.; Miyashiro, H.; Kobayashi, Y.; Usami, A.; Mita, Y.; Terada, N.; Hayamizu, K.; Tsuzuki, S.; Watanabe, M. *J. Electrochem. Soc.* **2008**, *155*, A421–A427.

5. Seki, S.; Ohno, Y.; Kobayashi, Y.; Miyashiro, H.; Usami, A.; Mita, Y.; Tokuda, H.; Watanabe, M.; Hayamizu, K.; Tsuzuki, S.; Hattori, M.; Terada, N. *J. Electrochem. Soc.* **2007**, *154*, A173–A177.

6. Hayashi, K.; Nemoto, Y.; Akuto, K.; Sakurai, Y. *J. Power Sources* **2005**, *146*, 689–692.

7. Garcia, B.; Lavallée, S.; Perron, G.; Michot, C.; Armand, M. *Electrochim. Acta* **2004**, *49*, 4583–4588.

8. Sakaebe, H.; Matsumoto, H.; Tatsumi, K. *J. Power Sources* **2005**, *146*, 693–697.

9. Ishikawa, M.; Sugimoto, T.; Kikuta, M.; Ishiko, E.; Kono, M. *J. Power Sources* **2006**, *162*, 658–662.

10. Matsumoto, H.; Sakaebe, H.; Tatsumi, K.; Kikuta, M.; Ishiko, E.; Kono, M. *J. Power Sources* **2006**, *160*, 1308–1313.

11. Angell, C. A.; Byrne, N.; Belieres, J.-P. *Acc. Chem. Res.* **2007**, *40*, 1228–1236.

12. Xu, W.; Angell, C. A. *Science* **2003**, *302*, 422–425.

13. Nakamoto, H.; Watanabe, M. *Chem. Commun.* **2007**, 2539–2541.

14. Nakamoto, H.; Noda, A.; Hayamizu, K.; Hayashi, S.; Hamaguchi, H.; Watanabe, M. *J. Phys. Chem. C* **2007**, *111*, 1541–1548.

15. Matsuoka, H.; Nakamoto, H.; Susan, M. A. B. H.; Watanabe, M. *Electrochim. Acta* **2005**, *50*, 4015–4021.

16. Noda, A.; Susan, M. A. B. H.; Kudo, K.; Mitsushima, S.; Hayamizu, K.; Watanabe, M. *J. Phys. Chem. B* **2003**, *107*, 4024–4033.

17. Susan, M. A. B. H.; Noda, A.; Mitsushima, S.; Watanabe, M. *Chem. Commun.* **2003**, 938–939.

18. Ogihara, W.; Kosukegawa, H.; Ohno, H. *Chem. Commun.* **2006**, 3637–3639.

19. Gorlov, M.; Kloo, L. *Dalton Trans.* **2008**, 2655–2666.

20. Lewandowski, A.; Świderska, A. *Solid State Ionics* **2004**, *169*, 21–24.

21. Shin, J.-H.; Henderson, W. A.; Tizzani, C.; Passerini, S.; Jeong, S.-S.; Kim, K.-W. *J. Electrochem. Soc.* **2006**, *153*, A1649–A1654.

22. Zhu, C.; Cheng, H.; Yang, Y. *J. Electrochem. Soc.* **2008**, *155*, A569–A575.

23. Kim, Y. H.; Cheruvally, G.; Choi, J. W.; Ahn, J. H.; Kim, K. W.; Ahn, H. J.; Choi, D. S.; Song, C. E. *Macromol. Symp.* **2007**, *249–250*, 183–189.

24. Sutto, T. E.; *J. Electrochem. Soc.* **2007**, *154*, P101–P107.

25. Fuller, J.; Breda, A. C.; Carlin, R. T. *J. Electrochem. Soc.* **1997**, *144*, L67–L70.

26. Yeon, S.-H.; Kim, K.-S.; Choi, S.; Cha, J.-H.; Lee, H. *J. Phys. Chem. B* **2005**, *109*, 17928–17935.

27. Singh, B.; Sekhon, S. S. *Chem. Phys. Lett.* **2005**, *414*, 34–39.

28. Klingshirn, M. A.; Spear, S. K.; Subramanian, R.; Holbrey, J. D.; Huddleston, J. G.; Rogers, R. D. *Chem. Mater.* **2004**, *16*, 3091–3097.

29. Noda, A.; Watanabe, M. *Electrochim. Acta* **2000**, *45*, 1265–1270.

30. Susan, M. A. B. H.; Kaneko, T.; Noda, A.; Watanabe, M. *J. Am. Chem. Soc.* **2005**, *127*, 4976–4983.

31. Rupp, B.; Schmuck, M.; Balducci, A.; Winter, M.; Kern, W. *Eur. Polym. J.* **2008**, *44*, 2986–2990.

32. Tigelaar, D. M.; Meador, M. A. B.; Bennett, W. R. *Macromolecules* **2007**, *40*, 4159–4164.

33. Tiyapiboonchaiya, C.; MacFarlane, D. R.; Sun, J.; Forsyth, M. *Macromol. Chem. Phys.* **2002**, *203*, 1906–1911.

34. He, Y.; Boswell, P. G.; Bühlmann, P.; Lodge, T. P. *J. Phys. Chem. B* **2007**, *111*, 4645–4652.

35. He, Y.; Lodge, T. P. *Chem. Commun.* **2007**, 2732–2734.

36. He, Y.; Lodge, T. P. *Macromolecules* **2008**, *41*, 167–174.

37. Shimano, S.; Zhou, H.; Honma, I. *Chem. Mater.* **2007**, *19*, 5216–5221.

38. Ueno, K.; Hata, K.; Katakabe, T.; Kondoh, M.; Watanabe, M. *J. Phys. Chem. B* **2008**, *112*, 9013–9019.

39. Hanabusa, K.; Fukui, H.; Suzuki, M.; Shirai, H. *Langmuir* **2005**, *21*, 10383–10390.

40. Kawauchi, T.; Kumaki, J.; Okoshi, K.; Yashima, E. *Macromolecules* **2005**, *38*, 9155–9160.

41. Yoshio, M.; Kagata, T.; Hoshino, K.; Mukai, T.; Ohno, H.; Kata, T. *J. Am. Chem. Soc.* **2006**, *128*, 5570–5577.

42. Ichikawa, T.; Yoshio, M.; Hamasaki, A.; Mukai, T.; Ohno, H.; Kato, T. *J. Am. Chem. Soc.* **2007**, *129*, 10662–10663.

43. Shimura, H.; Yoshio, M.; Hoshino, K.; Mukai, T.; Ohno, H.; Kato, T. *J. Am. Chem. Soc.* **2008**, *130*, 1759–1765.

44. Sax, J.; Ottino, J. M. *Polym. Eng. Sci.* **1983**, *23*, 165–176.

45. Singh, M.; Odusanya, O.; Wilmes, G. M.; Eitouni, H. B.; Gomez, E. D.; Patel, A. J.; Chen, V. L.; Park, M. J.; Fragouli, P.; Iatrou, H.; Hadjichristidis, N.; Cookson, D.; Balsara, N. P. *Macromolecules* **2007**, *40*, 4578–4585.

46. Panday, A.; Mullin, S.; Gomez, E. D.; Wanakule, N.; Chen, V. L.; Hexemer, A.; Pople, J.; Balsara, N. P. *Macromolecules* **2009**, *42*, 4632–4637.

47. Gomez, E. D.; Panday, A.; Feng, E. H.; Chen, V.; Stone, G. M.; Minor, A. M.; Kisielowski, C.; Downing, K. H.; Borodin, O.; Smith, G. D.; Balsara, N. P. *Nano Lett.* **2009**, *9*, 1212–1216.

48. Robitaille, C. D.; Fauteux, D. J. *J. Electrochem. Soc.* **1986**, *133*, 315–325.

49. Lascaud, S.; Perrier, M.; Vallée A.; Besner, S.; Prud'homme, J.; Armand, M. *Macromolecules* **1994**, *27*, 7469–7477.

50. Costa, L. T.; Ribeiro, M. C. C. *J. Chem. Phys.* **2006**, *124*, 184902.

51. Costa, L. T.; Ribeiro, M. C. C. *J. Chem. Phys.* **2007**, *127*, 164901.

Chapter 6

Microstructure Alignment in Thin Films of Concentrated Block Copolymer Solutions

6.1 Introduction

As discussed in Chapter 5, one limitation to the ionic conductivity of concentrated block copolymer/ionic liquid solutions is the isotropic orientation of microstructure grains. Thus, one way to potentially achieve increased conductivity in the concentrated block copolymer solutions is to align the microstructure parallel to the desired conductivity direction. This idea has been demonstrated by Yoshio, *et al.* who measured the anisotropic conductivity of polymerizable liquid crystalline molecules that possessed an ionic liquid moiety.[1] In the report by Yoshio, alignment of the self-assembled electrolyte microstructure was achieved by mechanical shearing. Mechanical shearing and related techniques, such as extrusion, have also been demonstrated as successful ways to achieve anisotropic alignment of self-assembled block copolymer microstructures.[2,3]

Additionally, alignment has been demonstrated in block copolymer thin films, where film thicknesses are typically less than several hundred nanometers. Alignment in block copolymer in thin films has been achieved via techniques such as solvent vapor annealing,[4–8] thermal annealing,[9,10] and annealing under an electric field.[11–14] With these techniques, alignment of the block copolymer microstructure perpendicular to the thin film surface can be achieved.

If a potential application for concentrated block copolymer/ionic liquid solutions is their use as electrolyte membranes for devices such as fuel cells or lithium batteries, then the desired orientation of the copolymer microstructure would be perpendicular to the film surface. This is illustrated in Figure 6.1, where the device electrodes are in contact with the electrolyte film surfaces, and the perpendicularly aligned conducting domains of the block copolymer microstructure result in direct paths of ion conduction between the electrodes.

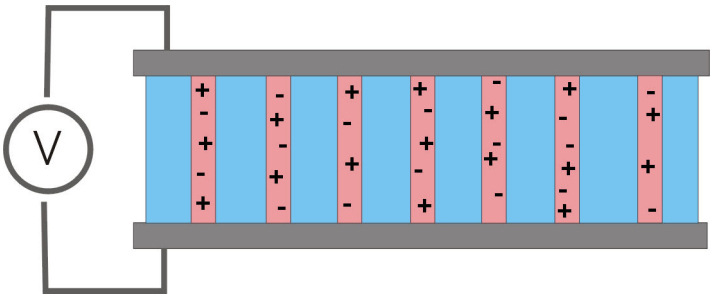

Figure 6.1: Schematic illustration of an electrolyte membrane consisting of a concentrated block copolymer/ionic liquid solution with microdomain alignment perpendicular to the film surface.

This chapter describes experiments aimed at studying the microstructure alignment in thin films of concentrated solutions of PS–PEO diblock copolymers in the ionic liquid [EMI][TFSI]. Thermal annealing is the main method presented in this chapter for modulating the microstructure of the block copolymer solution thin films. Preliminary experiments aimed at aligning the thin film copolymer microstructure via solvent vapor annealing were also conducted; however, limited results from these experiments have been obtained. Nevertheless, the experimental procedure for solvent vapor annealing will be presented, and potential future experiments and improvements will be discussed.

The microstructure of the PS–PEO/[EMI][TFSI] solutions in the bulk state was characterized via SAXS and presented in Chapter 4, and the ionic conductivity of the solutions was investigated via impedance spectroscopy and reported in Chapter 5.

6.2 Experimental

The PS–PEO copolymers used in the experiments described in this chapter are the same as those used in Chapters 4 and 5. Their synthesis and molecular characteristics are described in Section 2.2 and Table 2.1. The ionic liquid [EMI][TFSI] was synthesized as described in Section 2.3. The PS–PEO/[EMI][TFSI] solution thin films were prepared via spin coating on silicon wafers, as described in Section 2.9. The thicknesses for all the films discussed in this chapter are between 100–120 nm, as measured via variable angle spectroscopic ellipsometry.

Thermal annealing of the block copolymer thin films was performed simply by heating at 110 °C in a vacuum oven (ca. 10 mTorr). At the end of the desired annealing

time the block copolymer films were quickly cooled by removing them from the oven while still hot, and placing them on a thick piece of aluminum that had been stored in a freezer.

A fairly rudimentary set-up was employed for the solvent vapor annealing experiments. The copolymer thin films were simply placed under an inverted beaker along with a beaker filled with solvent. The beakers and the copolymer films were enclosed inside of a sealed plastic chamber that was slowly purged with a continuous flow of dry N_2. After the desired length of annealing time, the solvent beaker was removed and the copolymer films were kept under the inverted beaker, inside the sealed chamber with a slow N_2 purge for 24 hours. Subsequently, the films were dried under vacuum (ca. 10 mtorr) at room temperature for an additional 24 hours. After both thermal and solvent vapor annealing, the block copolymer thin films were stored in a vacuum-sealed desiccator.

The microstructure alignment of the block copolymer/ionic liquid thin films was characterized by imaging the surfaces of the films via scanning probe microscopy (SPM) (Section 2.10). All SPM experiments were performed in dynamic force (tapping) mode on a Veeco (DI) Nanoscope III multimode SPM, using tapping mode cantilevers with a force constant of 42 N/m, resonance frequency of 285 kHz and monolithic silicon probe tips (Arrow NCR, Nano World).

6.3 Results

Alignment of the copolymer microstructure of an SO(20–6)/[EMI][TFSI] solution with concentration of 92 wt% was investigated over varying lengths of thermal

annealing time. Based on the microstructure phase behavior for the bulk PS–PEO/[EMI][TFSI] solutions, presented in Chapter 4, the 92 wt% SO(20–6)/[EMI][TFSI] solution is expected to adopt a hexagonally packed cylinder microstructure, in which the cylindrical domains are composed of the PEO blocks and the ionic liquid. Additionally, thin films of the neat SO(20–6) copolymer were prepared and annealed as a comparison to the microstructure of the SO(20–6) 92 wt% solution films. Figures 6.2a and b show SPM phase contrast images of the as–spun films of the SO(20–6) 92 wt% solution and the neat SO(20–6) copolymer, respectively. The films in Figure 6.2 have not been subjected to any thermal annealing. In the SPM phase contrast images the film domains composed of the PS blocks of the copolymer appear lighter than the PEO/ionic liquid domains. As discussed in Section 2.10, this is due to the greater degree of energy dissipation involved in the probe tip–sample interactions encountered in the rubbery PEO/ionic liquid domains, as compared to the glassy PS domains of the microstructured copolymer film surface. As shown by the images in Figure 6.2, both films possess poorly ordered microstructure, at least at the film surface.

Figures 6.3a and b show images of the SO(20–6) 92 wt% solution, and neat SO(20–6) films after thermal annealing for two hours. As can be seen in Figure 6.3a, good alignment of the cylindrical microstructure perpendicular to the film surface is achieved in the 92 wt% solution film. The neat SO(20–6) film shown in Figure 6.3b is much more ordered than the as-spun film; however, it does not possess the same uniform perpendicular microstructure alignment as the 92 wt% solution film. The neat

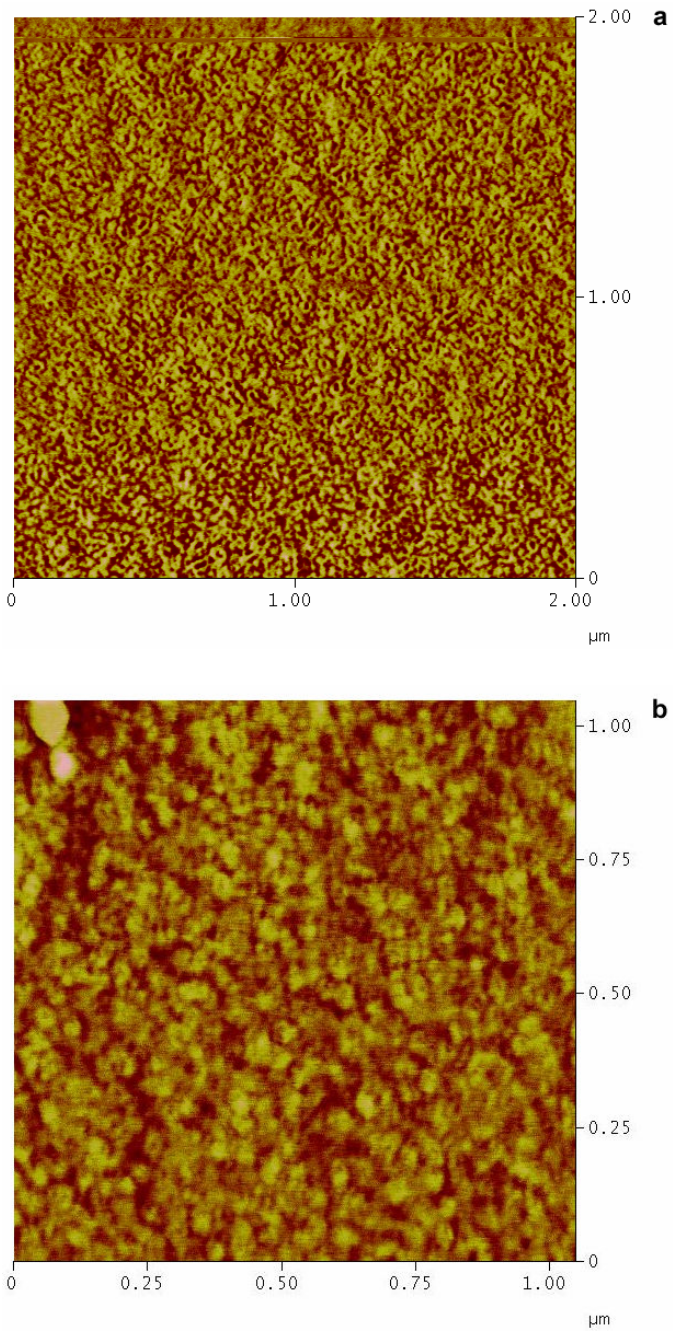

Figure 6.2: SPM images (phase contrast) of PS–PEO thin film surfaces with no thermal annealing. a) SO(20–6)/[EMI][TFSI] 92 wt%; b) neat SO(20–6).

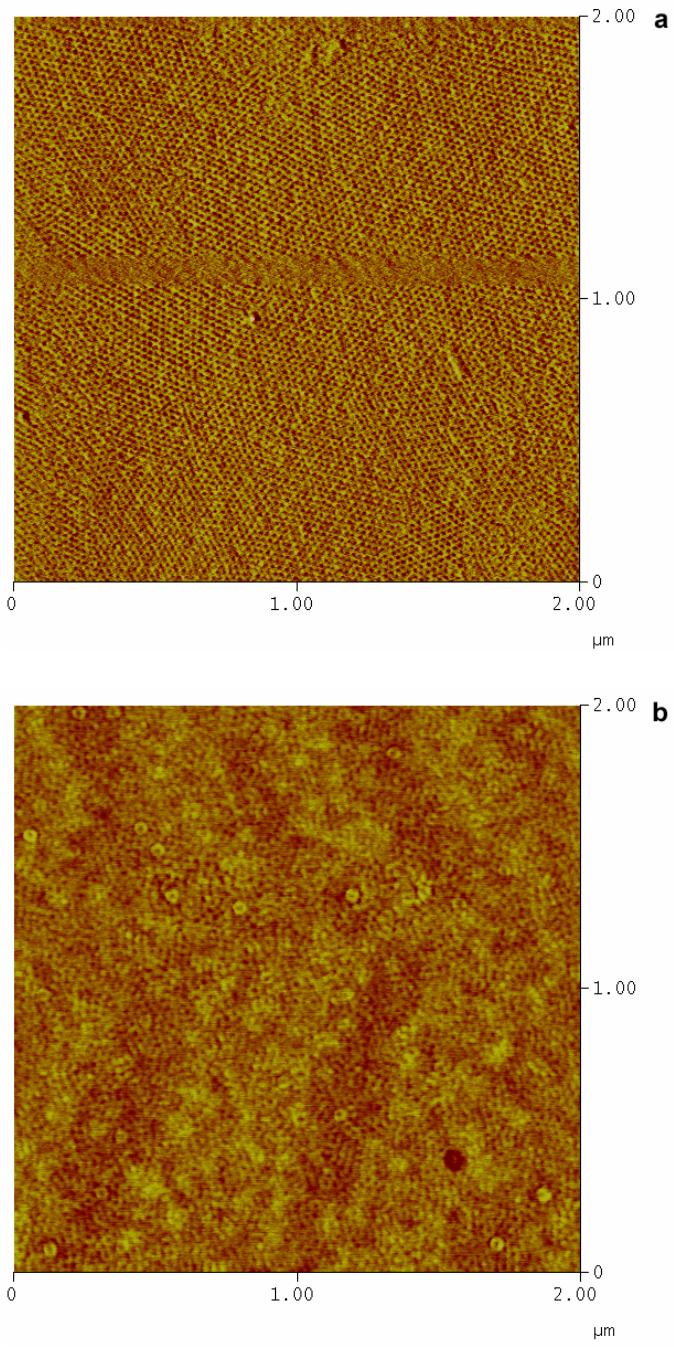

Figure 6.3: SPM images (phase contrast) of PS–PEO thin film surfaces after two hour thermal anneal at 110 °C under vacuum (~ 10 mTorr). a) SO(20–6)/[EMI][TFSI] 92 wt%; b) neat SO(20–6).

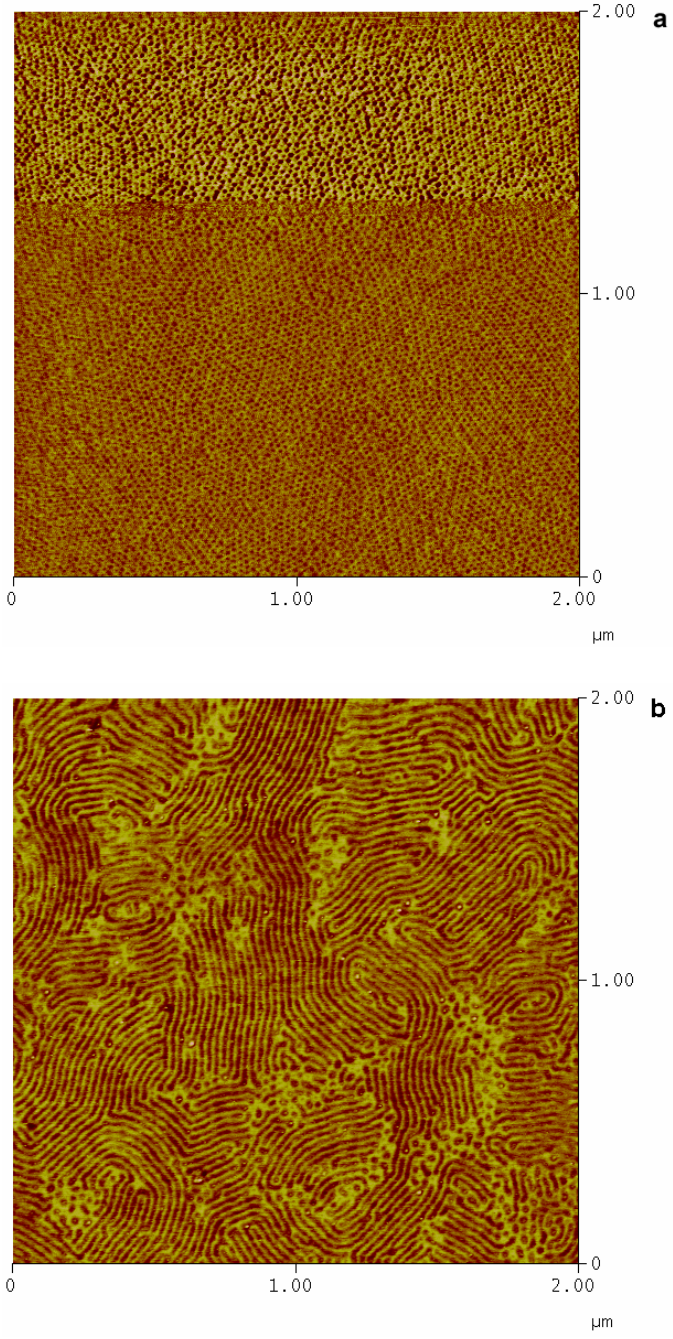

Figure 6.4: SPM images (phase contrast) of PS–PEO thin film surfaces after eight hour thermal anneal at 110 °C under vacuum (~ 10 mTorr). a) SO(20–6)/[EMI][TFSI] 92 wt%; b) neat SO(20–6).

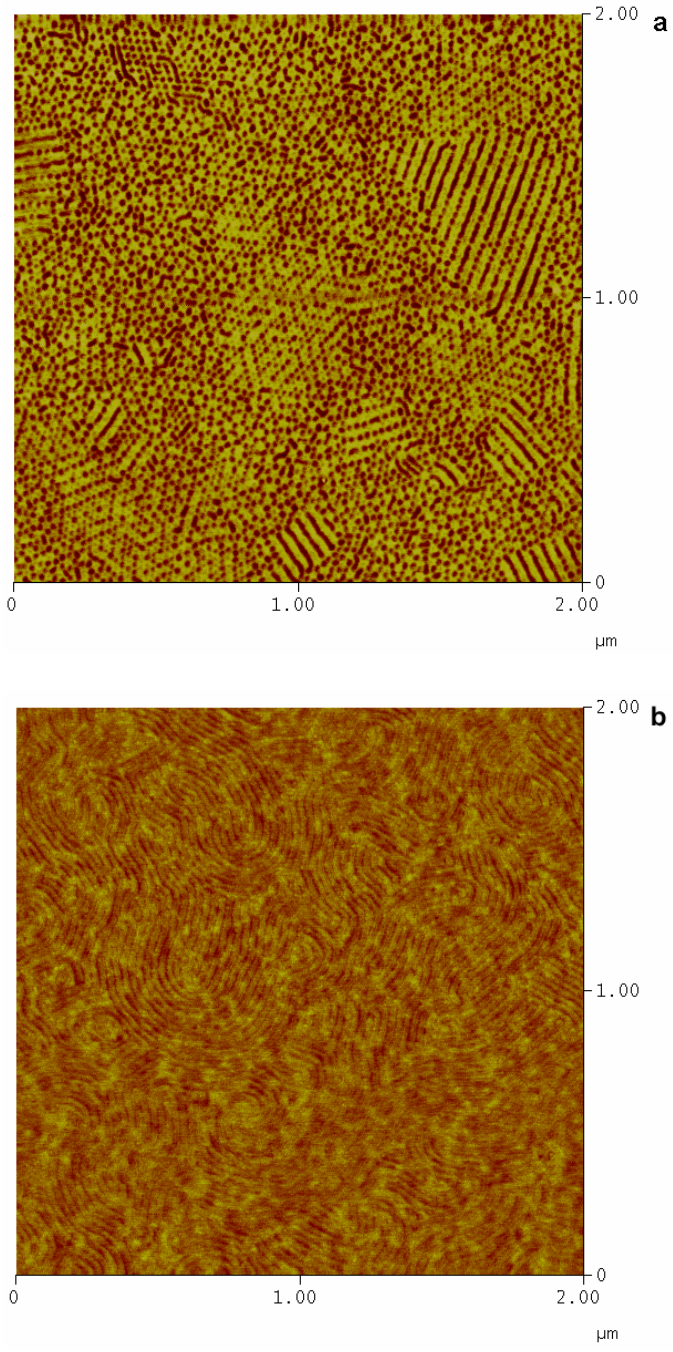

Figure 6.5: SPM images (phase contrast) of PS–PEO thin film surfaces after 16 hour thermal anneal at 110 °C under vacuum (~ 10 mTorr). a) SO(20–6)/[EMI][TFSI] 92 wt%; b) neat SO(20–6).

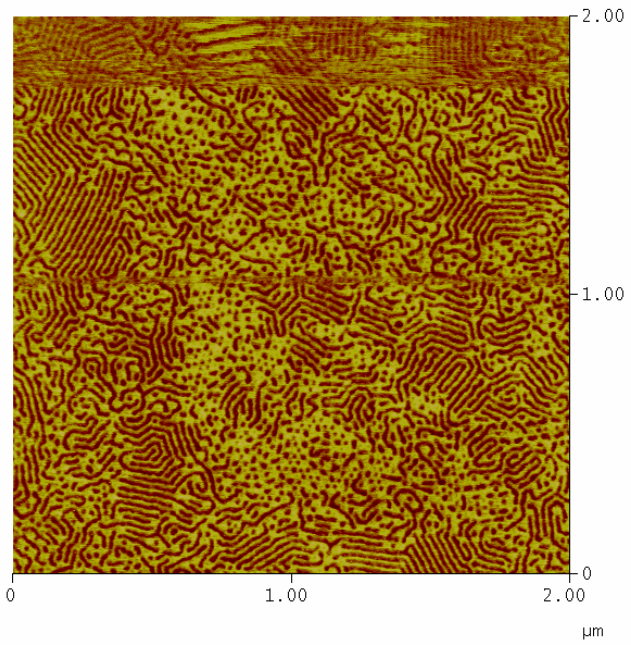

Figure 6.6: SPM image (phase contrast) of an SO(20–6)/[EMI][TFSI] thin film surface after 24 hour thermal anneal at 110 °C under vacuum (~ 10 mTorr).

copolymer film displays some perpendicular cylinder alignment along with short lengths of cylinders aligned parallel to the film surface.

Figures 6.4a and b show images of the 92 wt% and neat SO(20–6) films after thermal annealing for eight hours. The 92 wt% solution film shown in Figure 6.4a still possess mostly perpendicularly aligned cylinders; however, some short lengths of cylinders aligned parallel to the film surface can be seen. In the neat SO(20–6) film, the majority of the cylindrical domains are aligned parallel to the film surface after eight hours of annealing.

Figures 6.5a and b show the 92 wt% solution film and the neat SO(20–6) solution film after 16 hours of thermal annealing. Figure 6.5a shows a very interesting

image of the SO(20–6) 92 wt% solution microstructure in a state of transition between perpendicular and parallel alignment of the cylinder domains. There is a distinct increase in the diameter of the cylinders, as compared to the images from shorter annealing times, and the image also shows multiple areas were individual cylinders appear to be fusing together to form domains of cylinder alignment parallel to the film surface. Parallel alignment of the cylindrical domains relative to the film surface is observed for the neat SO(20–6) film after 16 hours of thermal annealing (Figure 6.5b).

After 24 hours of thermal annealing, more extensive parallel alignment of the cylindrical domains is observed for the 92 wt% solution film, as shown in Figure 6.6. However, some cylinders aligned perpendicular to the film surface are still observed in the image. Experiments at longer annealing times are necessary to determine if the SO(20–6)/[EMI][TFSI] film microstructure ultimately adopts completely parallel alignment to the film surface.

Additionally, thin films of the SO(20–6)/[EMI][TFSI] 92 wt% solution were prepared on glass substrates coated with indium tin oxide (ITO). The ITO coated glass substrates were cleaned, and the films were spin-coated using the same procedures described in Section 2.9 for films on silicon substrates. Figure 6.7 shows SPM phase images of the SO(20–6)/[EMI][TFSI] 92 wt% solution films on ITO/glass after thermal annealing under vacuum at 110 °C for two hours and eight hours. After only two hours of annealing (Figure 6.7a), the image of the 92 wt% solution film on ITO/glass resembles that of the 92 wt% solution film on silicon after annealing for eight, or 16 hours (Figures 6.4a and 6.5a). Figure 6.7b shows the 92 wt% solution film on ITO/glass

after eight hours of thermal annealing. The image shows that the majority of the cylindrical domains are aligned parallel to the film surface. The bright contrast regions in Figure 6.7b, which appear to be multiple cylinders in width, are possibly regions of the film surface where the PS blocks are beginning to form a surface layer due to the lower surface free energy of PS as compared to PEO. Alternatively, these regions could be imaging artifacts resulting from blunting or contamination of the SPM probe tip. A blunted or contaminated probe tip leads to reduced imaging resolution due the resulting increase in contact area with the sample surface. Thus the regions of wide cylinder structures in Figure 6.7b could represent regions of the film surface where the cylindrical domains are close enough together to result a in loss of domain boundary resolution in the phase image. Probe tip contamination was a frequent issue when performing SPM experiments with copolymer/ionic liquid solution films, most likely due to accumulation of ionic liquid on the tip over the course of the experiments. Occasionally, "cleaning" of the probe tip could be accomplished by retracting the cantilever from the film surface and applying a large drive amplitude in order to physically shake the contaminants from the tip.

Figure 6.8 shows a 92 wt% SO(20–6)/[EMI][TFSI] solution thin film on a silicon substrate that has been annealed under chloroform vapor for 24 hours. Interestingly, fairly uniform parallel alignment of the cylindrical microstructure relative to the film surface is observed.

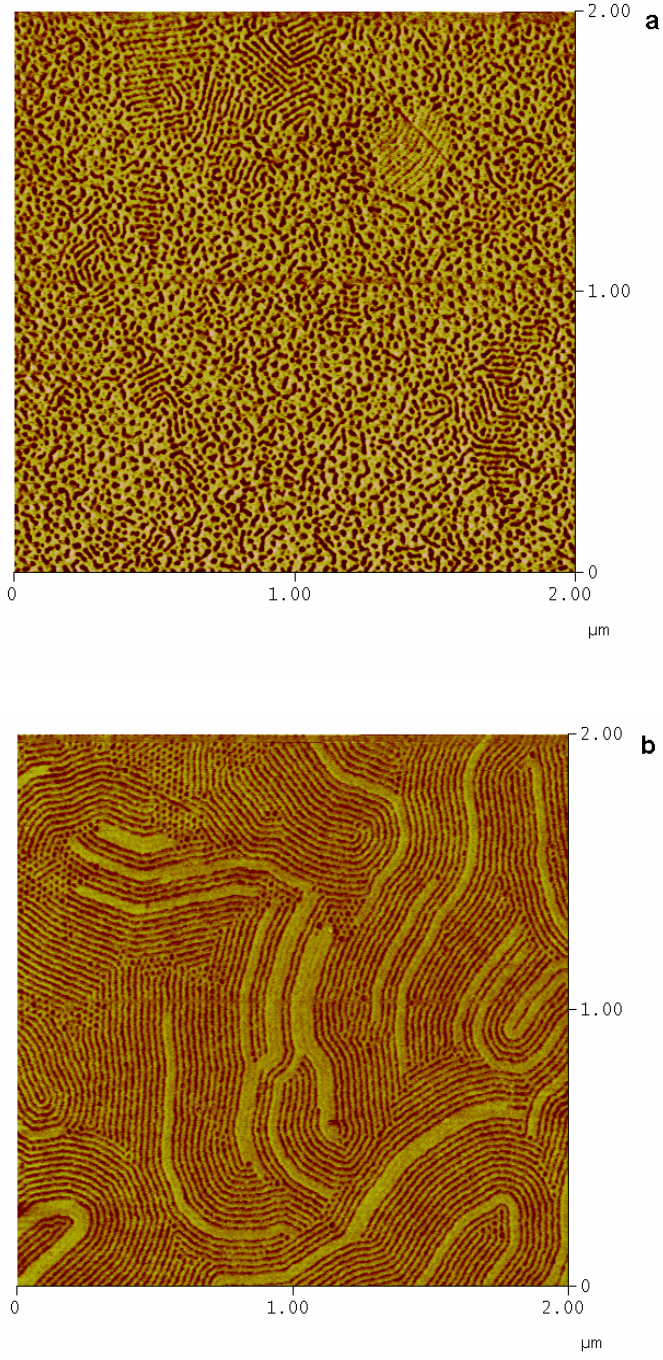

Figure 6.7: SPM images (phase contrast) of SO(20–6)/[EMI][TFSI] 92 wt% thin films on an ITO coated glass substrate after annealing at 110 °C under vacuum. a) two hour anneal; b) eight hour anneal.

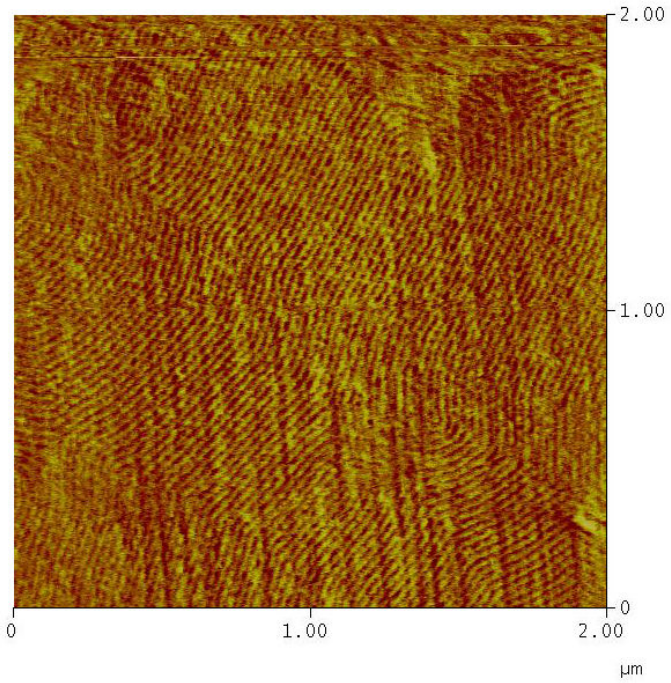

Figure 6.8: SPM image (phase contrast) of SO(20–6)/[EMI][TFSI] 92 wt% thin film on silicon after 24 hours of chloroform vapor annealing.

6.4 Discussion

The perpendicular alignment of the cylindrical microstructure of the SO(20–6)/[EMI][TFSI] 92 wt% solution and neat SO(20–6) thin films shown in Figures 6.3a and 6.3b is most likely a result of evaporation of the dichloromethane solvent during spin-coating of the films. It is noted that the neat SO(20–6) film shown in Figure 6.3b displays only moderate perpendicular order, compared to the 92 wt% solution film in Figure 6.3a. However, the neat film does possess a much higher degree of perpendicular alignment after two hours of thermal annealing, as compared with eight hours (Figure 6.4b). Similar results of perpendicular cylindrical microstructure alignment have been

reported by Lin, *et al.* for PS–PEO copolymers spin-coated from benzene.[15] However, one difference is that Lin reported perpendicular cylinder alignment in as–spun films with no thermal annealing, while the as–spun films shown in Figures 6.2a and b show poorly ordered microstructure. This difference is hypothesized to be a result of the higher vapor pressure for dichloromethane (~ 350 mmHg at 20 °C) than for benzene (~ 75 mmHg at 20 °C). As the solvent evaporates during spin-coating, the gradient in solvent concentration normal to the film surface creates an ordering front that propagates from the film surface to the substrate. Thus, faster evaporation of the dichloromethane solvent results in a much less ordered film surface as compared to films spin-coated from benzene. However, evaporation of the dichloromethane from the interior of the film is slower, and it is presumed that the cylindrical microstructure on the interior of the film orients perpendicular to the film surface. This presumption is supported by the appearance of the perpendicularly ordered microstructure at the film surface after two hours of thermal annealing, which allows the copolymer at the surface of the film to reorient and adopt the perpendicular alignment of the cylindrical domains on the interior of the film.

From the appearance of the thin film microstructures after extended thermal annealing, it is clear that the preferred alignment of the cylindrical microstructure is parallel to the film surface. This is a result of preferential interactions between the PEO/ionic liquid domains with the native oxide layer of the silicon substrate. The longer annealing times necessary for the transition from perpendicular to parallel orientation of the 92 wt% SO(20–6) solution films as compared with the neat SO(20–6)

films is likely a result of an increase in the degree of segregation between the copolymer microstructure domains upon addition of the ionic liquid, which results in slower microstructure reorientation.

The perpendicular orientation of the cylindrical domains in the SO(20–6) 92 wt% solution film, over a fairly large lateral area (Figure 6.3a), is also likely the result of a higher degree of microstructure order induced by an increase in the degree of segregation upon addition of the selective [EMI][TFSI] solvent. Wang, *et al.* have also reported an increased degree of ordering in thin films of a lamellar forming PS–PMMA diblock copolymer that was doped with a lithium salt.[10]

As can be seen in Figures 6.7a and b, the transition from perpendicular to parallel alignment of the cylindrical microstructure of the 92 wt% solution films occurs much more quickly on the ITO/glass substrates than on silicon. This suggests that the PEO/ionic liquid cylindrical domains experience greater preferential interactions with the ITO substrate surface than with the native oxide layer of the silicon substrate. Obviously more investigation of the behavior of the PS–PEO thin films on ITO/glass substrates is necessary before further conclusions can be drawn. Particularly, shorter annealing times than two hours are necessary to determine if the 92 wt% solution films actually achieve well ordered perpendicular alignment, as seen with the silicon substrate in Figure 6.3a. Additionally, comparison of the neat SO(20–6) alignment on the ITO/glass substrates is also necessary in order to gauge the effects of the ionic liquid on ordering and alignment of the block copolymer microstructure.

Interestingly, Figure 6.8 shows that solvent annealing of the 92 wt% SO(20-6)/[EMI][TFSI] solution under chloroform vapor leads to fairly uniform parallel alignment of the cylindrical microstructure relative to the film surface. Obviously, experiments involving shorter solvent vapor annealing times are necessary in order to determine if perpendicular alignment of the copolymer microstructure relative to the film surface can be obtained via solvent vapor annealing. Here, it is noted that chloroform is used for the solvent vapor annealing experiments due to its lower vapor pressure (160 mmHg at 20 °C) than dichloromethane. Some initial experiments with solvent vapor annealing of the block copolymer films were conducted with dichloromethane. However, ordering of the block copolymer microstructure was not observed in the SPM images, presumably due to the high rate of evaporation of the dichloromethane from the film surface. However, in light of the results from thermal annealing experiments, where the disordered film surfaces (Figures 6.2a and b) transitioned to fairly well ordered perpendicular cylinders, it would be instructive to attempt dichloromethane vapor annealing followed by short term thermal annealing in order to see if similar results could be obtained.

Characterization of the microstructure alignment at the film substrate interface is also necessary. Often, it is difficult to obtain perpendicular alignment of the copolymer thin film microstructure in immediate contact with the substrate due to preferential interactions that usually exist between the substrate and one of the copolymer blocks.[16,17] Attempts were made to remove the copolymer thin films from the silicon substrates in order to investigate cross-sections of the films via TEM. The basic

procedure used was modeled after several literature reports,[9,10,18] and consisted of first coating the film with epoxy and curing overnight at 65 °C. Then the epoxy coated films were immersed in liquid nitrogen in order to delaminate the epoxy coated thin film from the surface of the silicon substrate. Ultimately, however, the attempts to remove the films from the silicon substrates were unsuccessful, and thus the microstructure alignment of the copolymer thin films at the film–substrate interface has not been characterized. This is not to suggest that removal of the copolymer films form the substrate is impossible using the method described above. Only a few attempts were made at removing the thin films from the substrate, thus further attempts and technique refinement may produce success. Encouragingly, reports on PS–PEO and PS–PMMA copolymer thin films doped with atomic salts have shown that perpendicular alignment of the block copolymer microstructure at the film–substrate interface is achievable.[10,19] In these studies the preferential interactions between the PEO and PMMA blocks and the substrate were proposed to be overcome by the formation of ionic complexes between these blocks and the added salts. Thus, there is potential that the copolymer/ionic liquid solutions used in this project could display similar PEO–ion interactions, resulting in microstructure alignment perpendicular to the film–substrate interface.

6.5 Summary

Investigation of the microstructure orientation in thin films of a PS–PEO block copolymer and a concentrated PS–PEO/[EMI][TFSI] solution was performed using SPM to image the film surfaces. Perpendicular alignment of the cylindrical copolymer

microstructure, relative to the film surface, was observed after thermal annealing for short time periods (≤ 2 hours). Longer thermal annealing times led to alignment of the copolymer microstructure parallel to the film surface. Additionally, more uniform lateral order of the perpendicularly aligned copolymer microstructure was observed in the PS–PEO/[EMI][TFSI] solution film as compared to the neat PS–PEO copolymer film. This result was attributed to the relative increase in degree of segregation of the copolymer microstructure upon addition of the selective [EMI][TFSI] solvent. Furthermore, a faster transition to parallel microstructure alignment was observed for the PS–PEO/[EMI][TFSI] solution films on ITO coated glass substrates, as compared to silicon substrates. Finally, chloroform vapor annealing was shown to induce parallel alignment of the cylindrical microstructure for the 92 wt% SO(20–6)/[EMI][TFSI] solution films. The results presented here have barely scratched the surface of investigating the microstructure orientation behavior of thin films of concentrated copolymer/ionic liquid solutions. Further investigations of the effects of changing variables in both the film characteristics (*e.g.*, copolymer composition, solution concentration, film thickness) and microstructure modulation (*e.g.*, annealing method, annealing time, substrate identity) are necessary.

6.5 References

1. Yoshio, M.; Kagata, T.; Hoshino, K.; Mukai, T.; Ohno, H.; Kato, T. *J. Am. Chem. Soc.* **2006**, *128*, 5570–5577.

2. Tepe, T.; Schulz, M. F.; Zhao, J.; Tirrell, M.; Bates, F. S.; Mortensen, K.; Almdal, K. *Macromolecules* **1995**, *28*, 3008–3011.

3. Zalusky, A. S.; Olayo-Valles, R.; Wolf, J. H.; Hillmyer, M. A. *J. Am. Chem. Soc.* **2002**, *124*, 12761–12773.

4. Park, S.; Kim, B.; Xu, J.; Hofmann, T.; Ocko, B. M.; Russell, T. P. *Macromolecules* **2009**, *42*, 1278–1284.

5. Wang, Y.; Hong, X.; Liu, B.; Ma, C.; Zhang, C. *Macromolecules* **2008**, *41*, 5799–5808.

6. Cavicchi, K. A.; Russell, T. P. *Macromolecules* **2007**, *40*, 1181–1186.

7. Bang, J.; Kim, B. J.; Stein, G. E.; Russell, T. P.; Li, X.; Wang, J.; Kramer, E. J.; Hawker, C. J. *Macromolecules* **2007**, *40*, 7019–7025.

8. Kim, S. H.; Misner, M. J.; Xu, T.; Kimura, M.; Russell, T. P. *Adv. Mater.* **2004**, *16*, 226–231.

9. Wang, J.-Y.; Chen, W.; Roy, C.; Sievert, J. D.; Russell, T. P. *Macromolecules* **2008**, *41*, 963–969.

10. Wang, J.-Y.; Chen, W.; Sievert, J. D.; Russell, T. P. *Langmuir* **2008**, *24*, 3545–3550.

11. Xu, T.; Zvelindovsky, A. V.; Sevink, G. J. A.; Lyakhova, K. S.; Jinnai, H.; Russell, T. P. *Macromolecules* **2005**, *38*, 10788–10798.

12. Xu, T.; Zhu, Y.; Gido, S. P.; Russell, T. P. *Macromolecules* **2004**, *37*, 2625–2629.

13. Böker, A.; Elbs, H.; Hänsel, H.; Knoll, A.; Ludwigs, S.; Zettl, H.; Zvelindovsky, A. V.; Sevink, G. J. A.; Urban, V.; Abetz, V.; Müller, A. H. E.; Krausch, G. *Macromolecules* **2003**, *36*, 8078–8087.

14. Amundson, K.; Helfand, E.; Davis, D. D.; Quan, X.; Patel, S. S.; Smith, S. D. *Macromolecules* **1991**, *24*, 6546–6548.

15. Lin, Z.; Kim, D. H.; Wu, X.; Boosahda, L.; Stone, D.; LaRose, L.; Russell, T. P. *Adv. Mater.* **2002**, *14*, 1373–1376.

16. Xu, T.; Hawker, C. J.; Russell, T. P. *Macromolecules* **2003**, *36*, 6178–6182.

17. Ham, S.; Shin, C; Kim, E.; Ryu, D. Y.; Jeong, U.; Russell, T. P.; Hawker, C. J. *Macromolecules* **2008**, *41*, 6431–6437.

18. Xu, C.; Ohno, K.; Ladmiral, V.; Milkie, D. E.; Kikkawa, J. M.; Composto, R. J. *Macromolecules* **2009**, *42*, 1219–1228.

19. Kim, S. H.; Misner, M. J.; Yang, L.; Gang, O.; Ocko, B. M.; Russell, T. P. *Macromolecules* **2006**, *39*, 8473–8479.

Chapter 7

Summary and Outlook

7.1 Research Summary

The overall goal of this thesis project has been to better understand the self-assembly behavior of block copolymers in solutions where an ionic liquid is the solvent. Studies have involved investigating the dilute, as well as the concentrated, solution behavior of several different block copolymers in ionic liquids. Dilute solution studies of PS–PMMA and PB–PEO diblock copolymers in the ionic liquids [BMI][PF_6] and [EMI][TFSI] have shown that the ionic liquids behave as selective solvents which support the self-assembly of amphiphilic block copolymer micelles. Additionally, comparisons of the micelle morphologies formed by the same copolymer dissolved in [BMI][PF_6] and [EMI][TFSI] gave a measure of the relative selectivity of the two ionic liquid solvents. Furthermore, cryo-TEM investigations of the dilute block copolymer/ionic liquid solutions showed that ionic liquids are very compatible with the sample preparation and imaging procedures involved with cryo-TEM.

In moderate to highly concentrated block copolymer/ionic liquid solutions, lyotropic microstructure phase transitions were observed upon changing the solution concentration. In general, the lyotropic phase behavior of the block copolymer/ionic liquid solutions was found to be analogous to that observed for block copolymers diluted with more conventional organic solvents or water. Additionally, for some of the PB–PEO/ionic liquid samples studied, evidence was observed for the existence of the random network morphology, which has been reported for the same copolymers diluted with water. Finally, an increase in lamellar domain spacing of the concentrated block copolymer/ionic liquid solutions was observed with increasing ionic liquid content. Double logarithmic plots of domain spacing vs. copolymer concentration displayed negative slopes, and power law fits of the data gave values for the exponential term that were consistent with those reported for other block copolymers diluted with strongly selective solvents. Thus, the ionic liquids were shown to behave as strongly selective solvents, and the majority of the ionic liquid was assumed to be confined to the PEO domains of the microstructured PB–PEO and PS–PEO copolymers.

Due to partitioning of the selective ionic liquid solvents to the PEO domains of the block copolymers, the concentrated block copolymer/ionic liquid solutions were seen as potential systems for preparing simple nanostructured electrolyte materials. Thus, experiments were performed which were aimed at characterizing block copolymer/ionic liquid solution properties pertinent to applications as electrolyte materials. The ionic conductivity of the PS–PEO/[EMI][TFSI] solutions was characterized and found to be within the range of ~10^{-3} S/cm at 100 °C. Additionally,

these materials showed further promise, in that their ionic conductivity was observed to increase with both ionic liquid content and molecular weight of the PEO blocks of the copolymer.

Finally, preliminary investigations of the microstructure orientation in thin films of concentrated block copolymer/ionic liquid solutions were performed. These experiments were geared toward the idea of preparing electrolyte materials with anisotropically aligned nanostructures. In particular, it was found that perpendicular alignment of the cylindrical microstructure of a concentrated PS–PEO/[EMI][TFSI] solution thin film, spin-coated on a silicon substrate, could be attained via short term thermal annealing. Compared with the neat copolymer film, the concentrated solution possessed a higher degree of lateral order of the perpendicularly aligned cylindrical microstructure. This was attributed to an increase in the degree of segregation of the copolymer microstructure upon addition of the selective ionic liquid solvent.

7.2 Future Research

Due to the relatively small amount of research that has been conducted involving combinations of block copolymers and ionic liquids, multiple avenues exist for expanding upon the studies and results presented in this thesis.

7.2.1 General Self-Assembly Studies

Further studies of the general self-assembly behavior of block copolymers in dilute and concentrated solutions are necessary. Studies involving a wider and more systematic variation of the ionic liquid ion identities, and the copolymer block composition and identities will allow for broader characterization of the polymer–ionic

liquid, solute–solvent interactions which govern the morphology and lyotropic phase behavior of the block copolymers in solution. For example, investigations of how specific ion characteristics, such as cation alkychain length, or anion H–bond basicity, affect the ionic liquid solvent selectivity would be valuable. Additionally, investigations involving block copolymer/ionic liquid systems in which the ionic liquid behaves as only a slightly selective solvent, or as a neutrally good solvent, are needed.

7.2.2 Optimization of Nanostructured Electrolyte Materials

Additionally, future studies involving optimization of specific block copolymer ionic liquid systems for use as nanostructured electrolyte materials are also necessary. As discussed in Chapter 5, an increase in molecular weight of the copolymer block forming the conductive domains of the copolymer microstructure results in an increase in the ionic conductivity of the concentrated copolymer/ionic liquid solutions. Thus studies involving higher molecular weight analogues of the PS–PEO copolymers utilized in this thesis would be valuable. An additional result of increasing the molecular weight of the PS–PEO block copolymers would be an increase in the physical robustness of the electrolyte materials. The PS–PEO/ionic liquid solutions used in this thesis possessed poor physical properties. Qualitatively, they ranged from brittle solids to wax-like materials at low and moderate ionic liquid content, respectively. In comparison, Singh *et al.*, report elastic solid physical properties for electrolyte materials consisting of high molecular weight PS–PEO copolymers doped with [Li][TFSI].[1]

Furthermore, increasing the complexity of the copolymers from simple diblocks to multiblock copolymers would open a vast arena for investigations in optimizing the

properties of the microstructured electrolyte materials. For example, employing PS–PEO–PS triblocks would provide increased physical robustness as compared to the simple PS–PEO diblock materials. Another particular multiblock copolymer that may provide interesting results is a poly(isoprene-*b*-styrene-*b*-ethylene oxide) (ISO) triblock. Bates and coworkers have reported extensive studies on the phase behavior of ISO triblock copolymers in the pure state, and doped with lithium salts.[2,3] In studies of the microstructure phase map of the pure triblock samples, regions of copolymer composition characterized by triply periodic network microstructures were observed. Additionally, doping of the ISO copolymers with lithium salts resulted in a transition of the network microstructures to hexagonally packed cylinder microstructures. Thus, it would be interesting to investigate the effects of doping similar ISO triblocks with ionic liquids. It might be expected that an increase in the degree of block segregation upon addition of the selective ionic liquid solvent would lead to a loss of the network microstructures; however, if the network microstructures were retained these materials could potentially be utilized as unique electrolytes.

Even with optimization of the block copolymer component of the nanostructured electrolyte material, the ultimate conductivity of the electrolyte is limited by the conductivity of the ionic liquid component. The ionic liquid [EMI][TFSI] has been widely utilized in electrolyte studies due to its fairly high room temperature conductivity (~ 10^{-2} S/cm) and wide electrochemical window (~ 4.5 V). However, the synthesis of new ionic liquids, and potential for tuning their properties via new ion identities and combinations continues to expand. Thus, experiments with optimization

of the ionic liquid utilized to prepare the concentrated block copolymer/ionic liquid solutions are warranted.

7.2.3 Lithium Ion Conductivity

One area of investigation that is ultimately necessary if the concentrated block copolymer/ionic liquid solutions described in this thesis are to be used as electrolyte materials, are the effects of incorporation of the active electrolyte ions for a particular device (*e.g.*, Li^+ or H^+). In the case of lithium ion battery electrolytes, various reports have shown that addition of an ionic liquid to a solid electrolyte material consisting of a polymer doped with a lithium salt results in an increase in the ionic conductivity of the material, particularly at low temperatures.[4–6] Additionally, it has been shown that addition of lithium salts to a polymer/ionic liquid electrolyte material can result in an increase in the ionic conductivity. This increase persists up to a certain Li^+/ionic liquid ratio, after which a decrease in ionic conductivity is observed.[7] Similar results may be expected for the ionic conductivity behavior of concentrated block copolymer/ionic liquid solutions. Thus, Li^+ concentration could be utilized along with other variables, such as block copolymer molecular weight and ionic liquid identity, in order to tune the ionic conductivity of the concentrated block copolymer/ionic liquid solutions.

7.2.4 Thin Films

As discussed in Chapter 6, much more work is necessary in order to gain a better understanding of the microstructure alignment in thin films of concentrated block copolymer/ionic liquid solutions. Some of the many variables that could be investigated

include annealing duration (whether solvent or thermal), copolymer composition, solution concentration, substrate identity, and film thickness.

Additionally, investigation of the ionic conductivity of block copolymer/ionic liquid thin films possessing isotropically and anisotropically aligned microstructure would also be an interesting area for future research; however, developing an experimental procedure for performing conductivity measurements on the thin films may prove to be a challenge. The block copolymer/ionic liquid solution thin films described in Chapter 6, which were spin-coated on ITO/glass substrates are a potential step towards a sample configuration suitable for thin film conductivity measurements. For these samples electrode contact can be made with the bottom of the films via the conductive ITO substrate coating. Then evaporation of gold electrode contacts onto the surface of the films could potentially be one way to obtain conductive contact with the free film surface. Alternatively, current-sensing SPM could potentially be another method for measuring the conductivity of the block copolymer/ionic liquid thin films. In this technique the SPM probe tip is used as an electrode for measuring the conductivity between the surface of the film and ITO substrate. Both of the techniques described above have been utilized for measuring the conductivity of aligned polymer nanorods that were prepared using a block copolymer thin film template.[8]

7.3 References

1. Singh, M.; Odusanya, O.; Wilmes, G. M.; Eitouni, H. B.; Gomez, E. D.; Patel, A. J.; Chen, V. L.; Park, M. J.; Fragouli, P.; Iatrou, H.; Hadjichristidis, N.; Cookson, D.; Balsara, N. P. *Macromolecules* **2007**, *40*, 4578–4585.

2. Chatterjee, J.; Jain, S.; Bates, F. S. *Macromolecules* **2007**, *40*, 2882–2896.

3. Epps, T. H.; Bailey, T. S.; Waletzko, R.; Bates, F. S. *Macromolecules* **2003**, *36*, 2873–2881.

4. Shin, J.-H.; Henderson, W. A.; Tizzani, C.; Passerini, S.; Jeong, S.-S.; Kim, K.-W. *J. Electrochem. Soc.* **2006**, *9*, A1649–A1654.

5. Kim, Y. H.; Cheruvally, G.; Choi, J. W.; Ahn, J. H.; Kim, K. W.; Ahn, H. J.; Choi, D. S.; Song, C. E. *Macromol. Symp.* **2007**, *249–250*, 183–189.

6. Sutto, T. E. *J. Electrochem. Soc.* **2007**, *154*, P101–P107.

7. Marwanta, E.; Mizumo, T.; Nakamura, N.; Ohno, H. *Polymer* **2005**, *46*, 3795–3800.

8. Lee, J. I.; Cho, S. H.; Park, S.-M.; Kim, J. K.; Kim, J. K.; Yu, J.-W.; Kim, Y. C.; Russell, T. P. *Nano Lett.* **2008**, *8*, 2315–2320.

Bibliography

Abraham, M. A.; Moens, L., Eds. *Clean Solvents: Alternative Media for Chemical Reactions and Processing*; American Chemical Society: Washington, DC, 2002.

Abraham, M. H.; Zissimos, A. M.; Huddleston, J. G.; Willauer, H. D.; Rogers, R. D.; Acree, W. E. *Ind. Eng. Chem. Res.* **2003**, *42,* 413–418.

Alexandridis, P.; Lindman, B., Eds. *Amphiphilic Block Copolymers: Self-Assembly and Applications*; Elsevier Science: Amsterdam, 2000.

Allen, C; Maysinger, D.; Eisenberg, A. *Colloids and Surfaces B* **1999**, *16*, 3–27.

Amundson, K.; Helfand, E.; Davis, D. D.; Quan, X.; Patel, S. S.; Smith, S. D. *Macromolecules* **1991**, *24*, 6546–6548.

Anderson, J. L.; Ding, J.; Welton, T.; Armstrong, D. W. *J. Am. Chem. Soc.* **2002**, *124*, 14247–14254.

Angell, C. A.; Byrne, N.; Belieres, J.-P. *Acc. Chem. Res.* **2007**, *40*, 1228–1236.

Aniansson, E. A. G.; Wall, S. N. *J. Phys. Chem.* **1974**, *78*, 1024–1030.

Aniansson, E. A. G.; Wall, S. N.; Almgren, M.; Hoffmann, H.; Kielmann, I.; Ulbricht, W.; Zana, R.; Lang, J.; Tondre, C. *J. Phys. Chem.* **1976**, *80*, 905–922.

Armstrong, D. W.; He, L.; Liu, Y.-S. *Anal. Chem.* **1999**, *71*, 3873–3876.

Armstrong, J. P.; Hurst, C.; Jones, R. G.; Licence, P.; Lovelock, K. R. J.; Satterley, C. J.; Villar-Garcia, I. J. *Phys. Chem. Chem. Phys.* **2007**, *9*, 982–990.

Bai, Z.; He, Y.; Lodge, T. P. *Langmuir* **2008**, *24*, 5284–5290.

Bai, Z.; He, Y.; Young, N. P.; Lodge, T. P. *Macromolecules* **2008**, *41*, 6615–6617.

Baker, S. N.; Baker, G. A.; Bright, F. V. *Green Chem.* **2002**, *4*, 165–169.

Bang, J.; Jain, S.; Li, Z.; Lodge, T. P.; Pedersen, J. S.; Kesselman, E.; Talmon, Y. *Macromolecules* **2006**, *39*, 1199–1208.

Bang, J.; Kim, B. J.; Stein, G. E.; Russell, T. P.; Li, X.; Wang, J.; Kramer, E. J.; Hawker, C. J. *Macromolecules* **2007**, *40*, 7019–7025.

Baranyai, K. J.; Deacon, G. B.; MacFarlane, D. R.; Pringle, J. M.; Scott, J. L. *Aust. J. Chem.* **2004**, *57*, 145–147.

Barsoukov, E.; Macdonald, J. R., Eds. *Impedance Spectroscopy: Theory, Experiment, and Applications*; John Wiley & Sons, Inc.: Hoboken, 2005.

Bates, F. S.; Fredrickson, G. H. *Phys. Today* **1999**, *52*, 32–38.

Bellare, J. R. Cryo-Electron and Optical Microscopy of Surfactant Microstructures. Ph.D. Thesis, University of Minnesota, 1988.

Biedroń, T.; Bednarek, M.; Kubisa, P. *Macromol. Rapid Commun.* **2004**, *25*, 878–881.

Biedroń, T.; Kubisa, P. *J. Polym. Sci. Part A: Polym. Chem.* **2002**, *40*, 2799–2809.

Birshtein, T. M.; Zhulina, E. B. *Polymer* **1989**, *30*, 170–177.

Böker, A.; Elbs, H.; Hänsel, H.; Knoll, A.; Ludwigs, S.; Zettl, H.; Zvelindovsky, A. V.; Sevink, G. J. A.; Urban, V.; Abetz, V.; Müller, A. H. E.; Krausch, G. *Macromolecules* **2003**, *36*, 8078–8087.

Bonhôte, P.; Dias, A.-P.; Papageorgiou, N.; Kalyanasundaram, K.; Grätzel, M. *Inorg. Chem.* **1996**, *35*, 1168–1178.

Brazel, C. S.; Rogers, R. D., Eds. *ACS Symposium Series, 913*; American Chemical Society: Washington, DC, 2005.

Carmichael, A. J.; Seddon, K. R. *J. Phys. Org. Chem.* **2000**, *13*, 591–595.

Cavicchi, K. A.; Russell, T. P. *Macromolecules* **2007**, *40*, 1181–1186.

Chatterjee, J.; Jain, S.; Bates, F. S. *Macromolecules* **2007**, *40*, 2882–2896.

Chiappe, C.; Pieraccini, D. *J. Phys. Org. Chem.* **2005**, *18*. 275–297.

Chu, B. *Laser Light Scattering: Basic Principles and Practice*, 2nd ed.; Academic Press, Inc.:Boston, 1991.

Cleveland, J. P.; Anczykowski, B.; Schmid, A. E.; Elings, V. B. *Appl. Phys. Lett.* **1998**, *72*, 2613.

Cochran, E. W.; Garcia-Cervera, C. J.; Fredrickson, G. H. *Macromolecules* **2006**, *39*, 2449–2451.

Cochran, E. W.; Morse, D. C.; Bates, F. S. *Macromolecules* **2003**, *36*, 782–792.

Costa, L. T.; Ribeiro, M. C. C. *J. Chem. Phys.* **2006**, *124*, 184902.

Costa, L. T.; Ribeiro, M. C. C. *J. Chem. Phys.* **2007**, *127*, 164901.

Crossland, E. J. W.; Ludwigs, S.; Hillmyer, M. A.; Steiner, U. *Soft Matter* **2007**, *3*, 94–98.

Crowhurst, L.; Mawdsley, P. R.; Perez-Arlandis, J. M.; Salter, P. A., Welton, T. *Phys. Chem. Chem. Phys.* **2003**, *5*, 2790–2794.

Davidock, D. A.; Hillmyer, M. A.; Lodge, T. P. *Macromolecules* **2003**, *36*, 4682–4685.

Discher, B. M.; Won, Y.-Y.; Ege, D. S.; Lee, J. C.-M.; Bates, F. S.; Discher, D. E.; Hammer, D. A. *Science* **1999**, *284*, 1143–1146.

Earle, M. J.; Esperanca, J. M. S. S.; Gilea, M. A.; Lopes, J. N. C.; Rebelo, L. P. N.; Magee, J. W.; Seddon, K. R.; Widegren, J. A. *Nature* **2006**, *439*, 831–834.

Epps, T. H.; Bailey, T. S.; Waletzko, R.; Bates, F. S. *Macromolecules* **2003**, *36*, 2873–2881.

Favre, F.; Olivier-Bourbigou, H.; Commereuc, D.; Saussine, L. *Chem. Commun.* **2001**, 1360–1361.

Fernicola, A.; Scrosati, B.; Ohno, H. *Ionics* **2006**, *12*, 95–102.

Fetters, L. J.; Lohse, D. J.; Richter, D.; Witten, T. A.; Zirkel, A. *Macromolecules* **1994**, *27*, 4639–4647.

Fletcher, K. A.; Storey, I. A.; Hendricks, A. E.; Pandey, S.; Pandey, S. *Green Chem.* **2001**, *3*, 210–215.

Förster, S.; Berton, B.; Hentze, H.-P.; Krämer, E.; Antonietti, M.; Linder, P. *Macromolecules* **2001**, *34*, 4610–4623.

Fox, T. G.; Flory, P. J. *J. Polym. Sci.* **1954**, *14*, 315–319.

Fuller, J.; Breda, A. C.; Carlin, R. T. *J. Electrochem. Soc.* **1997**, *144*, L67–L70.

Fuller, J.; Carlin, R. T.; De Long, H. C.; Haworth, D. *J. Chem. Soc., Chem. Commun.* **1994**, 299.

Gale, R. J.; Gilbert, B.; Osteryoung, R. A. *Inorg. Chem.* **1978***, 17*, 2728–2729.

Galiński, M.; Lewandowski, A.; Stepniak, I. *Electrochim. Acta* **2006**, *51*, 5567–5580.

Garcia, B.; Lavallée, S.; Perron, G.; Michot, C.; Armand, M. *Electrochim. Acta* **2004**, *49*, 4583–4588.

García, R.; Pérez, R. *Surf. Sci. Rep.* **2002**, *47*, 197–301.

Glass, R.; Moeller, M.; Spatz, J. P. *Nanotechnology* **2003**, *14*, 1153.

Gomez, E. D.; Panday, A.; Feng, E. H.; Chen, V.; Stone, G. M.; Minor, A. M.; Kisielowski, C.; Downing, K. H.; Borodin, O.; Smith, G. D.; Balsara, N. P. *Nano Lett.* **2009**, *9*, 1212–1216.

Gordon, C. M.; Holbrey, J. D.; Kennedy, A. R.; Seddon, K. R. *J. Mater. Chem.* **1998**, *8*, 2627–2636

Gorlov, M.; Kloo, L. *Dalton Trans.* **2008**, 2655–2666.

Hajduk, D. A.; Kossuth, M. B.; Hillmyer, M. A.; Bates, F. S. *J. Phys. Chem. B* **1998**, *102*, 4269–4276.

Halperin, A. *Macromolecules* **1987**, *20*, 2943–2946.

Halperin, A.; Alexander, S. *Macromolecules* **1989**, *22*, 2403–2412.

Ham, S.; Shin, C; Kim, E.; Ryu, D. Y.; Jeong, U.; Russell, T. P.; Hawker, C. J. *Macromolecules* **2008**, *41*, 6431–6437.

Hamley, I. W.; Mai, S.-M.; Ryan, A. J.; Fairclough, J. P.; Booth, C. *Phys. Chem. Chem. Phys.* **2001**, *3*, 2972–2980.

Hamley, I. W.; *The Physics of Block Copolymers*, Oxford University Press, New York 1998.

Hanabusa, K.; Fukui, H.; Suzuki, M.; Shirai, H. *Langmuir* **2005**, *21*, 10383–10390.

Hanley, K. J. Block Copolymers: Phase Behavior in Neutral and Selective Solvents. Ph.D. Thesis, University of Minnesota, 2001.

Hanley, K. J.; Lodge, T. P. *J. Polym. Sci., Part B: Polym. Phys.* **1998**, *36*, 3101–3113.

Hanley, K. J.; Lodge, T. P.; Huang, C.-I. *Macromolecules* **2000**, *33*, 5918–5931.

Harrison, S.; Mackenzie, S. R.; Haddleton, D. M. *Chem. Commun.* **2002**, 2850–2851.

Harrison, S.; Mackenzie, S. R.; Haddleton, D. M. *Macromolecules* **2003**, *36*, 5072–5075.

Hashimoto, T.; Shibayama, M.; Kawai, H. *Macromolecules* **1983**, *16*, 1093–1101.

Hashimoto, T.; Tsutsumi, K.; Funaki,Y. *Langmuir*, **1997**, *13*, 6869–6872.

Hayashi, K.; Nemoto, Y.; Akuto, K.; Sakurai, Y. *J. Power Sources* **2005**, *146*, 689–692.

He, Y.; Boswell, P. G.; Bühlmann, P.; Lodge, T. P. *J. Phys. Chem. B* **2007**, *111*, 4645–4652.

He, Y.; Li, Z.; Simone, P.; Lodge, T. P. *J. Am. Chem. Soc.* **2006**, *128*, 2745–2750.

He, Y.; Lodge, T. P. *Chem. Commun.* **2007**, 2732–2734.

He, Y.; Lodge, T. P. *J. Am. Chem. Soc.* **2006**, *128*, 12666–12667.

He, Y.; Lodge, T. P. *Macromolecules*, **2008**, *41*, 167–174.

Helfand, E.; Tagami, Y. *J. Phys. Chem.* **1972**, *56*, 3592–3601.

Helfand, E.; Wasserman, Z. R. *Macromolecules* **1976**, *9*, 879–888.

Hillmyer, M. A.; *Adv. Polym. Sci.* **2005**, *190*, 137–181.

Hillmyer, M. A.; Bates, F. S. *Macromolecules* **1996**, *29*, 6994–7002.

Holbrey, J. D.; Reichert, W. M.; Nieuwenhuyzen, M.; Johnston, S.; Seddon, K. R.; Rogers, R. D. *Chem. Commun.* **2003**, 1636–1637.

Holbrey, J. D.; Seddon, K. R. *J. Chem. Soc., Dalton Trans.* **1999**, 2133–2139.

Hong, K.; Zhang, H.; Mays, J. W.; Visser, A. E.; Brazel, C. S.; Holbrey, J. D. Reichert, W. M.; Rogers, R. D. *Chem Commun.* **2002**, 1368–1369.

Huang, C.-I.; Lodge, T. P. *Macromolecules*, **1998**, *31*, 3556–3565.

Huddleston, J. G.; Visser, A. E.; Reichert, W. M.; Willauer, H. D.; Broker, G. A.; Rogers, R. D. *Green Chem.* **2001**, *3*, 156–164.

Hussey, C. L. *Pure & Appl. Chem.* **1988**, *60*, 1763–1772.

Ichikawa, T.; Yoshio, M.; Hamasaki, A.; Mukai, T.; Ohno, H.; Kato, T. *J. Am. Chem. Soc.* **2007**, *129*, 10662–10663.

Ishikawa, M.; Sugimoto, T.; Kikuta, M.; Ishiko, E.; Kono, M. *J. Power Sources* **2006**, *162*, 658–662.

Israelachvili, J. N. *Intermolecular and Surface Forces*; Academic Press: San Diego, 1991.

Jacquemin, J.; Husson, P.; Mayer, V.; Cibulka, I. *J. Chem. Eng. Data* **2007**, *52*, 2204–2211.

Jada, A.; Hurtrez, G.; Siffert, B.; Riess, G. *Macromol. Chem. Phys.* **1996**, *197*, 3697.

Jain, N.; Kumar, A.; Chauhan, S.; Chauhan, S. M. S. *Tetrahedron* **2005**, *61*, 1015–1060.

Jain, S. Aqueous Mixtures of Block Copolymer Surfactants. Ph.D. Thesis, University of Minnesota, 2005.

Jain, S.; Bates, F. S. *Macromolecules* **2004**, *37*, 1511–1523.

Jain, S.; Bates, F. S. *Science* **2003**, *300*, 460–464.

Jain, S.; Dyrdahl, M. H. E.; Gong, X.; Scriven, L. E.; Bates, F. S. *Macromolecules* **2008**, *41*, 3305–3316.

Jain, S.; Gong, X.; Scriven, L. E.; Bates, F. S. *Phys. Rev. Lett.* **2006**, *96*, 138304.

Jakes, J. *Collect. Czech. Chem. Commun.* **1995**, *60*, 1781.

Jastorff, B.; Mölter, K.; Behrend, P.; Bottin-Weber, U.; Filser, J.; Heimers, A.; Ondruschka, B.; Ranke, J.; Schaefer, M.; Schröder, H.; Stark, A.; Stepnowski, P.; Stock, F.; Störmann, R.; Stolte, S.; Welz-Biermann, U.; Ziegert, S.; Thöming, J. *Green Chem.* **2005**, *7*, 362–372.

Kamlet, M. J.; Abboud, J. L. M.; Taft, R. W. *Prog. Phys. Org. Chem.* **1981**, *13*, 485.

Kataoka, K.; Harada, A.; Nagasaki, Y. *Adv. Drug Deliver. Rev.* **2001**, *47*, 113.

Kawauchi, T.; Kumaki, J.; Okoshi, K.; Yashima, E. *Macromolecules* **2005**, *38*, 9155–9160.

Kesselman, E.; Talmon, Y.; Bang, J.; Abbas, S.; Li, Z.; Lodge, T. P. *Macromolecules* **2005**, *38*, 6779.

Khandpur, A. K.; Förster, S.; Bates, F. S.; Hamley, I. W.; Ryan, A. J.; Bras, W.; Almdal, K.; Mortensen, K. *Macromolecules* **1995**, *28*, 8796–8806.

Kim, S. H.; Misner, M. J.; Xu, T.; Kimura, M.; Russell, T. P. *Adv. Mater.* **2004**, *16*, 226–231.

Kim, S. H.; Misner, M. J.; Yang, L.; Gang, O.; Ocko, B. M.; Russell, T. P. *Macromolecules* **2006**, *39*, 8473–8479.

Kim, Y. H.; Cheruvally, G.; Choi, J. W.; Ahn, J. H.; Kim, K. W.; Ahn, H. J.; Choi, D. S.; Song, C. E. *Macromol. Symp.* **2007**, *249–250*, 183–189.

Klingshirn, M. A.; Spear, S. K.; Subramanian, R.; Holbrey, J. D.; Huddleston, J. G.; Rogers, R. D. *Chem. Mater.* **2004**, *16*, 3091–3097.

Koppel, D. E. *J. Chem. Phys.* **1972**, *57*, 4814

Kosmulski, M.; Gustafsson, J.; Rosenholm, J. B. *Thermichim. Acta* **2004**, *412*, 41–53.

Krossing, I.; Slattery, J. M.; Daguenet, C.; Dyson, P. J.; Oleinikova, A.; Weingärtner, H. *J. Am. Chem. Soc.* **2006**, *128*, 13427–13434.

Kubisa, P. *Prog. Polym. Sci.* **2004**, *29*, 3–12.

Lai, C.; Russel, W. B.; Register, R. A. *Macromolecules* **2002**, *35*, 841–849.

Lai, C.; Russel, W. B.; Register, R. A. *Macromolecules* **2002**, *35*, 4044–4049.

LaRue, I.; Adam, M.; Pitsikalis, M.; Hadjichristidis, N.; Rubinstein, M.; Sheiko, S. S. *Macromolecules* **2006**, *39*, 309–314.

Lascaud, S.; Perrier, M.; Vallée A.; Besner, S.; Prud'homme, J.; Armand, M. *Macromolecules* **1994**, *27*, 7469–7477.

Lee, J. I.; Cho, S. H.; Park, S.-M.; Kim, J. K.; Kim, J. K.; Yu, J.-W.; Kim, Y. C.; Russell, T. P. *Nano Lett.* **2008**, *8*, 2315–2320.

Leibler, L. *Macromolecules* **1980**, *13*, 1602–1617.

Leibler, L.; Orland, H.; Wheeler, J. C. *J. Phys. Chem.* **1983**, *79*, 3550–3557.

Lewandowski, A.; Świderska, A. *Solid State Ionics* **2004**, *169*, 21–24.

Lin, Z.; Kim, D. H.; Wu, X.; Boosahda, L.; Stone, D.; LaRose, L.; Russell, T. P. *Adv. Mater.* **2002**, *14*, 1373–1376.

Lodge, T. P. *Macromol. Chem. Phys.* **2003**, *204*, 265–273.

Lodge, T. P.; Bang, J.; Li, Z.; Hillmyer, M. A.; Talmon, Y. *Faraday Discuss.* **2005**, *128*, 1–12.

Lodge, T. P.; Hanley, K. J.; Pudil, B.; Alahapperuma, V. *Macromolecules* **2003**, *36*, 816–822.

Lodge, T. P.; Pudil, B.; Hanley, K. J. *Macromolecules* **2002**, *35*, 4707–4717.

Lu, J.; Yan, F.; Texter, J. *Prog. Polym. Sci.* **2009**, *34*, 431–448.

Lu, J.; Yi, S. S.; Kopley, T.; Qian, C.; Liu, J.; Gulari, E. *J. Phys. Chem. B* **2006**, *110*, 6655.

Lund, R.; Willner, L.; Richter, D.; Dormidontova, E. E. *Macromolecules* **2006**, *39*, 4566–4575.

Magonov, S. N.; Reneker, D. H. *Annu. Rev. Mater. Sci.* **1997**, *27*, 175–222.

Marwanta, E.; Mizumo, T.; Nakamura, N.; Ohno, H. *Polymer* **2005**, *46*, 3795–3800.

Matsen, M. W.; Bates, F. S. *Macromolecules* **1996**, *29*, 1091–1098.

Matsen, M. W.; Bates, F. S. *Macromolecules* **1996**, *29*, 7641–7644.

Matsen, M. W.; Schick, M. *Macromolecules* **1994**, *27*, 7157–7163.

Matsen, M. W.; Schick, M. *Phys. Rev. Lett.* **1994**, *72*, 2660–2663.

Matsumoto, H.; Sakaebe, H.; Tatsumi, K.; Kikuta, M.; Ishiko, E.; Kono, M. *J. Power Sources* **2006**, *160*, 1308–1313.

Matsuoka, H.; Nakamoto, H.; Susan, M. A. B. H.; Watanabe, M. *Electrochim. Acta* **2005**, *50*, 4015–4021.

Meli, L.; Lodge, T. P. *Macromolecules* **2009**, *42*, 580–583.

Messé, L.; Corvazier, L.; Young, R. N.; Ryan, A. J. *Langmuir* **2002**, *18*, 2564–2570.

Milhaupt, J. M.; Lodge, T. P.; Smith, S. D.; Hamersky, M. W. *Macromolecules* **2001**, *34*, 5561–5570.

Morton, M. *Anionic Polymerization: Principles and Practice*; Academic Press: New York, 1983.

Muldoon, M. J.; Gordon, C. M.; Dunkin, I. R. *J. Chem. Soc., Perkin Trans. 2* **2001**, 433–435.

Nakamoto, H.; Noda, A.; Hayamizu, K.; Hayashi, S.; Hamaguchi, H.; Watanabe, M. *J. Phys. Chem. C* **2007**, *111*, 1541–1548.

Nakamoto, H.; Watanabe, M. *Chem. Commun.* **2007**, 2539–2541.

Ndoni, S.; Papadakis, C. M.; Bates, F. S.; Almdal, K. *Rev. Sci. Instrum.* **1995**, *66*, 1090–1095.

Ngo, H. L.; LeCompte, K.; Hargens, L.; McEwan, A. B. *Thermochim. Acta* **2000**, *357–358*, 97–102.

Noda, A.; Hayamizu, K.; Watanabe, M. *J. Phys. Chem. B* **2001**, *105*, 4603–4610.

Noda, A.; Susan, M. A. B. H.; Kudo, K.; Mitsushima, S.; Hayamizu, K.; Watanabe, M. *J. Phys. Chem. B* **2003**, *107*, 4024–4033.

Noda, A.; Watanabe, M. *Electrochim. Acta* **2000**, *45*, 1265–1270.

Noolandi, J.; Hong, K. M. *Macromolecules* **1983**, *16*, 1443–1448.

Odian, G. *Priciples of Polymerization*, 4th ed.; John Wiley & Sons, Inc.: Hoboken, 2004.

Ogihara, W.; Kosukegawa, H.; Ohno, H. *Chem. Commun.* **2006**, 3637–3639.

Ohno, H., Ed. *Electrochemical Aspects of Ionic Liquids*; John Wiley & Sons, Inc.: Hoboken, 2005.

Ohno, H.; Nishimura, N. *J. Electrochem. Soc.* **2001**, *148*, E168–E170.

Oostergetel, G. T.; Esselink, F. J.; Hadziioannou, G. *Langmuir* **1995**, *11*, 3721.

Orazem, M. E.; Tribollet, B. *Electrochemical Impedance Spectroscopy*; John Wiley & Sons, Inc.: Hoboken, 2008.

Pacovská, M.; Procházka, K.; Tuzar, Z.; Munk, P. *Polymer* **1993**, *34*, 4585–4588.

Panday, A.; Mullin, S.; Gomez, E. D.; Wanakule, N.; Chen, V. L.; Hexemer, A.; Pople, J.; Balsara, N. P. *Macromolecules* **2009**, *42*, 4632–4637.

Pangborn, A. B.; Giardello, M. A.; Grubbs, R. H.; Rosen, R. K.; Timmers, F. J. *Organometallics* **1996**, *15*, 1518–1520.

Park, S.; Kim, B.; Xu, J.; Hofmann, T.; Ocko, B. M.; Russell, T. P. *Macromolecules* **2009**, *42*, 1278–1284.

Pârvulescu, V. I.; Hardacre, C. *Chem. Rev.* **2007**, *107*, 2615–2665.

Perrier, S.; Davis, T. P.; Carmichael, A. J.; Haddleton, D. M. *Eur. Polym. J.* **2003**, *39*, 417–422.

Plechkova, N.; Seddon, K. R. *Chem. Soc. Rev.* **2008**, *37*, 123–150.

Poole, C. F. *J. Chromatogr. A* **2004**, *1037*, 49–82

Rager, T.; Meyer, W. H.; Wegner, G. *Macromol. Chem. Phys.* **1999**, *200*, 1672–1680.

Reichardt, C. *Green Chem.* **2005**, *7*, 339–351.

Reichardt, C. *Solvents and Solvent Effects in Chemistry*, Wiley-VCH: Weinheim, 2003.

Remsing, R. C.; Swatloski, R. P.; Rogers, R. D.; Moyna, G. *Chem. Commun.* **2006**, 1271–1273

Robitaille, C. D.; Fauteax, D. J. *J. Electrochem. Soc.* **1986**, *133*, 315–325.

Roe, R.-J. *Methods of X-Ray and Neutron Scattering in Polymer Science*; Oxford University Press: New York, 2000.

Rogers, R. D.; Seddon, K. R., Eds. *ACS Symposium Series, 901*; American Chemical Society: Washington, DC, 2005.

Rupp, B.; Schmuck, M.; Balducci, A.; Winter, M.; Kern, W. *Eur. Polym. J.* **2008**, *44*, 2986–2990.

Sadron, C.; Gallot, B. *Makromol. Chem.* **1973**, *164*, 301–332.

Sakaebe, H.; Matsumoto, H.; Tatsumi, K. *J. Power Sources* **2005**, *146*, 693–697.

Savic, R.; Luo, L.; Eisenberg, A.; Maysinger, D. *Science* **2003**, *300*, 615.

Sax, J.; Ottino, J. M. *Polym. Eng. Sci.* **1983**, *23*, 165–176.

Schillén, K.; Yekta, A.; Ni, S.; Winnik, M. A. *Macromolecules* **1998**, *31*, 210–212.

Schröder, U.; Wadhawan, J. D.; Compton, R. G.; Marken, F.; Suarez, P. A. Z.; Consorti, C. S.; de Souza, R. F.; Dupont, J. *New J. Chem.* **2000**, *24*, 1009–1015.

Seki, S.; Ohno, Y.; Kobayashi, Y.; Miyashiro, H.; Usami, A.; Mita, Y.; Tokuda, H.; Watanabe, M.; Hayamizu, K.; Tsuzuki, S.; Hattori, M.; Terada, N. *J. Electrochem. Soc.* **2007**, *154*, A173–A177.

Seki, S.; Ohno, Y.; Miyashiro, H.; Kobayashi, Y.; Usami, A.; Mita, Y.; Terada, N.; Hayamizu, K.; Tsuzuki, S.; Watanabe, M. *J. Electrochem. Soc.* **2008**, *155*, A421–A427.

Semenov, A. N. *Sov. Phys. JETP* **1985**, *61*, 733–742.

Sheiko, S. S. *Adv. Polym. Sci.* **2000**, *151*, 61–174.

Shibayama, M.; Hashimoto, T.; Kawai, H. *Macromolecules* **1983**, *16*, 16–28.

Shimano, S.; Zhou, H.; Honma, I. *Chem. Mater.* **2007**, *19*, 5216–5221.

Shimura, H.; Yoshio, M.; Hoshino, K.; Mukai, T.; Ohno, H.; Kato, T. *J. Am. Chem. Soc.* **2008**, *130*, 1759–1765.

Shin, J.-H.; Henderson, W. A.; Tizzani, C.; Passerini, S.; Jeong, S.-S.; Kim, K.-W. *J. Electrochem. Soc.* **2006**, *153*, A1649–A1654.

Shin, J.-H.; Henderson, W. A.; Tizzani, C.; Passerini, S.; Jeong, S.-S.; Kim, K.-W. *J. Electrochem. Soc.* **2006**, *9*, A1649–A1654.

Shin, K.; Leach, K. A.; Goldbach, J. T.; Kim, D. H.; Jho, J. Y.; Tuominen, M.; Hawker, C. J.; Russell, T. P. *Nano Lett.* **2002**, *2*, 933–936.

Siegel, D. P.; Green, W. J.; Talmon, Y. *Biophys. J.* **1994**, *66*, 402.

Singh, B.; Sekhon, S. S. *Chem. Phys. Lett.* **2005**, *414*, 34–39.

Singh, M.; Odusanya, O.; Wilmes, G. M.; Eitouni, H. B.; Gomez, E. D.; Patel, A. J.; Chen, V. L.; Park, M. J.; Fragouli, P.; Iatrou, H.; Hadjichristidis, N.; Cookson, D.; Balsara, N. P. *Macromolecules* **2007**, *40*, 4578–4585.

Snedden, P.; Cooper, A. I.; Scott, K.; Winterton, N. *Macromolecules* **2003**, *36*, 4549–4556.

Štěpánek, M.; Procházka, K.; Brown, W. *Langmuir* **2000**, *16*, 2502–2507.

Susan, M. A. B. H.; Kaneko, T.; Noda, A.; Watanabe, M. *J. Am. Chem. Soc.* **2005**, *127*, 4976–4983.

Susan, M. A. B. H.; Noda, A.; Mitsushima, S.; Watanabe, M. *Chem. Commun.* **2003**, 938–939.

Sutto, T. E. *J. Electrochem. Soc.* **2007**, *154*, P101–P107.

Swatloski, R. P.; Spear, S. K.; Holbrey, J. D.; Rogers, R. D. *J. Am. Chem. Soc.* **2002**, *124*, 4974–4975.

Taft, R. W.; Abboud, J. L. M.; Kamlet, M. J.; Abraham, M. H. *J. Solution Chem.* **1985**, *14*, 153.

Tanford, C. *The Hydrophobic Effect: Formation of Micelles and Bilogical Membranes*, 2nd ed.; Wiley: New York, 1980.

Tepe, T.; Schulz, M. F.; Zhao, J.; Tirrell, M.; Bates, F. S.; Mortensen, K.; Almdal, K. *Macromolecules* **1995**, *28*, 3008–3011.

Tian, M.; Qin, A.; Ramireddy, C.; Webber, S. E.; Munk, P. *Langmuir* **1993**, *9*, 1741–1748.

Tigelaar, D. M.; Meador, M. A. B.; Bennett, W. R. *Macromolecules* **2007**, *40*, 4159–4164.

Tiyapiboonchaiya, C.; MacFarlane, D. R.; Sun, J.; Forsyth, M. *Macromol. Chem. Phys.* **2002**, *203*, 1906–1911.

Tokuda, H.; Hayamizu, K.; Ishii, K.; Susan, M. A. B. H.; Watanabe, M. *J. Phys. Chem. B* **2004**, *108*, 16593–16600.

Tokuda, H.; Hayamizu, K.; Ishii, K.; Susan, M. A. B. H.; Watanabe, M. *J. Phys. Chem. B* **2005**, *109*, 6103–6110.

Tokuda, H.; Ishii, K.; Susan, M. A. B. H.; Tsuzuki, S.; Hayamizu, K.; Watanabe, M. *J. Phys. Chem. B* **2006**, *110*, 2833–2839.

Triolo, A.; Mandanici, A.; Russina, O.; Rodriguez-Mora, V.; Cutroni, M.; Hardacre, C.; Nieuwenhuyzen, M.; Bleif, H.-J.; Keller, L.; Ramos, M. A. *J. Phys. Chem. B* **2006**, *110*, 21357–21364.

Ueki, T.; Watanabe, M. *Chem. Lett.* **2006**, *35*, 964–965.

Ueki, T.; Watanabe, M. *Langmuir* **2007**, *23*, 988–990.

Ueki, T.; Watanabe, M. *Macromolecules* **2008**, *41*, 3739–3749.

Ueki, T.; Watanabe, M.; Lodge, T. P. *Macromolecules* **2009**, *42*, 1315–1320.

Ueno, K.; Hata, K.; Katakabe, T.; Kondoh, M.; Watanabe, M. *J. Phys. Chem. B* **2008**, *112*, 9013–9019.

Vijayaraghavan, R.; MacFarlane, D. R. *Chem. Commun.* **2005**, 1149–1151.

Virgili, J. M.; Hexemer, A.; Pople, J. A.; Balsara, N. P.; Segalman, R. A. *Macromolecules* **2009**, *42*, 4604–4613.

Wakai, C.; Oleinikova, A.; Ott, M.; Weingärtner, H. *J. Phys. Chem. B* **2005**, *109*, 17028–17030.

Walden, P. *Bull. Acad. Imper. Sci. (St. Petersburg)* **1914**, 1800.

Wang, J.-Y.; Chen, W.; Roy, C.; Sievert, J. D.; Russell, T. P. *Macromolecules* **2008**, *41*, 963–969.

Wang, J.-Y.; Chen, W.; Sievert, J. D.; Russell, T. P. *Langmuir* **2008**, *24*, 3545–3550.

Wang, Y.; Balaji, R.; Quirk, R. P.; Mattice, W. L. *Polym. Bull.* **1992**, *28*, 333–338.

Wang, Y.; Hong, X.; Liu, B.; Ma, C.; Zhang, C. *Macromolecules* **2008**, *41*, 5799–5808.

Wanka, G.; Hoffmann, H.; Ulbricht, W. *Macromolecules* **1994**, *27*, 4145–4159.

Wasserscheid, P.; Welton, T., Eds. *Ionic Liquids in Synthesis*, 2nd ed.; Wiley-VCH: Weinheim, 2008.

Weingärtner, H. *Angew. Chem. Int. Ed.* **2007**, *46*, 2–19.

Weingärtner, H. *Z. Phys. Chem.* **2006**, *220*, 1395–1405.

Welton, T. *Chem. Rev.* **1999**, *99*, 2071–2083.

Wilkes, J. S.; Levisky, J. A.; Wilson, R. A.; Hussey, C. L. *Inorg. Chem.* **1982**, *21*, 1263.

Wilkes, J. S.; Zaworotko, M. J. *J. Chem. Soc., Chem. Commun.* **1992**, 965–967.

Williams, D. B.; Carter, C. B. *Transmission Electron Microscopy: A Textbook for Materials, Science*; Plenum Press: New York, 1996.

Willner, L.; Poppe, A.; Allgaier, J.; Monkenbusch, M.; Richter, D. *Europhys. Lett.* **2001**, *55*, 667–673.

Winterton, N. *J. Mater. Chem.* **2006**, *16*, 4281–4293.

Won, Y.-Y.; Brannan, A. K.; Davis, H. T.; Bates, F. S. *J. Phys. Chem. B* **2002**, *106*, 3354–3364.

Won, Y.-Y.; Davis, H. T.; Bates, F. S. *Macromolecules* **2003**, *36*, 953–955.

Won, Y.-Y.; Davis, H. T.; Bates, F. S. *Science* **1999**, *283*, 960–963.

Xie, H.; Li, S.; Zhang, S. *Green Chem.* **2005**, *7*, 606–608.

Xu, C.; Ohno, K.; Ladmiral, V.; Milkie, D. E.; Kikkawa, J. M.; Composto, R. J. *Macromolecules* **2009**, *42*, 1219–1228.

Xu, K. *Chem. Rev.* **2004**, *104*, 4303–4417.

Xu, T.; Hawker, C. J.; Russell, T. P. *Macromolecules* **2003**, *36*, 6178–6182.

Xu, T.; Zhu, Y.; Gido, S. P.; Russell, T. P. *Macromolecules* **2004**, *37*, 2625–2629.

Xu, T.; Zvelindovsky, A. V.; Sevink, G. J. A.; Lyakhova, K. S.; Jinnai, H.; Russell, T. P. *Macromolecules* **2005**, *38*, 10788–10798.

Xu, W.; Angell, C. A. *Science* **2003**, *302*, 422–425.

Yeon, S.-H.; Kim, K.-S.; Choi, S.; Cha, J.-H.; Lee, H. *J. Phys. Chem. B* **2005**, *109*, 17928–17935.

Yoshio, M.; Kagata, T.; Hoshino, K.; Mukai, T.; Ohno, H.; Kato, T. *J. Am. Chem. Soc.* **2006**, *128*, 5570–5577.

Young, W.-S.; Brigandi, P. J.; Epps, T. H. *Macromolecules* **2008**, *41*, 6276–6279.

Young, W.-S.; Epps, T. H. *Macromolecules* **2009**, *42*, 2672–2678.

Zaitsau, D. H.; Kabo, G. J.; Strechan, A. A.; Paulechka, Y. U.; Tschersich, A.; Verevkin, S. P.; Heintz, A. *J. Phys. Chem. A* **2006**, *110*, 7303–7306.

Zalusky, A. S.; Olayo-Valles, R.; Wolf, J. H.; Hillmyer, M. A. *J. Am. Chem. Soc.* **2002**, *124*, 12761–12773.

Zhang, H.; Hong, K.; Jablonsky, M.; Mays, J. W. *Chem. Commun.* **2003**, 1356–1357.

Zhang, H.; Hong, K.; Mays, J. W. *Macromolecules* **2002**, *35*, 5738–5741.

Zhang, L.; Barlow, R. J.; Eisenberg, A. *Macromolecules* **1995**, *28*, 6055.

Zhang, L.; Eisenberg, A. *Science* **1995**, *268*, 1728.

Zhang, S.; Li, N.; Zheng, L.; Li, X.; Gao, Y.; Yu, L. *J. Phys. Chem. B* **2008**, *112*, 10228–10223.

Zhao, D.; Liao, Y.; Zhang, Z. *Clean* **2007**, *35*, 42–48.

Zhu, C.; Cheng, H.; Yang, Y. *J. Electrochem. Soc.* **2008**, *155*, A569–A575.

Zhulina, E. B.; Adam, M.; LaRue, I.; Sheiko, S. S.; Rubinstein, M. *Macromolecules* **2005**, *38*, 5330–5351.